# Instabilités, ondes, et turbulence en rotation

Frederic Moisy

**Synthèse des travaux**
**présentée à l'Université Paris-Sud 11**

pour obtenir le

## Diplôme d'Habilitation à Diriger des Recherches

par

**Frédéric Moisy**

Maître de Conférences de l'Université Paris-Sud 11
Laboratoire Fluides, Automatique et Systèmes Thermiques (FAST)

# Instabilités, ondes, et turbulence en rotation

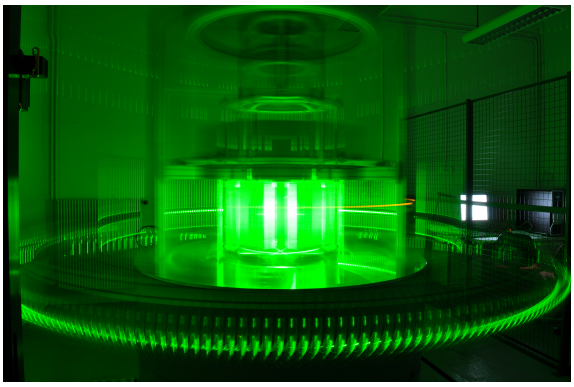

Soutenue le 10 septembre 2010, devant le jury composé de :

| | | |
|---|---|---|
| *Président* | Jean-Marc Chomaz | DR CNRS, LadHyX, Ecole Polytechnique |
| *Rapporteurs* | Claude Cambon | DR CNRS, Ecole Centrale de Lyon |
| | Stephan Fauve | Professeur, LPS, Ecole Normale Supérieure, Paris |
| | Patrice Le Gal | DR CNRS, IRPHE, Marseille |
| *Examinateurs* | Stuart Dalziel | Senior Lecturer, DAMTP, Cambridge |
| | Emmanuel Trizac | Professeur, LPTMS, Université Paris-Sud |
| *Invité* | Joël Sommeria | DR CNRS, LEGI, Grenoble |

# Remerciements

C'est un grand honneur que m'ont fait Claude Cambon, Jean-Marc Chomaz, Stuart Dalziel, Stephan Fauve, Patrice Le Gal, Joël Sommeria et Emmanuel Trizac, d'accepter de faire partie de ce jury de thèse d'habilitation. Je veux les remercier ici pour leur lecture critique et attentive de mes travaux, mais aussi pour leur confiance et leurs encouragements depuis de nombreuses années.

Je me trouve chanceux : mon parcours de chercheur a été jalonné de quelques grands noms de la physique et de la mécanique des fluides. Ils m'ont encouragé dans mon parcours, parfois sans le savoir, et leur personnalité, leur exigence, leur regard scientifique, déteignent sur mon travail depuis plus de dix ans. Merci donc pour tout cela à Yves Couder, Yves Gagne, Jean-Pierre Hulin, Javier Jiménez, Marc Rabaud, Patrick Tabeling, Laurette Tuckerman. C'est forcément un peu plus facile lorsque l'on peut s'asseoir sur les épaules de géants.

Puisque le diplôme d'habilitation permet l'encadrement de doctorants, je souhaite remercier ici ceux qui m'ont apporté leur confiance et que j'ai pu encadrer avant même l'obtention de ce diplôme : Cyprien Morize et Jémil Znaien[1], maintenant docteurs, ainsi que Cyril Lamriben, qui est en très bonne voie.

Le laboratoire FAST est un endroit qui me convient plutôt bien pour mes travaux de recherche. Outre les moyens confortables dont j'ai pu bénéficier pour mener à bien mes projets depuis mon recrutement en septembre 2000, j'apprécie également la grande liberté qui m'a été offerte dans le choix de mes thématiques de recherche. Je veux remercier ici Dominique Salin et Neil Ribe, directeurs successifs de ce laboratoire pendant cette dizaine d'année, qui ont su créer, maintenir et animer cet excellent contexte scientifique et humain. Je souhaite faire figurer en bonne place dans cette page toutes celles et tous ceux qui rendent la vie d'un chercheur plus facile, tant dans ses aspects techniques et expérimentaux — Alban Aubertin, Lionel Auffray, Christian Borget, Guy-Jean Michon, Babacar Ndoye, Rafaël Pidoux —, que dans ses aspects administratifs, de gestion et de service — Léonor Alves, Maryse Labrude, et Monique Sainte-Rose.

J'ai eu l'opportunité de collaborer avec un grand nombre de personnes pendant ces dix années passées au FAST. Leurs noms sont donnés dans le chapitre d'introduction qui suit, mais je les remercie ici chaleureusement pour tout ce qu'ils m'ont apporté. Je veux remercier en particulier les membres de l'équipe Instabilités et Turbulence, et notamment Marc Rabaud et Philippe Gondret, qui m'ont accueilli lors de mon arrivée au FAST et m'ont laissé rapidement développer mes projets. Je remercie également le tout nouveau petit groupe "Gyroflow", Pierre-Philippe Cortet et Cyril Lamriben, qui contribuent à porter avec beaucoup d'énergie la thématique de la turbulence en rotation qui me tient à cœur. Je veux remercier ici aussi celles et ceux qui se prêtent aux discussions de "sciences amusantes" à la cantine, qui comptent

[1] J'ai juste échoué de quelques 343 jours à notre petit concours de celui qui soutiendra en premier.

beaucoup pour moi. Enfin, je remercie les membres des projets ANR “HiSpeed PIV” et “GIMIC”, ainsi que ceux du GDR turbulence, qui ont beaucoup apporté à mon travail. Il y a encore beaucoup de projets dans les cartons ; tous n'aboutiront pas, mais tous ont donné lieu et continuent à alimenter des échanges passionants.

L'exercice veut que ce manuscrit soit centré sur mes activités de recherche. Pourtant, l'enseignement tient pour une part essentielle de mon activité, et sa frontière avec la recherche est un flou que j'entretiens avec plaisir. La plus grande partie de ce que je sais, notamment dans le domaine de la turbulence, c'est en l'enseignant que je l'ai appris. Je remercie ici tous mes collègues enseignants, particulièrement mes collègues du LIMSI et du FAST qui enseignent dans notre filière de mécanique physique, ainsi bien sûr que Mireille Bordelais, Catherine Groell et Nadège Ibis, qui organisent et animent la vie du bâtiment 507 avec énergie et bonne humeur.

Enfin, je remercie chaleureusement ici mes parents et ma famille, pour leur patience et leur confiance, ma belle-famille aussi,

et Esther, Carla, Pablo, pour leur présence et en m'excusant pour le temps qui manque, et leur petit frêre ou petite sœur à venir, à qui je promets de mieux savoir donner de ce temps.

Bures sur Yvette, le 20 septembre 2010.

# Table des matières

# Introduction

## Organisation de ce mémoire

Ce mémoire présente une synthèse de mes travaux de recherche effectués depuis mon recrutement au laboratoire FAST en septembre 2000. Mes travaux sont essentiellement organisés autour de 4 axes : les instabilités dans les écoulements de von Kármán, les ondes d'inertie, la turbulence en rotation, et les ondes de surface.

Ces 4 axes de recherche ont entre eux un certain nombre de connections, comme l'influence de la rotation sur la nature d'un écoulement laminaire ou turbulent, ou encore les systèmes d'ondes dispersives en interaction, qu'il s'agisse des ondes capillaires ou des ondes d'inertie en référentiel tournant. D'un point de vue expérimental, ces axes de recherche ont également en commun l'utilisation de méthodes de mesure optiques, qu'il s'agisse de la Vélocimétrie par Images de Particules (PIV), méthode aujourd'hui standard en mécanique des fluides, ou encore du "Synthetic Schlieren", que nous avons étendu au cas des ondes de surface (Free-Surface Synthetic Schlieren [99]).

Dans ce mémoire, je m'efforcerai de donner les grandes lignes de mes travaux selon ces 4 axes de recherche. D'autres contributions sont rapidement évoquées dans cette introduction, mais ne feront pas l'objet de développements dans les chapitres qui suivent. Chaque chapitre est suivi de quelques publications les plus significatives, indiquées ci-dessous en gras[2] :

- Chapitre 1 : Instabilités dans les écoulements de von Kármán (2000-2005) :
  1. Gauthier, Gondret, Moisy & Rabaud (J. Fluid Mech, 2002) [61]
  2. Moisy, Pasutto & Rabaud (Nonlinear Proc. Geoph 2003) [97]
  3. **Moisy, Doare, Pasutto, Daube & Rabaud (J. Fluid Mech, 2004)** [91]
  4. **Nore, Moisy & Quartier (Phys. Fluids, 2005)** [108].
- Chapitre 2 : Ondes d'inertie (depuis 2006) :
  1. Messio, Morize, Rabaud & Moisy (Exp. in Fluids, 2008) [86]
  2. **Cortet, Lamriben & Moisy (Phys. Fluids, 2010)** [36]
- Chapitre 3 : Turbulence en rotation (depuis 2004) :
  1. **Morize, Moisy & Rabaud (Phys. Fluids, 2005)** [104]
  2. Morize & Moisy (Phys. Fluids, 2006) [103]
  3. **Seiwert, Morize & Moisy (Phys. Fluids, 2008)** [120]

[2]L'ensemble des articles est disponible à l'adresse `www.fast.u-psud.fr/~moisy`.

4. **Moisy, Morize, Rabaud & Sommeria (J. Fluid Mech, sous presse, 2010)** [95].

– Chapitre 4 : Ondes de surface (depuis 2007) :

1. **Moisy, Rabaud & Salsac (Exp. in Fluids, 2009)** [99]
2. Eddi, Fort, Moisy & Couder (Phys. Rev. Lett., 2009) [51]

Chaque chapitre a pour objectif de situer le contexte et les enjeux des différentes contributions. Il ne s'agira pas de donner une revue des travaux existants, mais simplement d'offrir une bibliographie restreinte à quelques contributions, soit parce qu'elles fondent ou ont motivé directement mes travaux, soit parce qu'elles constituent des développements récents interessants qui pourront orienter mes recherches dans le futur. Enfin, je présenterai dans les chapitres 2, 3 et 4 quelques pistes de recherche pour les années à venir.

Cette introduction est l'occasion de mettre en avant l'ensemble des collaborateurs qui ont contribué aux travaux présentés dans ce mémoire.

### Avant le FAST

Après ma thèse, effectuée au Laboratoire de Physique Statistique (ENS Paris) sous la direction de Patrick Tabeling et Hervé Willaime, et portant sur l'étude de la turbulence pleinement développée dans l'hélium à basse température [88], j'ai eu l'opportunité de travailler en collaboration avec Javier Jiménez (Ecole Aéronautique, Madrid). L'objectif de cette étude était de caractériser la distribution spatiale des structures tourbillonnaires intenses (Moisy & Jimenez (2004,2006) [92, 93]), à partir d'une base de données de simulation numérique directe de turbulence isotrope. Ces travaux ne sont pas repris dans ce mémoire.

### Instabilités dans les écoulements de von Kármán

J'ai abordé l'étude des instabilités en cavité interdisque à partir de 2000, à la suite des travaux de thèse de Georges Gauthier au FAST [60]. Cette étude s'est concentrée principalement sur les instabilités de cisaillement dans l'écoulement en contrarotation différentielle à grand rapport d'aspect (cavité fine), et a bénéficié des premières mesures de vélocimétrie par images de particules mises en œuvre au laboratoire.

Ce travail a été mené avec Marc Rabaud et Philippe Gondret au FAST, Olivier Daube au LME (Université d'Evry), ainsi que Thomas Pasutto (stage de Master 2) et Olivier Doaré (alors ATER au FAST). Il s'est poursuivi en 2004 par une caractérisation des bifurcations dans l'écoulement de von Kármán exactement contra-rotatif, avec en particulier le résultat d'une mise en évidence expérimentale de cycles hétéroclines. Ce second volet a été mené en collaboration avec Caroline Nore (LIMSI, Université Paris-Sud) et Laurette Tuckerman (LIMSI, PMMH-ESPCI), avec l'aide de Laurent Quartier (LPS, ENS).

### Ondes d'inertie et turbulence en rotation

Ces deux axes de recherche, qui constituent les chapitres 2 et 3 de ce mémoire, ont été introduits en 2004 au laboratoire FAST. Ils ont donné lieu à deux thèses, celle de Cyprien

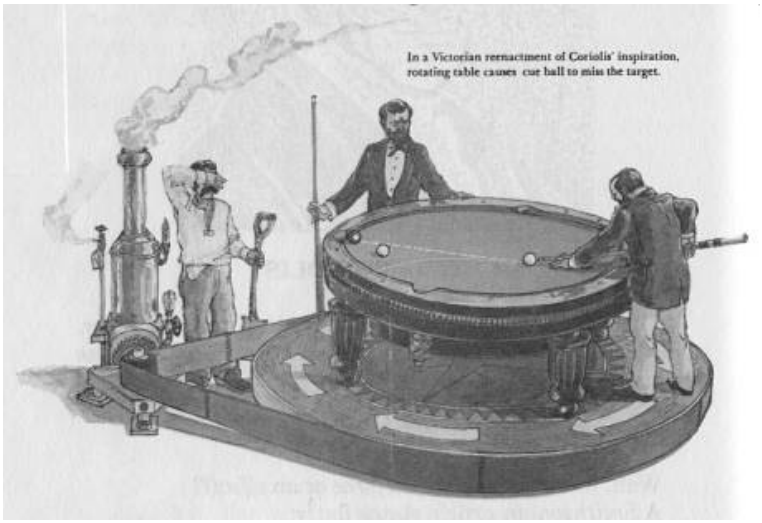


FIG. 1 – Les travaux de G.G. Coriolis portent sur la théorie mathématique des effets du jeu de billard (1835, 174 p.), ainsi que sur les forces vives dans les mouvements relatifs des Machines (1832 et 1835, 48 p.) [33]. Cette illustration est issue de l'article de vulgarisation d'A. Linn (1983) [76].

Morize (soutenue en 2006) [101], co-encadrée avec Marc Rabaud, et celle de Cyril Lamriben, co-encadrée avec Pierre-Philippe Cortet (débutée en 2009).

Cette thématique autour des écoulements en rotation a pu démarrer grâce à une plateforme tournante (la "*petite*" plateforme), gracieusement cédée par Alexandre Stegner, qui avait été conçue lors de sa thèse au Laboratoire de Météorologie Dynamique (ENS). Le montage a ensuite bénéficié d'améliorations successives, au gré des expériences menées avec Cyprien Morize, Laura Messio, Guangkun Tan, Jacopo Seiwert, Lionel Agostini, Thomas Serandon. L'heure de la retraite a désormais probablement sonné pour cette plateforme.

Par ailleurs, cette thématique a bénéficié d'une collaboration fructueuse avec Joël Sommeria au laboratoire LEGI à Grenoble. Une campagne de mesure sur la plateforme Coriolis (la "*grande*" plateforme), réalisée en février 2005, a pu être menée avec Cyprien Morize, grâce à l'implication et à la grande disponibilité de Henri Didelle et Samuel Viboud.

Cette aventure continue désormais au laboratoire FAST, avec la mise en place en 2009 d'une nouvelle plateforme tournante, baptisée "Gyroflow" (la "*moyenne*" plateforme). La conception et la mise en service de ce nouvel équipement a mobilisé beaucoup de monde : Patrice Jenffer, Alban Aubertin, Lionel Auffray, Raphael Pidoux, Christian Borget et Guy-Jean Michon. C'est maintenant en compagnie de Cyril Lamriben et de Pierre-Philippe Cortet, arrivés en 2009 au laboratoire, que je poursuis mes recherches dans cette thématique.

Les progrès dans ce sujet difficile ont été rendus possibles grâce à de nombreuses discussions, principalement dans le cadre du GDR Turbulence ou du projet ANR Blanc "HiSpeedPIV" (2006-2010). Parmi ces nombreux échanges, je souhaite citer en particulier ceux avec Claude Cambon et Fabien Godeferd (Ecole Centrale de Lyon), Sébastien Galtier (IAS, Université Paris-Sud), Maurice Rossi (Institut Jean Le Rond D'Alembert), Charles Baroud (LadHyX, Ecole Polytechnique), Thierry Dauxois (ENS Lyon), Leo Maas (Université d'Utrecht) et Herman Clercx (Université de Technologie d'Eindhoven).

### Ondes de surface

L'étude des ondes de surface, débutée en 2007, constitue le quatrième et dernier chapitre de ce mémoire. Cette étude, menée avec Marc Rabaud, est en fait constituée de 2 volets distincts : Un premier volet métrologique, en 2007-08, a permis le développement d'une méthode optique de mesure de la topographie d'une interface liquide, que nous avons baptisée Free-Surface Synthetic Schlieren (FS-SS). L'aspect métrologique de ce travail a bénéficié de la participation expérimentale de Kevin Salsac et d'Edouard Pinsolle (stagiaires), ainsi que de fructueuses discussions avec John D'Errico, Maurice Rossi et Guy Demoment. Dans un second temps, une étude des ondes transverses générées par l'oscillation d'un obstacle immergé, basée sur la méthode FS-SS, a été démarrée avec Guy-Jean Michon (FAST). Eric Sultan (FAST) nous a rejoints récemment pour participer à la modélisation de ces ondes.

Cet axe de recherche a donné lieu à deux collaborations actives. Une première, avec Yves Couder, Emmanuel Fort et Antonin Eddi (MSC, Université Denis Diderot - Paris 7), a porté sur l'étude d'un système physique original introduit par Y. Couder en 2005 [37], appelé un "marcheur" (une goutte liquide interagissant avec le champ d'onde qu'elle génère par son rebond sur un bain liquide vibré verticalement). Une seconde collaboration avec Germain Rousseau (Université de Nice), démarrée en 2008, vise à mettre à profit la méthode FS-SS pour la caractérisation de ressauts hydrodynamiques, dans le problème plus général de l'interaction de paquets d'ondes advectés par un écoulement à vitesse variable. Enfin, des discussions avec les groupes d'Elie Raphaël (ESPCI) et de Christophe Clanet (LadHyx) ont débuté afin d'appliquer cette méthode au problème de la traînée de sillage.

### Mélange turbulent induit par gravité

Le problème du mélange de deux fluides miscibles de densité différentes a été initié par Jean-Pierre Hulin au FAST en 2001 [43]. Une clef de ce problème réside dans le lien entre les propriétés du mélange au niveau macroscopique, caractérisé par un coefficient de diffusion effectif, et le transfert de masse à petite échelle induit par la turbulence. La mise en place de mesures de PIV depuis 2007, dans le cadre de la thèse de Jémil Znaien (2009) [145], a permis de caractériser finement les différents régimes d'écoulement. Cette étude s'est poursuivie en 2008 par des mesures couplées PIV-LIF, dans le cadre du stage post-doctoral de Yukie Tanino, avec l'objectif de caractériser expérimentalement le transport de masse dans ce système. Ces travaux ont bénéficié d'un grand nombre de discussions dans le cadre du projet ANR "Gimic", notamment avec John Hinch (DAMTP, Cambridge), Dominique Salin (FAST), et autour des équipes Bernard Castaing à l'ENS Lyon et de Jacques Magnaudet à l'IMFT Toulouse.

Ces travaux, présentés en détail dans la thèse de Jémil Znaien [145] ainsi que dans les articles Znaien *et al.* (2009,2010) [146, 147], ne sont pas repris dans ce manuscrit.

### Développements logiciels

On peut constater une convergence croissante d'intérêts et de compétences entre le monde des expérimentateurs et celui des numériciens. L'expérimentateur en mécanique des fluides, surtout s'il utilise des techniques de traitement d'images de type PIV ou synthetic Schlieren, est confronté à des volumes de stockage et de traitement croissants, et doit développer des compétences de plus en plus pointues en informatique.

Dans le cadre de mes travaux de recherche, j'ai développé une bibliothèque de fonctions sous Matlab intitulée PIVMat, dédiée au traitement des champs de vecteurs pour les ap-

plications de PIV et de FS-SS. Cette "*toolbox*" est distribuée gratuitement sous licence BSD (Berkeley software distribution license), et est aujourd'hui utilisée par une trentaine de groupes environ. Cette bibliothèque a pu bénéficier depuis 2005 d'un grand nombre de suggestions et d'améliorations proposées par cette petite communauté d'utilisateurs[3].

### Soutiens financiers

Outre le soutien financier des organismes de tutelle du laboratoire FAST (CNRS, Université Paris-Sud, Université Pierre et Marie Curie), mes travaux ont pu bénéficier d'un certain nombre de soutiens : Bourse Qualité Recherche de l'Université Paris-Sud et Action Spécifique de l'UPMC en 2002 (pour l'achat du système de PIV basse-cadence), projet blanc ANR "HiSpeedPIV" en 2006-2010 avec le LIMSI, l'IAS, l'IJLRA, l'ENSTA et le LadHyX, et enfin un soutien par le "Triangle de la Physique" en 2009-2010 pour la mise en place de la nouvelle plateforme tournante "Gyroflow".

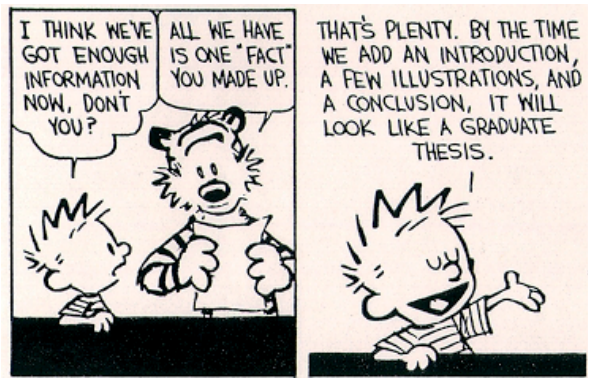


[3]La liste des contributeurs est donnée sur la page `www.fast.u-psud.fr/pivmat/html/pivmat_thanks.html`.

# Curriculum Vitæ

## Etat Civil

Frédéric Moisy
35 ans, né le 28 novembre 1974 à Paris 13ème,
Marié, 2 enfants,
Nationalité française

## Situation actuelle

Maître de Conférences à l'Université Paris-Sud, 60ème section
Recruté en septembre 2000, titularisé en septembre 2002.
Délégation CNRS à mi-temps depuis Septembre 2008.

Laboratoire FAST (Fluides, Automatique et Systèmes Thermiques)
UMR 7608, Université Pierre et Marie Curie, Université Paris-Sud 11.
Bâtiment 502, rue du Belvédère
Campus Universitaire
91405 Orsay Cedex

Tel : 01 69 15 80 37
Mel : `moisy@fast.u-psud.fr`
Page web : `http://www.fast.u-psud.fr/~moisy`

## Formation

1997 D.E.A. Champs, Particules, Matières, option Matière Ordre et Désordre, Université Pierre et Marie Curie - Paris 6 (mention bien).

2000 Doctorat de l'Université Pierre et Marie Curie - Paris 6 : "Etude expérimentale des fluctuations de vitesse, de température et de pression en turbulence développée" (direction P. Tabeling), au Laboratoire de Physique Statistique, ENS, obtenu le 25 Janvier 2000, mention très honorable avec félicitations du jury.

## Activités de Recherche

– Depuis 2007, Mélange turbulent induit par gravité. Collaboration avec J.P. Hulin (FAST), B. Castaing (ENS Lyon), J. Magnaudet (IMFT Toulouse), J. Hinch (DAMTP Cam-

bridge).
- Depuis 2006 Mesures d'interfaces fluides déformées par corrélations d'images réfractées ; application à l'étude des ondes transverses. Collaboration avec Y. Couder (MSC, Université Paris-Diderot).
- Depuis 2004, Turbulence en rotation : Déclin d'énergie, asymétrie cyclone-anticyclone, intermittence. Expériences en cuve tournante au FAST Campagne de mesures sur la plateforme "Coriolis" (LEGI, Grenoble), en collaboration avec J. Sommeria.
- 2000-2005 Instabilités entre disques tournants. Collaborations avec O. Daube (LME, Université d'Evry) et C. Nore (LIMSI, Univ. Paris-Sud).
- 2000-2003 Géométrie des structures intenses en turbulence isotrope. Collaboration avec J. Jiménez, Ecole d'Aéronautique, Univ. Politecnica, Madrid (2 séjours, 3 mois).
- 1997-2000 Turbulence et mélange dans l'hélium à basse température (Thèse de doctorat au LPS - ENS, avec P. Tabeling).
- 1998 Mesures de pression dans un tourbillon étiré. Collaboration avec P. Petitjeans, Laboratoire de Physique et Mécanique des Milieux Hétérogènes, ESPCI, Paris.
- 1998 Visualisation de structures de basse pression par cavitation en turbulence développée. Collaboration avec E. Bodenschatz, Laboratory of Atomic and Solid State Physics, Cornell University (séjour de 2 mois).

## Distinctions

- Prix du 9ème colloque Alain Bouyssy, Université Paris-Sud, février 2001.
- Prix "Gallery of Fluid Motion", Amrican Physical Society, Division of Fluid Dynamics, novembre 2002.
- Prime d'Encadrement Doctoral et de Recherche (2006-2010), puis Prime d'Excellence Scientifique (depuis 2010).

## Projets financés

- Porteur du projet Triangle de la Physique "GeoFlow" (2009-2010), montant : 70 000 euros.
- Porteur du projet ANR blanc "HiSpeed PIV" (2006-2010), montant : 500 000 euros partagés entre 4 laboratoires.
- Bourse Qualité Recherche de l'Université Paris-Sud, projet "Vélocimétrie par images de particules" (2002) : 23 000 euros
- Action Spécifique UPMC, projet "Vélocimétrie par images de particules" (2002) : 30 000 euros

### Responsabilités collectives

- 2009-2010, co-responsable du Master 2 Recherche "Dynamique des Fluides" (directeur : G. Labrosse).
- A partir de septembre 2010, responsable du Master 2 "Dynamique des Fluides et Energétique".
- Membre du comité scientifique du GDR "Turbulence" (depuis 2008).

- Président du comité d'expert pour le poste MCF 0247 (Université Paris-Sud, 2010). Membre du comité d'expert pour le poste MCF 1859 (Université Paul Sabatier, Toulouse, 2009).
- Membre élu de la commission de spécialistes 60-62º sections (2002-2008).
- Membre du Conseil de Laboratoire (2000-2004, puis depuis 2009).
- Mise en place et maintenance du site web du FAST (depuis 2003).

## Encadrements

### Thèses

- Cyprien Morize, co-encadré (50%) avec Marc Rabaud, Université Denis Diderot - Paris 7, soutenue le 29 septembre 2006. Actuellement maître de conférences à l'Université Paris-Sud 11.
- Jemil Znaien, co-encadré (30%) avec Jean-Pierre Hulin, Université Paris-Sud 11, soutenue le 2 octobre 2009. Actuellement post-doc à l'Université de Technologie d'Eindhoven.
- Cyril Lamriben, débutée en octobre 2009.

### Stages

- Benjamin Truchot (INSA Rouen, juin-juillet 2001)
- Yohan Atzori (Licence de mécanique, février 2002)
- Thomas Pasutto (DEA DFT, mars-juin 2002)
- Cyprien Morize (DEA DFT, mars-juin 2003)
- Sébastien Kiesgen (Magistère Paris-Sud, avril-juin 2004)
- Laura Messio (ENS Cachan, mai-juin 2005)
- Jules Casoli (ENS Ulm, juillet 2005)
- Doaa Kamal (L3 Mécanique Physique, février 2006)
- Adrien Minière (M1 Mécanique Physique, mai-juillet 2006)
- Jacopo Seiwert (M2 Physique des Liquides, novembre 2006 - juillet 2007)
- Kévin Salsac (M1 Mécanique Physique, mai-juillet 2007)
- Joran Rolland (M1 Physique Fondamentale)
- Edouard Pinsolle (M1 Physique Fondamentale)
- Lionel Agostini (M2 DFT, mars-juin 2008)
- David Bourgeois (M1 Mécanique Physique, mai-juillet 2009)
- Thomas Serandon (M1 Physique Fondamentale, mai-juillet 2009)

## Jurys de thèse

- Examinateur de la thèse de Florent Ravelet, soutenue au CEA Saclay le jeudi 22 septembre 2005.
- Examinateur de la thèse de Rudie Kunnen, soutenue à l'Université de Technologie d'Eindhoven, Pays-Bas, le 7 octobre 2008.
- Examinateur de la thèse de Waleed Mouhali, soutenue à l'Observatoire de Meudon, le 25 novembre 2009.
- Rapporteur de la thèse de Matthieu Mercier, soutenue à l'Ecole Normale Supérieure de Lyon, le 29 juin 2010.

– Rapporteur de la thèse de Nicolas Grisouard, soutenance prévue le 29 octobre 2010 à l'Université Joseph Fourier, Grenoble.

## Enseignements

J'ai effectué entre 2000 et 2008 un service plein d'enseignement (192 h/an) à l'Université Paris-Sud. Entre 2008 et 2010, j'ai bénéficié d'une demi-décharge d'enseignement (96 h/an) dans le cadre d'une délégation CNRS.

L'essentiel de mon activité d'enseignement s'intègre actuellement dans le Master de Mécanique Physique de l'Université Paris-Sud, ainsi que, dans une moindre mesure, dans le Magistère de Physique Fondamentale.

Les points forts de mon activité d'enseignement sont :

– **Turbulence** : Dans ce cours intégré (i.e. cours + TD, total 52 h) de Master 1 et Master 2 de Mécanique Physique, je m'attache à donner les bases de la turbulence à la fois concernant l'approche physique (mécanismes de cascade d'énergie, intermittence etc.), mais aussi concernant l'approche ingénierie (modélisations des tenseurs de contrainte, modèles du type $k - \epsilon$ très utilisé dans les codes industriels).
– **Simulations numériques en Matlab** : Unité optionnelle en Licence L2 (mention mathématiques et physique), que j'ai participé à mettre en place avec F. Issard-Roch en 2005-2006. Ce module vise à donner aux étudiants les outils pour modéliser des phénomènes issus de la physique, la chimie, la biologie, l'économie etc., et de les simuler de façon interactive sous Matlab. J'ai introduit une unité optionelle similaire pour la Licence L3 de Mécanique Physique (ouverture en 2010), plus centrée sur des problèmes issus de la mécanique. Le choix de ce langage de programmation s'appuie sur son utilisation croissante tant dans le domaine académique qu'industriel.
– **Méthodes expérimentales en mécanique des fluides** : (Master 1 et 2 de Mécanique Physique). Ce cours intégré présente les différentes méthodes expérimentales utilisées en mécanique des fluides (Anémométrie à fil chaud, Anémométrie Laser Doppler, Vélocimétrie par Images de Particules), avec un accent mis sur la mise en œuvre pratique. En Master 1, ce cours intégré est complété depuis la rentrée 2006 par un stage d'une semaine sur les installations expérimentales de l'ENSTA, stage dont j'ai participé à la mise en place et que je co-encadre avec O. Cadot (ENSTA) et L. Pastur (LIMSI).

### Responsabilités

Depuis septembre 2009, j'assure avec Claudine Dang Vu et Gérard Labrosse la co-responsabilité du Master 2 "Acoustique Physique, Dynamique des Fluides, Fluides Complexes".

En septembre 2010, le Master de Mécanique Physique rejoint le Master de Physique Appliquée et Mécanique "PAM", ce qui conduit à une redéfinition importante du paysage des Masters de sciences de l'Université Paris-Sud. Depuis 2008 j'ai participé activement à la mise en place de ce nouveau Master, notamment en ce qui concerne la rédaction du contrat quadriennal 2010-2013.

Enfin, à partir de septembre 2010, je prends la responsabilité du Master 2 "Dynamique des Fluides et Energétique" (refonte des parcours R et P de la spécialité précédente).

# Publications

Index $h = 9$ (i.e., 9 publications ont été citées au moins 9 fois), mesuré sur ISI Web of Knowledge en juin 2010.

### Publications avec comité de lecture

1. C. Lamriben, P.P. Cortet, F. Moisy, L. Maas, Excitation of inertial modes in a closed grid turbulence experiment under rotation, Phys. Fluids (soumis, 2010).
2. J. Znaien, F. Moisy, J.P. Hulin, Flow structure and momentum transport for buoyancy driven mixing flows in long tubes at different tilt angles, Phys. Fluids (soumis, 2010).
3. F. Moisy, C. Morize, M. Rabaud, J. Sommeria, Decay laws, anisotropy and cyclone-anticyclone asymmetry in decaying rotating turbulence, J. Fluid Mech (sous presse, 2010).
4. P.P. Cortet, C. Lamriben, F. Moisy, Viscous spreading of an inertial wave beam in a rotating fluid, Phys. Fluids **22**, 086603 (2010).
5. J. Znaien, Y. Hallez, F. Moisy, J. Magnaudet, J.P. Hulin, D. Salin and E. J. Hinch, Experimental and numerical investigation of flow structure and momentum transport in a turbulent buoyancy-driven flow inside a tilted tube, Phys. Fluids **21**, 115102 (2009).
6. A. Eddi, E. Fort, F. Moisy, Y. Couder, Unpredictable tunneling of a classical wave-particle association, Phys. Rev. Lett. **102**, 240401 (2009).
7. F. Moisy, M. Rabaud, K. Salsac, A Background-oriented Schlieren method for the measurement of the topography of a liquid interface, Exp. in Fluids **46** (6), 1021-1036 (2009).
8. J. Seiwert, C. Morize, F. Moisy, On the decrease of intermittency in decaying rotating turbulence, Phys. Fluids **20**, 071702 (2008).
9. L. Messio, C. Morize, M. Rabaud, F. Moisy : Experimental observation using particle image velocimetry of inertial waves in a rotating fluid, Exp. in Fluids **44**, 519-528 (2008).
10. C. Morize, F. Moisy : Energy decay of rotating turbulence with confinement effects, Phys. Fluids **18**, 065107 (2006).
11. C. Morize, F. Moisy, M. Rabaud : Decaying grid-generated turbulence in a rotating frame, Phys. Fluids **17**, 095105 (2005)
12. C. Nore, F. Moisy, L. Quartier : Experimental observation of near-heteroclinic cycles in the von Karman swirling flow, Phys. Fluids **17**, 064103 (2005).
13. F. Moisy and J. Jimenez : Geometry and clustering of intense structures in isotropic turbulence, J. Fluid Mech **513**, 111-133 (2004).
14. F. Moisy, O. Doaré, T. Pasutto, O. Daube, M. Rabaud : Experimental and numerical study of the shear layer instability between two counter-rotating disks, J. Fluid Mech **507**, 175-202 (2004).
15. F. Moisy : Supercritical bifurcation of a spinning hoop, Am. J. Phys. **71**, 999-1004 (2003).
16. F. Moisy, T. Pasutto, M. Rabaud, Instability patterns in the flow between counter-rotating disks, Nonlinear Processes in Geophysics **10** (3), 281-288 (2003).
17. G. Gauthier, P. Gondret, F. Moisy, M. Rabaud : Instabilities in the flow between co and counter-rotating disks, J. Fluid Mech **473**, 1-21 (2002).

18. F. Moisy, H. Willaime, J.S. Andersen, P. Tabeling : Passive scalar intermittency in low temperature helium flows, Phys. Rev. Lett. **86** (21), 4827-4830 (2001).
19. La Porta, G.A. Voth, F. Moisy, E. Bodenschatz : Using cavitation to measure statistics of low-pressure events in large-Reynolds-number turbulence, Phys. Fluid **12** (6), 1485-1496 (2000).
20. H. Willaime, J. Maurer, F. Moisy, P. Tabeling : Turbulence over arrays of obstacles in low temperature helium gas, Eur. Phys J.B **18**, 363-369 (2000).
21. F. Moisy, P. Tabeling, H. Willaime : Kolmogorov Equation in fully developed turbulence, Phys. Rev. Lett. **82**, 3994-3997 (1999).

### Article en préparation

1. F. Moisy, G.J. Michon, M. Rabaud, Cross-waves induced by vertical oscillations of a fully immersed vertical plate, pour Phys. Fluids.

### Articles de vulgarisation

1. F. Moisy, C. Lamriben, P.P. Cortet, M. Rabaud : Gyroflow - Une plateforme tournante pour la simulation des écoulements géophysiques, Plein Sud, Numéro spécial recherche 2010-2011 (soumis en 2010).
2. F. Moisy, T. Pasutto, G. Gauthier, P. Gondret et M. Rabaud : Spiral patterns in swirling flows, Europhysics News **34** (3), 104-107 (2003).
3. G. Gauthier, P. Gondret, F. Moisy, M. Rabaud : Patterns between two rotating disks, Phys. Fluids **14** (9), S7 (2002). [Gallery of Fluid Motion]
4. F. Moisy, T. Pasutto, G. Gauthier, P. Gondret et M. Rabaud : Instabilités spirales entre disques tournants, Bull. S.F.P. **135**, 4-8 (2002).

### Comptes-rendus de conférences internationales avec comité de lecture

1. F. Moisy, L. Agostini, G. Tan, Structure functions and energy transfers in a decaying rotating turbulence experiment, 12th Euromech European Turbulence Conference, Marburg, Sept. 7 - 10, 2009.
2. F. Moisy, M. Rabaud, E. Pinsolle, Measurement by Digital Image Correlation of the topography of a liquid interface, ISFV13 - 13th International Symposium on Flow Visualization, and FLUVISU12 - 12th French Congress on Visualization in Fluid Mechanics, Paper 326, July 1-4, 2008, Nice (2008).
3. M. Rabaud, F. Moisy, Optical measurement of ship waves by Digital Image Correlation, International Conference on Innovation in High Performance Sailing Yachts, 29-30 May 2008, Lorient, France, ISBN 978-1-905040-46-9e, pages 23-25 (2008).
4. C. Morize, F. Moisy, M. Rabaud, J. Sommeria : Dynamics of the anisotropy in decaying rotating turbulence with confinement effects, Congrès Français de Mécanique (2007).
5. C. Morize, F. Moisy, M. Rabaud, J. Sommeria : On the cyclone-anticyclone asymmetry in decaying rotating turbulence, CD-ROM Conference on Turbulence and Interactions TI2006, May 29 - June 2, 2006, Porquerolles, France (2006).

6. F. Moisy, C. Morize, M. Rabaud : The decay law of grid turbulence in a rotating tank, CD-ROM Conference on Turbulence and Interactions TI2006, May 29 - June 2, 2006, Porquerolles, France (2006).
7. F. Moisy, J. Jimenez : Clustering of intense structures in isotropic turbulence : numerical and experimenal evidence, IUTAM Symposium on Elementary Vortices and Coherent Structures : Significance in Turbulence Dynamics, Kyoto, Japan, 26-28 October 2004. Ed. S. Kida, Springer-Verlag, 3-12 (2006).
8. F. Moisy, C. Morize and M. Rabaud : Energy spectrum in rotating turbulence, XXIst ICTAM Conference, Warsaw, CD-ROM ISBN 83-89697-01-1 (2004).
9. Doaré, F. Moisy et O. Daube : Etude expérimentale et numérique de l'instabilité entre disques contrarotatifs, 16ème congrès francophone de mécanique (2003).
10. Daube, P. Le Queré, F. Moisy and M. Rabaud : Numerical and Experimental investigation of the stability of the 3D flow between two counter-rotating disks, Proceeding 2nd International Conference on Computational Fluid Dynamics, 485-490 (2002).
11. F. Moisy, H. Willaime, J.S. Andersen et P. Tabeling : Passive scalar intermittency : Statistics of the Cliffs, in "Advances in Turbulence VIII", Ed. by C. Dopazo, CIMNE Barcelona, 835-838 (2000).
12. F. Moisy et P. Petitjeans : Pressure measurements in a stretched vortex, in "Vortex Structure and Dynamics", Lecture Notes in Physics, Ed. by A. Maurel and P. Petitjeans, 252-262 (2000).
13. F. Moisy, A. La Porta, G.A. Voth et E. Bodenschatz : Using cavitation as a probe of low-pressure filaments in turbulence, in "Vortex Structure and Dynamics", Lecture Notes in Physics, Ed. by A. Maurel and P. Petitjeans, 263-274 (2000).
14. J. Jiménez, F. Moisy, P. Tabeling et H. Willaime : Scaling and structure in isotropic turbulence, in "Intermittency in turbulent flows", Ed. by C. Vassilicos, Cambridge Univ. Press, 193-212 (1999).
15. F. Belin, F. Moisy, P. Tabeling et H. Willaime : Worms in a turbulence experiment, from hot wire time series, Trends in Mathematics, Birkhäuser Verlag Basel/Switzerland, 129 (1999).

## Logiciels libres

2 Toolboxes pour Matlab, distribuées sous licence BSD (Berkeley software distribution license) :

1. PIVMat - A PIV post-processing and data analysis toolbox for Matlab `http://www.fast.u-psud.fr/pivmat`
2. EzyFit - A free curve fitting toolbox for Matlab `http://www.fast.u-psud.fr/ezyfit`

D'autres outils Matlab pour la mécanique des fluides ou le traitement d'images sont disponibles sur la page `http://www.fast.u-psud.fr/moisy/ml` .

## Rapporteur

Activité de *referee* pour les revues suivantes :

– J. Fluid. Mech. : 7 articles
– Phys. Fluids : 5 articles
– Exp. Fluids : 3 articles
– Physica D : 3 articles
– Phys. Rev. E : 1 article
– Europhys. Lett. : 1 article
– Autres (Naturewissenshaften, Meccanica...) : 6 articles

Expertises :
– 1 projet ANR blanc 2008
– 1 projet incubateur Agoranov 2005.

## Séminaires et Communications

### Séminaires invités de laboratoire

1. ETH Zurich, 24 septembre 2009.
2. Rencontres Nicoises de Mécanique des fluides, juin 2009.
3. Max Planck Insitute, Goettingen, 30 janvier 2008.
4. Université Eindhoven TU/e, 16 janvier 2008.
5. Université du Havre, 26 mai 2005 : séminaire invité pour l'année mondiale de la physique.
6. Sciences de la Terre, Orsay, 23 novembre 2004.
7. Laboratoire des Ecoulements Géophysiques et Industriels, Grenoble, 14 Octobre 2004.
8. Laboratoire de Modélisation en Mécanique, Jussieu, 11 Juin 2004
9. PMMH, ESPCI, 10 janvier 2003.
10. LadHyX, Polytechnique, 5 décembre 2000.
11. FAST, Orsay, novembre 2000.
12. IUSTI, Marseille, 24 mars 2000.
13. Laboratoire Cassini, Observatoire de la Côte d'Azur, Nice, 23 mars 2000.
14. FAST, Orsay, 15 mars 2000.
15. School of Aeronautics, Madrid, 1er mars 2000.
16. Laboratoire de Mécanique, Le Havre, 4 février 2000.
17. Laboratoire de Physique Statistique, ENS, 13 octobre 1999.
18. Séminaire "Stability, Transition and Turbulence", Cornell University, Ithaca, février 1998.

### Conférences internationales

1. Euromech 519, "Mixing and dispersion in flows dominated by rotation and buoyancy", Rolduc (Pays-bas), 20-23 juin 2010 : **Invited keynote lecture**.
2. Ecole d'hiver "New Challenges in Turbulence Research", Les Houches, february 21 - 26, 2010 : **Invited keynote lecture**.
3. European Turbulence Conference 12, Marburg, 7-10 septembre 2009.

4. Isaac Newton Institute for Mathematical Sciences, Workshop “Rotating stratified turbulence and turbulence in the atmosphere and oceans”, Cambdridge, UK, 8-12 décembre 2008.
5. Isaac Newton Institute for Mathematical Sciences, Workshop “Structures and Waves in Anisotropic Turbulence”, Warwick, UK, 2-7 novembre 2008.
6. APS Division of Fluid Dynamics, Salt Lake City, novembre 2007 (3 abstracts).
7. TI 2006 “Turbulence and Interactions”, Porquerolles, 29 mai - 2 juin 2006.
8. APS Division of Fluid Dynamics, Chicago, novembre 2005 (3 abstracts).
9. IUTAM “Elementary Vortices and Coherent Structures”, Kyoto, 26-28 octobre 2004.
10. Euromech 448 “Vortex dynamics and field interaction”, Paris, 6-10 septembre 2004.
11. 21st ICTAM Conference, Varsovie, 15-21 août 2004.
12. 5th Euromech Fluid Mechanics Conference, Toulouse, 1-5 septembre 2003.
13. EGS “27th General Assembly of the European Geophysical Society”, Nice, mars 2002.
14. TMR Research Network “Intermittency in Turbulence Systems”, Porto, 18-21 avril 2001.
15. APS Division of Fluid Dynamics, Washington, 19-21 novembre 2000.
16. European Turbulence Conference VIII, Barcelone, 27-30 juin 2000.
17. Workshop franco-allemand “Transport et mélange dans les écoulements turbulents réactifs et non réactifs”, 31 mars 2000, Paris. Conférencier invité.
18. APS March Meeting, Atlanta, 20-26 mars 1999.
19. TMR Research Network “Intermittency in Turbulence Systems”, Paris, 5-6 décembre 1998.
20. 20eme Conférence Internationale IUPAP de Physique Statistique, Paris, 20-24 juillet 1998.

# Chapitre 1

# Instabilités dans les écoulements de von Kármán

## 1.1 Introduction

### 1.1.1 Ecoulements géophysiques

Si les écoulements en rotation constituent un chapitre classique, et parfois aride, de la mécanique des fluides, la richesse des phénomènes physiques, et en particulier des problèmes de stabilité, recèle encore un grand nombre de questions ouvertes. Le rôle central joué par la rotation dans les écoulements naturels (océan, atmosphère) ou dans les applications industrielles est à l'origine d'une littérature fournie depuis près d'un siècle [65, 49, 142].

Historiquement, ce sont les observations issues des expéditions polaires de l'océanographe Nansen, à la fin du XIXème siècle, qui ont initié ce chapitre de la mécanique des fluides. A partir de ces observations, Ekman, en 1905, décrit l'influence de la rotation de la Terre sur les courants océaniques générés par l'action du vent : c'est la fameuse spirale d'Ekman (voir la figure 1.1), qui ne reçut une démonstration par des mesures directes dans l'océan que 90 ans plus tard [29].

Il faut toutefois noter ici que la rotation n'est pas le seul ingrédient des écoulements géophysiques : la stratification et le confinement en constituent les deux autres ingrédients essentiels, et c'est la combinaison de ces 3 effets qui fournit les briques de bases à la description des grandes circulations océaniques ou atmosphériques.

A l'instar de ce premier chapitre, les 2 chapitres qui suivent portent également sur les écoulements en rotation. Cependant, ces 2 chapitres suivants sont consacrés au cas d'une rotation d'ensemble forte, pour laquelle la description pertinente se fait dans le référentiel tournant (faible nombre de Rossby). Le présent chapitre, en revanche, concerne les écoulements confinés en rotation différentielle de type "von Kármán" [142]. Ce terme générique recouvre les écoulements en cavité cylindrique générés par la rotation des disques supérieur et/ou inférieur, et éventuellement de la paroi latérale. Mis à part dans le cas d'une co-rotation importante des disques, la description naturelle de l'écoulement se fait ici dans le référentiel fixe, de sorte que le nombre de Rossby n'est pas un paramètre pertinent ici.

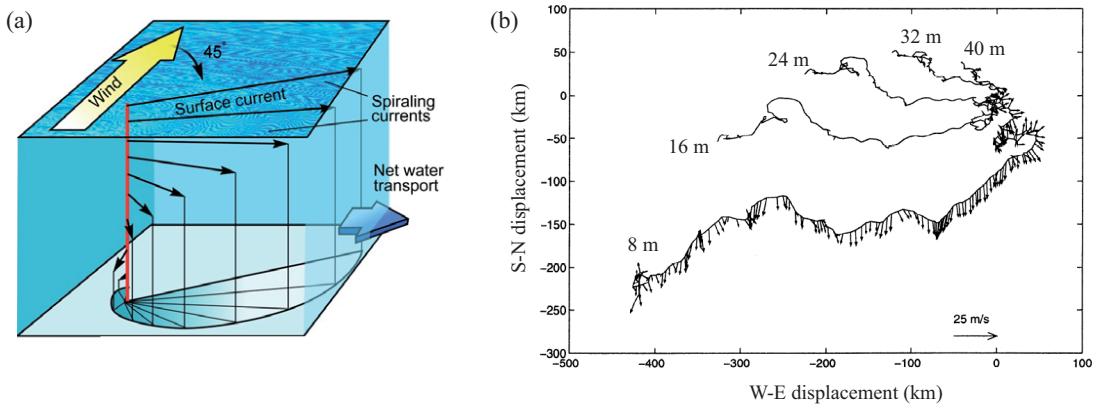


FIG. 1.1 – (a) Spirale d'Ekman : La friction du vent induit en surface une couche d'eau défléchie à 45° sur la droite par la force de Coriolis (dans l'hémisphère Nord), et un transport net à 90° intégré sur la profondeur. D'après J. Cassano, University of Colorado at Boulder (Copyright 2006 by John Wiley & Sons, Inc.) (b) Trajectoires de traceurs à différentes profondeurs, reconstruites à partir de mesures de vitesse par profilométrie acoustique, montrant de façon directe l'écoulement de spirale d'Ekman (mesures effectuées dans l'Océan Pacifique, au large de la Californie). D'après Chereskin (1995) [29].

### 1.1.2 L'écoulement de von Kármán turbulent

Mes travaux sur les écoulements de von Kármán ont débuté en 1997, lors de ma thèse effectuée au Laboratoire de Physique Statistique [96, 140, 88, 90] ainsi que lors d'une collaboration avec E. Bodenshatz (Université de Cornell) [73]. Ces travaux antérieurs à mon arrivée au FAST portaient sur l'écoulement de von Kármán turbulent, généré par la rotation différentielle ou la contra-rotation de disques munis de pales, induisant un forçage dit "inertiel". Cet écoulement ne faisait pas l'objet d'une étude en tant que tel, mais constituait un système modèle permettant d'obtenir une turbulence très développée dans un volume de fluide restreint. Depuis les travaux pionniers de Douady *et al.* (1991) [47], cet écoulement de von Kármán turbulent (qui reçu alors le nom "machine à laver française") a eu un impact significatif sur la compréhension de la turbulence en général, et sur le dynamisme de la communauté turbulente française en particulier.

Les travaux plus récents présentés dans ce chapitre (2000-2005) concernent d'une certaine façon le "vrai" écoulement de von Kármán, celui entraîné par des disques lisses (forçage par couches limites), et se concentrent sur les motifs d'instabilités associés aux premières bifurcations de l'état de base. Cette géométrie constitue une situation épurée du point de vue des symétries, offrant un terrain de jeu privilégié pour comprendre et caractériser les instabilités. Pour autant, la nature de cet écoulement de base reste centrale dans la compréhension des comportements d'intermittence à grande échelle qui apparaissent à grand nombre de Reynolds, et qui ont été caractérisés depuis en détail par le "Groupe Instabilités et Turbulence" au CEA [115]. Enfin, le choix de cette géométrie pour la mise en évidence de l'effet dynamo dans un écoulement turbulent, choix qui s'est avéré judicieux en 2007 [100], fournit *a posteriori* une justification de premier ordre pour ces études sur l'écoulement de von Kármán.

Dans la suite de ce chapitre, on rappellera brièvement la structure de l'écoulement de base ainsi que les différentes instabilités apparaissant dans les écoulements entre disques rotatifs. On distingue en particulier les situations de couches de cisaillement libres, liées à une rotation différentielle "en volume", de celles de couches limites sur disques en rotation. Nous présente-

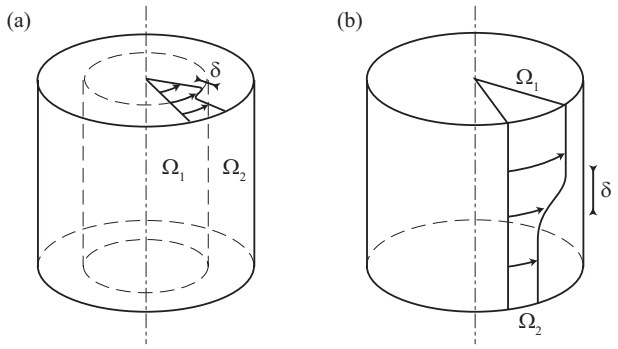


FIG. 1.2 – Situations génériques de rotation différentielle. (a), gradient radial de vitesse angulaire, faisant apparaître une vorticité verticale ; (b), Gradient vertical de vitesse angulaire, faisant apparaître une vorticité radiale.

rons ensuite nos résultats expérimentaux, obtenus dans deux types de géométrie : la situation de "cavité plate" en co- ou contra-rotation [60, 61, 91], puis celle de cavité de rapport d'aspect proche de 1 en exacte contrarotation, en mettant l'accent sur le rôle des symétries dans la nature des bifurcations successives observées [110, 109, 108]. Enfin, nous mettrons ces derniers résultats en perspective, dans le contexte des phénomènes des bifurcations turbulentes observées dans cet écoulement à beaucoup plus haut nombre de Reynolds.

## 1.2 Position du problème

### 1.2.1 Stabilités d'une rotation différentielle

D'une manière générale, une rotation d'ensemble a un caractère stabilisant, du fait de la nature stable de l'équilibre entre force centrifuge et gradient de pression : il s'agit de l'application du critère de Rayleigh pour un écoulement de moment cinétique strictement croissant avec le rayon [28]. Cette stabilité conduit à la possibilité de propager des ondes, appelées ondes d'inertie, auxquelles le chapitre 2 est consacré. Une illustration de cette stabilisation est le problème classique de la convection thermique de Rayleigh-Bénard entre 2 plaques planes : une rotation d'ensemble autour d'un axe perpandiculaire aux parois augmente le nombre de Rayleigh critique (instabilité de Küpper-Lortz [28]). A noter que l'écoulement bifurqué, lui, n'est pas nécessairement stabilisé par la rotation d'ensemble : en effet, dans cet exemple, l'instabilité secondaire vers un écoulement instationnaire s'effectue, elle, pour un nombre de Rayleigh inférieur à celui trouvé en l'absence de rotation.

Une rotation différentielle, en revanche, est associée en plus à de la déformation, et donc à du cisaillement, pouvant conduire à une déstabilisation de l'écoulement principal. Deux situations génériques de rotation différentielle peuvent être distinguées, associées à une variation radiale ou verticale de la vitesse angulaire (figures 1.2a et b respectivement), et correspondant aux situations barotropes et baroclines des écoulements géophysiques. La variation radiale de vitesse angulaire a été étudiée dans les expériences modèles de Hide & Titman (1967) [67] et de Niino & Misawa (1984) [107], tandis que la variation verticale est celle intervenant dans l'écoulement de type von Kármán contra-rotatif. Dans les deux cas, la couche de cisaillement libre qui en résulte peut être instable, par un mécanisme générique du type Kelvin-Helmholtz,

modifié par les effets centrifuges et/ou de courbure des lignes de courant.

Dans le cas d'une variation radiale de la vitesse angulaire (figure 1.2a), bien que l'équilibre force centrifuge - gradient de pression reste vérifié, celui-ci peut devenir instable : on parle d'instabilité centrifuge. Le critère de stabilité est donné dans ce cas par le critère de Rayleigh [28], analogue au critère du point d'inflexion dans le cas d'un écoulement parallèle.

### 1.2.2 Structure et stabilité des couches limites

La stabilité de l'écoulement de couche limite au voisinage d'une paroi en rotation, bien que présentant également une situation de rotation différentielle, est très différente du cas de couches de cisaillement libres évoqué précédemment. Tandis que les couches limites rectilignes sont par nature spatialement inhomogènes, l'épaisseur constante des couches limites sur parois tournantes, $\delta = (\nu/\Omega)^{1/2}$, issue de l'équilibre entre la force centrifuge et la friction visqueuse, peut leur donner l'apparence d'une plus grande simplicité. La structure intrinsèquement tridimensionelle de ces couches limites vient toutefois grandement compliquer leur analyse.

Nous présentons brièvement dans la suite la structure de la couche limite sur un disque infini, puis en présence de confinement vertical et radial, pour enfin décrire les différents mécanismes d'instabilité. Seuls les principaux résultats sont rappelés ici, le lecteur pourra se reporter à la revue de Zandbergen et Dijkstra (1987) [142] pour un exposé complet (voir aussi plus récemment l'introduction très complète donnée par Serre (2000) [121]).

#### Disque tournant unique infini

Dans le cas d'un disque tournant unique de rayon infini, la seule échelle de longueur du système est l'épaisseur de couche limite, $\delta = (\nu/\Omega)^{1/2}$. Il est alors possible de construire des solutions autosimilaires, pour lesquelles la vitesse horizontale adimensionnée par $\Omega r$ ne dépend que de la coordonnée axiale réduite $z/\delta$. L'éjection centrifuge au voisinage du disque "boucle à l'infini", conduisant à une aspiration axiale du fluide, de vitesse caractéristique $\simeq (\nu\Omega)^{1/2}$.

En généralisant à la situation d'un disque infini tournant à vitesse angulaire $\Omega_d$, en contact avec un demi-espace de fluide tournant à vitesse angulaire $\Omega_f$, l'épaisseur de couche limite devient $\delta = (\nu/|\Delta\Omega|)^{1/2}$, avec $\Delta\Omega = \Omega_f - \Omega_d$. On distingue alors classiquement 3 configurations [55] :

(i) couche limite d'Ekman, $\Omega_f \simeq \Omega_d$,

(ii) couche limite de von Kármán, $\Omega_f = 0$ et $\Omega_d \neq 0$,

(iii) couche limite de Bödewadt, $\Omega_f \neq 0$ et $\Omega_d = 0$.

La configuration (i), qui décrit la situation d'une faible déviation autour d'une rotation solide, est particulièrement importante pour les écoulements géophysiques : c'est le problème initialement motivé par les courants marins induit par le vent (§ 1.1). Formulée dans le référentiel tournant à vitesse $\Omega_d$, cette configuration permet une linéarisation des équations de Navier-Stokes vis-à-vis du nombre de Rossby ($Ro = \Delta\Omega/\Omega \ll 1$) et admet une solution analytique. Cette solution décrit la fameuse spirale d'Ekman dans la couche limite, associée aux phénomènes de *pompage* ou d'*injection* d'Ekman, de vitesse verticale $w = \delta_E \Delta\Omega$, dans le cas d'une rotation relative *cyclonique* ($\Delta\Omega > 0$) ou *anticyclonique* ($\Delta\Omega < 0$) respectivement. Cette situation joue un rôle important pour le problème de la turbulence en rotation décrit au chapitre 3.

Le problème général des couches limites de von Kármán (ii) et de Bödewadt (iii), étant par nature non-linéaire ($Ro \simeq O(1)$), est plus compliqué. Des solutions autosimilaires existent

également, mais ne peuvent être calculées que numériquement. Ces solutions correspondent toutefois à des écoulements qualitativement similaires à la situation linéaire d'Ekman, avec notamment un pompage ou une injection du fluide dans la couche limite selon le signe de $\Delta\Omega$. Par abus de langage, ces couches limites de von Kármán et de Bödewadt sont parfois aussi appelées "couches d'Ekman", étant sous-entendu qu'il s'agit alors de cas extrêmes de couches d'Ekman pleinement non-linéaires.

**Deux disques tournants infinis**

Batchelor (1951) [6] généralisa la situation précédente au cas de l'écoulement entre deux disques infinis, dont les vitesses angulaires sont notées conventionellement $\Omega_t$ et $\Omega_b$, séparés d'une distance $h$. La structure de l'écoulement est alors gouvernée par 2 nombres sans dimension : soit les deux nombres de Reynolds $Re_{t,b} = \Omega_{t,b}h^2/\nu$, soit l'un de ces deux nombres et le rapport de rotation $s = \Omega_t/\Omega_b$. Ce rapport $s$ permet de distinguer les configurations dites de cavité rotor-stator ($s = 0$), d'écoulements corotatif ($s > 0$) et contra-rotatif ($s < 0$) ; notons que la situation $|s| > 1$ se ramène simplement à une situation $|s| \leq 1$ en interchangeant les 2 disques. Le nombre de Reynolds — pour simplifier, celui correspondant au disque le plus rapide — permet de distinguer le cas d'un écoulement présentant une couche limite bien développée ($h \gg \delta$, soit $Re \gg 1$) du cas d'une variation continue du profil de vitesse entre les deux disques, du type écoulement de Couette de torsion.

Bien que les équations du problème à deux disques tournants infinis soit très proches de celles du problème du disque unique infini, la situation s'avère plus compliquée : l'absence de conditions aux limites en $r = \infty$ conduit à une multiplicité de solutions. Parmi celles-ci se trouvent les deux solutions célèbres prédites par Batchelor (1951) et Stewartson (1953) : Dans le cas rotor-stator ($s = 0$), Batchelor avait conjecturé un écoulement constitué d'un cœur inviscide tournant à vitesse angulaire $\Omega_c$ entre deux couches limites, tandis que la solution proposée par Stewartson était constituée d'une unique couche limite sur le disque en rotation. L'étude numérique de Szeto (1978) a clos le débat en démontrant que seule la solution de Batchelor était stable, donc physiquement réaliste. Toujours dans le cas rotor-stator, la vitesse de rotation du coeur inviscide de la solution de Batchelor a pu être prédite analytiquement par Rasmussen (1971), par un raisonement basé sur l'équilibre des débits pompés par le disque tournant : $\Omega_c = 0.313\Omega_d$.

**Deux disques tournants finis**

Dans une réalisation expérimentale d'écoulements entre disques tournants, le rayon $R$ des disques est fini. Dans ce cas, un troisième nombre sans dimension intervient, le rapport d'aspect $\Gamma = R/h$, et il devient nécessaire de spécifier la nature des conditions aux limites sur la paroi latérale cylindrique. Dans les cas les plus simples, cette paroi latérale peut être immobile, ou tourner à la vitesse de l'un des deux disques – chacune de ces deux possiblités ayant été examinée expérimentalement dans la suite. Tandis que le problème des deux disques infinis présente une multiplicité de solutions, le choix de la condition aux limites ici permet de lever cette dégénérescence [14]. En particulier, lorsque la cavité est fermée, la structure de l'écoulement correspond à celle prédite par Batchelor (1951), soit un cœur inviscide en rotation séparé de 2 couches limites. D'autres conditions aux limites plus élaborées, avec flux radial imposé, ou présence d'un "moyeu" central fixe ou lui-même en rotation, ont également été abondamment étudiées en raison de leurs applications industrielles (disques durs, turbomachines etc.)

Notons que dans la limite de cavités très alongées ($\Gamma \gg 1$), on peut s'attendre à ce que la condition aux limites latérale ait une influence marginale sur la structures des couches limites. Bien que les solutions autosimilaires issues de l'analyse pour disques infinis ne soient plus valides pour $\Gamma < \infty$, celles-ci peuvent néanmoins constituer une approximation raisonable pour des cavités suffisamment fines, du moins pour une gamme de rayons modérée. Ainsi, une couche limite centrifuge, de type Ekman (plus précisément von Kármán), sera présente sur le disque le plus rapide, et une couche limite centripète, de type Bödewadt, sur le disque le plus lent (ou immobile). Cette description naïve est toutefois mise en défaut dans le cas de l'écoulement contra-rotatif, comme nous le verrons plus loin.

#### Stabilité des couches limites

Du point de vue de la stabilité, les écoulements de couches limites sur parois tournantes que nous venons de décrire, bien que présentant une situation de rotation différentielle, ne présentent pas de point d'inflexion dans le profil azimuthal de vitesse, et sont donc *a priori* stables vis-à-vis d'un mécanisme du type "Kelvin-Helmhlotz". Cependant, la présence d'un écoulement de recirculation radial induit par la variation de vitesse azimuthale peut, lui, induire un point d'inflexion dans le profil de vitesse : l'instabilité inflexionelle qui en résulte est dite "cross-flow", et a été classifiée du "type I" dans la littérature [142, 121]. Elle se traduit par une brisure de l'axisymétrie, et l'apparition de bras spiralés, caractérisés par l'angle le plus instable pour lequel la combinaison des écoulements radiaux et azimuthaux conduit au profil de vitesse inflexionnel.

Plus subtilement, la viscosité, qui a un rôle stabilisant dans les cas de rotation différentielle en volume, peut avoir ici un rôle déstabilisant : on parle alors d'instabilité visqueuse, de "type II". L'interprétation physique de ce second mécanisme n'est pas aisée, mais l'on peut noter qu'il intervient également dans le cas de couches limites rectilignes (ondes de Tollmien-Schliechting). Cette instabilité ne brise pas l'axisymétrie, et se manifeste par une modulation radiale de la couche limite.

Pour ces deux types d'instabilité, c'est dans la situation d'un écoulement radial décéléré, et donc au voisinage du disque tournant le plus lentement (couche centripète de Bödewadt), que ces instabilités se développent. En régime instationnaire, c'est donc l'écoulement de "spin-down" (ralentissement de la rotation solide) qui est le plus instable comparé à l'écoulement de "spin-up" (mise en rotation solide).

## 1.3 Expériences

### 1.3.1 Les dispositifs expérimentaux

Dans les expériences que nous avons menées, les 3 types d'instabilité décrits précédemment ont été rencontrées et analysées en détail : instabilité de cisaillement dans les couches de cisaillement libres, et instabilités inflexionelle et visqueuse (types I et II) dans les couches limites centripètes. Ces expériences ont été menées dans les deux configurations suivantes :

1. "Cavité plate" (§ 1.3.2, Fig. 1.3a) [61, 91] : cellule dont la paroi latérale tourne à la vitesse du disque le plus rapide, pris comme étant le disque supérieur. Cette configuration a été explorée en rotor-stator, co- et contrarotation, pour des rapports d'aspects élevés, $\Gamma = 2$ à 21.

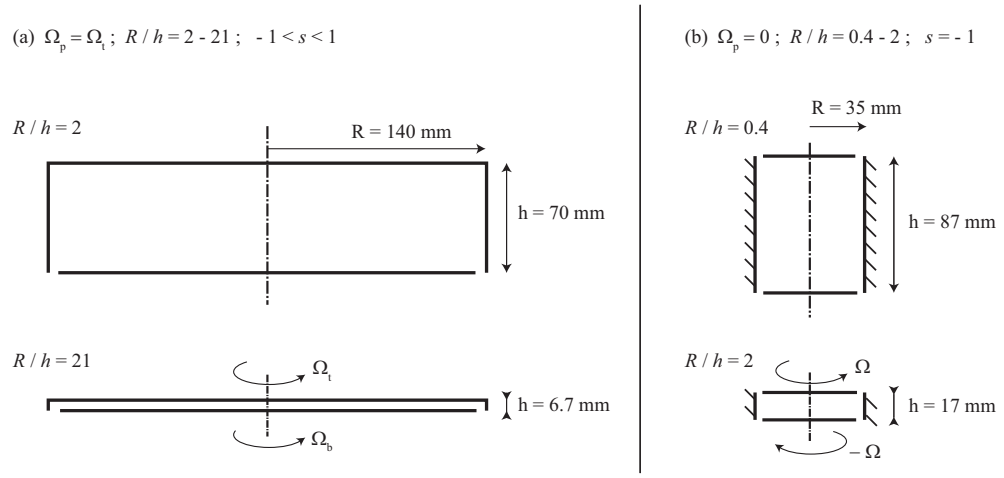


FIG. 1.3 – Schéma des deux cellules expérimentales utilisées dans l'étude des instabilités en cavités tournantes. (a) Cavité "plate", dont la paroi latérale est solidaire du disque supérieur, pour les écoulements en contra et co-rotation [61, 91]. (b) Cavité "carrée", dont la paroi latérale est fixe, pour l'écoulement en exacte contra-rotation uniquement [108]. L'espace entre disques et paroi latérale est exagéré pour des raisons de visibilité.

2. "Cavité carrée" (§ 1.3.3, Fig. 1.3b) [108] : cellule symétrique, dont la paroi latérale est fixe. Cette configuration a été explorée en exacte contrarotation uniquement ($s = -1$), pour des cavités de rapport d'aspect[1] proche de l'unité, $\Gamma = 0.4$ à 2.

Le dispositif de la "cavité plate" est issu d'un premier montage décrit par Gauthier *et al.* (1999, 2002) [60, 61] destiné à l'étude des instabilités de couche limite. J'ai modifié par la suite le montage initial afin de permettre un accès optique latéral, nécessaire aux mesures de PIV dans le plan vertical. Une description détaillée du nouveau montage est donnée dans Moisy *et al.* (2004) [91].

Le dispositif de la "cavité carrée" est issu d'un montage réalisé par L. Quartier au Laboratoire de Physique Statistique (ENS), pour permettre des visualisations destinées à explorer les instabilités observées dans les simulations numériques de Nore *et al.* (2003, 2004) [110, 109]. Le montage ainsi que les mesures de PIV sont présentées en détail dans Nore *et al.* (2005) [108].

Dans nos études sur la "cavité plate", nous nous sommes restreints à une caractérisation des instabilités au voisinage du seuil. En revanche, dans le cas particulier de la "cavité carrée" en exacte contra-rotation, nous avons pu détailler plus avant les bifurcations successives faisant apparaître des écoulements instationnaires à mesure que le nombre de Reynolds est augmenté.

### 1.3.2 Instabilités dans l'écoulement en "cavité plate"

Trois grandes classes d'instabilité ont été observées dans l'écoulement en "cavité plate", et sont résumées dans le tableau 1.1. Les deux premières, axisymétriques (C) et spirales positives ($S^+$), sont des instabilités de la couche limite centripète (de type Bödewadt), présentes dans toutes les configurations de rotation ($-1 \leq s \leq 1$), tandis que la troisième, donnant lieu à des spirales négatives ($S^-$), est une instabilité de couche de cisaillement libre, présente uniquement

[1] Dans l'article Nore *et al.* (2005) [108], la définition du rapport d'aspect était $\Gamma = h/R$, inverse de la convention utilisée dans les autres articles. La notation $\Gamma = R/h$ sera systématiquement reprécisée dans cette partie.

| Motif | Nature de l'instabilité | Domaine d'étude |
|---|---|---|
| Axisymétrique (C) | Instabilité visqueuse (type II) de la couche limite centripète | Rotor-stator pour $\Gamma = 9 - 47$ [60], Co- et contra-rotation à $\Gamma = 21$ [61] |
| Spirales ($S^+$) | Instabilité inflexionelle (type I) de la couche limite centripète | Rotor-stator [60], Co- et contra-rotation à $\Gamma = 21$ [61] |
| Spirales ($S^-$) | Instabilité de cisaillement libre | Contra-rotation à $\Gamma = 21$ [61] et à $\Gamma = 2 - 21$ [91] |

TAB. 1.1 – Les 3 motifs d'instabilités étudiés dans la "cavité plate".

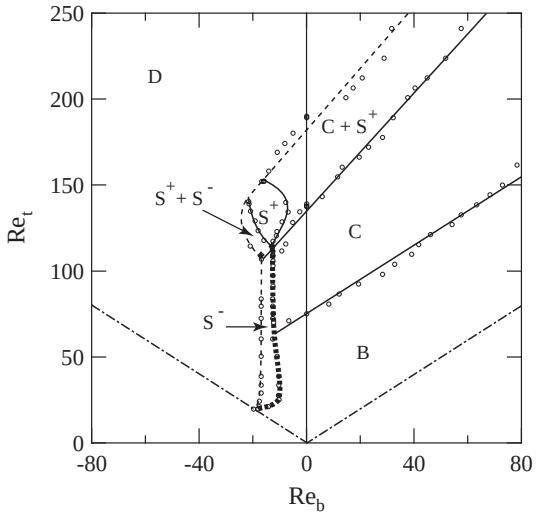


FIG. 1.4 – (a) Diagramme de stabilité dans le plan $(Re_b, Re_t)$ pour un rapport d'aspect $\Gamma = R/h = 21$ fixé. La ligne épaisse pointillée correspond au seuil de l'instabilité de cisaillement conduisant aux spirales négatives. D'après Gauthier *et al.* (2002) [61].

en contra-rotation ($s < 0$). Les termes "positifs" et "négatifs" se réfèrent au sens d'enroulement des spirales, vers le centre (respectivement vers l'extérieur) dans le sens de rotation du disque tournant le plus rapidement.

J'évoquerai ici rapidement les 2 premières classes d'instabilité, et je détaillerai plus avant la troisième, qui constitue une contribution originale de mon travail.

### Instabilités de la couche limite centripète

L'écoulement en cavité rotor-stator présente une couche limite centrifuge sur le disque tournant (ici le disque supérieur) et une couche limite centripète sur le disque immobile (inférieur). Des travaux antérieurs [60] ont permis de montrer que la couche limite supérieure était autosimilaire sur une extension radiale assez prononcée, $0.3 < r/R < 0.8$, avec $\delta_t/(\nu/\Omega_t)^{1/2} \simeq 2.2$. En revanche, la couche limite inférieure n'est pas autosimilaire, et s'épaissit aux faibles rayons, avec $\delta_b/(\nu/\Omega_t)^{1/2} \simeq 2 - 6$. C'est cette couche limite inférieure qui se déstabilise, donnant lieu aux motifs axisymétriques associés à une instabilité visqueuse (type II) [60] ainsi qu'aux spirales positives ($S^+$) associés à une instabilité inflexionelle (type I).

Ces travaux ont été prolongés par l'étude de l'influence de la rotation du disque inférieur sur ces deux instabilités, en se restreignant au cas d'une cavité de grand rapport d'aspect, $\Gamma = 21$ [61]. L'essentiel des résultats est résumé sur le diagramme de la figure 1.4. Sur ce diagramme, l'axe vertical ($Re_b = 0$) représente la configuration rotor-stator de référence. Le résultat principal de cette étude est que la corotation du disque inférieur à tendance à stabiliser l'écoulement : les seuils d'instabilités $Re_{t,c}$ des motifs C et $S^+$ sont des fonctions croissantes de $Re_b$. Concernant les cercles propagatifs C, cette stabilisation n'est en fait qu'apparente : dans le référentiel du disque inférieur, le seuil relatif $Re'_t = (\Omega_t - \Omega_b)h^2/\nu$ s'avère inchangé, de l'ordre de 75. Ce résultat indique que la force de Coriolis n'a pas d'effet sur le mécanisme d'instabilité visqueuse responsable de la formation de ces structures.

En revanche, la stabilisation du motif $S^+$ est réelle : la courbe de stabilité est donnée par $Re_{t,c} \simeq 135 + 1.7Re_b$, et le seuil relatif $Re'_t$ dans le référentiel lié au disque inférieur est cette fois-ci une fonction croissante de $Re_b$. La force de Coriolis a donc bien un effet stabilisant sur cette instabilité inflexionelle. Une origine de cette stabilisation par la rotation d'ensemble réside probablement dans l'évolution de la couche limite centripète : Non autosimilaire dans le cas rotor-stator, son épaisseur tend à diminuer et devenir constante dans le cas co-rotatif. Cette observation est compatible avec la limite d'une couche d'Ekman du problème linéaire pour $s \to 1$ ($Ro \ll 1$), dont l'autosimilarité est beaucoup plus robuste à rapport d'aspect fini que celle de la couche de Bödewadt.

**Instabilités de cisaillement libre**

En plus des deux motifs d'instabilités de couche limite précédents, l'écoulement contra-rotatif à suffisamment grand rapport de contra-rotation fait apparaître un motif d'instabilité appelé "spirales négatives" (voir la figure 1.4 dans le cas $\Gamma = 21$). A faible rapport d'aspect, pour $\Gamma = R/h$ entre 2 et 10, cette instabilité donne lieu à des motifs sous forme d'un ensemble de tourbillons corotatifs d'axe quasi-vertical, disposés le long d'un cercle. La figure 1.5 en donne une illustration, obtenue par mesures de PIV dans le plan horizontal à mi-hauteur, ainsi que par une simulation numérique réalisée dans les mêmes conditions. Dans ce régime, le rayon du cercle décroit lorsqu'augmente $\Omega_t$, conduisant à un nombre de tourbillons (mode azimuthal) lui-aussi décroissant. A plus fort rapport d'aspect, l'interaction de ces tourbillons avec les couches limites conduisent à la formation de bras spiraux.

L'origine de ce motif se trouve dans la structure de l'écoulement de base contrarotatif (fig. 1.6). Tandis que l'écoulement rotor-stator est constitué d'une unique cellule de recirculation, provenant de l'éjection centrifuge sur le disque tournant (disque supérieur), la contra-rotation du disque inférieur peut, au-delà d'un rapport de contra-rotation critique, elle aussi générer une éjection centrifuge [45, 91]. Ce rapport de contra-rotation est d'ordre $|s| \simeq 0.1$ à nombre de Reynolds suffisament élevé. Deux flux radiaux de direction opposée apparaissent alors sur le disque inférieur, conduisant à la présence d'une ligne de stagnation circulaire et à la formation de 2 cellules de recirculation contra-rotatives. Ce cercle de stagnation est à l'origine du décollement de la couche limite centripète, qui conduit à la formation d'une couche de cisaillement libre entre les deux disques. C'est cette couche de cisaillement qui peut être sujette à une déstabilisation, et qui conduit aux motifs de spirales négatives observés.

Le rôle de cette couche de cisaillement décollée dans l'instabilité de l'écoulement contra-rotatif a également été mis en évidence par Lopez *et al.* (2002) [80], dans une configuration analogue à rapport d'aspect $\Gamma$ plus faible (cavité plus épaisse), conduisant à un ensemble de tourbillons quasi-verticaux de forme évasée. Grâce à une variation systématique du rapport

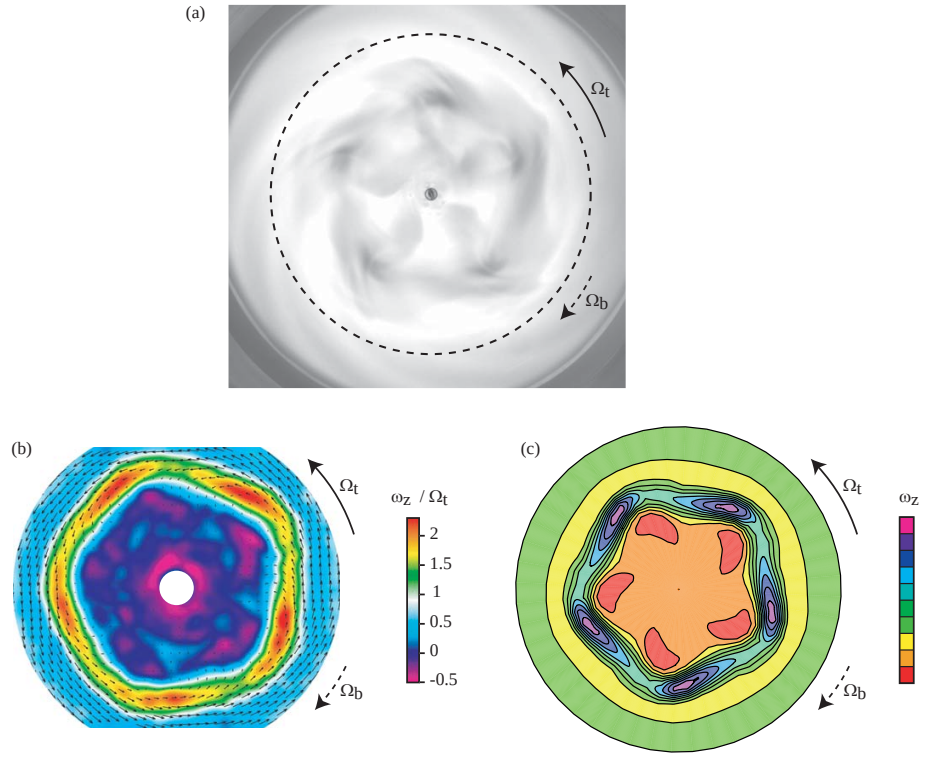


FIG. 1.5 – Exemple de motif issu de l'instabilité de cisaillement dans l'écoulement entre deux disques contrarotatifs : (a) Visualisations par particules réfléchissantes (Kalliroscope). (b) Mesures par Vélocimétrie par Images de particules. (c) Simulation numérique. Le cercle pointillé en (a) indique les domaines de visualisation de (b) et (c), $r/R < 0.6$. Pour (b) et (c), la couleur code la vorticité axiale. Rapport d'aspect $\Gamma = R/h = 7$, $Re_t \simeq 250$, $s \simeq -0.23$. D'après Moisy *et al.* (2004) [91].

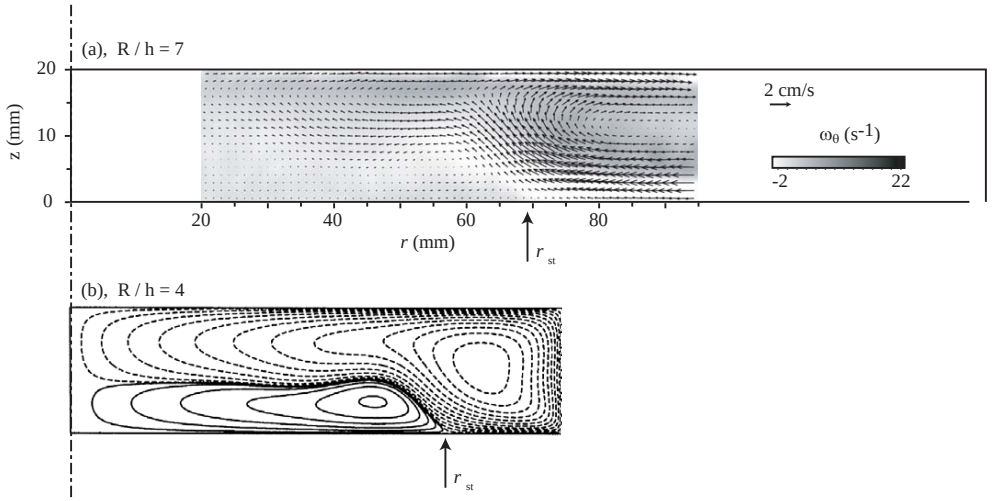


FIG. 1.6 – Ecoulement dans le plan vertical, montrant l'existence de deux cellules de recirculation dans le cas contrarotatif, et d'un cercle de stagnation sur le disque, de rayon $r_{st}$. (a) Mesures par PIV, pour $\Gamma = 7$, $Re_t = 130$, $s = -0.15$ ; (b) Contours de la fonction de courant, obtenu par simulation axisymétrique par Lopez (1998) [79], pour $\Gamma = 4$, $Re_t = 63$, $s = -0.5$ (figure inversée pour respecter la convention de rotation des disques utilisée ici).

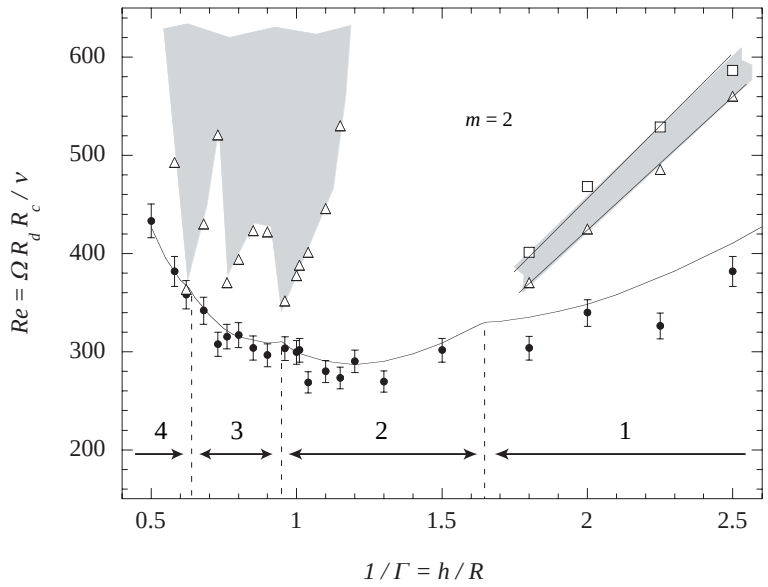


FIG. 1.7 – Diagramme de stabilité de l'écoulement exactement contra-rotatif ($s = -1$) en fonction de l'inverse du rapport d'aspect. Les chiffres indiquent les modes critiques $m_c$. Les symboles sont obtenus à partir de visualisations [108], tandis que le trait plein correspond à des résultats numériques [110]. Les zones grisées correspondent aux écoulements instationnaires.

d'aspect, nous avons donc pu mettre ici en évidence une continuité entre les motifs tourbillonnaires de Lopez *et al.* (2002) à $\Gamma$ modéré, et les spirales négatives décrites dans Gauthier *et al.* (2002) [61] à $\Gamma$ plus élevé [91].

### 1.3.3 Ecoulement de von Kármán exactement contra-rotatif

#### Instabilité de la couche de cisaillement médiane

Dans la configuration d'exacte contra-rotation à rapport d'aspect d'ordre 1 et paroi latérale fixe (la "cavité carrée"), l'écoulement présente une couche de cisaillement horizontale (comme illustré en figure 1.2b), séparant deux cellules de recirculation associées à la rotation de chaque disque. Cette couche de cisaillement est de même nature que la couche décollée décrite en § 1.3.2, si ce n'est que la ligne de stagnation circulaire qui y est associé est maintenant sur la paroi latérale, à mi-hauteur entre les deux disques.

Tout comme précédemment, cette couche de cisaillement est sujette à une instabilité de type Kelvin-Helmholtz, donnant lieu à des tourbillons radiaux corotatifs. La courbe de stabilité marginale de cette instabilité pour différents rapports d'aspect (figure 1.7) montre un excellent accord entre les simulations et nos mesures [108]. Qualitativement, la diminution du mode le plus instable $m$ avec le rapport d'aspect $h/R$ est liée à l'épaississement de la couche de cisaillement, conduisant à un plus petit nombre de tourbillons pouvant tenir dans la périphérie.

#### Symétries et bifurcations

La nature des bifurcations susceptibles d'intervenir dans les écoulements en cavité axisymétrique dépend du détail des symétries des conditions aux limites. Tandis que l'écoulement de base hérite de toutes les symétries du forçage, les différentes bifurcations sont classiquement

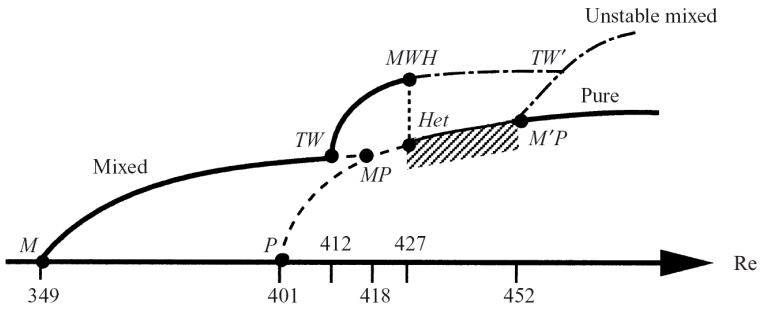


FIG. 1.8 – Diagramme de bifurcation de l'écoulement exactement contra-rotatif ($s = -1$) pour un rapport d'aspect $h/R = 2$, obtenu numériquement par Nore *et al.* (2003) [110].

associées à des brisures successives de ces symétries, l'écoulement bifurqué ne possédant alors que des symétries issues d'un sous-groupe des symétries initiales.

En plus de la symétrie axiale (invariance par rotation $S_\theta$ d'angle $\theta$ quelconque), déjà présente dans la configuration de "cavité plate" décrite précedemment, l'écoulement de von Kármán avec paroi latérale fixe et disques en exacte contra-rotation ($s = -1$) présente une symétrie supplémentaire. En effet, cette géométrie est invariante par rotation d'un angle $\pi$ autour de n'importe quel axe horizontal dans le plan médian, noté $R_\pi(\theta_0)$, où $\theta_0$ est l'angle de l'axe par rapport à une direction de référence arbitraire [108]. Le fait que les rotations $S_\theta$ et $R_\pi(\theta_0)$ ne commutent pas confère à cette configuration un groupe de symétrie plus général, noté $O(2)$. Ces symétries jouent un rôle fondamental dans la richesse du diagramme de bifurcation de cette configuration (fig. 1.8), qui a été caractérisé en détail par Nore *et al.* (2003,2004) [110, 109].

Pour des nombres de Reynolds au-delà de la courbe de stabilité marginale, l'écoulement devient bien plus compliqué, avec notamment l'apparition de solutions instationnaires (en grisé dans la figure 1.7). Si l'on se concentre sur le cas particulier $h/R = 2$, dont le diagramme de bifurcation complet est représenté en figure 1.8, le mode le plus instable est le mode $m = 1$, appelé "mode mixte" (M). A mesure que le nombre de Reynolds est augmenté, ce mode stationnaire cède la place à une onde propagative modulée, puis à des quasi-cycles hétéroclines, pour aboutir enfin à une nouvelle solution stationnaire $m = 2$, appelée "mode pur" (P). Les termes "mixte" et "pur" sont liés aux harmoniques excitées par les non-linéarités : le mode mixte combine des harmoniques paires et impaires, tandis que le mode pur ne fait intervenir que des harmoniques paires. Ces solutions instationnaires sont issues de la compétition entre les modes stationnaires $m = 1$ et $m = 2$. Parmi ces solutions instationnaires, nous allons nous concentrer plus particulièrement dans la suite sur les quasi-cycles hétéroclines.

### Cycles hétéroclines

Un cycle hétérocline est une structure remarquable d'un système dynamique en présence d'un degré suffisament élevé de symétries, qui peut intervenir lorsque coexistent deux ou plusieurs points fixes instables, équivalents du point de vue des symétries. Ces solutions instables correspondent à des points selles dans l'espace des phases, dont les directions instables et stables sont connectées deux à deux (contrairement à un cycle homocline, dans lequel une direction stable et instable d'un même point fixe sont connectées entre elles). Le système décrit alors un cycle, passant un temps croissant au voisinage de chaque point fixe, à mesure qu'il

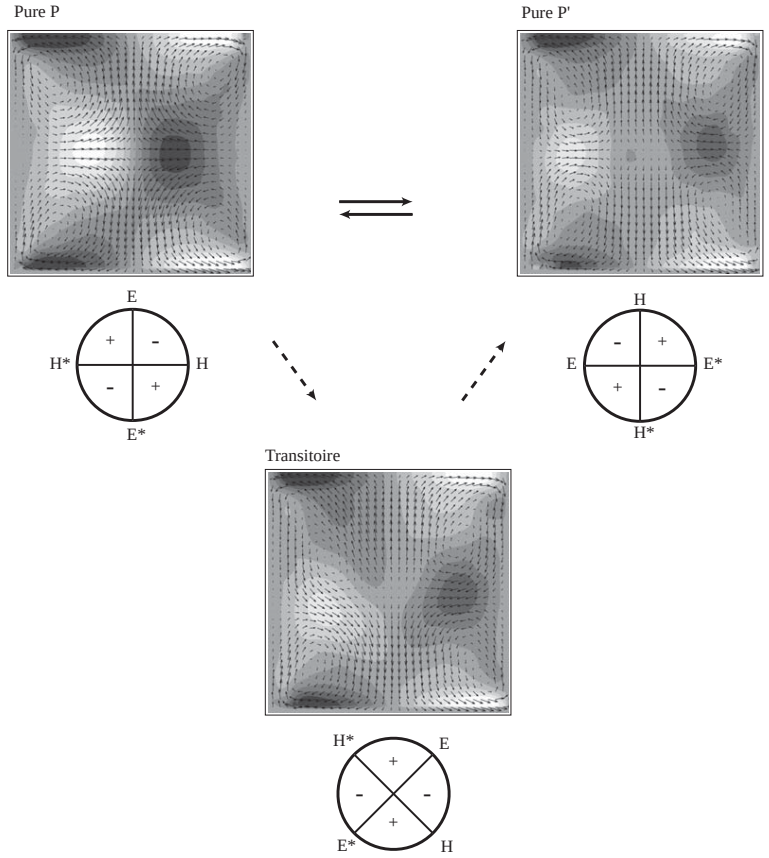


FIG. 1.9 – Champs de vitesse mesurés par PIV dans le plan vertical, illustrant le quasi-cycle hétérocline observé dans l'expérience. L'écoulement oscille entre les 2 modes purs P et P', mais transite irrégulièrement vers un mode transitoire favorisé par un défaut de symétrie.

s'approche chaque fois plus près de chacun d'entre eux. Cette structure remarquable des systèmes dynamiques en présence de symétries a bénéficié d'un intérêt soutenu suite aux travaux de Busse & Heikes (1980) [18] sur l'instabilité de Küppers-Lortz (convection thermique en présence de rotation).

L'écoulement de von Kármán contra-rotatif présente de tels états instables symétriques purs $m = 2$, notés $P$ et $P'$, issus d'une résonnance entre les modes $m = 1$ et $m = 2$. Le système présente des oscillations entre ces deux états instables, que nous avons caractérisées en détails (figures 1.9 et 1.10). Certaines propriétés de ces cycles sont en très bon accord avec les résultats numériques de Nore *et al.* (2004) [109], en particulier la gamme de nombre de Reynolds sur laquelle ils sont observés et les symétries attendues des 2 états $P$ et $P'$. En revanche, il existe deux différences importantes entre les oscillations observées expérimentalement et numériquement, révélatrices des caractéristiques intrinsèques de ces cycles hétéroclines.

Tandis que la période des oscillations est strictement constante dans les simulations, celle-ci est plus erratique dans les expériences (fig. 1.10). En fait, ni simulation ni expérience n'observe la caractéristique essentielle d'un véritable cycle hétérocline, à savoir la croissance et la divergence du temps de passage du système au voisinage de chaque mode instable [18]. C'est d'ailleurs pour cette raison que l'on parle de "quasi-cycle hétérocline". Dans les deux cas le bruit semble responsable de ce comportement : Dans les simulations le bruit résulte

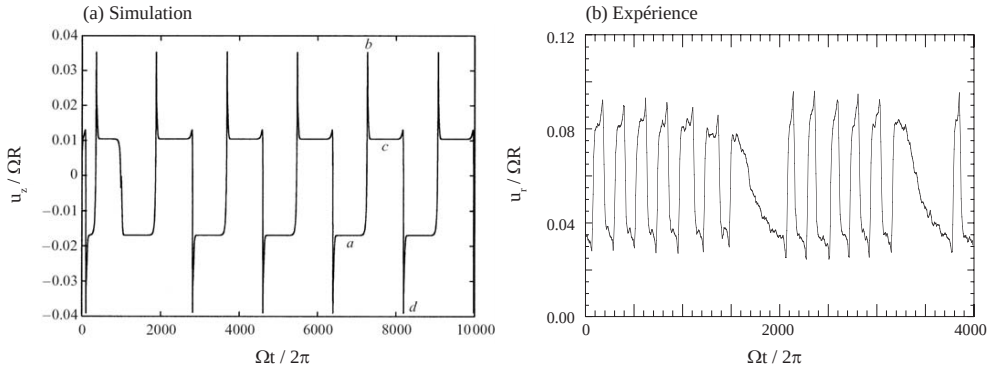


FIG. 1.10 – Séries temporelles illustrant les différences entre les quasi-cycles hétéroclines observés numériquement et expérimentalement. (a) Composante verticale issue de la simulation numérique, pour $Re = 435$, montrant une rapide convergence vers une oscillation strictement périodique entre deux plateaux [110]. (b) Composante radiale mesurée par PIV, pour $Re = 469$, montrant l'oscillation entre deux plateaux avec un temps d'approche croissant, ponctuée irrégulièrement de phases de relaxation [108].

de la discrétisation du système, qui finit par approcher chaque point instable du cycle à une même distance finie à chaque itération, conduisant à sélectionner une période d'oscillation arbitraire mais précisément définie, dépendant de la précision du calcul. Dans les expériences, c'est un bruit aléatoire qui vient dévier stochastiquement le système à chaque itération, là encore conduisant à une certaine périodicité, mais approximative cette fois-ci : chaque cycle a sa durée propre, dont seule la moyenne est reproductible.

Une seconde différence apparaît dans ces séries temporelles : les oscillations mesurées dans l'expériences sont parfois ponctuées de phases de relaxations vers un troisième état, hors cycle hétérocline (état "transitoire" dans la figure 1.9). Ce troisième état est probablement associé à un mode sélectionné par un défaut de symétrie de la cellule expérimentale. En effet, lorsque la dynamique du système devient très lente, celui-ci devient extrêmement sensible à des imperfections même minimes (légère ellipticité de la cellule par exemple). Ainsi, au cours du cycle, le système peut venir explorer des trajectoires autres et rester "coincé" un certain temps dans un état biaisé par une légère asymétrie du système, avant de revenir osciller entre les deux points fixes instables.

Ces observations sont finalement assez riches d'enseignement sur la nature de ces cycles hétéroclines. Fruits du degré élévé de symétries du problème hydrodynamique, ces cycles restent très délicats à observer, tant dans les réalisations expérimentales (extrême sensibilité aux défauts géométriques) que numériques (influence des erreurs d'arrondis) de cet écoulement.

## 1.4 Et l'écoulement de von Kármán turbulent ?

La complexité des bifurcations successives et des scénarios de transition vers la turbulence de l'écoulement de von Kármán (voir la figure 1.8) résulte de l'existence de plusieurs modes instables et de leur compétition. On pourrait penser que la richesse des régimes d'écoulement décrits ici à bas nombre de Reynolds ($Re \lesssim 500$) disparaît à haut nombre de Reynolds, suivant l'hypothèse classique de symétries restaurées au sens statistique en régime turbulent [57]. Mais il n'en est rien : même pour des nombres de Reynolds dans la gamme $10^4 - 10^6$, des bifurcations et des structures persistantes à grande échelle (comme illustrées en figure 1.11a) sont toujours présentes !

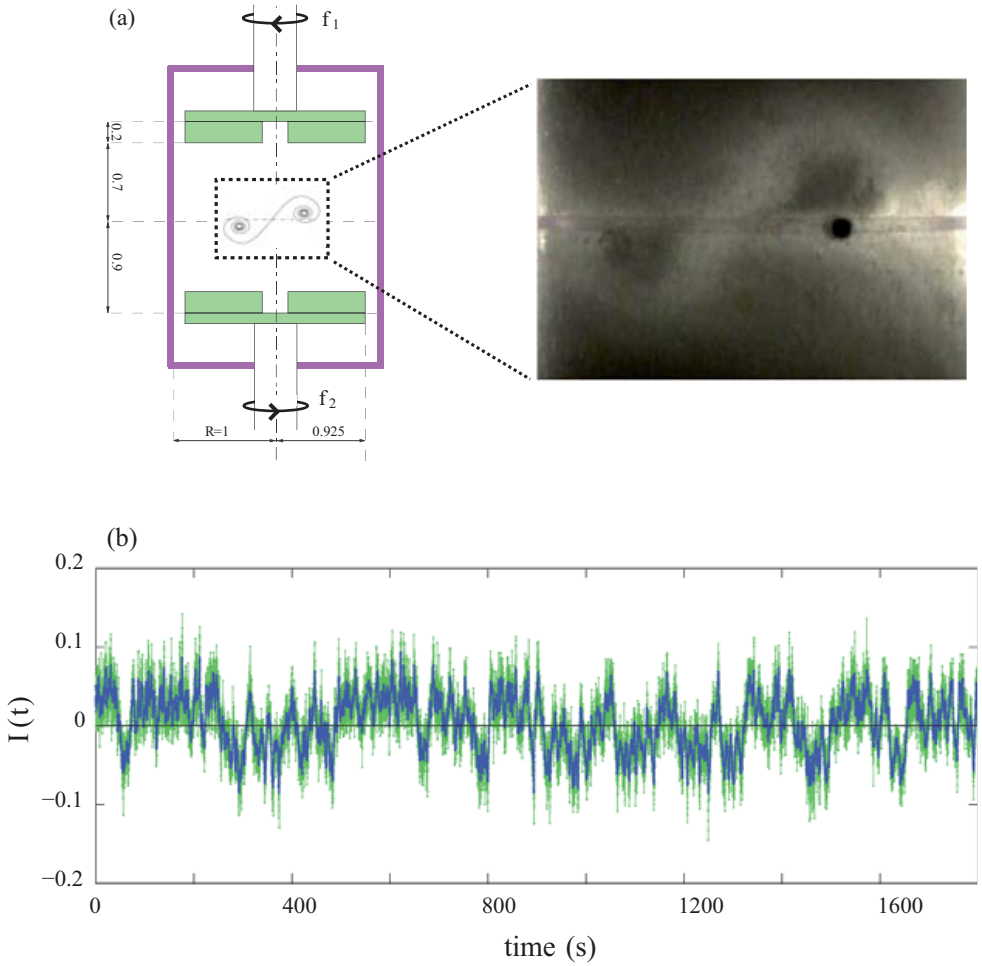


FIG. 1.11 – (a) Ecoulement de von Kármán turbulent ($Re = 29000$), dont la couche de cisaillement médiane se compose de façon intermittente de structures en tourbillons radiaux, similaires à ceux observés à bas nombre de Reynolds. D'après Cortet *et al.* (2009) [35]. (b) Evolution du moment angulaire normalisé, mesuré dans le plan vertical. Cette quantité mesure, de façon indirecte mais plus robuste, la position instantannée de la couche de mélange. On observe un signal intermittent, avec des temps de séjours prolongés au voisinage de deux états métastables symétriques à $\pm 0.05$. D'après Cortet *et al.* (2010) [34].

Cette richesse suprenante de comportements de l'écoulement de von Kármán turbulent a fait l'objet d'études approfondies ces dernières années, dans le groupe de F. Daviaud, B. Dubrulle et A. Chiffaudel au CEA Saclay. Une grande sensibilité de l'écoulement, caractérisée par la divergence d'une pseudo-susceptibilité, est observée dans une certaine gamme de nombres de Reynolds, suggérant l'existence d'une "bifurcation turbulente" de l'écoulement (Cortet *et al.* (2010) [34]). Cette susceptibilité élevée est illustrée en figure 1.11(b) : l'évolution temporelle du "moment angulaire normalisé" (quantité liée à la position de la couche de cisaillement médiane) montre des sauts intermittents entre deux états métastables symétriques [34]. Dans certaines configurations du forçage, une bifurcation sous-critique, avec un comportement hystérétique, est également observée entre un écoulement à une cellule ou deux cellules de recirculation toroïdales [115].

Ces observations peuvent sembler paradoxales, si l'on considère naïvement que la turbulence à haut nombre de Reynolds constitue un état à grand nombre de degrés de liberté indépendants. Cependant, on sait que tel n'est pas le cas : l'enrichissement du spectre à haute fréquence lorsqu'est augmenté le nombre de Reynolds n'implique pas l'appauvrissement du spectre à basse fréquence. La persistance de détachement tourbillonnaire dans les sillages turbulents de type Bénard-von Kármán, caractérisés par des nombres de Strouhal à $Re \simeq 10^6$ comparables à ceux obtenus pour $Re \simeq 10^2$, illustre ce caractère multiéchelle. De manière similaire, Brown et Roshko (1974) [16] avaient déjà observé, dans une couche de mélange turbulente, la persistence de structures à grande échelle similaires aux tourbillons de Kelvin-Helmholtz de l'instabilité primaire de la couche de mélange laminaire.

Ces observations soulèvent la question délicate de la pertinence d'une décomposition de Reynolds (écoulement moyen + fluctuations) dans certains situations : même si la définition de la décomposition elle-même reste évidemment mathématiquement justifiée, quel est le sens physique de l'écoulement moyen ainsi obtenu par moyenne d'ensemble si celui-ci n'est jamais approché par le système de façon instantanée ? Comment anticiper la dynamique lente d'un tel système (et *a fortiori* la reproduire numériquement), lorsque l'on voit que l'échelle de temps de ces battements peut atteindre plusieurs milliers de temps de retournement ? Enfin, comment prévoir si un système turbulent donné présentera ou non une telle dynamique lente ?

Ces questions sont ouvertes, mais elles permettent au moins de clore ce premier chapitre sur cette note optimiste pour le mécanicien des fluides expérimentateur : si les simulations numériques s'avèrent incontournables pour l'analyse et la compréhension de certains phénomènes, la découverte de phénomènes nouveaux risque de faire encore longtemps le bonheur des seuls expérimentateurs.

*J. Fluid Mech.* (2004), *vol.* 507, *pp.* 175–202.  
DOI: 10.1017/S0022112004008833 Printed in the United Kingdom

# Experimental and numerical study of the shear layer instability between two counter-rotating disks

By F. MOISY[1], O. DOARÉ[1]†, T. PASUTTO[1], O. DAUBE[2] AND M. RABAUD[1]

[1]Laboratoire FAST, Bâtiment 502, Campus Universitaire, F-91405 Orsay Cedex, France
[2]CEMIF/LME, Université d'Evry, 40 Rue du Pelvoux, F-91020 Evry Cedex, France

(Received 8 September 2003 and in revised form 5 January 2004)

The shear layer instability in the flow between two counter-rotating disks enclosed by a cylinder is investigated experimentally and numerically, for radius-to-height ratio $\Gamma = R/h$ between 2 and 21. For sufficiently large rotation ratio, the internal shear layer that separates two regions of opposite azimuthal velocities is prone to an azimuthal symmetry breaking, which is investigated experimentally by means of visualization and particle image velocimetry. The associated pattern is a combination of a sharp-cornered polygonal pattern, as observed by Lopez *et al.* (2002) for low aspect ratio, surrounded by a set of spiral arms, first described by Gauthier *et al.* (2002) for high aspect ratio. The spiral arms result from the interaction of the shear layer instability with the Ekman boundary layer over the faster rotating disk. Stability curves and critical modes are experimentally measured for the whole range of aspect ratios, and are found to compare well with numerical simulations of the three-dimensional time-dependent Navier–Stokes equations over an extensive range of parameters. Measurements of a local Reynolds number based on the shear layer thickness confirm that a shear layer instability, with only weak curvature effect, is responsible for the observed patterns. This scenario is supported by the observed onset modes, which scale as the shear layer radius, and by the measured phase velocities.

## 1. Introduction

The stability of the flows between rotating disks, or von Kármán (1921) swirling flows, has been addressed for a long time, mostly in the rotor–stator configuration, i.e. between one rotating and one stationary disks (Zandbergen & Dijkstra 1987). Of practical interest for laboratory experiments is the case of finite disks, for which no similarity solutions exist. The nature and the stability of the flow then strongly depends on the radius-to-height ratio, $\Gamma = R/h$, and the rotation ratio, $s = \Omega_b/\Omega_t$ ($t$ and $b$ refer to the top and bottom disks respectively). Most of the studies deal with the rotor–stator configuration, $s = 0$, and it is only recently that the intermediate cases, $-1 < s < 1$, have been addressed experimentally and numerically (Lopez 1998; Lopez *et al.* 2002; Gauthier *et al.* 2002; Nore *et al.* 2003, 2004). Other parameters may also be taken into account, such as the presence of a central hub or the end condition of the sidewall; these extra parameters are of practical importance, for instance in hard

† Present address: ENSTA/UME, Chemin de la Hunière, F-91761 Palaiseau Cedex, France.

disk systems, for which $\Gamma \sim O(10)$ and $s = 1$ (Humphrey, Schuler & Webster 1995), or turbomachines. The quasi-solid-body rotation limit, $s \approx 1$, is of great importance in geophysical flows (Stewartson 1953; Hide & Titman 1967; Früh & Read 1999).

The investigation of the flow in rotor–stator $\Gamma \sim O(1)$ cavities has been mainly motivated by the experimental observation of vortex breakdown in the form of recirculatory bubble by Escudier (1984). The axisymmetry breaking of the base flow gives rise to rotating waves, analysed in detail by Gelfgat, Bar-Yoseph & Solan (2001), Blackburn & Lopez (2002) and Serre & Bontoux (2002) for $\Gamma < 1$. For flatter cavities, $\Gamma \sim O(10)$, the recent experimental studies have mainly focused on the boundary layer instabilities in the rotor–stator case (Gauthier, Gondret & Rabaud 1999; Schouveiler, Le Gal & Chauve 2001), further characterized numerically by Serre, Crespo del Arco & Bontoux (2001). Two classes of instability are observed: axisymmetric propagating vortices and positive spirals. These studies have been extended to differential rotation of the disks by Gauthier *et al.* (2002) for $\Gamma = 20.9$. It was shown that co-rotating and weak counter-rotating flows only weakly affect the properties of the boundary layer instabilities, like linearly shifting the instability thresholds or the onset modes.

The flow between counter-rotating disks appears to be much richer: in addition to the boundary layer instabilities, free shear layer instabilities also take place, which have been the subject of much recent experimental and numerical effort. In the simplest flow configuration, with exact counter-rotating disks and a stationary sidewall, the axisymmetric base flow becomes unstable through a Kelvin–Helmholtz instability of the equatorial free shear layer, giving rise to radial co-rotating vortices. The complete scenario of bifurcations in this configuration, for aspect ratios $\Gamma$ between $1/2$ and 3, has been numerically investigated by Nore *et al.* (2003, 2004).

In the less symmetric case of counter-rotating disks with a rotating sidewall and arbitrary rotation ratio, the instability mechanism basically remains the same, although the geometry of the internal shear layer becomes more complex. The main difference is that a sufficiently large rotation ratio is needed for the transition layer to detach from the slower rotating disk and give rise to a free shear layer. The reason is that for sufficiently large rotation ratio, the structure of the meridional flow drastically changes, evolving from a one-cell to a two-cell recirculation flow, with a stagnation circle on the slower disk, which is responsible for the detachment of the shear layer into the bulk of the flow. This property was first described experimentally and numerically by Dijkstra & van Heijst (1983) for $\Gamma = 14.3$, and further characterized by Lopez (1998) for $2 \leqslant \Gamma \leqslant 8$ from axisymmetric numerical simulations.

Detailed investigation of the instability of this internal shear layer by means of dye visualization and three-dimensional numerical simulations, restricted to $\Gamma = 2$ and $\Omega_i h^2/\nu = 250$, has been performed by Lopez *et al.* (2002) and Marques, Gelfgat & Lopez (2003). These authors observed patterns of wavenumber 4 and 5, in the form of funnel-like vortices. At the same time, for a very different aspect ratio $\Gamma = 20.9$, Gauthier *et al.* (2002) reported a new instability pattern of wavenumber 9 to 11, in the form of a set of spiral arms. This pattern was given the name of 'negative' spirals, because they roll up to the centre in the direction of the slower disk. Although the morphology of the funnel-like vortices and the negative spirals patterns strongly differs, the issue of a possible continuity between them was first raised by Gauthier *et al.* (2002) and Moisy, Pasutto & Rabaud (2003). The purpose of this paper is to address this issue from a detailed analysis of the instability patterns for a wide range of aspect ratio $\Gamma$, between 2 and 21.

The influence of the curvature and rotation on the stability of internal shear layers has received considerable interest (Dolzhanskii, Krymov & Manin 1990). In addition

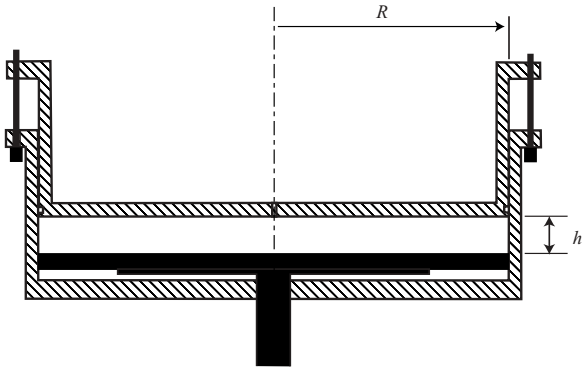


FIGURE 1. Experimental cell. The cylinder (hatched regions), made of transparent Plexiglas, rotates with angular velocity $\Omega_t$, while the bottom disk (black) rotates in the opposite sense with angular velocity $\Omega_b$.

to the classical Kelvin–Helmholtz instability, centrifugal effects may also occur, which are stabilizing or destabilizing (Yanase *et al.* 1993; Liou 1994). The extreme case where rotation dominates the dynamics plays a central role in geophysical flows. After the pioneering study of Hide & Titman (1967), laboratory experiments focused on weak shear compared to the background rotation, showing patterns in the form of circular chains of eddies, with complex nonlinear mode selection and eddy clustering (Niino & Misawa 1984; Konijnenberg *et al.* 1999; Früh & Read 1999). Closer to our experiment, Rabaud & Couder (1983) have investigated the stability of a two-dimensional forced circular shear layer in a split-annulus tank without background rotation, further studied numerically by Chomaz *et al.* (1988) and Bergeron *et al.* (2000). Although in these experiments the rotation only weakly affects the shear layer instability, patterns in the form of circular chains of eddies are observed as well, the number of which decreases as the Reynolds number is increased.

The outline of the paper is as follows: § 2 briefly presents the experimental set-up, and § 3 summarizes the numerical methods. The steady axisymmetric base flow is described in § 4, with special attention paid to the existence domain of the two-cell recirculating flow. Instability patterns and onset curves are described in § 5 from particle image velocimetry (PIV) measurements and numerical simulations. In § 6 the instability is characterized in terms of a local Reynolds number based on the internal shear layer. Systematic measurements of the onset modes and phase velocities are presented, and are shown to compare well with a classical Kelvin–Helmholtz instability mechanism. Some concluding remarks are finally offered in § 7.

## 2. Experimental set-up

### 2.1. *Experimental cell*

The experimental cell, sketched in figure 1, is adapted from that of Gauthier *et al.* (2002) to allow lateral visualization and lighting. It consists of a rotating cylinder of radius $R = 140$ mm, in which a disk of the same radius located at the bottom of the cavity rotates at a different speed. The cylinder and its upper cover (top disk) are made of Plexiglas, to allow visualizations from above and from the side, while the bottom disk is made of black painted brass to improve the visualization contrast. The thickness

of the cell $h$ can be varied from a few millimetres to 7 cm, using wedges between the upper disk and the cylinder rim.

The angular velocities of the top and bottom disks, $\Omega_t$ and $\Omega_b$, can be set independently, from 0 to 10 rad s$^{-1}$. Since we are only concerned with the counter-rotation flow in the present paper, there is no ambiguity in the sign of the angular velocities, which are taken positive. The upper disk is the faster one, $\Omega_t \geqslant \Omega_b$, throughout the paper, except in § 5.2 where the influence of the rotating sidewall is investigated. For both experimental and numerical visualizations, the flow is seen from above, the upper disk rotates anticlockwise while the bottom one rotates clockwise.

Water–glycerol mixture and silicone oils have been used as working fluids, allowing the spanning of a range of kinematic viscosity $\nu$ between $1.0 \times 10^{-6}$ and $50 \times 10^{-6}$ m$^2$ s$^{-1}$ at 20 °C. Viscosity changes due to temperature drift during experiments (about 2% per degree for both glycerol and silicone oils) were controlled, and all the uncertainties finally lead to an accuracy of 3% in the determination of the Reynolds numbers.

### 2.2. *Dimensionless numbers*

The flow is characterized by three dimensionless numbers: two Reynolds numbers based on each disk velocity and the aspect ratio $\Gamma = R/h$. Since two lengthscales, $R$ and $h$, are present in this geometry, freedom exists in the definition of the Reynolds numbers. The basic Reynolds numbers are here based on the cell thickness $h$,

$$Re_i = \Omega_i h^2/\nu, \tag{2.1}$$

where $i = b, t$ denotes the bottom and top disks. In the limit of very large $\Gamma$, the cell radius $R$ has a vanishingly small influence on the flow and these Reynolds numbers $Re_i$ are expected to be the relevant control parameters. In particular they allow one to distinguish between separated and merged boundary layers situations. On the other hand, for a flatter cavity $\Gamma \approx O(1)$, both $R$ and $h$ are relevant, so that the Reynolds numbers based on the thickness and the peripheral velocities, $\Gamma Re_i = \Omega_i Rh/\nu$, are also of interest. In the present study, the Reynolds numbers $Re_i$ are of order 10–2000, and the aspect ratio $\Gamma$ has been varied between 2 and 20.9.

In some cases, the set of parameters ($\Gamma$, $Re_t$, $s$), where $s = \Omega_b/\Omega_t = Re_b/Re_t$ is the counter-rotation ratio, is more convenient than ($\Gamma$, $Re_t$, $Re_b$). Since we are only concerned with the counter-rotation case here, the ratio $s$ is taken always positive. Note that this definition contrasts with the one adopted by Gauthier *et al.* (2002), where $s < 0$ was taken for the counter-rotating regime and $s > 0$ for the co-rotating regime.

### 2.3. *Measurement techniques*

Qualitative insight into the flow structure is obtained from visualization of the light reflected by anisotropic flakes seeding the flow. We make use of Kalliroscope† when the working fluid is water–glycerol mixture, and Iriodin‡ when it is silicone oil. The flow is illuminated by a concentric circular light source, and pictures are obtained using a CCD camera located above, along the disk axis.

More quantitative measurements have been performed using a particle image velocimetry (PIV) apparatus¶. Small borosilicate particles, 11 μm in diameter, seeding the flow are used as tracer, illuminated by a laser sheet of thickness 0.5 mm produced

† Kalliroscope Corporation, 264 Main Street, Box 60, Groton, MA 01450, USA.
‡ Iriodin: Pigments sold by Merck Corporation.
¶ Flowmaster 3, LaVision GmbH, Anna-Vandenhoeck-Ring 19, D-37081 Goettingen, Germany.

by a double-pulsed Nd:Yag (25 mJ/pulse) and a cylindrical lens. Images are acquired with a double-buffer high-resolution camera (12 bits, $1280 \times 1024$ pixels), synchronized with the laser at a rate of 4 frame pairs per second. The velocity fields are averaged over four successive individual fields, i.e. for 1 s, a value much lower than the characteristic timescale of the flow.

The structure of the axisymmetric base flow in the meridional plane is obtained with a vertical laser sheet lighting. The cylindrical wall allows undistorted pictures in the central part of the cell, $r \leqslant 0.7R$. The important out-of-plane azimuthal velocity component strongly constrains the time delay between two succesive frames, of order 4 ms. A resolution of 0.5 mm can be achieved, except near the disks where the important vertical gradient and out-of-plane velocity component prevent resolution of the boundary layers. The bifurcated patterns are investigated using horizontal laser sheet lighting between the two disks and the camera above. For these measurements, a sufficiently large disk separation $h$ and a perfectly horizontal laser sheet are required due to the important vertical gradients. For these reasons, systematic measurements were only possible for low aspect ratio, $\Gamma = 3$ and 7. Another important constraint arises from the important variability in the velocity, from mm s$^{-1}$ near the centre up to 10 cm s$^{-1}$ in periphery, making difficult the choice of a unique time delay between the frames and window size for the PIV computations. Typical time delays of order of 30 ms were chosen for measurements near the centre, where the instability patterns essentially occur.

## 3. Numerical method

The numerical simulations of the three-dimensional flow between counter-rotating disks for various aspect ratios have been carried out by solving the time-dependent Navier–Stokes equations. In addition, a linear stability analysis of the steady axisymmetric base flow has also been performed. These calculations were performed along the lines of the general methodology developed in Gadoin, Le Quéré & Daube (2001), Daube & Le Quéré (2002) and Nore *et al.* (2003), to numerically investigate flow instabilities. For this purpose, several computational tools have been used, which are based upon the use of the same spatial discretization; details may be found in Barbosa & Daube (2001).

### 3.1. *Spatial discretization*

The different unknowns are first expanded in truncated Fourier series over $N$ modes in the azimuthal direction. The coefficients of this expansion are then discretized in the $(r, z)$-planes by means of mimetic finite difference operators (Hyman & Shashkov 1997):

(i) A staggered, uniform or non-uniform, grid in cylindrical coordinates $(r, \theta, z)$ is used. The only unknown located on the axis $r = 0$ is the axial component $\omega_z$ of the vorticity, therefore avoiding the singularity at $r = 0$, since no terms containing $1/r$ have to be considered on the axis.

(ii) The first-order divergence and curl differential operators are discretized by means of the Gauss and Stokes theorems written on elementary cells and the second-order differential operators are constructed as compounds of these first-order discrete operators.

(iii) The nonlinear terms are written as $(\nabla \times \boldsymbol{v}) \times \boldsymbol{v}$ and discretized such that they do not contribute to energy production, as in the continuum case. They are classically computed in the physical space with the usual 3/2 rule.

### 3.2. *Computation of the base flow*

Since the computation of the steady axisymmetric base flow is needed, even when it is unstable, the usual procedure, which consists of obtaining steady-state solutions by letting $t \to \infty$ in a time-stepping code, must be rejected in favour of a Newton–Raphston method. The main drawback of this approach is that the Jacobian matrix of the Navier–Stokes operator is huge and ill-conditioned. To overcome these difficulties, we have used the Stokes preconditioned Newton method proposed by Tuckerman (1989) and Mamum & Tuckerman (1995).

### 3.3. *Time discretization*

Since we are primarily interested in the transition to unsteadiness, the temporal scheme is of great importance. We use a second-order time-marching procedure with an implicit discretization of the linear terms and an explicit Adams–Bashforth-type extrapolation of the nonlinear terms. This procedure is used for both the full nonlinear and the linearized computations. The computation of each time step therefore amounts to the resolution of a so-called generalized Stokes problem for $(\boldsymbol{v}^{n+1}, p^{n+1})$, the values of the velocity and of the pressure at time $(n+1)\Delta t$:

$$\left.\begin{aligned} \left(\frac{3Re}{2\Delta t}\boldsymbol{I} - \nabla^2\right)\boldsymbol{v}^{n+1} + \nabla p^{n+1} &= \boldsymbol{S}^{n,n-1}, \\ \nabla\cdot\boldsymbol{v}^{n+1} &= 0. \end{aligned}\right\} \tag{3.1}$$

The source terms $\boldsymbol{S}^{n,n-1}$ contain all the quantities which were evaluated at the previous time steps. In this time-discretized problem, the velocity–pressure coupling is handled by means of an incremental projection method (Goda 1979; Daube & Le Quéré 2002).

### 3.4. *Computational features*

Both uniform and non-uniform grids are used, depending on the aspect ratio $\Gamma = R/h$. For moderate aspect ratio, $\Gamma \leqslant 10$, a uniform grid is found to be sufficient. For instance, the computations for $\Gamma = 7$ have been carried out on a uniform grid $(r, \theta, z)$, with a resolution of $401 \times 32 \times 101$.

For larger aspect ratio, a non-uniform grid is used. The meshes in the $z$-direction are defined by means of a double hyperbolic tangent function, allowing refinement both in the boundary layers along the disks and in the sheared region at mid-height of the cavity. In the $r$-direction, the grid is uniform up to $r = 3R/4$ and then geometrically refined up to the sidewall. A maximum resolution of $513 \times 78 \times 97$ has been used in the case $\Gamma = 21$.

The time steps are chosen with respect to stability considerations, yielding a number of time steps per revolution within the range 500–1000. Noteworthy is the fact that using a second-order time stepping ensures the independence of the results with respect to the time step.

## 4. Base flow

### 4.1. *Structure of the meridional flow*

We first focus on the steady axisymmetric base flow in the counter-rotating regime, by means of PIV measurements and numerical simulation of the axisymmetric Navier–Stokes equations.

Superimposed on the essentially azimuthal velocity field, each disk tends to impose a meridional recirculation flow. The outward flow induced by the faster disk (here

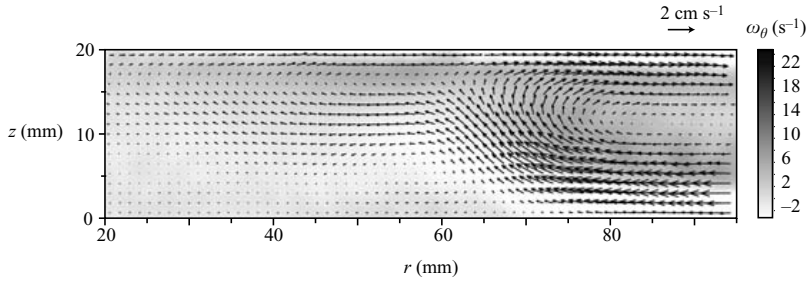


FIGURE 2. Experimental velocity field of the base flow in the meridional plane, and azimuthal vorticity field $\omega_\theta$ (grey scale), for $\Gamma = 7$, $Re_t = 130$ and $s = 0.154$. Note that only the region $0.14 \leqslant r/R \leqslant 0.68$ is shown.

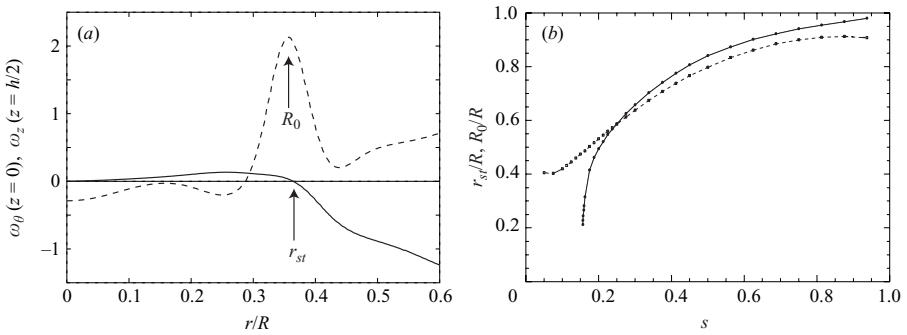


FIGURE 3. (*a*) Vorticity profiles from axisymmetric simulations, illustrating the definitions of the stagnation radius, $r_{st}$, and the shear layer radius, $R_0$. —, Azimuthal vorticity $\omega_\theta$ on the bottom disk $z = 0$; – –, vertical vorticity $\omega_z$ at mid-height $z = h/2$. $\Gamma = 7$, $Re_t = 250$, $s = 0.164$ ($Re_b = 41$). (*b*) —, Stagnation radius $r_{st}/R$; – –, location $R_0/R$ of the maxium of the vertical vorticity at mid-height, as functions of the rotation ratio $s$, for $\Gamma = 7$, $Re_t = 114$.

the top disk) recirculates at large radius towards the centre of the slower disk due to the lateral confinement. At low rotation ratio, the centrifugal effect of the slower disk is not strong enough to counteract the inward flow from the faster disk, and the meridional flow simply consists of a single recirculating cell, similar to that of the rotor–stator or co-rotating cases. On the other hand, when the rotation ratio is increased above a certain value, the slower disk induces a centrifugal flow too, and the meridional flow becomes organized into a two-cell recirculating structure, associated with a stagnation circle on the slower disk where the radial component of the velocity vanishes, as illustrated by the PIV measurements in figure 2.

In the two-cell regime, the presence of a stagnation circle has important consequences on the structure of the base flow, as can be seen in figure 10(*a*) – that will be described in § 5.3. The axial vorticity at mid-height, $\omega_z(z = h/2)$, plotted in figure 3(*a*) as a function of the radius, shows a pronounced maximum that separates an inner region of low angular velocity, which rotates with the bottom disk, from an outer region which rotates with the faster disk. In the same figure, the azimuthal vorticity profile on the bottom disk, $\omega_\theta$ ($z = 0$), is also shown. The location where $\omega_\theta$ crosses zero defines the stagnation radius, $r_{st}$, separating an inner region, where the

flow close to the bottom disk is outward, from an outer region where it is inward. It appears that the radius of maximum vorticity, $R_0$, approximately coincides with the stagnation radius. Measurements of $R_0$ as a function of $s$, shown in figure 3($b$) in the case $\Gamma = 7$, confirm that this radius closely follows the stagnation radius $r_{st}$. As the rotation ratio is increased, the annular shear layer and the stagnation circle are pushed outward, as the result of the increasing centrifugal effect of the slower disk, and take value close to 1 in the limit of the exact counter-rotation $s \to 1$. However, this figure clearly shows that the shear layer exists for all $s > 0$, while the stagnation circle only exists for sufficiently high rotation ratio, $s \geqslant s_0$. This means that, although the slower disk rotation may not be strong enough to develop an outward recirculation flow, it causes the inward boundary layer to decelerate, leading to a local increase of the vertical velocity. As a consequence, negative angular momentum of the slower (bottom) disk is advected upwards, leading to an annular shear layer even in the absence of a stagnation circle. But in any case, this mechanism is strongly enhanced by the presence of the stagnation circle for $s \geqslant s_0$, which detaches the inward boundary layer into the bulk of the flow, and an intense annular shear layer is encountered when the stagnation circle is present. This annular shear layer is prone to a shear instability that breaks the axisymmetry of the base flow as the rotation ratio $s$ is increased, leading to the flow patterns described in section § 5.

### 4.2. *Existence domain of the stagnation circle*

The two-cell structure of the counter-rotating flow was first reported by Dijkstra & van Heijst (1983), from axisymmetric simulation and experimental investigation at $\Gamma = 14.3$. Despite a moderate resolution, these authors gave clear evidence of a minimum rotation ratio for the stagnation circle to appear. This was further observed numerically by Lopez (1998) for smaller aspect ratios, $\Gamma = 2$, 4, and 8. Measurements at $\Gamma = 20.9$ were carried out by Gauthier *et al.* (2002) for various Reynolds numbers, and it was suspected that the stagnation circle was always present at the onset of negative spirals. However, due to uncertainty in the experimental method, no clear conclusion on the role of the stagnation circle was drawn. In order to remove this uncertainty, a systematic study of the stagnation circle has been carried out using axisymmetric stationary simulations for $\Gamma$ ranging from 1 to 28, focusing on its existence domain as function of the parameters ($\Gamma$, $Re_t$, $s$).

Values of the normalized stagnation radius, $r_{st}/R$, are shown in figure 4 as a function of the rotation ratio $s = \Omega_b/\Omega_t$ for various values of $Re_t$ (the aspect ratio is kept at $\Gamma = 7$). In the limit of high Reynolds numbers, the different curves collapse into a single master curve, starting from $r_{st} \approx 0$ for $s = s_0 \approx 0.10$. For lower Reynolds numbers, higher values of $s$, around 0.2–0.5, are needed for the two-cell structure to develop, and the stagnation circle directly appears at a non-zero radius.

The minimum counter-rotation ratio $s_0$ for various aspect ratios is plotted as a function of $Re_t$ in figure 5. These curves separate the lower part, $s < s_0$, where only one recirculating cell exists, from the upper part, $s \geqslant s_0$, where the two cells are present. On the same figure, experimental determinations of $s_0$, obtained for $\Gamma = 20.9$ from the data of Gauthier *et al.* 2002 (see their figure 7), are also shown, and compare rather well with the present numerical results.

For sufficiently large aspect ratio, the critical ratio $s_0$ decreases from $s_0 \approx 0.67 \pm 0.02$ in the limit of low Reynolds numbers, and saturates towards a constant value $s_0 \approx 0.100 \pm 0.003$ for higher Reynolds numbers. It is worth pointing that the $Re_t \to 0$ limit is in excellent agreement with the computation of Dijkstra & van Heijst (1983) (see their Appendix A.3), who predicted a limiting value $s_0 = 2/3$ for the Stokes

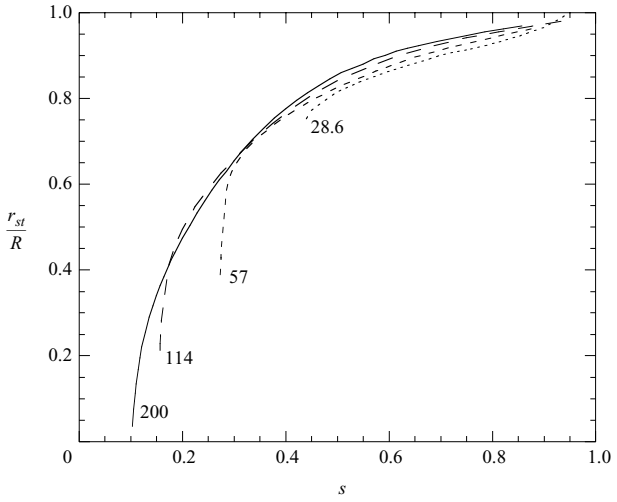


FIGURE 4. Normalized stagnation radius $r_{st}/R$ as a function of the counter-rotation ratio $s = Re_b/Re_t$ for $\Gamma = 7$, from axisymmetric simulations. The corresponding Reynolds number of the top disk, $Re_t$, is indicated.

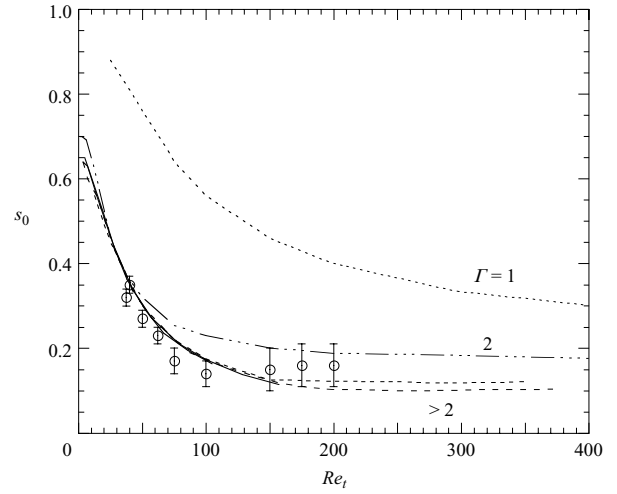


FIGURE 5. Critical counter-rotation ratio $s_0$ as a function of $Re_t$. Lines: numerical results, for various aspect ratios, $\Gamma = 1, 2, 4, 7, 14, 21$ and 28 (from top to bottom). ○, Experimental measurements, for $\Gamma = 20.9$.

flow. However, the much larger Reynolds number of their experiments and numerical simulations did not allow them to confirm this result.

The collapse of the different curves $s_0 = f(Re_t)$ for high aspect ratio, $\Gamma > 4$, is remarkable. The reason is that for a flat cavity, the radius $R$ does not play an important role in the flow structure, so that the Reynolds number $Re_t = \Omega_t h^2/\nu$ based on the thickness $h$ is the only relevant parameter in the problem. This similarity breaks

for lower aspect ratio, around $\Gamma < 4$, for which the minimum counter-rotation ratio $s_0$ significantly increases, suggesting a stabilizing influence of the sidewall on the stagnation circle formation.

In the high aspect ratio case, the crossover between the Stokes regime, where $s_0 \to 2/3$, and the higher Reynolds number regime, where $s_0 \approx 0.10$, takes place at $Re_t \approx 60$. Above this crossover, separated boundary layers appear over each disk, with $\delta_t + \delta_b < h$, where $\delta_t$ and $\delta_b$ are the top and bottom boundary layer thickness. Both $\delta_t$ and $\delta_b$ are controlled by the faster disk, and scale as $\delta = (\nu/\Omega_t)^{1/2}$. Using the values $\delta_t/\delta \simeq 2.2$ and $\delta_b/\delta \sim 4.5$ reported by Gauthier *et al.* (2002) gives a rough estimate for the transition Reynolds number,

$$Re_t = \Omega_t h^2/\nu \approx (2.2 + 4.5)^2 \approx 45. \tag{4.1}$$

Although slightly smaller, this value is of the same order as the crossover $Re_t \approx 60$ in figure 5. One may conclude that, for $Re_t > 60$, the stagnation radius results from the competition between well-defined boundary layers, while for $Re_t < 60$ it results from purely viscous effects.

## 5. Instability patterns

### 5.1. *Visualizations*

On increasing the Reynolds number, the axisymmetric base flow becomes unstable, leading to instability patterns that can be visualized from the light reflected from the anisotropic flakes, as shown in figure 6 for aspect ratio $\Gamma = R/h$ ranging from 6.1 to 20.9.

The instability patterns basically consist of a sharp-cornered polygon of $m$ sides, surrounded by a set of $2m$ outer spiral arms. However, the combination of these two aspects of the pattern can only be seen simultaneously for some modes and values of the aspect ratio. The lower modes observed for low aspect ratio essentially show the polygon pattern (figure 6*a–c*, with $m = 3$, 4 and 5), similar to those observed by Lopez *et al.* (2002) at $\Gamma = 2$ using dye visualization. In figure 6(*b*), both the $m = 4$-sided polygon and the surrounding $2m = 8$ spiral arms can be seen. In addition a set of $m$ inner arms connecting the corners of the polygon to the centre also appears, which become spiral arms as the aspect ratio $\Gamma$ is increased (figure 6*d–f*, with $m = 7$ and 11). Both the $m$ inner arms and the $2m$ outer arms can be seen in figure 6(*f*), and the corners of the polygon appear as bright V-shaped patterns where the $m$ arms split into $2m$ arms. On the other hand only the $m$ inner spiral arms can be seen in figure 6(*e*). In this figure the polygon and the outer spiral arms extend to larger radii, where visualization is not possible due to the cylindrical rim.

The spiral arms seen here correspond to the negative spirals described by Gauthier *et al.* (2002), where the observations were restricted to $\Gamma = 20.9$. The name of 'negative' spirals has been chosen because they roll up to the centre in the direction of the slower disk – but also to distinguish them from the positive spirals, a pattern that arises from an instability of the inward boundary layer close to the slower disk, and which is also present in the rotor–stator and co-rotating flows.

Close to the onset, the pattern slowly rotates as a whole, in the sense of the faster or the slower disk, with an angular velocity of order of one tenth of the faster rotating disk. Measurements of phase velocities are given in § 6.3. As the Reynolds number is increased slightly beyond their transition values, higher-order modes quickly superimpose on the fundamental one, eventually leading to a disordered pattern. Only

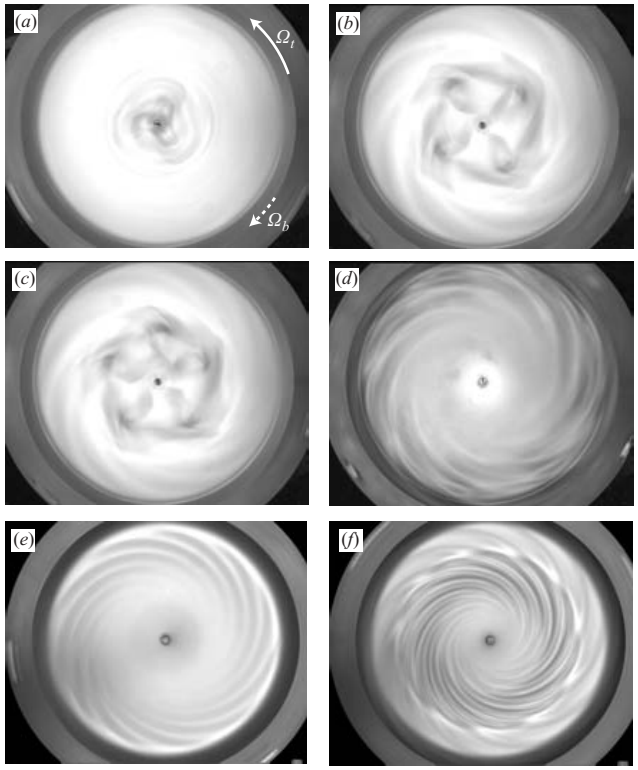


FIGURE 6. Instability patterns visualized by seeding flakes. (*a*) $(\Gamma, Re_t, Re_b) = (6.1, 584, 79)$, showing a mode $m = 3$. (*b*) (7, 282, 47.1), $m = 4$. (*c*) (7, 282, 51.8), $m = 5$. (*d*) (10.8, 60.6, 26.8), $m = 7$. (*e*) (20.9, 46, 10.5), $m = 11$. (*f*) (20.9, 74, 13.6), $m = 11$. The flow is only visible on a central region, $r \leqslant 0.83R$, due to the shadow from the cylindrical rim. Disk rotations are indicated by the arrows in (*a*).

the patterns at the onset are considered here, and the Reynolds numbers are kept close to that for the onset of the instability.

The relationship between the light intensity reflected by the flakes and the velocity gradient tensor field of the flow is non-trivial in the general case (Gauthier, Gondret & Rabaud 1998). Although the intensity field may represent the depth-averaged orientation of the flakes, screening effects from the upper regions may considerably alter the interpretation of the observed patterns, so that the three-dimensional flow structure cannot be directly inferred from the visualizations of figure 6. This visualization method is nevertheless convenient as a first approach, as it allows us to easily define the domains of parameters of interest where more quantitative measurements are to be performed.

### 5.2. *Onset curves*

The experimental onset curves of the patterns are shown in figure 7 in the plane of parameters $(Re_t, Re_b)$ for various aspect ratios $\Gamma$ ranging between 2 and 20.9. These curves are obtained by slowly increasing the bottom disk angular velocity $\Omega_b$ at fixed value of $\Omega_t$ and visually inspecting the intensity pattern of the light reflected by the

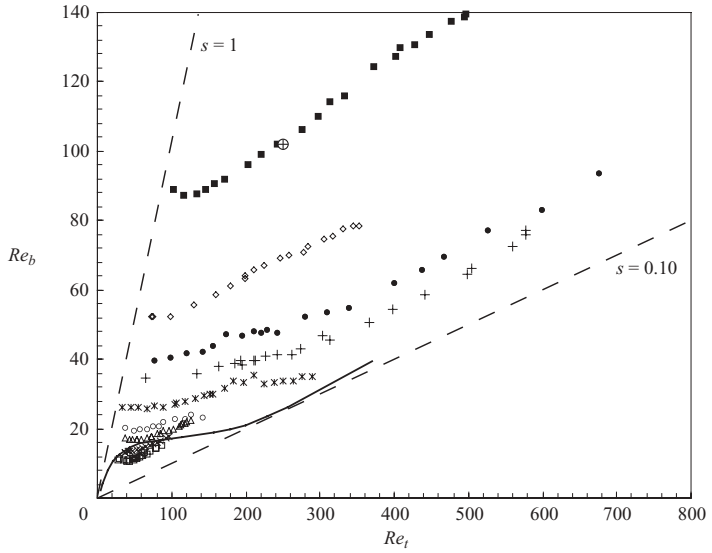


FIGURE 7. Stability curves for various aspect ratios $\Gamma = R/h$ from 2 to 21. ■, $\Gamma = 2$; ◇, 3; ●, 5.2; +, 7; ⋆, 9.3; ○, 12.6; △, 14.4; ×, 18; □, 20.9; ⊕, Instability threshold obtained by Lopez *et al.* (2002), at $\Gamma = 2$. The continuous line indicates the stagnation circle onset for $\Gamma = 7$, and separates the one-cell domain (lower region) from the two-cell domain (upper region). The dashed lines indicate the exact counter-rotation slope, $s = 1$, and the slope $s = s_0 \simeq 0.10$ corresponding to the onset of the two-cell structure at high Reynolds number.

flakes. No hysteresis is observed within our experimental uncertainty, of around 3%. The scatter mainly originates from the very large growth time of the instability close to the onset, which can be as large as 100 rotation periods of the faster disk. For high aspect ratio, boundary layer instabilities arise at moderate Reynolds numbers, and the onset curves for the shear layer instability become defined only for a restricted range of $Re_t$. It is worth pointing out that, although no hysteresis is observed for the instability threshold, noticeable hysteresis is present for the onset mode, which will be described in § 6.2. The point $(\Gamma, Re_t, Re_b) = (2, 250, 102)$ obtained by Lopez *et al.* (2002), also shown in figure 7, is in excellent agreement with the present results.

In the same figure the line separating the one-cell and two-cell domains is also plotted for $\Gamma = 7$. This curve is given by $Re_b = s_0 Re_t$, where $s_0(\Gamma, Re_t)$ is the minimum rotation ratio for the two-cell structure and the associated stagnation circle to appear (see figure 5). Similar curves are obtained for other aspect ratios, not shown here for clarity. From figure 7 it appears that the stability curves essentially fall into the two-cell domain, except for the highest aspect ratio, around $\Gamma > 16$, for which the instability arises in the upper part of the one-cell domain. Note that, for low aspect ratios, the presence of the two-cell structure is not a sufficient condition for the base flow to become unstable, and a much higher $Re_b$ is needed for the instability to arise.

Figure 8 shows the same data as in figure 7, but plotted in the plane of parameters $(\Gamma Re_t, \Gamma Re_b)$. Using this new set of parameters, the onset curves tend to collapse reasonably well, except for those corresponding to the lowest aspect ratios, $\Gamma = 2$ and 3, which significantly depart from it. The curves start from $\Gamma Re_b \approx 200 \pm 40$ and collapse towards a constant rotation ratio line, $s \approx 0.13 \pm 0.01$, slightly beyond the

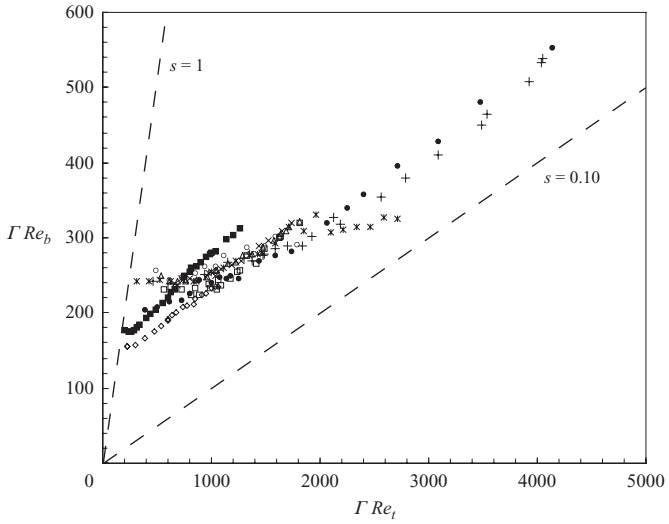


FIGURE 8. Stability curves. Same data as in figure 7, but plotted in the ($\Gamma Re_t$, $\Gamma Re_b$) plane of parameters. The axisymmetric base flow is stable in the lower region.

rotation ratio for the onset of the two-cell structure, which takes place at $s_0 \approx 0.10$ for high Reynolds numbers.

The approximate collapse of the onset curves in figure 7 indicates that the polygon pattern and the negative spirals arise from the same instability mechanism, a shear layer instability, although the nonlinear saturation leads to very a different morphology. Taking the shear $\Omega R/h$ as an estimate for the growth rate of the instability, and $h^2/\nu$ for the damping timescale, then the natural control parameter is $(\Omega R/h)h^2/\nu \sim \Gamma Re$. This is a rough estimate, since the instability takes place for radii that may be much lower than the cell radius $R$, but it is supported well by the approximate collapse of the data observed for $\Gamma \geqslant 4$.

As the sidewall rotates with one of the two disks, the flow configuration is not invariant by reflection with respect to the horizontal plane. The influence of the sidewall is expected to be negligible in the limit of large aspect ratio $\Gamma$, but may be significant for the range of $\Gamma$ spanned in the present study. It may therefore be of interest to compare the stability curve of the actual flow configuration with that of the symmetric configuration. We call *configuration A* (resp. *B*) the situation where the sidewall rotates with the faster (resp. slower) disk. Figure 9(*a*) shows the stability curve in configurations $A$ and $B$ for an aspect ratio $\Gamma = 7.2$ in the plane of parameters ($Re_{\mathrm{fast}}$, $Re_{\mathrm{slow}}$), the Reynolds numbers based respectively on the faster and slower rotating disk.

The thresholds in configuration $B$ appear to be around 10% lower than that of configuration $A$, with no significant trend as the Reynolds number is varied. In configuration $A$, the fluid rotation due to the faster disk is sustained by the co-rotating sidewall, and the resulting flow at the periphery of the cell is closer to a solid-body rotation. As a result, the stagnation circle where the centrifugal effects of each disk balance is smaller, and the internal shear layer is weakened, so that configuration $A$ is more stable than $B$. The normalized threshold difference $(Re_{\mathrm{slow},A} - Re_{\mathrm{slow},B})/Re_{\mathrm{slow}}$, plotted as a function of the aspect ratio in figure 9(*b*), shows a decrease proportional

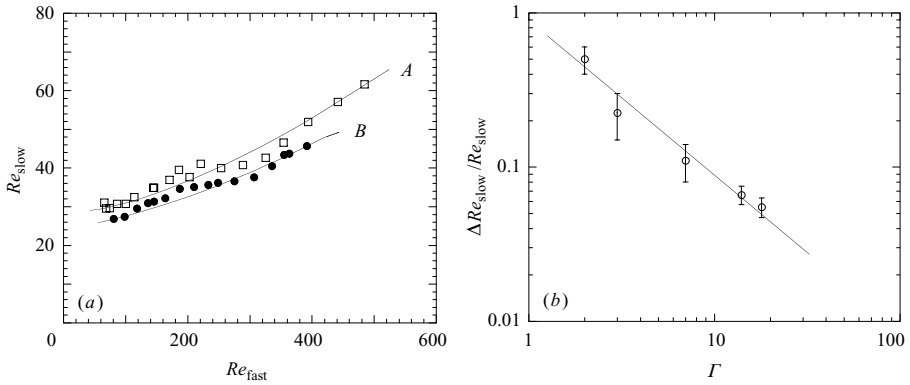


FIGURE 9. (*a*) Stability curves for an aspect ratio $\Gamma = 7.2$. □, Configuration *A*: the sidewall rotates with the faster disk; ●, Configuration *B*: the sidewall rotates with the slower disk. (*b*) Relative deviation of the threshold between configurations *A* and *B* as a function of $\Gamma$. The line shows $0.9\Gamma^{-1}$, and the error bars reflect the variability of the deviation along the curves from (*a*).

to $\Gamma^{-1}$, indicating that the boundary condition at $r = R$ has an influence of order of $h/R$ on the instability threshold. This difference between configurations *A* and *B* remains small for high aspect ratio, and in the following we will restrict ourselves to the configuration *A*.

### 5.3. *Numerical and experimental description of the flow patterns*

In order to obtain further insight into the instability mechanism of the counter-rotating flow, PIV measurements and numerical simulations have been performed close to the onset.

Figure 10 shows the horizontal velocity field and the associated vertical vorticity field, measured by PIV at mid-height, $z = h/2$, for $\Gamma = 7$. As previously, only one quarter of the velocity vectors are shown, and the vorticity colour map has been rescaled by the angular velocity of the top disk. Figure 10(*a*) shows the axisymmetric base flow, while the three bifurcated fields in (*b*), (*c*) and (*d*) show azimuthal modulations of modes $m = 5$, 4 and 3, obtained for increasing $(Re_t, Re_b)$ along the onset curve. The annular shear layer is found to evolve towards a sharp-cornered polygonal pattern, each side containing a local minimum and maximum of vorticity. The modulation of the vorticity level along the shear layer is similar to the classical Kelvin–Helmholtz 'cat's eyes' pattern for the linear case. The vorticity maxima are located slightly downstream of the corners of the polygon, which probably results from a nonlinear deformation of an initially symmetric chain of vorticity extrema. Flatter cavities (figures 11*a*, for $\Gamma = 9.3$, and 11*b*, for $\Gamma = 14$) show the same modulated shear layer, but the vertical confinement leads to a saturated pattern that becomes more complex than the one observed for low $\Gamma$. In addition to the polygonal shear layer, a set of *m* inner spiral arms appears in the centre of the flow, where local vorticity minima, of the same sign as the slower rotating disk, becomes concentrated.

Because of the above-mentioned limitations of the PIV measurements, the structure of the vorticity field for even flatter cavities can only be investigated from the numerical simulations. For $\Gamma = 21$, illustrated in figure 12, the annular shear layer appears to be much thinner, leading to a higher-order mode, here $m = 11$. The

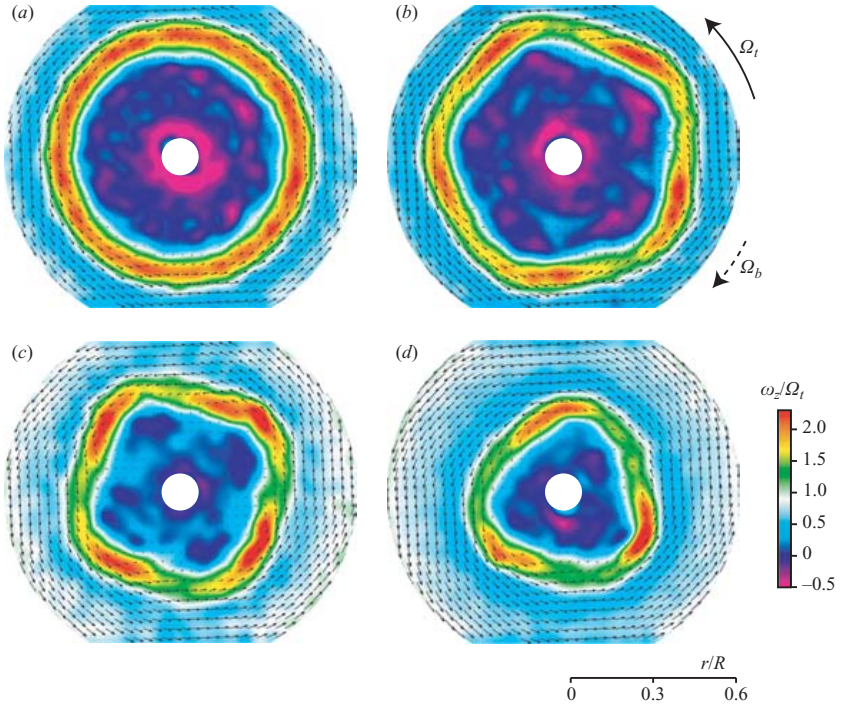


FIGURE 10. Experimental velocity and vorticity fields $\omega_z$ at mid-height $\Gamma = 7$; (*a*) is below the onset, and (*b–d*) are for increasing Reynolds numbers along the onset curve. (*a*) $(Re_t, Re_b) = (240, 40)$; (*b*) (240, 43); (*c*) (289, 45); (*d*) (341, 50).

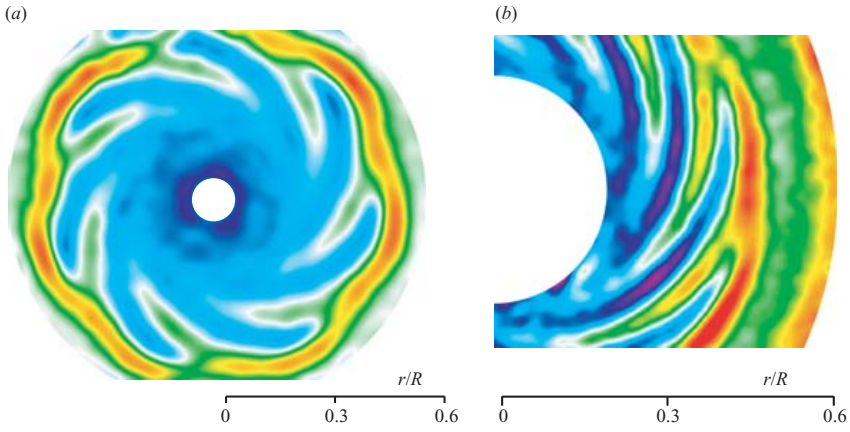


FIGURE 11. Experimental vorticity fields $\omega_z$ at mid-height. (*a*) $(\Gamma, Re_t, Re_b) = (9.3, 183, 28.5)$, mode $m = 7$. (*b*) (14, 80, 19), mode $m = 8$. The colour maps are the same as in figure 10.

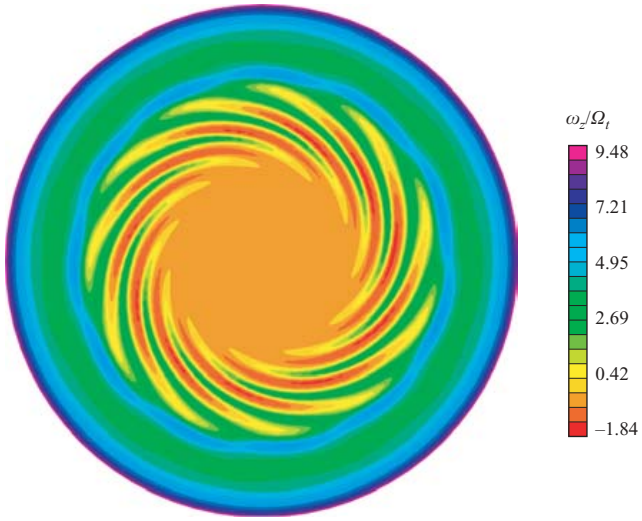


FIGURE 12. Numerical axial vorticity field $\omega_z$ at mid-height $z = h/2$ for $\Gamma = 21$, $Re_t = 67$, $Re_b = 14.3$, showing a mode $m = 11$. Only the central region $r \leqslant 0.95R$ is shown.

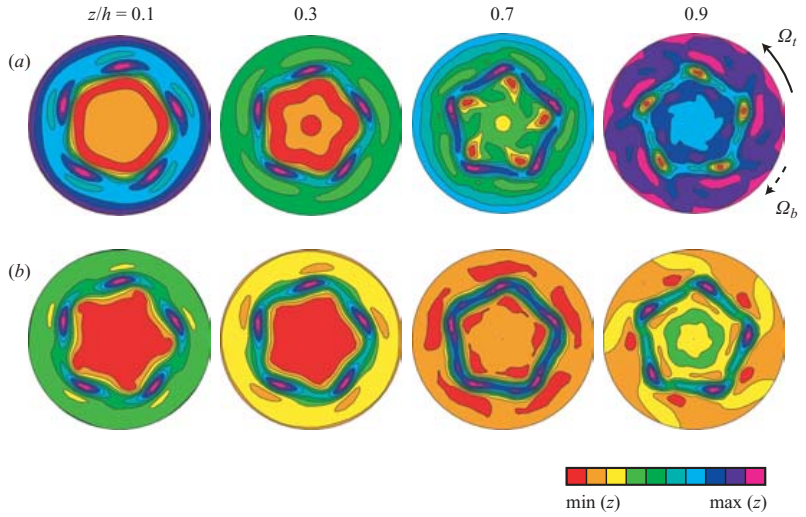


FIGURE 13. Numerical axial vorticity $\omega_z$ (*a*) and axial velocity $v_z$ (*b*) at different heights $z/h = 0.1$ (close to the slower disk), 0.3, 0.7 and 0.9 (close to the faster disk), for $\Gamma = 7$, $Re_t = 250$, $Re_b = 57$, showing a mode $m = 5$. The colour maps for both $\omega_z$ and $v_z$ are normalized by their minimum and maximum on each field. Only the central region $r/R \leqslant 0.6$ is shown.

similarity with the visualization in figure 6(*e*) is remarkable. Only the $m$ inner spiral arms can be seen, suggesting that the $2m$ outer spiral arms are outside the mid-height plane.

The three-dimensional structure of the pattern can be inferred from the numerical vertical vorticity and velocity fields shown in figure 13 for $\Gamma = 7$, for heights $z$ ranging

from $0.1h$ (close to the slower disk) up to $0.9h$ (close to the faster disk). From these figures, the vertical structure of the polygonal shear layer and the influence of the boundary layers of each disk can be seen.

It is remarkable that the locations of the vorticity extrema approximately coincide for each field, suggesting that the flow structure is roughly invariant along the vertical direction, except close to the disks where the boundary layers occur. Along these columnar vortices strong upward flow is present, which advects negative vorticity from the bottom to the top disk. Close to the faster disk (4th slice), the outer spiral arms appear surrounding the polygonal shear layer. Slight vorticity modulations show $2m$ extrema along the azimuthal direction, similar to the $2m$ outer spiral arms seen in figure 6($c$). These spiral arms result from the interaction of the shear layer primary instability pattern in the bulk of the flow with the centrifugal Ekman boundary layer over the faster disk. The Ekman layer advects the perturbation outwards with an anticlockwise rotation, resulting in the observed negative spirals. Since they are mainly localized near the top disk, these negative spirals can clearly be seen in the seeding flakes visualizations in figure 6, although they are associated with very weak vorticity modulation.

### 5.4. *Growth rates and nonlinear saturation of the instability*

We now investigate the growth rates and the nonlinear saturation of the bifurcated flow slightly above the onset. The energy of the instability pattern may be defined as the difference between the total energy of the flow and the energy of the unstable axisymmetric base flow. Since the unstable base flow obviously cannot be deduced from experimental measurements of the bifurcated flow, we approximate it by the azimuthal average of the total energy. Note that we are only dealing with the contribution of the horizontal components of the velocity at a given height, since the vertical component is not accessible from the present two-dimensional PIV measurements. Within these approximations, the energy per unit mass of the bifurcated flow at a given height can be written

$$\Delta E = \frac{1}{2}\frac{1}{\pi R^2}\int_0^{2\pi}\int_0^R \{[v_r(r,\theta)-\bar{v}_r(r)]^2 + [v_\theta(r,\theta)-\bar{v}_\theta(r)]^2\} r \,\mathrm{d}r\,\mathrm{d}\theta, \qquad (5.1)$$

where the overbars denote the azimuthal average of the horizontal components of the instantaneous velocity field. Since the bifurcated state is very sensitive to the distance to the threshold, the PIV measurements have been performed at small aspect ratio, $\Gamma = 3$, where a wider range of Reynolds numbers can be explored before secondary instabilities occur. For this aspect ratio the pattern is confined to small radii, and the radial integration in equation (5.1) has been restricted to the range $0 \leqslant r \leqslant 0.64R$.

Figure 14($a$) shows the energy $\Delta E$ as a function of time for a fixed value $Re_t = 280$, after a sudden increase of $Re_b$ at $t \approx 0$, from a value slightly below the threshold, 70, up to values between 75 and 79. At $t = 0$, the flow is axisymmetric, and the non-zero value of $\Delta E$ simply corresponds to the noise level of the PIV measurements and the azimuthal average procedure. For $Re_b \in [75, 78]$, after a transient growth, the energy saturates towards a constant value, $\Delta E_s$, which is plotted in figure 14($b$) as a function of $Re_b$. The corresponding flow patterns are shown in figure 15. Above the instability threshold, $Re_{b,c} \approx 74$ here, the energy linearly increases proportionally to $Re_b - Re_{b,c}$, as expected for a supercritical bifurcation. Similar results were reported by Gauthier *et al.* (2002) in the case $\Gamma = 20.9$, and we believe that the bifurcation remains supercritical for the whole range of aspect ratio spanned in this paper. For

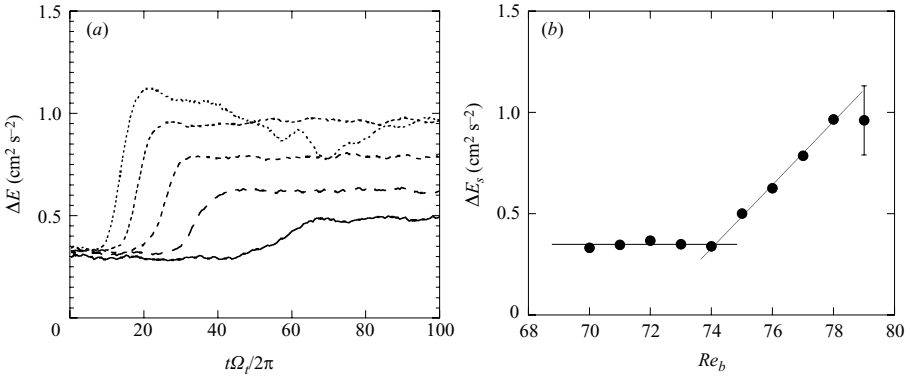


FIGURE 14. (*a*) Energy of the non-axisymmetric part of the flow, equation (5.1), as function of time, after a sudden increase of $Re_b$ at $t = 0$ s from 70 to 75, 76, 77, 78 and 79 (from solid line to short-dashed line), computed from the velocity fields of figure 15 ($\Gamma = 3$ and $Re_t = 280$). (*b*) Energy of saturation of the bifurcated state as a function of $Re_b$.

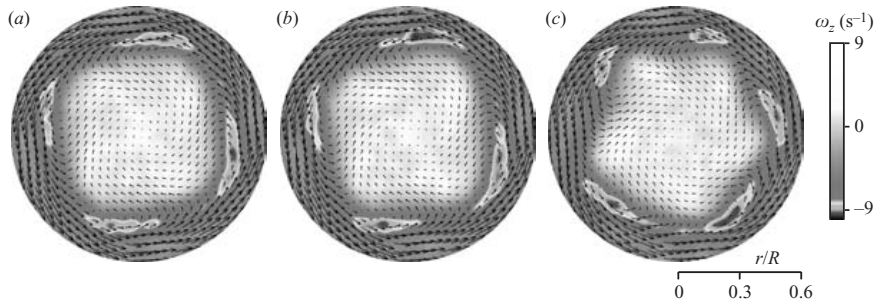


FIGURE 15. Experimental velocity and vorticity fields for $\Gamma = 3$ and $Re_t = 280$. (*a*) $Re_b = 75$; (*b*) $Re_b = 77$; (*c*) $Re_b = 79$. The grey scale has been chosen in order to emphasize the local vorticity extrema of the shear layer.

$Re_b = 79$, the pattern is a non-steady combination of modes $m = 4$ and 5 (figure 15*c*), and $\Delta E$ does not show saturation, as depicted by the error bar in figure 14(*b*).

Linear computations have been performed for the same flow parameters, $\Gamma = 3$ and $Re_t = 280$, in order to provide further insight into the observed modes. Figure 16 shows the growth rate $\sigma$ of each mode as a function of $Re_b$. The most unstable mode is $m = 3$ at $Re_b = 72.3$, but it is closely followed by the mode $m = 4$, which becomes more unstable for $Re_b > 73.9$. This mode $m = 3$ was not observed experimentally, probably due to our limited resolution on the Reynolds numbers, of order of 3%. If $Re_b$ is further increased, the dominant mode becomes $m = 5$, for $Re_b = 78.9$, in good agreement with the experiment (figure 15). Note that the growth rates cannot be inferred from the experimental measurements of figure 14(*a*), because only the very late time before saturation can be observed experimentally, and the earlier exponential growth falls largely below the experimental noise level.

The numerically observed modes for $\Gamma = 3$ and 7 are summarized in the marginal stability curves in figure 17. The experimentally observed modes at $\Gamma = 3$ are also shown for comparison. In both cases the critical mode is $m = 3$. These curves show the

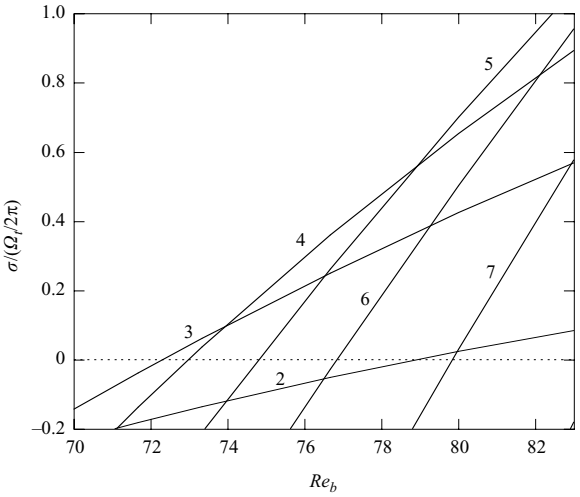


FIGURE 16. Non-dimensional growth rate of the different modes as a function of $Re_b$, for $\Gamma = 3$, $Re_t = 280$.

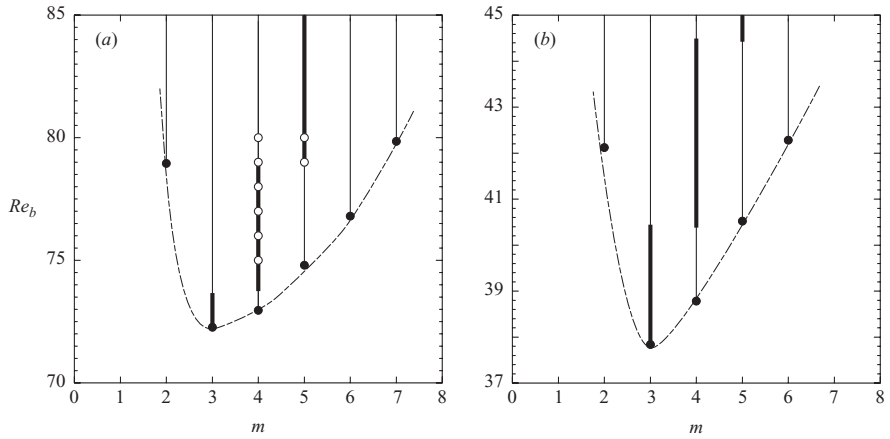


FIGURE 17. Marginal stability curves obtained from the linear computations for $Re_t = 280$. ●, critical Reynolds number $Re_b$ for a given mode $m$; thick line, most unstable mode. The dashed curve joining the points is guide for the eye. (*a*) $\Gamma = 3$, $Re_{b,c} = 72.3$; ○, experimentally observed modes. (*b*) $\Gamma = 7$, $Re_{b,c} = 37.8$.

important sensitivity of the most unstable mode slightly beyond the instability threshold. This sensitivity remains of the order of the experimental uncertainty, around 3%, making difficult any accurate determination of the onset mode. The restricted range of experimentally observed modes compared to the linearly unstable modes may be the result of a nonlinear wavenumber selection, such as the Eckhaus instability (Ahlers *et al.* 1986).

Since in the experiment the Reynolds number cannot be kept close to the transition, one may expect nonlinearities to significantly affect the selected modes. In order to

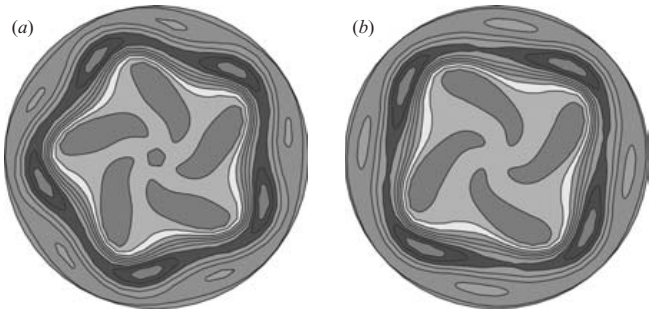


FIGURE 18. Iso-vorticity levels at mid-height obtained for the same parameters, $\Gamma = 3$, $Re_t = 280$, $Re_b = 80$, starting from different initial conditions: (*a*) from sudden increase of $Re_b$ from 70, showing a mode $m = 5$; (*b*) from progressive increase of $Re_b$ from 70, showing a mode $m = 4$. Only the central circle $r \leqslant 0.65R$ is shown.

check this point, nonlinear computations have been performed at $\Gamma = 3$, $Re_t = 280$ and $Re_b = 80$, i.e. 11% beyond the transition. For these values, linear computations show that the modes $m = 2$ to 7 are unstable, the most unstable being the mode $m = 5$ (see figure 16).

Figure 18 shows the long-time evolution of two computations performed for the same flow parameters, which differ only by the initial condition. The axisymmetric stable flow for $Re_b = 70$ is taken as the initial condition for the first computation (figure 18*a*), in a similar way as for the experiments, where $Re_b$ was suddenly increased from 70 to a value above the threshold. For the second computation (figure 18*b*), the bottom Reynolds number has been gradually increased from 70 up to 80 in four steps, waiting for the saturation of the flow at each step (typically 300 rotation periods of the faster disk). While the first computation (*a*) shows a mode $m = 5$, the second one (*b*) shows a mode $m = 4$. For similar values of $Re_b$ (see figure 15*c*), the experiment shows a mixed state, dominated by modes 4 and 5. The progressive increase of $Re_b$ in the second case probably constrained the flow to follow the metastable branch $m = 4$, although other branches may be more unstable. These observations clearly illustrate the sensitivity of the observed pattern to the initial condition. They are in good agreement with a number of experimental observations, where strong hysteresis is observed for the modes, although no hysteresis is present in the value of the threshold. This situation is generic for systems where the geometrical confinement leads to azimuthal wavenumber quantization (see, e.g., Rabaud & Couder 1983).

## 6. Characterization of the shear layer instability

### 6.1. *Local control parameter for the shear layer instability*

The experimental and numerical vorticity fields in figures 10–13 indicate that the basic mechanism responsible for the observed flow pattern is a shear layer instability. In order to confirm this observation, and to test any possible influence of the curvature, the local Reynolds number $Re_l$ based on the thickness $w$ of the shear layer and the velocity jump $\Delta U$ across it can be computed:

$$Re_l = \Delta U w/\nu. \tag{6.1}$$

It is expected that, just below the onset of the instability, this local Reynolds number reaches a unique critical value.

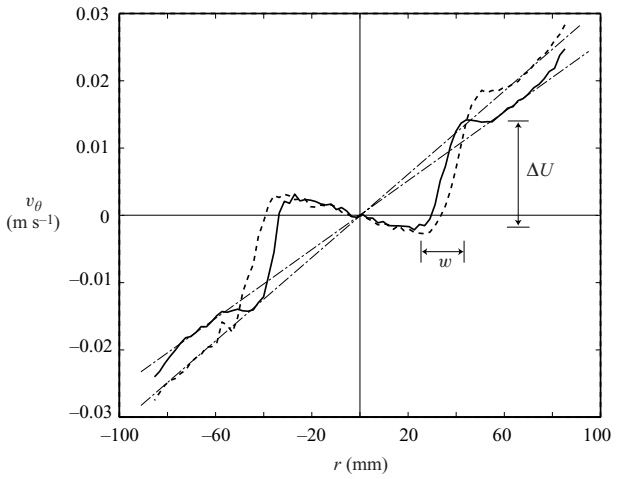


FIGURE 19. Azimuthal velocity profiles $v_\theta(r)$ computed from PIV fields at mid-height $z = h/2$, measured just below the onset of instability, for $\Gamma = 7$. – –, $Re_t = 239$; —, $Re_t = 277$. The corresponding solid-body rotation profiles $v_\theta(r) = 0.3\Omega_t r$ are also shown for both $Re_t$ (– - –). Only the central circle $r \leqslant 0.6R$ is measured. The definitions of the shear layer thickness $w$ and velocity jump $\Delta U$ are sketched for the curve —.

A series of PIV measurements for $\Gamma = 7$ along the onset curve has been performed, and the shear layer thickness and velocity difference have been extracted from the velocity fields. Figure 19 shows two azimuthal velocity profiles, averaged over $[0, \pi]$ (negative $r$ corresponds to the other half $[\pi, 2\pi]$). The two profiles correspond to two different top Reynolds numbers but, in each case, the bottom Reynolds number has been set just below its corresponding critical value. Both profiles consist of two sections of quasi-solid-body rotation separated by a rather sharp velocity front. The inner region rotates in the direction of the slower disk, with an angular velocity of about $-0.5\Omega_b$, and the outer region rotates with the faster disk, at $\sim 0.3\Omega_t$. While the former value probably strongly depends on the height $z$, it is interesting to note that the latter value is close to the angular velocity found in the inviscid core of the Batchelor (1951) flow, $v_\theta(r) \approx 0.313\Omega_t r$ (see Zandbergen & Dijkstra 1987).

From this figure the velocity jump $\Delta U$ is computed as the difference between the surrounding extrema across the front, and the thickness $w$ as the distance between these extrema. Only the horizontal projection of the thickness is actually measured. However, since the shear layer was shown to be almost vertical (see the numerical vorticity fields in figure 13), at least for moderate $\Gamma$, the apparent thickness gives a reasonable estimate for the actual one. This thickness is found to be of order the gap between the disks, $w \approx (0.6 \pm 0.1)h$, and shows no significant variation with the Reynolds number. The scaling $w \propto h$, although not tested experimentally for other aspect ratios, is in qualitative agreement with experimental and numerical fields (see figures 11 and 12), from which the shear layer thickness appears to decrease as $\Gamma$ is increased.

The local Reynolds number computed from these measurements is shown in figure 20($a$) as a function of $Re_t$. Although $Re_t$ is varied from 140 to 370, $Re_l$ remains approximately constant, giving evidence that this Reynolds number is the relevent local control parameter for the instability. The scatter is significant, and is mainly due

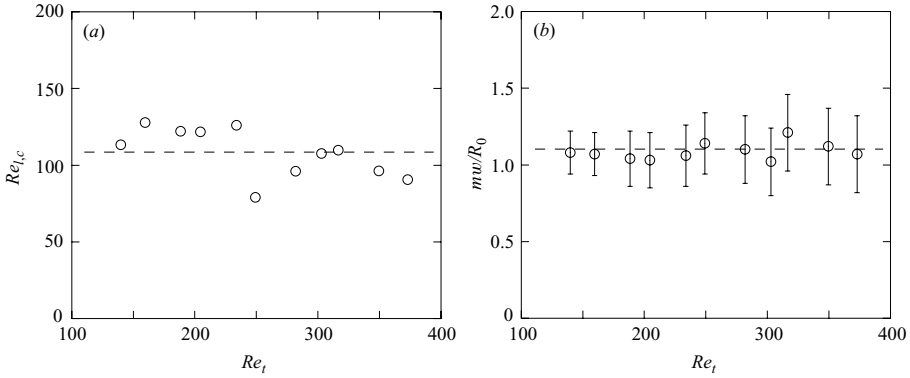


FIGURE 20. (*a*) Critical local Reynolds number $Re_{l,c}$ based on the shear layer thickness as a function of $Re_t$ for $\Gamma = 7$. For each measurement, the bottom Reynolds number $Re_b$ is fixed to its transition value. (*b*) Corresponding normalized wavenumber $m\,w/R_0$.

to the precision in the measurement of $w$, but the critical local Reynolds number can be estimated as

$$Re_{l,c} \approx 110 \pm 20. \tag{6.2}$$

This value is in qualitative agreement with the threshold $Re \approx 85 \pm 10$ measured by Rabaud & Couder (1983) from the circular shear layer experiment. Our slightly higher value may be due to the overestimation of the apparent shear layer thickness, or to some stabilizing effect due to the particular geometry of the annular shear layer. It is worth pointing out that, for the range of Reynolds number $Re_t$ spanned here, the relative curvature of the shear layer, $w/R_0$ (where $R_0$ is the shear layer radius), increases from 0.16 to 0.52. However, this important variation does not significantly affect the threshold $Re_l$, suggesting that the curvature has only weak effect on the stability of this shear layer.

The approximate collapse of the onset curves in the plane of parameters ($\Gamma Re_t$, $\Gamma Re_b$), observed in figure 8, follows from this constant $Re_l$ at the onset. Taking $R_0\Omega_t$ as an estimate for the velocity jump $\Delta U$, and using $w \sim h$ for the shear layer thickness, then the condition $Re_l = \Delta U w/\nu \approx$ const simply yields $R_0 h \Omega_t/\nu = \Gamma Re_t R_0/R \approx$ const, confirming the experimental finding that the Reynolds numbers $\Gamma Re_i$ are the most relevant global control parameters to describe the onset curves. However, the link between the global and local control parameters, $\Gamma Re_t$ and $Re_l$, remains non-trivial because of the additional ratio $R_0/R$, and may account for the systematic deviations observed in figure 8.

One consequence of this shear layer instability mechanism is that the critical wavelength should scale as the thickness $w$ of the shear layer (Drazin & Reid 1979). As a result, the number of vortices along the shear layer is expected to scale as $2\pi R_0/w$. This is indeed the case, as shown in figure 20(*b*), where the normalized wavenumber $mw/R_0$ is plotted as a function of $Re_t$. The observed constant value,

$$\frac{m\,w}{R_0} \approx 1.10 \pm 0.15, \tag{6.3}$$

confirms this picture, leading to a wavelength $\lambda = 2\pi R_0/m \approx (5.7 \pm 0.8)w$. Here again this finding compares well with the circular shear layer experiment of Rabaud & Couder (1983), for which the shear layer radius is constrained by the geometry of the

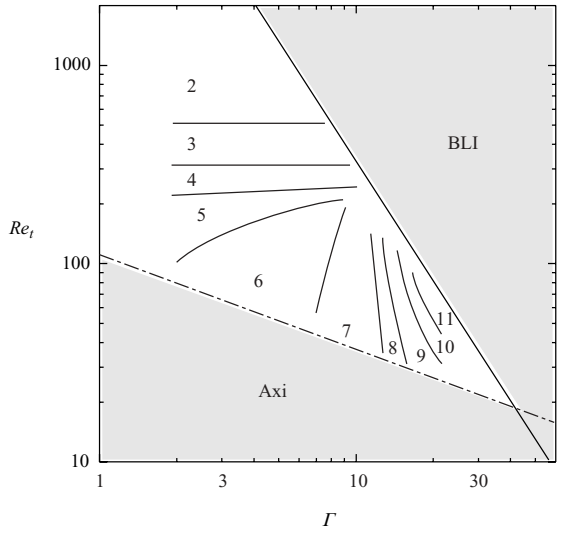


FIGURE 21. Experimental regime diagram of the onset modes in the plane $(\Gamma, Re_t)$, where $\Gamma = R/h$ is the aspect ratio and $Re_t$ the top Reynolds number (the bottom Reynolds number, $Re_b$, is fixed at its transition value). The numbers indicate the onset modes, and the transition lines separate regions of constant onset mode. Modes between $m = 2$ and 11 are observed, for $\Gamma$ between 2 and 21. In the upper region, denoted BLI ($Re_t > 31 \times 10^3 \Gamma^{-2}$), boundary layer instabilities occur in addition to the shear layer instability. In the lower domain, denoted Axi ($Re_t < 105\Gamma^{-1/2}$), the axisymmetric base flow remains stable.

apparatus. In the present rotating disks experiment, this radius $R_0$ is not fixed, but is determined by the competition of the centrifugal effects on each disk.

From the $m \propto R_0$ law observed here for $\Gamma = 7$, one may deduce that the onset mode is a decreasing function of $Re_t$, since the increasing centrifugal effect of the faster disk tends to decrease the radius of the shear layer $R_0$. This is indeed the case (see, e.g., figure 10), at least for moderate aspect ratios $\Gamma$; for higher aspect ratios the interaction with the boundary layers significantly affects this behaviour, as shown in the next section.

### 6.2. *Onset modes*

The observed modes are found to depend not only on the Reynolds numbers and the aspect ratio, but also on the time history of the control parameters $(Re_b, Re_t)$, as shown in § 5.4. As a consequence, the only quantity that may be summarized is the critical mode that first becomes unstable just at the onset when slowly approaching the onset curve from below.

Figure 21 shows the experimental regime diagram for the onset mode in the plane of parameters $(\Gamma, Re_t)$. For each value of the top Reynolds number, $Re_t$, the bottom Reynolds number, $Re_b$, has been fixed at its corresponding critical value (see figure 7), so that the set of three parameters $(\Gamma, Re_t, Re_b)$ reduces to two. In this diagram, the lines delimit regions where a unique onset mode is experimentally observed. As noted in § 5.4, the sensitivity of the observed mode slightly beyond the onset curve is important (see figure 17), so that the observed mode $m$ may occasionally overestimate the actual onset mode, shifting the transition lines between modes upwards.

This diagram is restricted to a triangle in the plane ($\Gamma$, $Re_t$). In the domain denoted Axi, below a line given by

$$Re_t \approx (105 \pm 9)\Gamma^{-1/2}, \tag{6.4}$$

the flow is found to remain axisymmetric. In this domain the shear layer is probably stabilized by the thick boundary layers that fill an important part of the vertical gap, but no simple argument is found to explain the observed $\Gamma^{-1/2}$ behaviour.

The domain above the upper line, denoted BLI for 'boundary layer instability', corresponds to the destabilization of the inward boundary layer on the slower rotating disk, giving rise to the propagating circles and positive spirals that have been described in detail by Gauthier *et al.* (2002). Since the boundary layer stability is controlled by a local Reynolds number, $Re_r = \Omega r^2/\nu$, an approximate condition for stability is that $Re_r < Re_c$ for all $r < R$, leading to a line $\Omega_t R^2/\nu = Re_c$, or equivalently

$$Re_t = \Omega_t h^2/\nu = Re_c \Gamma^{-2}. \tag{6.5}$$

This is indeed the case, and we determine experimentally $Re_c \approx (31 \pm 2) \times 10^3$. Note that although measurements of the critical mode were sometimes possible slightly beyond this upper limit, we choose to restrict ourselves to the situation where the boundary layers remain stable.

For high Reynolds number, $Re_t > 200$ (i.e. only for $\Gamma < 12$), the transition lines between modes are nearly horizontal, i.e. the onset modes $m$ are essentially controlled by the top Reynolds number, $Re_t$, and take values from 5 down to 2 as $Re_t$ is increased. The corresponding flow pattern essentially consists of the sharp-cornered polygon, as seen in figure 6(*a–c*). The onset mode $m = 4$ reported by Lopez *et al.* (2002) for $(\Gamma, Re_t) = (2, 250)$ agrees with the $m = 4$ domain in figure 21, which extends between $Re_t = 230 \pm 10$ and $320 \pm 20$. In this regime, the boundary layers over each disk are well separated, $\delta = (\nu/\Omega_t)^{1/2} < h/12$, so that the dynamics of the annular shear layer can be seen as essentially two-dimensional. The onset mode then only depends on the shear layer radius $R_0$ and thickness $\delta \sim h$, in agreement with the law $m \propto R_0$ observed in the previous section for $\Gamma = 7$ (equation (6.3)). As a consequence, while the Reynolds number based on the azimuthal velocity, $\Gamma Re_t = Rh\Omega_t/\nu$, is the most relevant control parameter for the instability threshold (see figure 8), the Reynolds number $Re_t = h^2\Omega_t/\nu$ is the one that controls the onset mode in the $Re_t > 200$ domain.

For lower Reynolds numbers, $Re_t < 200$, this behaviour does not hold any more and the regime diagram becomes more complex. In this regime, the flow is fully three-dimensional, with thick boundary layers, $\delta > h/12$, that may strongly interact with the annular shear layer. The corresponding flow pattern now evolves towards the spiral arms of figure 6(*d–f*). As $\Gamma$ is increased, the transition lines between modes become nearly vertical, and their slope becomes negative for $\Gamma > 12$. As a consequence, the critical mode is an increasing function of $Re_t$, in contrast to the low aspect ratio case. This new behaviour is in agreement with the results of Gauthier *et al.* (2002) at $\Gamma = 20.9$, where modes 9, 10 and 11 were reported for increasing Reynolds numbers.

We finally note that extrapolating the boundaries of the two domains Axi and BLI towards higher aspect ratio suggests that the shear layer instability described here should only be observed for $\Gamma < 40$. For higher aspect ratio, the boundary layers would become unstable as soon as they become separated, probably inhibiting or strongly affecting the shear layer instability. Other instability mechanisms may also appear for such high aspect ratios, such as the turbulent spots in the torsional Couette flow described by Cros & Le Gal (2002) in the rotor–stator configuration.

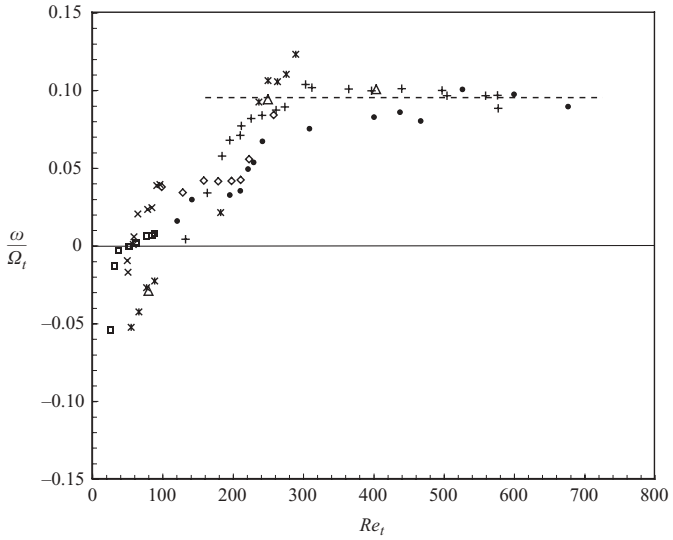


FIGURE 22. Normalized phase velocity $\omega/\Omega_t$ at the onset as a function of $Re_t$ for various aspect ratios $\Gamma$. Experiment: $\diamond$, $\Gamma = 3$; $\bullet$, 5.2; $+$, 7; $\star$, 9.3; $\times$, 17; $\square$, 20.9. Numerics: $\triangle$, $\Gamma = 7$. The dashed line is $\omega/\Omega_t = 0.095$.

### 6.3. *Phase velocities*

Because of the asymmetry of the flow, the instability patterns are not steady, but rather appear as rotating waves, characterized by a well-defined drift velocity $\omega$. Figure 22 shows the experimentally measured angular phase velocity at the onset, $\omega$, normalized by the top angular velocity, $\Omega_t$, as a function of $Re_t$ for various aspect ratios. Values obtained from numerical simulations, for $\Gamma = 7$, are also plotted and are found to compare well with the experimental results. Although the scatter is significant, the different curves appear to collapse reasonably well. The phase velocity is found to increase, starting from slightly negative values for low $Re_t$, crossing zero for $Re_t \sim 50$–$100$, and finally saturating towards a constant positive value for $Re_t > 250$:

$$\frac{\omega}{\Omega_t} \approx 0.095 \pm 0.01. \tag{6.6}$$

For high Reynolds numbers, the shear layer can be seen as essentially two-dimensional, with no significant influence of the boundary layers. The constant phase velocity $\omega/\Omega_t$ observed in this case is similar to the classical linear Kelvin–Helmholtz case, for which the phase velocity is given by the average of the two stream velocities (Drazin & Reid 1979). Extending this result to the annular case yields $\omega = (\Omega_1 + \Omega_2)/2$, where $\Omega_1$ and $\Omega_2$ are respectively the inner and outer angular velocities on each side of the shear layer. These angular velocities are non-trivial functions of the bottom and top disk velocities, $\Omega_b$ and $\Omega_t$. However, a rough estimate for $\omega$ may be obtained by neglecting $\Omega_1$, and taking $\Omega_2 \approx 0.3\Omega_t$ as for the classical Batchelor flow (see figure 19). These approximations yield $\omega/\Omega_t \approx 0.3/2 \approx 0.15$, which is in reasonable agreement with the observed limit, $\omega/\Omega_t \approx 0.095 \pm 0.01$. The much lower values for $\omega$ found in the lower Reynolds number regime, $Re_t < 250$, probably result from the

interaction with the thicker boundary layers, which tend to slow down the pattern rotation.

## 7. Conclusion

This paper describes a joint laboratory and numerical study of the instability patterns in the flow between counter-rotating disks, spanning a range of aspect ratio $\Gamma = R/h$ between 2 and 21. This study is restricted to the situation where the boundary layers remain stable, focusing on the shear layer instability that occurs only in the counter-rotating regime. For sufficiently large counter-rotation, the shear layer that separates two regions of opposite angular velocities is prone to an azimuthal symmetry breaking. The associated pattern is a combination of a sharp-cornered polygonal shear layer with $m$ vorticity extrema, surrounded by a set of $m$ inner and $2m$ outer spiral arms. At small aspect ratio and large velocity, only the $m$-sided polygon is observed, where the mode $m$ decreases as the top Reynolds number is increased. On the other hand, for higher $\Gamma$, only the spiral arms remain, their number now increasing as the top Reynolds number is increased. These observations are in remarkable agreement with the three-dimensional numerical simulations performed for the same values of the parameters ($\Gamma$, $Re_t$, $Re_b$).

Focusing on the low aspect ratio case, $\Gamma < 10$, where PIV measurements are possible, we further characterized the instability in terms of local Reynolds number $Re_l$ based on the shear layer thickness $w$. The constant value of this Reynolds number at the onset of the instability, $Re_{l,c} \approx 110 \pm 20$, confirms that the transition originates from a shear layer instability. Consequently, the critical mode $m$ scales as $R_0/w$, where $R_0$ is the radius of the annular shear, which results from the competition between the centrifugal effects of each disk. In other words, the instability patterns can be simply seen as a set of vortices of size $\sim w$ regularly filling the shear layer perimeter. As a result, the onset mode is a decreasing function of the Reynolds number, since the shear layer radius decreases as the faster disk becomes more dominant.

All these findings indicate that this instability of the flow between counter-rotating disks can simply be described in terms of a classical Kelvin–Helmholtz instability, where curvature has only a weak effect, and that the surrounding spiral arms result from the interaction of this unstable shear layer with the Ekman boundary layers over the faster disk. These observations for various aspect ratios reveal the continuity between the patterns observed by Lopez *et al.* (2002) for $\Gamma \leqslant 2$ and the 'negative spirals' of Gauthier *et al.* (2002) for $\Gamma = 21$.

We gratefully acknowledge G. Gauthier, P. Gondret, G. M. Homsy, C. Nore, L. S. Tuckerman and J. E. Wesfreid for fruitful discussions. We are indebted to G. Chauvin, R. Pidoux and C. Saurine for experimental help. The computations were carried out on the NEC-SX5 computer of the Institut du Développement et des Ressources en Informatique Scientifique (IDRIS) of the Centre National pour la Recherche Scientifique (CNRS) (project no. 0327).

## REFERENCES

Ahlers, G., Cannell, D. S., Dominguez-Lerma, M. A. & Heinrichs, R. 1986 Wavenumber selection and Eckhaus instability in Couette-Taylor flow. *Physica* D **23**, 202–219.

Batchelor, G. K. 1951 Note on a class of solutions of the Navier–Stokes equations representing steady rotationally–symmetric flow. *Q. J. Mech. Appl. Maths* **4**, 29–41.

Barbosa, E. & Daube, O. 2001 A finite differences method in cylindrical coordinates for 3D incompressible flows. *ECCOMAS CFD Conference, Swansea, UK* (CD-ROM ISBN 0905 091 12 4).

Bergeron, K., Coutsias, E. A., Lynov, J. P. & Nielsen, A. H. 2000 Dynamical properties of forced shear layers in an annular geometry. *J. Fluid Mech.* **402**, 255–289.

Blackburn, H. M. & Lopez, J. M. 2002 Modulated rotating waves in an enclosed swirling flow. *J. Fluid Mech.* **465**, 33–58.

Chomaz, J. M., Rabaud, M., Basdevant, C. & Couder, Y. 1988 Experimental and numerical investigation of a forced circular shear layer. *J. Fluid Mech.* **187**, 115–140.

Cros, A. & Le Gal, P. 2002 Spatiotemporal intermittency in the torsional Couette flow between a rotating and a stationary disk. *Phys. Fluids* **14**, 3755–3765.

Daube, O. & Le Quéré, P. 2002 Numerical investigation of the first bifurcation for the flow in a rotor-stator cavity of radial aspect ratio 10. *Computers Fluids* **31**, 481–494.

Dijkstra, D. & van Heijst, G. J. F. 1983 The flow between finite rotating disks enclosed by a cylinder. *J. Fluid Mech.* **128**, 123–154.

Dolzhanskii, F. V., Krymov, V. A. & Manin, D. Yu. 1990 Stability and vortex structures of quasi-two-dimensional shear flows. *Sov. Phys. Usp* **33** (7), 495–520.

Drazin, P. G. & Reid, W. H. 1979 *Hydrodynamic Instability*. Cambridge University Press.

Escudier, M. P. 1984 Observations of the flow produced in a cylindrical container by a rotating end wall. *Exps. Fluids* **2**, 179–186.

Früh, W. G. & Read, P. L. 1999 Experiments on a barotropic rotating shear layer. Part 1. Instability and steady vortices. *J. Fluid Mech.* **383**, 143–173.

Gadoin, E., Le Quéré, P. & Daube, O. 2001 A general methodology to investigate flow instabilities in complex geometries: application to natural convection in enclosures. *Intl J. Numer. Meth. Fluids* **37**, 175–208.

Gauthier, G., Gondret, P. & Rabaud, M. 1998 Motions of anisotropic particles: application to visualization of three-dimensional flows. *Phys. Fluids* **10**, 2147–2154.

Gauthier, G., Gondret, P. & Rabaud, M. 1999 Axisymmetric propagating vortices in the flow between a stationary and a rotating disk enclosed by a cylinder *J. Fluid Mech.* **386**, 105–126.

Gauthier, G., Gondret, P., Moisy, F. & Rabaud, M. 2002 Instabilities in the flow between co- and counter-rotating disks. *J. Fluid Mech.* **473**, 1–21.

Gelfgat, A. Y., Bar-Yoseph, P. Z. & Solan, A. 2001 Three-dimensional instability flow in a rotating lid–cylinder enclosure. *J. Fluid Mech.* **438**, 363–377.

Goda, K. 1979 A multistep technique with implicit difference schemes for calculating two or three dimensional cavity flows. *J. Comput. Phys.* **30**, 76–95.

Hide, R. & Titman, C. W. 1967 Detached shear layers in a rotating fluid. *J. Fluid Mech.* **29**, 39–60.

Humphrey, J. A. C., Schuler, C. A. & Webster, D. R. 1995 Unsteady laminar-flow between a pair of disks corotating in a fixed cylindrical enclosure. *Phys. Fluids* **7**, 1225–1240.

Hyman, J. M. & Shashkov, M. 1997 Natural discretization for the divergence, gradient and curl on logically rectangular grids. *Comput. Math. Appl.* **33**, 81–104.

von Kármán, T. 1921 Laminar und turbulente reibung. *Z. Angew. Math.* **1**, 233–252.

van de Konijnenberg, J. A., Nielsen, A. H., Rasmussen, J. J. & Stenum, B. 1999 Shear flow instability in a rotating fluid. *J. Fluid Mech.* **387**, 177–204.

Liou, W. W. 1994 Linear instability of curved free shear layers. *Phys. Fluids* **6**, 541–549.

Lopez, J. M. 1998 Characteristics of endwall and sidewall boundary layers in a rotating cylinder with a differentially rotating endwall. *J. Fluid Mech.* **359**, 49–79.

Lopez, J. M., Hart, J. E., Marques, F., Kittelman, S. & Shen, J. 2002 Instability and mode interactions in a differentially-driven rotating cylinder. *J. Fluid Mech.* **462**, 383–409.

Mamum, C. K. & Tuckerman, L. S. 1995 Asymmetry and Hopf bifurcation in spherical Couette flow. *Phys. Fluids* **7**, 80–91.

Marques, F., Gelfgat, A. Yu. & Lopez, J. M. 2003 Tangent double Hopf bifurcation in a differentially rotating cylinder flow. *Phys. Rev.* E **68**, 016310, 1–13.

Moisy, F., Pasutto, T. & Rabaud, M. 2003 Instability patterns between counter-rotating disks. *Nonlinear Processes Geophys.* **10**, 281–288.

Niino, H. & Misawa, N. 1984 An experimental and theoretical study of barotropic instability. *J. Atmos. Sci.* **41**, 1992–2011.

Nore, C., Tartar, M., Daube, O. & Tuckerman, L. S. 2004 Survey of instability thresholds of flow between exactly counter-rotating disks. *J. Fluid Mech.* (in press).

Nore, C., Tuckerman, L. S., Daube, O. & Xin, S. 2003 The 1:2 mode interaction in exactly counter-rotating von Kármán swirling flow. *J. Fluid Mech.* **477**, 51–88.

Rabaud, M. & Couder, Y. 1983 Instability of an annular shear layer. *J. Fluid Mech.* **136**, 291–319.

Schouveiler, L., Le Gal, P. & Chauve, M.-P. 2001 Instabilities of the flow between a rotating and stationary disk. *J. Fluid Mech.* **443**, 329–350.

Serre, E. & Bontoux, P. 2002 Vortex breakdown in a three-dimensional swirling flow. *J. Fluid Mech.* **459**, 347–370.

Serre, E., Crespo del arco, E. & Bontoux, P. 2001 Annular and spiral patterns in flows between rotating and stationary discs. *J. Fluid Mech.* **434**, 65–100.

Stewartson, K. 1953 On the flow between two rotating coaxial disks. *Proc. Camb. Phil. Soc.* **49**, 333–341.

Tuckerman, L. S. 1989 Steady-state solving via Stokes preconditioning: Recurrence relations for elliptic operators. *11th International Conference on Numerical Methods in Fluid Dynamics* (ed. D. L. Dwoyer, M. Y. Hussaini & R. G. Voigt). Lecture Notes in Physics, vol. 323, pp. 573–577. Springer.

Yanase, S., Flores, C., Métais, O. & Riley, J. J. 1993 Rotating free-shear flows. I. Linear stability analysis *Phys. Fluids* A **5**, 2725–2737.

Zandbergen, P. J. & Dijkstra, D. 1987 Von Kármán swirling flows. *Annu. Rev. Fluid Mech.* **19**, 465–91.

# Experimental observation of near-heteroclinic cycles in the von Kármán swirling flow

C. Nore
*Département de Physique, Université Paris XI, 91405 Orsay Cedex, France and Laboratoire d'Informatique pour la Mécanique et les Sciences de l'Ingénieur, CNRS, Boîte Postale 133, 91403 Orsay Cedex, France*

F. Moisy[a)]
*Fluides, Automatique et Systèmes Thermiques, Bâtiment 502, Campus Universitaire, 91405 Orsay Cedex, France*

L. Quartier
*Laboratoire de Physique Statistique, Ecole Normale Supérieure, 24 rue Lhomond, 75231 Paris Cedex 05, France*

(Received 15 September 2004; accepted 12 April 2005; published online 27 May 2005)

The bifurcations and the nonlinear dynamics of the von Kármán swirling flow between exactly counterrotating disks in a stationary cylinder are experimentally investigated by means of visualizations and particle image velocimetry. A regime diagram of the different flow states is determined as a function of the height-to-radius ratio $\Gamma$ and the Reynolds number Re based on disks rotation speed and cylinder radius. Among the steady and time-dependent states found in the experiment, robust near-heteroclinic cycles, which link two unstable states of azimuthal wavenumber $m=2$, are observed and characterized in detail for $\Gamma=2$. These are compared with the numerical findings of Nore *et al.* ["The 1:2 mode interaction in exactly counter-rotating von Kármán swirling flow," J. Fluid Mech **477**, 51 (2003)], with a particular emphasis on the influence of the imperfection and the noise of the experimental setup. © *2005 American Institute of Physics*. [DOI: 10.1063/1.1926827]

## I. INTRODUCTION

A characteristic feature of dynamical systems in the presence of symmetries is the possible existence of robust heteroclinic cycles.[1–4] A heteroclinic cycle connects a set of saddle points in a certain range of parameters, and the time spent in the neighborhood of each saddle point increases indefinitely as the cycle is approached. This phenomenon has gained increasing attention after the work of Busse and Heikes[5] on a dynamical model describing the behavior of the Küppers–Lortz instability of rotating convection rolls.[6] In a certain range of control parameters, a system of rolls is unstable to rolls at an angle of about 60°. This behavior can be described by a set of three coupled nonlinear real ordinary equations,[5] which was first proposed as a model for population biology.[7] Nonrotating convection also provides physical situations where the competition between two modes may create heteroclinic cycles. Indeed a normal form involving four real amplitude equations was derived for convection in two superimposed fluid layers, heated from below and separated by a conducting plate.[8] This normal form was exhaustively analyzed by Proctor and Jones[9] and Armbruster *et al.*[10] as the 1:2 mode resonance in the presence of $O(2)$ symmetry. The ubiquitous occurrence of $m:n$ mode resonances has been revealed in two-dimensional Rayleigh–Bénard convection without Boussinesq symmetry,[11,12] in turbulent boundary layers,[13,14] and in the Kuramoto–Sivashinsky equation[15] using dynamical system theory.

In contrast, experimental observations of heteroclinic cycles are less common. Hu *et al.*[16] have investigated multiple instabilities of rotating layers of fluid heated from below, including the already mentioned Küppers–Lortz instability. Its experimental signature is the propagation of fronts where rolls of one orientation grow to replace rolls in the unstable orientation. An experiment in a porous plug burner at low pressure shows ordered patterns of cellular flame consisting of concentric rings of cells.[17,18] In certain regions of parameter space, these rings appear intermittently, persisting for various periods of time and abruptly changing to the same or different number of cells.

The flow in cylindrical geometries produced by rotating disks with internal shear layers provides another example where heteroclinic cycles may be found, as first shown by Nore *et al.*[19] in numerical computations. This flow configuration has recently been the subject of considerable interest, as it provides a simple hydrodynamical system where the symmetries play a key role in the sequence of bifurcations.[19–25] In the particular case of exactly counterrotating disks with a stationary sidewall at a height-to-radius ratio $\Gamma=2$, when the disk rotation rate is increased, the axisymmetric basic state becomes unstable through a transition which resembles the Kelvin–Helmholtz instability of the equatorial azimuthal free shear layer created by the counterrotation of the top and bottom disks. This instability gives rise to steady states with one or two corotating radial vortices

[a)]Electronic mail: moisy@fast.u-psud.fr

 

generated by the saturation of the corresponding azimuthal mode. Accompanying this instability are more complex dynamics such as traveling waves, modulated traveling waves, and heteroclinic cycles. These cycles connect two states, each containing two corotating vortices and related by $\pi/2$ rotation about the cylinder axis.

The critical Reynolds numbers for this flow have been investigated when the aspect ratio is varied between 0.5 and 3 and the counterrotation of the two disks maintained.[25] The 1:2 codimension-two point at which the $m=1$ and the $m=2$ thresholds coincide has been located at $\Gamma(1:2)=1.64$. Heteroclinic cycles may occur in a large region of parameter space when the $m=1$ threshold precedes that of the $m=2$, i.e., when $\Gamma>\Gamma(1:2)$, but only extremely near the codimension-two point when the order is reversed [i.e., when $\Gamma<\Gamma(1:2)$]. At $\Gamma=2$, only periodic cycles with heteroclinic type behavior have been numerically observed and are thus called near-heteroclinic cycles.[19] As was first pointed out by Busse and Heikes,[5] numerical noise prevents the flow from staying an indefinite amount of time in a neighborhood of a saddle state, leading to a periodic cycle.

The main purpose of this paper is to experimentally investigate the sequence of states which occur when the Reynolds number is varied for aspect ratios between 0.5 and 2.5, and to characterize in detail the near-heteroclinic cycles observed at $\Gamma=2$. The outline of the paper is as follows: Sec. II describes the experimental setup and visualization and measurement systems. In Sec. III, the regime diagram and the steady states obtained for different aspect ratios are reported. Section IV describes the symmetries of the flow, and numerical results for the case $\Gamma=2$ are summarized. Section V is devoted to the study of the steady and unsteady flow states for $\Gamma=2$, with a particular emphasis on the near-heteroclinic cycles. Section VI contains our conclusion.

## II. EXPERIMENTAL SETUP

### A. Experimental cell

The experimental cell is sketched in Fig. 1. The cylindrical container, made of Plexiglas, of inner radius $R_c=35.5$ and 120 mm long, is mounted vertically. The working fluid is silicon oil of kinematic viscosity $\nu=10^{-4}\,\mathrm{m^2\,s^{-1}}$ at 25 °C. The top and bottom disks, of radius $R_d=34.5$ mm, are immersed into the fluid that totally fills the cylinder. The distance between the disks, $H$, can be adjusted between a few millimeters up to 89 mm. In the present paper, the aspect ratio, defined as $\Gamma=H/R_c$, is varied between 0.5 and 2.5. Finally, the cylinder is immersed into a rectangular water tank, in order to minimize optical distortion.

The disks are driven by a dc motor, and constrained to rotate with exactly opposite velocities. The angular velocity $\Omega$ can be set between 10 and 64 rad/s with a stability of 0.1%. Typical runs are of $10^4$ rotations, and the waiting time between runs is at least 2000 rotations in order to avoid transient effects. The temperature, measured in the outer water bath, showed a maximum drift of ±0.1 °C during a run, leading to an uncertainty of ±0.3% for the viscosity. The Reynolds number, based on the cylinder radius $R_c$ and the disk velocity $\Omega R_d$,

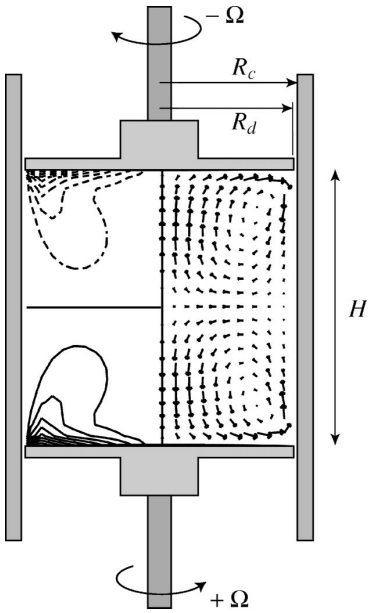


FIG. 1. Experimental cell. The inset illustrates azimuthal velocity contours (left) and the meridional velocity field (right) of the axisymmetric flow determined by numerical simulation (Ref. 19).

$$\mathrm{Re}=\Omega R_d R_c/\nu,$$

is varied between 140 and 600. Note that, in the numerical simulations of Nore *et al.*,[19,25] the two radii are equal and denoted by $R$, so that the two control parameters are simply given by $\Gamma=H/R$ and $\mathrm{Re}=\Omega R^2/\nu$.

The basic axisymmetric steady flow is also depicted in Fig. 1. It consists of a predominant equatorial shear layer produced by the counterrotating top and bottom disks, and separating two regions with opposite senses of azimuthal velocities (left part of Fig. 1). Two second-order recirculation zones due to Ekman pumping in the neighborhood of each disk (right part of Fig. 1) converge at midheight and form an inward radial jet.

### B. Flow visualization

Visualizations using Iriodin flakes were performed in order to determine the various flow states which occur as the control parameters $(\Gamma,\mathrm{Re})$ are varied. Although crude, this visualization method is convenient as a first approach, as it allows us to easily define the onset modes and the associated critical Reynolds numbers.

Two mirrors, placed at angles of 120° on each side of the cylinder, allow for visualization around the whole perimeter. The pictures, taken from a charge-coupled device (CCD) camera, were processed in order to unfold the three views: the front view is shown in the left picture, while the side views were reversed and rescaled, and are shown in the middle and right pictures (see Figs. 2 and 3).

Along the equatorial shear layer, the vertical velocity vanishes and the Iriodin flakes are essentially horizontal. Therefore the shear layer appears as a dark horizontal line when seen by reflection and as a bright line when seen by

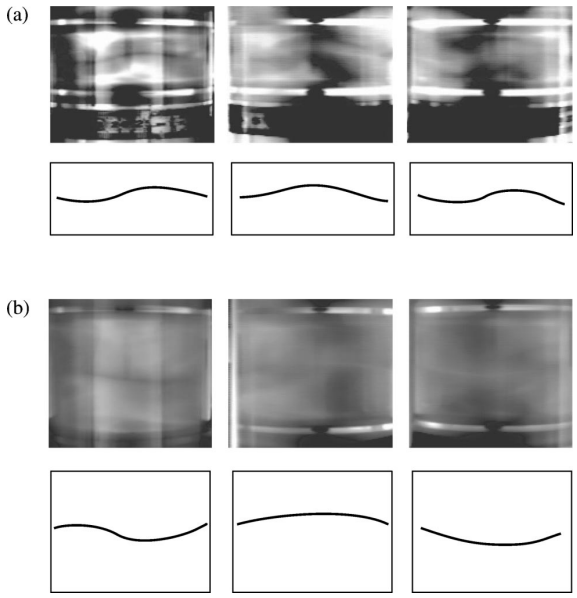


FIG. 2. Azimuthal modulation of the shear layer, as observed using Iriodin flakes, for various aspect ratios $\Gamma$. The pictures were processed in order to unfold the three views: the front view is shown in the left picture, while the side views are reversed and rescaled, and are shown in the middle and right pictures. The shear layer is seen by reflection in the left picture (dark line) and by transmission in the two other pictures (bright line). The mode corresponds to the number of extrema along the unfolded perimeter. The lines drawn below the pictures are guides for the eye. (a) $\Gamma=0.75$, $m_C=3$. (b) $\Gamma=1.5$, $m_C=2$.

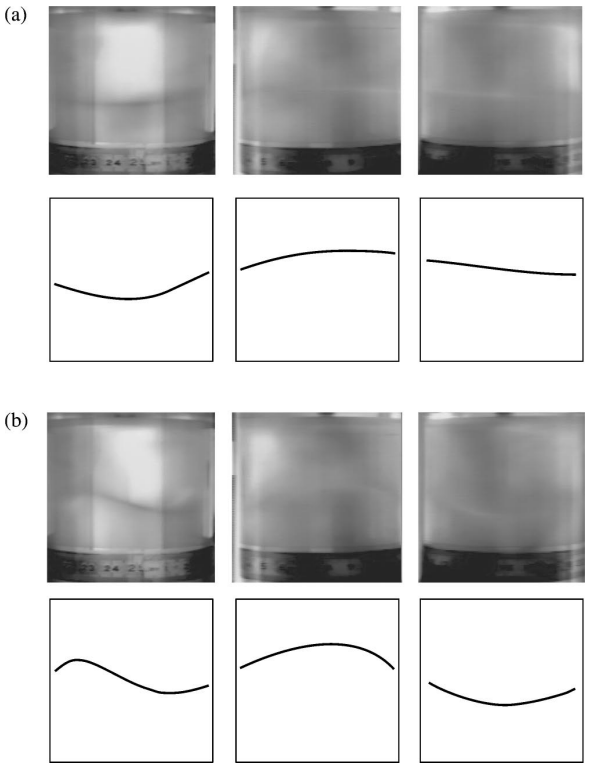


FIG. 3. Same as Fig. 2 with (a) $\Gamma=2$, $m_C=1$. (b) $\Gamma=2$, $m=2$.

transmission. In the figures, the light source being on the same side as the camera, the front view shows a dark line, while the two side views show a bright line.

### C. Velocity measurements

Velocity fields in a meridional plane $(x,z)$ were measured using a particle image velocimetry (PIV) system. For these measurements, the distance $H$ was set at 71 mm, leading to an aspect ratio $\Gamma=H/R_c=2$. Small borosilicate particles, 11 $\mu$m in diameter, are used as tracer, illuminated by a vertical laser sheet of thickness $b\simeq 0.5$ mm produced by a double pulsed Nd:YAG laser (YAG—yttrium aluminum garnet). Images are acquired with a double-buffer high resolution camera ($1280\times 1024$ pixels, 4096 gray levels), synchronized with the laser at a rate of 1 frame pair per second.

The main difficulty for the PIV measurements in this geometry arises from the large azimuthal velocity component of the flow, which strongly constrains the time delay $\delta t$ between the two frames of a pair. The out-of-plane azimuthal velocity is of the order of $\Omega R$ and dominates the in-plane meridional components to be measured, which are of the order of $0.1\ \Omega R$. In order to keep an acceptable number of common particles between the two frames of a pair, the time delay $\delta t$ has to be kept of the order of $b/\Omega R$. As a consequence, the particle displacement in the meridional plane is small of the order of $0.1b\simeq 0.05$ mm $\simeq 1$ pixel. With azimuthal velocities of the order of $\Omega R\simeq 0.5$–$2$ m s$^{-1}$, the time delay $\delta t$ typically ranges from 0.5 to 2 ms. Window sizes of $32\times 32$ pixels, with an overlap of 16 pixels, are used for the PIV computations. The final velocity fields are defined on a $64\times 64$ grid, with a resulting spatial resolution of 1 mm. In the following figures, only one out of four velocity vectors is shown for clarity.

## III. REGIME DIAGRAM AND FLOW STATES

Systematic measurements of the onset Reynolds numbers have been performed from visualization of the Iriodin flakes, for aspect ratios $\Gamma$ ranging between 0.5 and 2.5. The regime diagram in Fig. 4 summarizes our observations in the plane of parameters $(\Gamma,\mathrm{Re})$. These onset Reynolds numbers have been obtained by slowly increasing the angular velocity and visually inspecting the light reflected and transmitted by the flakes.

The thresholds are found in excellent agreement with the numerical results of Nore *et al.*,[25] shown as the lower solid line, except for large $\Gamma$ where the experimental thresholds are slightly lower than the numerical ones, probably due to experimental noise which may slightly anticipate the bifurcation of the basic flow.

Examples of flow visualizations are given in Figs. 2 and 3. For low Reynolds numbers, the stable equatorial shear layer shows an exactly horizontal line at midheight, which becomes modulated as the Reynolds number is increased. The shear layer is sketched below the pictures to guide the eye. The corresponding mode can be easily determined as the number of extrema along the unfolded perimeter. The first three figures, Figs. 2(a), 2(b), and 3(a), obtained slightly

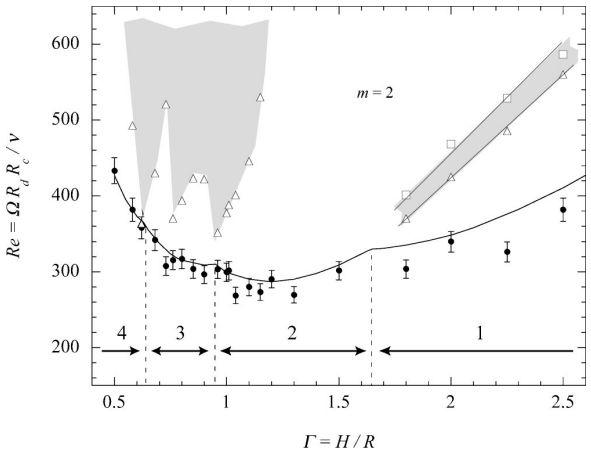


FIG. 4. Experimental regime diagram, obtained from visualization. ●, steady nonaxisymmetric state with critical mode $m_C$, △, time-dependent state, □, steady nonaxisymmetric state with mode $m \neq m_C$. Error bars for △ and □ are the same as for ●. The gray region represents various unsteady states. —, numerical threshold, - - -, lines indicating the codimension-two points, $\Gamma(3:4)=0.63$, $\Gamma(2:3)=0.95$, and $\Gamma(1:2)=1.64$. The numbers above the horizontal arrows indicate the onset mode $m_C$.

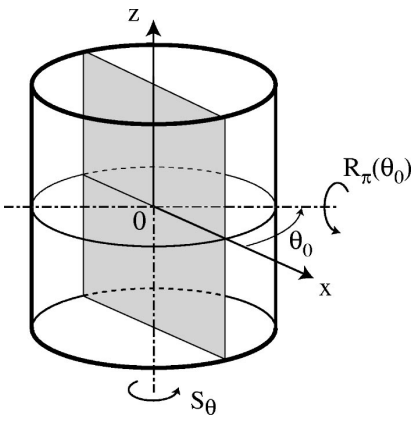


FIG. 5. Sketch of the two symmetries, $S_\theta$ and $R_\pi(\theta_0)$, of the flow between exactly counterrotating disks. The meridional plane where the PIV measurements are performed defines the $(x,z)$ plane, in gray.

above the onset, show the critical modes $m_C=3$, 2, and 1 that appear for the aspect ratios 0.75, 1.5, and 2, respectively. In the case $\Gamma=2$, another stationary mode $m=2$ is also obtained for higher Reynolds number, as shown in Fig. 3(b).

The first flow state found above the onset is always stationary, with an azimuthal modulation $m_C$ which decreases from 4 to 1 as $\Gamma$, i.e., the height, is increased. The experimentally observed onset modes fall into the expected regions shown by the horizontal arrows, delimited by the numerically determined codimension-two points sketched as vertical dashed lines in Fig. 4.

The subsequent states for larger Reynolds number depend strongly on the aspect ratio. For $\Gamma > \Gamma(1:2)=1.64$, in addition to the critical mode $m_C=1$, a higher order stationary mode $m=2$ is also found when the Reynolds number is increased. These two modes, shown in Figs. 3(a) and 3(b) for $\Gamma=2$, correspond to what are called the mixed mode *M* and the pure mode *P*, respectively, and will be described in detail in Sec. V. A narrow band of time-dependent states is experimentally observed between these two steady states. The upper and lower limits of this unsteady band are roughly straight lines that converge towards the codimension-two point at $\Gamma(1:2)$, as predicted theoretically[1,2,10] and confirmed numerically.[25] In this band, two time-dependent states, traveling waves (TW), and near-heteroclinic cycles (Het) are experimentally observed, but they are not easy to distinguish from the visualizations. These two states will be described in detail in Sec. V for $\Gamma=2$.

For the range of aspect ratios $1.2<\Gamma<1.5$, in the $m_C=2$ region, the flow remains stationary up to the highest Reynolds number investigated, $\mathrm{Re}\simeq 600$. Lower aspect ratios, $\Gamma \leqslant 1.2$, for which $m_C \geqslant 2$, show complex unsteady states. Traveling waves with strong nonlinear interactions, sometimes leading to intermittent vortex pairing, may be observed. The lower limit of this unsteady region is somewhat scattered, sometimes closely approaching the critical curve, in particular, near the codimension-two points at $\Gamma(3:4)=0.63$ and $\Gamma(2:3)=0.95$. No upper limit for this region is observed, at least for $\mathrm{Re}<600$. The complex flow states in this region could result from resonance between modes $m \geqslant 2$, and have not yet been explored.

## IV. SYMMETRIES AND FLOW STATES FOR $\Gamma=2$

In order to obtain more insight into the sequence of bifurcations and the mode competition that takes place as the Reynolds number is increased, a careful analysis of the symmetries of the flow is essential. A complete description of these symmetries can be found in Nore *et al.*,[19] and they are only briefly presented here.

### A. Symmetries of the exactly counterrotating flow

The base flow produced in a cylinder driven by the rotation of the top and bottom disks is axisymmetric, i.e., invariant under rotation by any angle $\theta$ about the cylinder axis, which we denote by $S_\theta$ (see Fig. 5). The present case of exactly counterrotating disks is unique in possessing an additional symmetry of rotation of $\pi$ about any horizontal axis in the equatorial plane. We denote this rotation by $R_\pi(\theta_0)$, where $\theta_0 \in [0,\pi)$ is the direction of the horizontal axis. This additional symmetry is equivalent to combined reflections in $\theta=\theta_0$ and in $z=0$. The main point is that rotation about the $z$ axis and about a horizontal axis do not commute, and hence, the group generated by the operators $S_\theta$ and $R_\pi(\theta_0)$ is isomorphic to $O(2)$. This symmetry group $O(2)$ is especially important for the sequence of bifurcations present in this system, and is, in particular, the key ingredient for the heteroclinic cycles that take place between two rotated modes $m=2$ at $\Gamma=2$.

In the present experiment, only the velocity field in a $(x,z)$ meridional plane, which defines by convention the origin $\theta=0$, is measurable by PIV (see Fig. 5). It is therefore of interest to consider the restriction of the above three-dimensional symmetries to this meridional plane. Note that,

TABLE I. Symmetries of the various flow states and corresponding numerical and experimental critical Reynolds numbers for $\Gamma=2$. ($^*$) These modes may also be invariant under $s_x$ and $s_0$ for special values of $\theta_0$ (see text).

| State | Symmetry | Symmetry in $(x,z)$ plane | Numerical threshold | Experimental threshold |
|---|---|---|---|---|
| Basic state | $S_\theta$, $R_\pi(\theta_0)$ | $s_z$, $s_x$ | … | … |
| Mixed mode ($M$) | $R_\pi(\theta_0)$ | ($^*$) | 349.0 | 350±4 |
| Traveling waves (TW) | … | … | 411.6 | 420±4 |
| Modulated waves (MW) | … | … | 427.3 | Not observed |
| Heteroclinic cycles (Het) | … | … | 427.4 | 450±8 |
| Pure mode ($P$) | $S_\pi$, $R_\pi(\theta_0)$ | $s_z$, ($^*$) | 452 | 480±4 |

in this restriction, we consider only the velocity components within the meridional plane, and not the component perpendicular to it.

Consider first states which are axisymmetric. In the meridional plane, these states are invariant under reflection in the $z$ axis, acting on coordinates as $(x,z)\rightarrow(-x,z)$, which we denote by $s_z$. This is also the case for even wavenumber states, those which are invariant under discrete rotations $S_\theta$ with $\theta=2\pi/m$ for even $m$. Consider now states which are invariant under some reflection $R_\pi(\theta_0)$, where $\theta_0$ is an arbitrary angle chosen by the system. These states are not necessarily symmetric in the $(x,z)$ meridional plane where the PIV measurements are performed, unless $\theta_0$ takes on one of two special values. If $\theta_0$ is along the $x$ axis ($\theta_0=0$), then invariance under $R_\pi(\theta_0)$ reduces to reflection in the $x$ axis, denoted by $s_x$ and acting as $(x,z)\rightarrow(x,-z)$. If $\theta_0$ is normal to the plane ($\theta_0=\pi/2$), then invariance under $R_\pi(\theta_0)$ is the central symmetry relative to the origin, denoted by $s_0$, which is equivalent to combined reflection in $x$ and $z$, i.e., $s_0=s_xs_z$. These symmetries in the meridional plane, $s_z$, $s_x$, and $s_0$, are especially useful as they provide a convenient way of identifying the flow patterns obtained by PIV in Sec. V.

### B. Numerical results for $\Gamma=2$

The particular case of the aspect ratio $\Gamma=2$ shows the following sequence of bifurcations as the Reynolds number is increased:[19] basic flow; steady state with $m=1$, called mixed mode $M$; traveling waves; modulated traveling waves; near-heteroclinic cycles; and steady states with $m=2$, called pure mode $P$. The symmetries and the critical Reynolds numbers of these states are described here, and are summarized in Table I.

For low Reynolds number, the basic state inherits the $O(2)$ symmetry from the geometric configuration. In the meridional plane, it is thus invariant under $s_z$ and $s_x$. For $\mathrm{Re}>349.0$, this basic state loses stability to the $m=1$ mode, giving rise to a stationary state with one elliptic point in the equatorial plane and a diametrically opposite hyperbolic point. This state is called the mixed mode $M$, because the nonlinear interactions produce both even and odd harmonics. The other stationary bifurcated flow is obtained for $\mathrm{Re}\geqslant452$. It is a $m=2$ mode and consists of two radial corotating vortices in the equatorial plane, located on two diametrically opposite elliptic points $E$ and $E^*$, and separated by two hyperbolic points $H$ and $H^*$. Two orientations of this state are sketched in Fig. 6. This state is called the pure mode $P$ since only even harmonics are present. Both the mixed mode $M$ and the pure mode $P$ break the invariance under $S_\theta$, while preserving the invariance under $R_\pi(\theta_0)$. As seen in the preceding section, this invariance does not lead to any particular symmetry in the meridional plane where the PIV measurements are performed, except for special orientations of $\theta_0$ which lead to the horizontal reflection symmetry $s_x$ or the central symmetry $s_0$. In addition, since it involves only even Fourier components, the pure mode $P$ is also invariant under $S_\theta$ for $\theta=\pi$, and is consequently invariant under $s_z$ in the meridional plane.

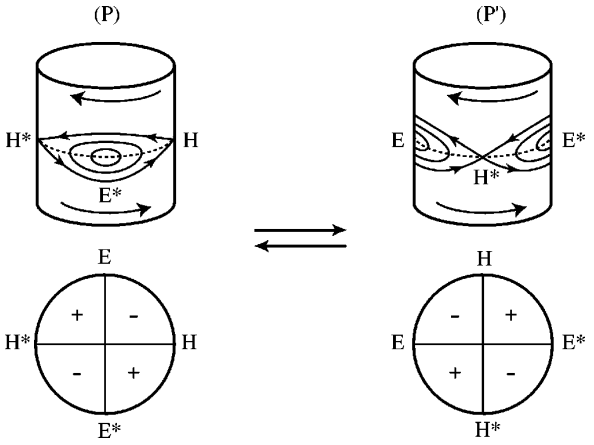


FIG. 6. (Bottom) Sketch of vertical velocity variations in the equatorial plane of the pure modes $P$ and $P'$. The +(−) sign designates upward (downward) vertical velocities. The heteroclinic cycle connects $P$ and $P'$, related by rotation of $\pi/2$. The radial vortices are centered on the diametrically opposite elliptic points $(E,E^*)$ and are located at right angle from the hyperbolic points $(H,H^*)$. (Top) Perspective representations of the two corotating vortices separated by the two hyperbolic points $(H,H^*)$.

For intermediate Reynolds numbers between these two steady states, $411.6\leqslant\mathrm{Re}\leqslant452$, three types of time-dependent states have been numerically reported. For $411.6\leqslant\mathrm{Re}\leqslant427.3$, right or left TW are observed, which break both the $S_\theta$ and the $R_\pi(\theta_0)$ symmetries. These waves become modulated in a very narrow range of Reynolds numbers, $427.3\leqslant\mathrm{Re}\leqslant427.4$. For $\mathrm{Re}>427.4$, the solution follows an attracting near-heteroclinic cycle which links two unstable pure states $P$ and $P'$, obtained by rotation of $\pi/2$ about the cylinder axis (see Fig. 6). These cycles are stable up to $\mathrm{Re}=452$, where the steady pure mode $P$ becomes stable. Although the flow during the near-heteroclinic cycle presents no exact spatial symmetry, during the quasistationary phases in the neighborhood of the states $P$ and $P'$ it does inherit the symmetries of the pure mode state, i.e., invariance under $s_z$ (because of the even harmonic content) and possibly the invariances under $s_x$ and therefore also $s_0$ (for special orientations of $\theta_0$).

The numerically computed near-heteroclinic cycles found in Nore *et al.*[19] are characterized by periodic oscillations between pure mode states $P$ and $P'$ separated by rapid changes through odd-wavenumber-dominated states. The period is controlled by the equal time $\tau$ spent in the neighbor-

hoods of $P$ and $P'$. This duration $\tau$ increases from 550 up to 900 rotation periods when the Reynolds number Re increases from 428 to 435. Two distinct heteroclinic type regimes were observed in the simulations: a two-plateau and a four-plateau oscillation. These two regimes originate from two possible paths connecting the two saddle points $P$ and $P'$. Although no systematic conclusion could be reached in the simulations due to the prohibitive computation time, both the Reynolds number and the choice of the initial conditions seemed to play a role in favoring one of these two regimes.

## V. PIV ANALYSIS OF THE FLOW STATES FOR $\Gamma=2$

Systematic measurements of the velocity fields in the meridional plane $(x,z)$ have been performed for $\Gamma=H/R_c=2$, with the aim of further characterization of the near-heteroclinic cycles. In Table I, the experimentally observed flow states are summarized, and the corresponding critical Reynolds numbers are compared to the numerical ones.

### A. Steady states

Figure 7 shows the meridional velocity field $(u_x,u_z)$ for the three different steady states observed at $\Gamma=2$: (a) the basic state for $\mathrm{Re}<350\pm4$; (b) the mixed mode $M$ for $350\pm4<\mathrm{Re}<420\pm4$; (c) the pure mode $P$ for $\mathrm{Re}>480\pm4$. These velocity fields are time averaged over the whole run. The experimental thresholds, given in Table I, are in very good agreement with the numerical ones, with discrepancies that do not exceed 6%.

Contour levels of the velocity $u_x$ are also shown, and are especially useful in depicting the symmetries of the various flow states. In the basic state, Fig. 7(a), the contour levels are even in $z$ and almost odd in $x$; the residual asymmetry in $x$ probably results from a slight misalignment of the laser sheet with the meridional plane, leading to a contamination from the large azimuthal component of the velocity. As shown in Sec. IV, this corresponds to invariance under the reflection symmetries $s_x$ and $s_z$, which traces back to the $O(2)$ symmetry of the basic state. The mixed mode $M$, Fig. 7(b), shows symmetry neither in $x$ nor in $z$, since the $R_\pi(\theta_0)$ symmetry for a mixed mode does not lead to any symmetry in an arbitrary meridional plane. The departure from reflection symmetry can be verified by carefully looking at the velocity vectors near the vertical axis of Fig. 7(b) which are not symmetric under $s_0$. In the pure mode $P$, Fig. 7(c), the vertical reflection symmetry $s_z$ of the contour levels is recovered, as the trace of the presence of only even harmonics.

It must be noted that the experimentally observed mixed and pure modes always show similar velocity fields in the meridional PIV plane, even for different initial conditions. In particular, the $s_0$ or $s_x$ symmetries are never observed for these flow patterns, as would be the case for a flow state invariant under the $R_\pi(\theta_0)$ symmetry with $\theta_0=0$ or $\pi/2$. A geometric defect in the setup, probably the residual ellipticity of the cylindrical container (of about 0.7%), is thought to be responsible for this systematic bias of the azimuthal symmetry breaking. This imperfection probably has no influence on the transition from the basic to the mixed state. However, by forcing the flow in a preferred direction, it may delay the

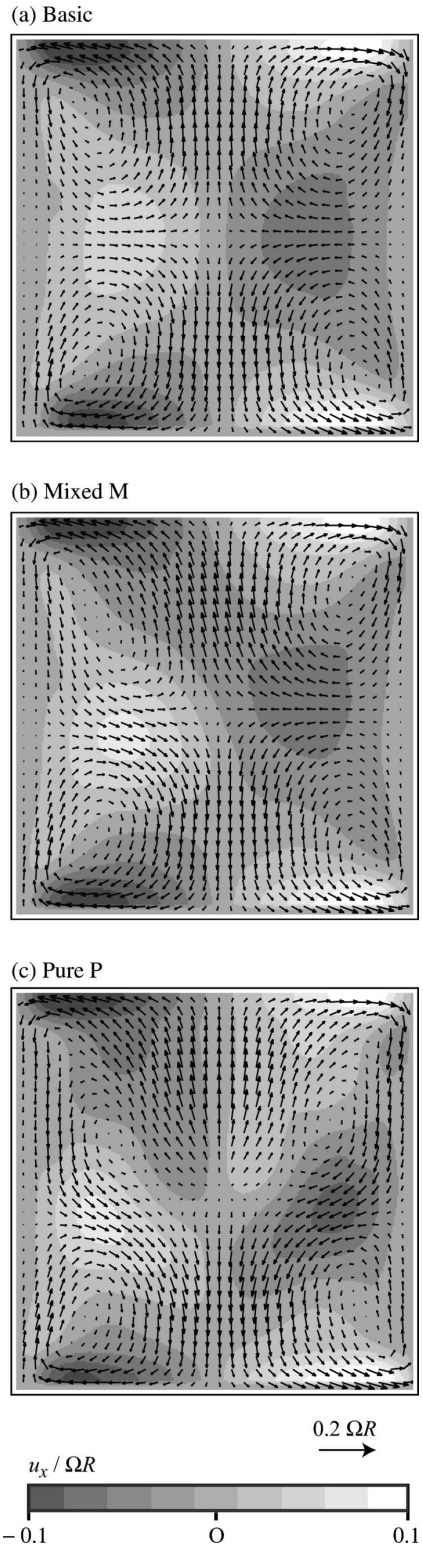


FIG. 7. Meridional velocity field $(u_x,u_z)$ and contour levels of $u_x$ of the three steady states. (a) Basic state at $\mathrm{Re}\simeq280$, invariant under the horizontal and vertical reflection symmetries $s_x$ and $s_z$. (b) Mixed mode $M$ at $\mathrm{Re}\simeq415$, which does not show any invariance as can be verified on the arrows near the vertical axis. (c) Pure mode $P$ at $\mathrm{Re}\simeq550$, invariant under the vertical reflection symmetry $s_z$.

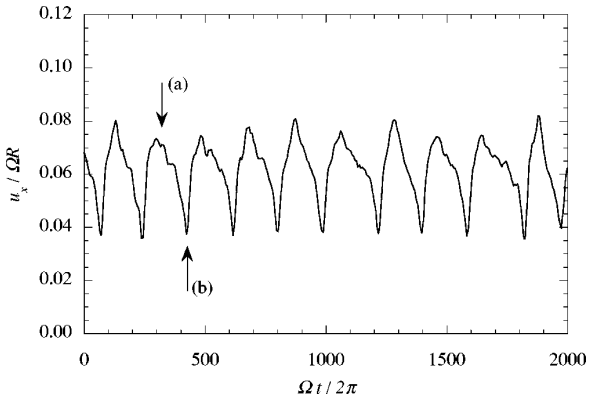


FIG. 8. Time series of $u_x(x=-R/2,z=0)$ corresponding to the traveling waves TW for $\mathrm{Re}\simeq 440$. The labels (a) and (b) refer to the velocity fields in Fig. 9.

transitions toward the subsequent states. This may explain the above mentioned shifts, of the order of 6%, between the numerical and the experimental thresholds (see Table I).

### B. Traveling waves

The mixed mode state loses stability at $\mathrm{Re}\simeq 420\pm 4$, giving rise to a first time-dependent state, as illustrated by the time series in Fig. 8 for $\mathrm{Re}\simeq 440$. This figure shows nearly periodic oscillations, with a period of $190\pm 15$ rotations, of the horizontal velocity $u_x$, measured at the location $(x,z)=(-R/2,0)$.

This first time-dependent state can be identified as the TW state, by inspecting the velocity fields in Fig. 9. These fields correspond to the two characteristic phases that are labeled (a) and (b) in the time series. They are more noisy than those for the steady states, as they have been averaged over only a few instantaneous velocity fields. As expected, these fields do not present any particular symmetry, since the traveling waves break both the $S_\theta$ and the $R_\pi(\theta_0)$ symmetries. It must be noted, however, that Fig. 9(b) appears to be similar to the steady mixed mode shown in Fig. 7(b), which is invariant under $R_\pi(\theta_0)$. This resemblance indicates that the asymmetric (under $R_\pi$) component of the traveling wave state is indeed weak.

The theoretical analysis shows that these traveling waves originate from a drift pitchfork bifurcation,[26] and thus have infinite period at onset. In the range of Reynolds numbers

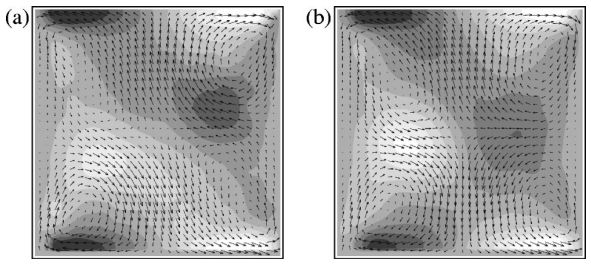


FIG. 9. Velocity fields of the traveling waves TW for $\mathrm{Re}\simeq 440$ (see Fig. 8). The velocity scale and contour levels gray scale are as that in Fig. 7.

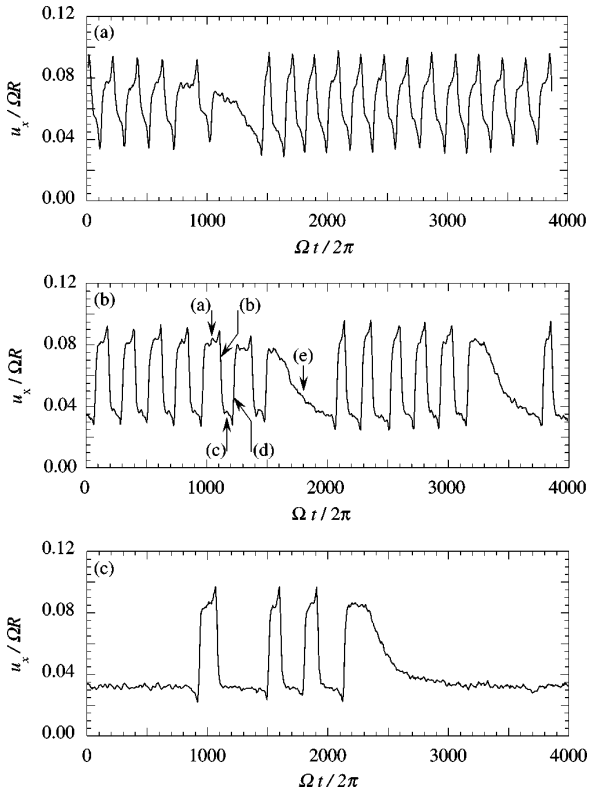


FIG. 10. Time series of $u_x(x=-R/2,z=0)$, corresponding to the near-heteroclinic cycle state (Het), for $\mathrm{Re}\simeq 452$, 469, and 478. The labels (a)–(e) in the second time series refer to the velocity fields in Fig. 11.

where the traveling waves are observed, the measured period remains of the order of $190\pm 15$ rotations. Numerically, the period was found to decrease as the Reynolds number is increased as predicted by theory. However, because of the small range of Reynolds number where this pattern can be observed, no measurable change in the period has been detected experimentally. Note also that the modulated waves (MW), which were observed only in a very narrow range of Reynolds numbers in the simulations, $427.3\leqslant \mathrm{Re}\leqslant 427.4$ (see Table I), have not been observed in the experiments. The very fine range of Reynolds number where they should be observed is well beyond the experimental uncertainty. Moreover, the geometrical differences between the experimental and the numerical configurations, in particular, the cylinder-to-disk radius ratio $R_c/R_d$ of 1.03 instead of 1, cannot allow us to expect a perfect agreement for the observed flow states and their critical Reynolds numbers.

### C. Near-heteroclinic cycles

When the Reynolds number is increased above 450, the time series cease to show a strictly periodic behavior. Instead, irregular oscillations between two states, punctuated by slow relaxation phases toward a third state, are observed, as shown by the time series in Fig. 10 obtained for increasing Reynolds number, $\mathrm{Re}\simeq 452$, 469, and 478. As the Reynolds

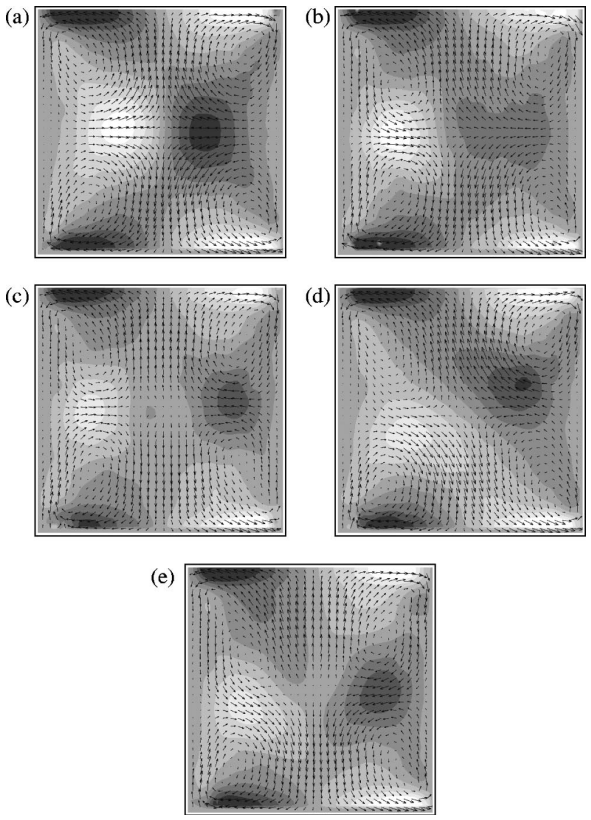


FIG. 11. Velocity fields of the near-heteroclinic cycle state (Het) for Re $\simeq 469$. The fields (a) and (c), approximately invariant under the vertical reflection symmetry $s_z$, correspond to the pure states $P$ and $P'$ (plateaux of approximately constant $u_x$ in Fig. 10). The fields (b) and (d) are instantaneous velocity fields corresponding to the spikes in Fig. 10 that connect the plateaux (a) and (c). The field (e) in the long relaxation phase is the pure mode favored by an experimental defect resembling the pure mode in Fig. 7(c).

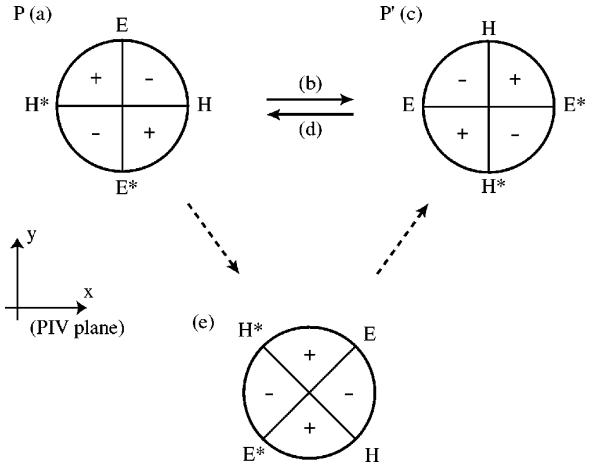


FIG. 12. Sketch of the experimental near-heteroclinic cycle connecting the two pure modes $P$ (a) and $P'$ (c) [double arrow (b) and (d)], punctuated by excursions toward the favored pure mode (e) oriented at 45° from the diameters $EE^*$ and $HH^*$ (dashed arrows). The labels (a)–(e) refer to those of Figs. 10 and 11. The PIV plane is aligned with the $x$ axis.

number approaches the upper bound, $\mathrm{Re} \simeq 480$, the relaxation phases are found to be longer and more frequent.

The velocity fields corresponding to the different phases of the second time series, labeled (a)–(e), are shown in Fig. 11. The fields (a) and (c) correspond, respectively, to the upper and the lower plateaux of the oscillations, the rapid changes between them are denoted by (b) and (d), and the last field (e) corresponds to the slow relaxation phase.

Visual inspection of the symmetries of the fields (a)–(d) allows us to identify this second time-dependent state as the Het state connecting the two unstable pure modes $P$(a) and $P'$(c). The two velocity fields (a) and (c) are indeed approximately invariant under the vertical reflection symmetry $s_z$, as expected for pure modes $m=2$ with only even harmonics. This property distinguishes without ambiguity the heteroclinic cycle state from the traveling wave state (see Fig. 9), which is not invariant under $s_z$. In addition, the two fields (a) and (c) appear to be also approximately invariant under $s_x$ (and hence under $s_0 = s_x s_z$), so that the vertical velocity component is almost zero on the equatorial line $z=0$. The comparison with the sketches of the equatorial plane in Fig. 12, where the sign of $u_z$ is shown, indicates that the PIV plane where the measurements are performed appears to be approximately aligned either with the two hyperbolic points $H$ and $H^*$ [Fig. 12(a)], or with the two elliptic points $E$ and $E^*$ [Fig. 12(c)]. This confirms that the two unstable states $P$ and $P'$ of the cycle are related by a $\pi/2$ rotation.[27] The fields corresponding to the rapid changes between $P$ and $P'$ shown in Figs. 11(b) and 11(d) are, as expected, states of mixed (even and odd) harmonic content that connect the two pure modes. The field (b) is approximately invariant under the $s_x$ symmetry, while the field (d) is invariant under the $s_0$ symmetry. The characteristic time of these transient phases is of about $20 \pm 5$ rotations, which is of the order of the time scale of the advection by the meridional components of the velocity.

Finally, the last field in Fig. 11(e), which corresponds to the slow relaxation phases that appear intermittently during the cycles (a)–(d), makes the above description in terms of a heteroclinic cycle more complex. This additional state, which is invariant under $s_z$ but not under $s_x$, resembles the steady pure mode observed at larger Reynolds numbers [see Fig. 7(c)], with two large counterrotating vortices in the upper cylinder half and two smaller ones in the lower half. The negative values of $u_z$ along the equatorial line $z=0$ indicate that the PIV plane now falls in between the two diameters $EE^*$ and $HH^*$ [see Fig. 12(e)], i.e., at $\approx 45°$ from the pure states $P$ and $P'$ of the cycle. As noted in Sec. V A, this particular orientation of the steady pure mode seems to be favored by a slight asymmetry in the experimental setup. This suggests that the imperfection of the experiment, although weak, has a deep influence on the observed near-heteroclinic cycles, and would be, in particular, responsible for the relaxation phases that intermittently interrupt the oscillations between $P$ and $P'$ (see the dashed arrows in Fig. 12).

### D. Plateau durations of the near-heteroclinic cycles

For Reynolds numbers close to the lower bound where the near-heteroclinic cycle state is found, $\mathrm{Re} \simeq 450$, apart from the slow relaxation phases toward the favored pure mode (e), the plateau duration $\tau$ is approximately constant of the order of 100 rotations. These plateau durations become uneven as the Reynolds number is increased, with a mean duration $\langle \tau \rangle$ that gradually increases [200 rotations for $\mathrm{Re} \simeq 469$ in Fig. 10(b)]. In addition, the relaxation phases (e) are longer and more frequent, and are preceded by a gradual increase of the plateau durations, as clearly seen in Fig. 10(b). This scenario of a gradual increase of the plateau durations interrupted by an excursion toward the favored pure mode (e) and back to the plateau oscillations (a)–(d) is observed in most of the time series.

The broad distribution of plateau durations at fixed Reynolds number is a genuine property of the approach toward a heteroclinic cycle in the presence of noise.[28] The plateau duration is indeed controlled by the time spent by the system in the neighborhoods of the two unstable states $P$ and $P'$. These two states being saddle points, there is no intrinsic time scale for this approach, which should tend to infinity in the absence of noise.[5] When a certain amount of noise $\epsilon \ll 1$ is present, the system approaches one of the saddle points along its attracting direction as $\exp(-\lambda_s t)$ down to a distance of the order of $O(\epsilon)$. Meanwhile, it moves away along the repulsing direction as $\exp(\lambda_u t)$, until it reaches a distance $\sim O(1)$ at which it escapes from the saddle point. Here $\lambda_s$ and $\lambda_u$ are the absolute values of the leading eigenvalues in the stable and unstable directions, respectively. As a consequence, the mean plateau duration is given by[28]

$$\langle \tau \rangle \simeq \frac{1}{\lambda_u} |\ln \epsilon|.$$

The distribution of $\tau$ cannot be deduced from this crude description and depends on the statistical properties of the noise. The observed increase of the mean plateau duration $\langle \tau \rangle$ as the Reynolds number is increased presumably does not originate from the noise of the system, which should not evolve significantly over this small range of Reynolds numbers $\mathrm{Re} \in [450, 480]$, but is more likely due to a Re dependence of the unstable eigenvalue $\lambda_u$. This eigenvalue is indeed expected to vanish at $\mathrm{Re} \simeq 480$, when the heteroclinic cycle branch disappears and the pure mode branch becomes stable, which should lead to an infinite mean plateau duration.

Note that an ideal heteroclinic cycle without any noise nor geometrical defect should lead to infinitely increasing plateau durations.[9,10] This could explain the gradual increase of the plateau durations before the relaxation phases (e) observed in most time series. In contrast, the simulations of Nore *et al.*[19] only showed strictly periodic cycles with a fixed finite period. In the numerics, various sources of noise, such as round-off errors and temporal discretization, by systematically bringing the system to the same distance from the saddle points, may have a saturating effect on the period of the cycles. In our experiment, both the noise and the geometrical bias seem to play an important role in the observed near-heteroclinic cycles. First, the presence of noise may prevent the system from staying an infinite time close to one of the unstable states. Second, the geometrical defect seems to enable the system to explore another path toward the favored pure mode state. However, a systematic characterization of the duration statistics is well beyond the available data, and would require much longer acquisition times in a perfectly stable system.

## VI. CONCLUSION AND DISCUSSION

We have experimentally investigated the dynamics of the exactly counterrotating von Kármán swirling flow at low Reynolds numbers and for different height-to-radius aspect ratios $\Gamma \in [0.5, 2.5]$. Visualizations based on Iriodin flakes have demonstrated that the first instability gives rise to stationary vortex patterns, the number of vortices increasing as $\Gamma$ decreases. The experimental thresholds are in good agreement with the numerical findings.[25] A survey of the subsequent flow states that take place for higher Reynolds numbers has been performed. In the particular case of $\Gamma = 2$, all flow states observed in the numerical simulations have been recovered except for a single state, the modulated traveling waves, which occur numerically in a very narrow range of Reynolds numbers.

For the first time, experimental evidence is given for the existence of robust heteroclinic cycles in this flow, as predicted by the numerical simulations of Nore *et al.*[19] for $\Gamma = 2$. This regime originates from a resonance between two stationary states, $m = 1$ and $m = 2$, in the presence of the $O(2)$ symmetry. It is worth pointing out that the existence of steady bifurcated states and heteroclinic cycles depends strongly on the exact counterrotation of the top and bottom disks. For a rotation ratio different from $-1$, the $O(2)$ symmetry would have been broken, and the system would have only kept the axisymmetry $SO(2)$. Therefore, the patterns would have generically rotated and the heteroclinic cycles would have been destroyed by this symmetry breaking, see, e.g., Porter and Knobloch.[29] The experimental setup used in the present study, where a single dc motor drives the two disks, constrains the rotation ratio to be exactly $-1$, thus allowing us to experimentally observe the steady bifurcated states and the heteroclinic cycles.

Perhaps the most interesting observation concerning the near-heteroclinic cycles is the broad distribution of the time spent in the vicinity of each unstable pure mode state and the excursions toward another pure mode favored by a geometrical imperfection. While for low Reynolds numbers approximately periodic oscillations are found, uneven periods are encountered as the Reynolds number is increased, showing increasing plateau durations followed by long relaxation phases toward the favored pure mode state. These oscillations differ from the strictly periodic near-heteroclinic cycles reported in the numerical simulations of Nore *et al.*[19] In our experimental realization of the von Kármán flow, both noise and geometrical defects, although weak, play a role in the observed irregular oscillations, and only further investigation can show which of the two is of primary importance.

## ACKNOWLEDGMENTS

This work was benefited from fruitful discussions with Yves Couder, Olivier Le Maître, Marc Rabaud, and Laurette Tuckerman and from very interesting suggestions from the referees.

[1] J. Guckenheimer and P. Holmes, "Structurally stable heteroclinic cycles," Math. Proc. Cambridge Philos. Soc. **103**, 189 (1988).
[2] M. Golubitsky, I. Stewart, and D. Schaeffer, *Singularities and Groups in Bifurcation Theory*, Applied Mathematics Sciences Vol. 69 (Springer, New York, 1988).
[3] M. Krupa and I. Melbourne, "Asymptotic stability of heteroclinic cycles in systems with symmetry," Ergod. Theory Dyn. Syst. **15**, 121 (1995).
[4] M. Krupa, "Robust heteroclinic cycles," J. Nonlinear Sci. **7**, 129 (1997).
[5] F. H. Busse and K. E. Heikes, "Convection in a rotating layer: A simple case of turbulence," Science **208**, 173 (1980).
[6] G. Küppers and D. Lortz, "Transition from laminar convection to thermal turbulence in a rotating fluid layer," J. Fluid Mech. **35**, 609 (1969).
[7] R. M. May and W. J. Leonard, "Nonlinear aspects of competition between three species," SIAM J. Appl. Math. **29**, 243 (1975).
[8] C. A. Jones and M. R. E. Proctor, "Strong spatial resonance and travelling waves in Bénard convection," Phys. Lett. A **121**, 224 (1987).
[9] M. R. E. Proctor and C. A. Jones, "The interaction of two spatially resonant patterns in thermal convection. Part 1. Exact 1:2 resonance," J. Fluid Mech. **188**, 301 (1988).
[10] D. Armbruster, J. Guckenheimer, and P. Holmes, "Heteroclinic cycles and modulated traveling waves in systems with O(2) symmetry," Physica D **29**, 257 (1988).
[11] S. Cox, "Mode interactions in Rayleigh-Bénard convection," Physica D **95**, 50 (1996).
[12] I. Mercader, J. Prat, and E. Knobloch, "Robust heteroclinic cycles in two-dimensional Rayleigh–Bénard convection without Boussinesq symmetry," Int. J. Bifurcation Chaos Appl. Sci. Eng. **12**, 2501 (2002).
[13] N. Aubry, P. Holmes, J. L. Lumley, and E. Stone, "The dynamics of coherent structures in the wall region of a turbulent boundary layer," J. Fluid Mech. **92**, 115 (1988).
[14] P. Holmes, J. L. Lumley, and G. Berkooz, *Turbulence, Coherent Structures, Dynamical Systems and Symmetry* (Cambridge University Press, Cambridge, 1996).
[15] I. G. Kevrekidis, B. Nicolaenko, and J. C. Scovel, "Back in the saddle again: A computer assisted study of the Kuramoto-Sivashinsky equation," SIAM J. Appl. Math. **50**, 760 (1990).
[16] Y. Hu, W. Pesch, G. Ahlers, and R. E. Ecke, "Convection under rotation for Prandtl numbers near 1: Küppers-Lortz instability," Phys. Rev. E **58**, 5821 (1998).
[17] E. Stone, M. Gorman, M. El Hamdi, and K. A. Robbins, "Identification of intermittent ordered patterns as heteroclinic connections," Phys. Rev. Lett. **76**, 2061 (1996).
[18] A. Palacios, G. H. Gunaratne, and M. Gorman, "Cellular pattern formation in circular domains," Chaos **7**, 463 (1997).
[19] C. Nore, L. S. Tuckerman, O. Daube, and S. Xin, "The 1:2 mode interaction in exactly counter-rotating von Kármán swirling flow," J. Fluid Mech. **477**, 51 (2003).
[20] F. Marques, J. M. Lopez, and J. Shen, "Mode interactions in an enclosed swirling flow: A double Hopf bifurcation between azimuthal wavenumbers 0 and 2," J. Fluid Mech. **455**, 263 (2002).
[21] J. M. Lopez, J. E. Hart, F. Marques, S. Kittelman, and J. Shen, "Instability and mode interactions in a differentially driven rotating cylinder," J. Fluid Mech. **462**, 383 (2002).
[22] F. Marques, A. Yu. Gelfgat, and J. M. Lopez, "Tangent double Hopf bifurcation in a differentially rotating cylinder flow," Phys. Rev. E **68**, 016310 (2003).
[23] F. Moisy, O. Doaré, T. Pasutto, O. Daube, and M. Rabaud, "Experimental and numerical study of the shear layer instability between two counter-rotating disks," J. Fluid Mech. **507**, 175 (2004).
[24] J. M. Lopez and F. Marques, "Mode competition between rotating waves in a swirling flow with reflection symmetry," J. Fluid Mech. **507**, 265 (2004).
[25] C. Nore, M. Tartar, O. Daube, and L. S. Tuckerman, "Survey of instability thresholds of flow between exactly counter-rotating disks," J. Fluid Mech. **511**, 45 (2004).
[26] P. Coullet and G. Iooss, "Instabilities of one-dimensional cellular patterns," Phys. Rev. Lett. **64**, 866 (1990).
[27] Comparisons with the numerical computations [see Fig. 16(c) in the paper of Nore *et al.* (Ref. 19)] allow us to further identify the orientation of the observed states $P$ and $P'$. The velocity field of the state $P$ [Fig. 11(a)] shows a unique hyperbolic point at the center $(x,z)=(0,0)$, indicating that the two peripherical hyperbolic points $H$ and $H^*$ are close to the PIV plane where the measurements are performed [see Fig. 12(a)]. On the other hand, two hyperbolic points can be seen near the cylinder axis for the state $P'$ [Fig. 11(c)], indicating that the PIV plane now cuts through the two elliptic points $E$ and $E^*$ [see Fig. 12(c)].
[28] E. Stone and P. Holmes, "Random perturbations of heteroclinic attractors," SIAM J. Appl. Math. **50**, 726 (1990).
[29] J. Porter and E. Knobloch, "Dynamics in the 1:2 spatial resonance with broken reflection symmetry," Physica D **201**, 318 (2005).

# Chapitre 2

# Ondes d'inertie

## 2.1 Introduction

Un écoulement en rotation permet la propagation d'ondes d'un type particulier, appelées "ondes d'inertie" ou "ondes gyroscopiques" [28, 65, 75, 49]. Ces ondes transverses, dispersives et anisotropes, jouent un rôle fondamental dans les écoulements géophysiques et astrophysiques, et constituent pour cette raison un sujet d'étude majeur en mécanique des fluides. Elles partagent un certain nombre de similitudes avec les ondes internes, qui se propagent dans les fluides stratifiés [135, 75]. Dans les écoulements océaniques, les effets de la rotation sont en général couplés à la dynamique de la surface libre, comme dans le cas des marées, ou bien à la stratification, conduisant alors à un système d'ondes mixtes gravito-inertielles[1]. La figure 2.1 illustre la manifestation de telles ondes dans le phénomène de marée interne quasi-inertielle (de période proche de celle d'une onde inertielle pure à la latitude considérée). Le déferlement de ces ondes joue potentiellement un rôle important dans les processus de mélange et dans l'équilibre thermique global des océans.

Bien que l'effet de la rotation de la terre soit secondaire comparé à celui de la stratification dans la plupart des situations d'intérêt géophysique, la dynamique des ondes inertielles constitue en soi un sujet d'étude fondamental. Leur compréhension est essentielle pour le problème de la turbulence en rotation, qui fera l'objet du chapitre suivant. C'est d'ailleurs là que se trouve notre motivation initiale pour l'étude des ondes d'inertie. En effet, dans la limite d'une forte rotation d'ensemble (faible nombre de Rossby), un écoulement turbulent en rotation peut se décrire comme un système d'ondes d'inertie aléatoires en interaction faible, dans un état dit de "turbulence d'onde" [58, 23]. L'anisotropie des transferts d'énergie en turbulence en rotation, et la dynamique quasi-bidimensionelle qui en résulte, trouvent leur origine dans le caractère anisotrope de la relation de dispersion des ondes d'inertie [19].

Cette étude expérimentale sur les ondes d'inertie a débuté en 2006, par une première série d'expériences réalisées sur une petite plateforme tournante, avec L. Messio, C. Morize et M. Rabaud [86]. Dans cette première expérience, une onde d'inertie conique est générée par l'oscillation verticale d'un disque dans un cylindre en rotation, et les mesures par PIV sont effectuées dans des plans horizontaux. Cette étude s'est poursuivie en 2009 avec P.-P. Cortet et C. Lamriben, grâce à la nouvelle plateforme tournante "Gyroflow", permettant d'accéder cette fois-ci à la structure verticale de l'écoulement, sur des champs de vision de taille bien

[1] On peut encore citer le cas des ondes "MAC" (Magnetic - Archimedean - Coriolis) dans les fluides conducteurs et stratifiés en rotation, pertinentes dans les étoiles et dans le noyau liquide des planètes.

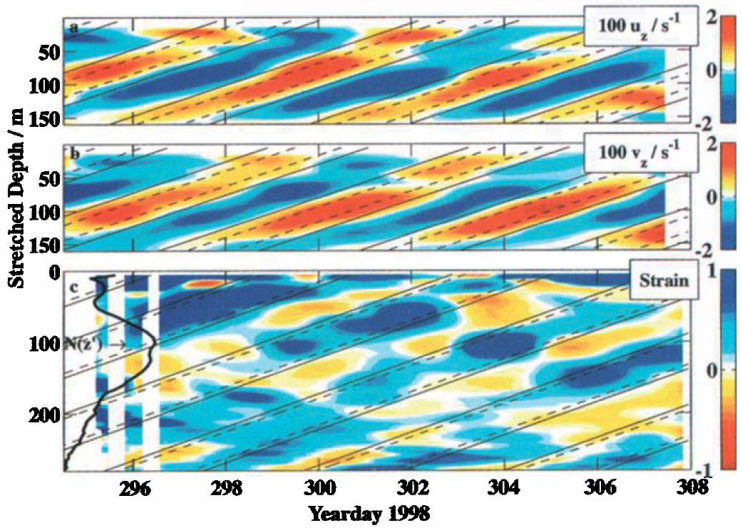


FIG. 2.1 – Vitesse et déformation mesurées en mer de Banda en Indonésie, d'après Alford & Cregg (2001) [2]. On voit une onde de marée interne quasi-inertielle, de période 4.4 jours, se propageant vers la surface.

plus importante [36]. Cette nouvelle expérience a permis une description fine de la structure d'un faisceau plan d'onde d'inertie, et plus particulièrement une comparaison quantitative du déclin de l'onde avec une solution de similitude décrivant les effets de la viscosité.

Dans la suite de ce chapitre, nous décrirons brièvement les propriétés de dispersion anisotrope des ondes d'inertie, en les comparant au cas des ondes internes. Les solutions de similitude dans le cas d'un faisceau d'onde généré par une source localisée seront ensuite présentées, les détails étant donnés dans l'article Cortet *et al.* (2010) [36] en annexe. Nous conclurons sur quelques pistes de recherche futures, incluant le problème de la dérive de Stokes et les effets non linéaires (instabilité paramétrique et déferlement d'ondes d'inertie), en connection avec le chapitre suivant sur la turbulence en rotation.

## 2.2 Position du problème

### 2.2.1 Régimes d'écoulements soumis à une rotation d'ensemble

Il est instructif pour commencer d'examiner les différents cas limites pouvant être déduits d'une analyse dimensionelle de l'équation de Navier-Stokes exprimée dans un référentiel tournant, de vecteur de rotation $\mathbf{\Omega} = \Omega \mathbf{e}_z$ :

$$\partial_t \mathbf{u} + (\mathbf{u} \cdot \nabla)\mathbf{u} = -\frac{1}{\rho}\nabla p - 2\mathbf{\Omega} \times \mathbf{u} + \nu \nabla^2 \mathbf{u} \tag{2.1}$$

(où la pression $p$ inclut la force centrifuge, $\frac{1}{2}\rho(\mathbf{\Omega} \times \mathbf{r})^2$). On adimensionne les différents termes de cette équation par les échelles caractéristiques de vitesse $U$, de longueur $L$, de temps $T$ et, en anticipant le régime d'équilibre géostrophique dans la limite de forte rotation, de pression $\rho \Omega U L$. L'équation (2.1) devient

$$Ro_T \partial_t \mathbf{u}^* + Ro(\mathbf{u}^* \cdot \nabla)\mathbf{u}^* = -\nabla p^* - \mathbf{e}_z \times \mathbf{u}^* + RoRe^{-1}\nabla^2 \mathbf{u}^*, \tag{2.2}$$

où l'on a introduit le nombre de Reynolds $Re = UL/\nu$, le nombre de Rossby $Ro = U/2\Omega L$ et le nombre de Rossby temporel, $Ro_T = 1/2\Omega T$. Le choix usuel $T = U/L$ conduit à confondre les 2 nombres de Rossby, mais il convient de les distinguer ici, si l'on souhaite examiner séparément les effets linéaires (ondes d'inertie sans intéraction) et non-linéaires (turbulence d'onde).

Les différents régimes d'écoulements que l'on peut lire de l'équation (2.2) sont :

1. $Ro \ll 1$, $Ro_T \ll 1$ et $Re \gg Ro$ : équilibre géostrophique, qui conduit au théorème de Taylor-Proudman (Sec. 2.2.3).
2. $Ro \ll 1$ et $Ro_T \leq 1$ : petites oscillations (linéaires) autour de l'équilibre géostrophique, donnant lieu à des ondes propagatives (ce chapitre).
3. $Ro \simeq Ro_T <$ ou $\simeq O(1)$ et $Re \gg 1$ : régime de "turbulence d'ondes", faiblement non-linéaire, ou de "turbulence en rotation", fortement non-linéaire (chapitre 3).

A noter que la présence de confinement fait intervenir une échelle de longueur supplémentaire, $H$, qui introduit un nouveau nombre sans dimension, usuellement le nombre d'Ekman, $Ek = \nu/2\Omega H^2 = (L/H)^2\, Ro\, Re^{-1}$. L'échelle $H$ pertinente est ici la dimension le long de l'axe de rotation, et l'on voit qu'un nouveau temps caractéristique associé à ce confinement apparait : il s'agit du temps d'Ekman, $T_E = H/(\nu\Omega)^{1/2}$, qui intervient classiquement dans le problème de la mise en rotation d'un fluide (spin-up) [65].

### 2.2.2 Stabilité de la rotation solide

Comme nous l'avons déjà évoqué au § 1.2.1, une rotation d'ensemble a en général un effet stabilisant sur un écoulement, car l'équilibre entre force centrifuge et gradient de pression centripète est un équilibre stable. Une perturbation de cet équilibre conduit en effet, en l'absence de dissipation, à une oscillation de pulsation propre $2\Omega$, dont l'origine physique est la conservation du moment cinétique (dans le référentiel fixe) ou, de façon équivalente, la manifestation de la force de Coriolis comme "force de rappel" (dans le référentiel tournant). Dans toute la suite, par commodité, nous raisonnerons dans le référentiel tournant uniquement.

L'incompressibilité du fluide fait que l'oscillation considérée n'est pas locale, mais mobilise un continuum de particules fluides. Ces particules effectuent à l'unisson un mouvement de translation circulaire "anticyclonique", c'est-à-dire opposé au sens de rotation du référentiel, mais ne sont pas en rotation (la composante de la vorticité normale au plan d'oscillation est nulle).

### 2.2.3 Théorème de Taylor-Proudman

Un résultat clef des écoulements en rotation est le **théorème de Taylor-Proudman** [28, 49], qui établit que les champs de vitesse et de pression d'un écoulement lent dans un référentiel tournant à vitesse angulaire $\mathbf{\Omega} = \Omega \mathbf{e}_z$ doivent être invariants par translation le long de l'axe de rotation $\mathbf{e}_z$ : l'écoulement est bidimensionnel (2D).

Une erreur d'interprétation fréquente de ce théorème consiste à en déduire que cet écoulement à 2 dimensions est également à 2 composantes (2C-2D). Cependant, la "3ème composante" $u_z$ n'est pas nulle *a priori*, mais découle des conditions aux limites et/ou des conditions intiales. Ainsi, un écoulement de Taylor-Proudman est en général un écoulement "3C-2D", dont la dynamique est purement bidimensionelle. Dans un tel écoulement, le champ de vitesse vertical $u_z(x, y, t)$ est régi par l'équation d'évolution d'un champ scalaire passif advecté par l'écoulement 2D horizontal $(u_x, u_y)$, à la manière du champ de concentration d'un colorant.

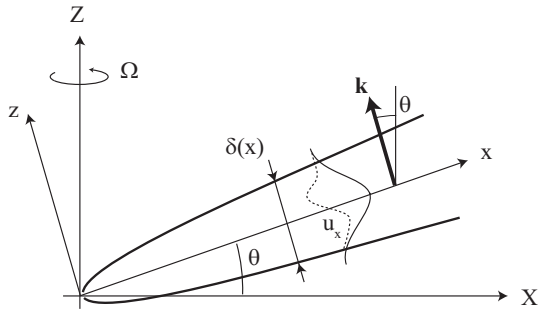


FIG. 2.2 – Géométrie d'un faisceau d'onde localisé, et référentiel local $(x, z)$ dans lequel est effectuée l'analyse d'écoulement quasi-parallèle. Le profil de vitesse pointillé ne représente que la composante $u_x$ de la vitesse ; il existe une composante perpendiculaire $u_y$, tel que le vecteur $\mathbf{u}$ décrive un cercle anticyclonique dans le plan incliné $(x, y)$. La viscosité induit un épaississement du faisceau en $\delta(x) \sim x^{1/3}$.

Le confinement vient en général contraindre cet écoulement 3C-2D. Dans le cas d'un fluide parfait, en présence de parois horizontales, la condition de vitesse nulle aux parois impose $u_z = 0$ dans tout l'écoulement, et donc un écoulement 2C-2D (à noter que cette condition n'est plus strictement valable pour un fluide visqueux : l'existence de couches limites induit une vitesse verticale non nulle, $u_z = \delta_E \omega_z$, avec $\delta_E = (\nu/\Omega)^{1/2}$ : c'est le pompage d'Ekman [65]). Cependant, l'effet du confinement agit sur un temps caractéristique donné par le temps d'Ekman $T_E$ (voir § 2.2.1). Si celui-ci est grand comparé au temps d'instationarité $T$, la limite d'écoulement non confiné peut être considérée de façon transitoire, et la solution générale 3C-2D de Taylor-Proudman est alors pertinente. Cette subtilité prendra toute son importance dans le chapitre suivant au sujet de la transition 3D → 2D d'une turbulence en rotation.

### 2.2.4 Ondes d'inertie

Le théorème de Taylor-Proudman ne s'applique que pour des mouvements relatifs lents : cela signifie que les temps caractéristiques associés aux instationnarités $(u/(\partial u/\partial t) \simeq O(T))$ et aux non-linéarités $(u/(\mathbf{u}\nabla u) \simeq O(L/U))$ sont tous deux négligeables par rapport à $T_\Omega = (2\Omega)^{-1}$ (soit $Ro \ll 1$ et $Ro_T \ll 1$). Si tel n'est pas le cas, on obtient alors un système d'ondes d'inertie dès lors que $Ro_T \leq 1$, compatible avec le théorème de Taylor-Proudman dans la limite $Ro_T \to 0$.

Pour comprendre le caractère anisotrope des ondes d'inertie, partons d'une particule test animée d'un mouvement périodique de pulsation $\sigma < 2\Omega$. Défléchie à angle droit par la force de Coriolis, cette particule sera animée d'un mouvement de translation circulaire, mais cette fois-ci selon un plan oblique, car son accélération $\sigma u$ doit être compensée par la composante de la force de Coriolis dans ce plan, $2\Omega u \cos\theta$, avec $\theta$ l'angle entre la verticale et la normale à ce plan[2].

Ces ondes transverses (en conséquence de l'incompressibilité) et circulaires, polarisées de façon anticyclonique, sont gouvernées par la relation de dispersion

$$\sigma = 2\Omega \frac{k_z}{|\mathbf{k}|} = 2\Omega \cos\theta, \tag{2.3}$$

[2]Il en va de même pour un pendule de Foucault, dont le plan d'oscillation fait un tour complet en $T_\Omega = 1$ jour au pôle Nord, mais en un temps supérieur $T_\Omega / \cos\theta$ en tout autre point (et infini à l'Equateur).

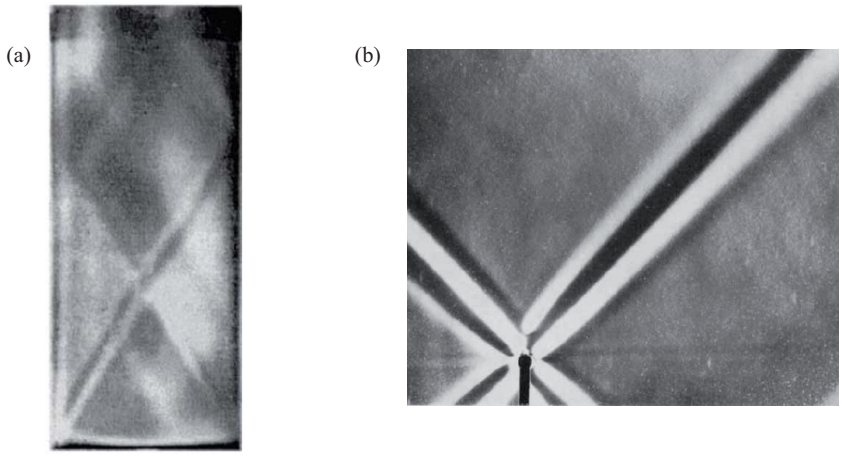


FIG. 2.3 – (a) Ondes d'inertie présentant des réflections multiples dans un cylindre en rotation, visualisées par paillettes réfléchissantes. D'après McEwan (1970) [84]. (b) Faisceau d'onde interne en fluide stratifié, émis par un cylindre horizontal vibré verticalement, et visualisé par la méthode de strioscopie (schlieren). D'après Thomas & Stevenson (1972) [130].

où $\theta$ est l'angle entre l'axe de rotation selon $z$ et le vecteur d'onde $\mathbf{k}$ (fig. 2.2). Un certain nombre de propriétés remarquables se déduisent de cette relation de dispersion :

1. Elles sont anisotropes : leur direction de propagation dépend de leur pulsation.
2. Elles sont dispersives : Leur vitesse de phase $\sigma/k$ est fonction de $k$.
3. Leur vitesse de phase ($\mathbf{c} = \sigma\mathbf{k}/|\mathbf{k}|^2$) et leur vitesse de groupe ($\mathbf{c}_g = \nabla_k\sigma$) sont perpendiculaires[3].
4. Enfin, une fréquence de forçage ne sélectionne pas de longueur d'onde. Les longueurs d'ondes excitées sont donc données par la géométrie du forçage, ou bien par l'échelle de longueur visqueuse.

Pour une onde générée par une perturbation localisée, le paquet d'onde aura une géométrie conique pour une source ponctuelle, ou bien en "croix de St. André" (selon la terminologie usuelle pour les ondes internes [106]) pour une source linéaire horizontale. La figure 2.3(a) illustre un tel motif conique, présentant des réflections multiples dans une cavité cylindrique [84].

### 2.2.5 Ondes d'inertie vs. ondes internes

Il est intéressant de noter la grande proximité entre la relation de dispersion des ondes d'inertie (2.3) et celle des ondes internes en fluide stratifiée,

$$\sigma = N \sin\theta, \tag{2.4}$$

où $N = (-(g/\rho)\partial\rho/\partial z)^{1/2}$ est la fréquence de Brunt-Väisälä [106, 130], qui correspond à la pulsation propre d'oscillation des particules fluides soumises à la force de flottaison. Si les

[3]Cette propriété est une conséquence générique d'une relation de dispersion indépendante de $|\mathbf{k}|$ : la vitesse de groupe est normale aux surfaces iso-$\sigma$, lesquelles sont des cônes contenant le vecteur d'onde, et donc la vitesse de phase.

propriétés de dispersion anisotrope de ces deux systèmes d'onde sont similaires [135, 75] (voir la figure 2.3b), la proximité entre les équations (2.3) et (2.4) peut être toutefois trompeuse. En effet, dans la limite de mouvements très lents ($\sigma \to 0$), les ondes inertielles se ramènent à une structuration de type *cigare* (conformément au théorème de Taylor-Proudman), i.e. des objets 1D vivant dans un espace 2D, tandis que les ondes internes se ramènent à une structuration de type *pancake*, i.e. des objets 2D vivant dans un espace 1D. Cette différence topologique est fondamentale, et ne permet pas en particulier de décrire de façon équivalente les états de turbulence d'onde de ces deux systèmes [19].

En raison de leur grande importance dans les écoulements géophysiques, les ondes internes ont été abondamment étudiées, à la fois théoriquement (voir Voisin (2003) [136] pour une bibliographie extensive) et en laboratoire [125, 63]. Une autre raison peut expliquer le déséquilibre entre la littérature abondante sur les ondes internes et celle plus restreinte sur les ondes d'inertie : les mesures en fluide stratifié sont plus aisées à mettre en œuvre qu'en référentiel tournant. Plus spécifiquement, il est possible de caractériser le champ de densité directement de manière optique pour un fluide stratifié (méthode de strioscopie, ou plus récemment de "synthetic Schlieren" [125, 39]), tandis que seule une mesure de vitesse par PIV est possible pour les ondes d'inertie.

## 2.3 Expériences

Deux plateformes tournantes ont été utilisées pour cette étude, que nous nous contentons de décrire brièvement ici. Ce sont ces deux mêmes plateformes qui sont utilisées pour les expériences de turbulence en rotation décrites au chapitre 3. Nous appelerons ces deux plateformes "petite" et "moyenne", par comparaison à la "grande" plateforme Coriolis, à Grenoble, dont il sera question au chapitre 3.

### 2.3.1 La "petite" plateforme tournante

La "petite" plateforme est un anneau circulaire de 80 cm de diamètre, sur lequel est posé une cuve parallélépipédique en verre, de 35 cm de coté et 55 cm de hauteur (figure 2.4). La vitesse angulaire maximale est de 0.7 Hz, et la charge embarquée maximale de l'ordre de 100 kg. La particularité de cette plateforme est d'offrir un accès optique par le dessous, permettant d'utiliser facilement l'accès supérieur pour effectuer le mouvement de translation du générateur d'onde (ce chapitre), ou de la grille (chapitre suivant). Une description plus détaillée de cette petite plateforme peut être trouvée dans Morize (2006) [101].

La petite taille de cette plateforme tournante restreint les mesures de PIV à des champs horizontaux. En effet, sur cette plateforme la caméra est située sous la cuve, et est embarquée dans le référentiel tournant, tandis que la nappe laser est émise d'un laser situé dans le référentiel fixe.

Les expériences d'ondes d'inertie réalisées sur cette petite plateforme sont décrites dans l'article Messio *et al.* (2008) [86]. Le dispositif expérimental monté sur cette plateforme est strictement axisymétrique : la cuve utilisée est circulaire, tandis que la source de l'onde est un disque de 2.1 cm de diamètre centré sur l'axe de rotation. Ainsi, le paquet d'onde a une forme conique, et les champs de PIV horizontaux mesurés à une certaine distance sous la source intersectent ce cône sous forme d'un anneau où se concentre l'énergie de l'onde (figure 2.6a).

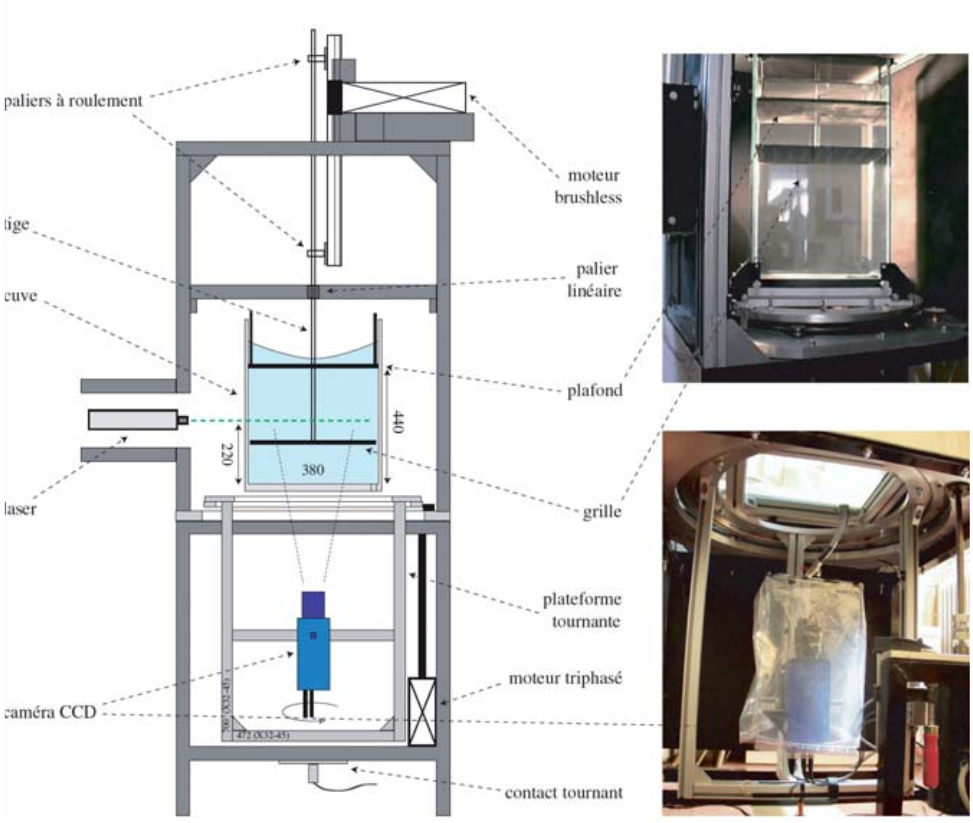


FIG. 2.4 – Schéma et photos de la "petite" plateforme tournante. D'après Morize (2006) [101].

### 2.3.2 Gyroflow (la "moyenne" plateforme tournante)

"Gyroflow" est une nouvelle plateforme tournante, qui a été concue en 2008, et a été réalisée et livrée au FAST au printemps 2009 (figure 2.5). Cette plateforme est un plateau optique polyvalent de 2 m de diamètre, capable d'embarquer jusqu'à 1 tonne d'expérience en rotation, à une vitesse angulaire maximale de 0.5 Hz[4]. Une spécificité de cette plateforme est sa grande stabilité mécanique : selon la charge embarquée, la constance de la vitesse angulaire $\Delta\Omega/\Omega$ est assurée entre 2 et $5 \times 10^{-4}$. Un ordinateur embarqué, piloté à distance via un collecteur tournant, permet l'acquisition des images ainsi que le pilotage du laser dans le référentiel tournant.

L'intéret majeur d'une plateforme de grande dimension est de pouvoir embarquer un système de PIV complet, source laser incluse, et ainsi de réaliser des mesures selon des plans d'orientation quelconque, sans limitation sur la taille des champs, avec un très bon rapport signal/bruit. Cette possibilité d'accéder aux vitesses dans le plan vertical est mise à profit ici pour les ondes d'inertie, et le sera plus encore au chapitre suivant pour l'étude de la structuration verticale de la turbulence en rotation.

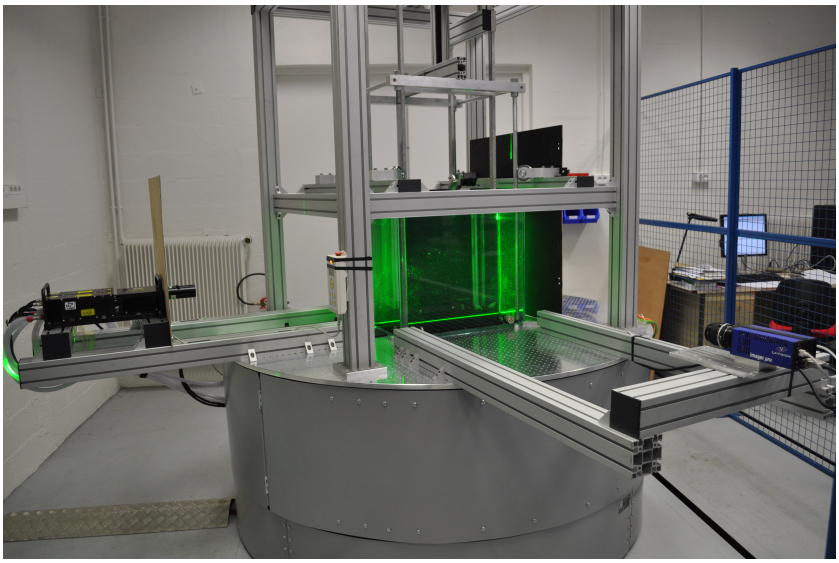

FIG. 2.5 – La plateforme tournante "Gyroflow", installée au FAST en 2009. Sur cette image on voit le laser pulsé embarqué (à gauche), et une caméra PIV (à droite).

### 2.3.3 Effets visqueux - solutions de similitude

Les expériences présentées ci-après visent à caractériser l'étalement diffusif d'un faisceau d'onde d'inertie localisé. Si l'atténuation d'une onde d'inertie monochromatique par l'effet de la viscosité donne classiquement lieu à un déclin temporel exponentiel, l'effet de la viscosité sur un faisceau d'onde localisé est plus subtil.

Deux situations ont été examinées : une onde conique générée par une source ponctuelle sur la "petite" plateforme [86], et une onde bidimensionelle en "croix de Saint André" générée par une source linéaire sur la plateforme Gyroflow [36]. Dans le premier cas, l'atténuation de l'onde est de nature à la fois géométrique et visqueuse, tandis qu'elle est purement visqueuse dans le second cas. Pour cette raison, nous ne décrirons ici que la géométrie bidimensionnelle, la plus simple pour comparaison avec les solutions de similitude de ce problème.

Dans le cas d'un forçage localisé dans l'espace, un spectre large de vecteurs d'onde est excité, dont l'orientation est prescrite par la relation de dispersion. En l'absence de viscosité, l'interférence entre tous les plans oscillants associés à ces vecteurs d'onde s'annulent, sauf en un plan unique décrivant une oscillation circulaire anticyclonique. En présence de viscosité, une dissipation de l'onde va intervenir, en raison du cisaillement entre les plans oscillants. A mesure que l'énergie se propage, les plus grands nombres d'onde sont atténués en premier, et le spectre se concentre sur les nombres d'onde les plus petits, conduisant à un élargissement du faisceau (figure 2.2).

On peut montrer que l'atténuation de l'onde suit alors une loi de puissance, résultant de la combinaison des atténuations exponentielles des différentes composantes de Fourier de l'onde. Cet élargissement peut se retrouver de façon qualitative, en considérant que pendant un temps $t$, l'énergie va se propager sur une distance $x = c_g t$, avec la vitesse de groupe donnée par $c_g = (\sigma/k)\tan\theta \simeq \sigma\delta\tan\theta$, et $\delta$ l'échelle transverse caractéristique. Pendant ce même temps $t$, l'énergie va être diffusée latéralement, sur une distance $\delta \simeq \sqrt{\nu t}$. En égalisant ces temps de

[4]Une vidéo de cette plateforme est disponible sur la page `www.fast.u-psud.fr/gyroflow` .

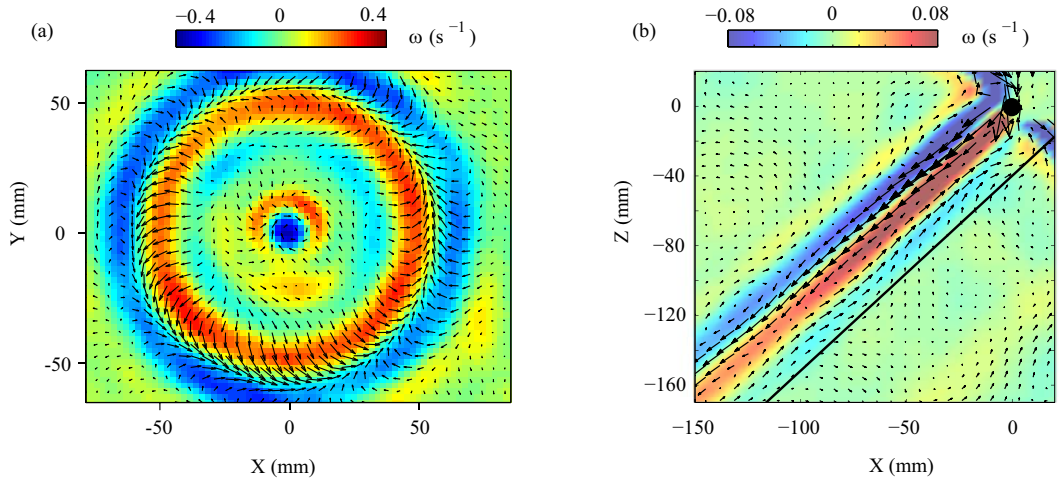


FIG. 2.6 – Champs de vitesse et de vorticité (couleur) d'une onde d'inertie émise par l'oscillation verticale d'un disque (a) ou d'un cylindre horizontal (b). (a), Coupe horizontale du paquet d'onde conique, conduisant à un anneau (d'après Messio *et al.* (2008) [86]). (b), Coupe verticale du paquet d'onde en "croix de St. André" (d'après Cortet *et al.* (2010) [36]).

propagation longitudinale et de diffusion latérale, on obtient l'épaississement (fig. 2.2)[5] :

$$\delta(x) \simeq \left(\frac{\nu x}{\sigma \tan\theta}\right)^{1/3}. \tag{2.5}$$

Dans le cas d'une onde interne en fluide stratifiée, une solution de simulitude pour cet étalement visqueux a été donnée dans l'article fondateur de Thomas & Stevenson (1972) [130] (voir aussi Peat (1978) [111] pour l'extension au cas d'une onde en milieu tournant et stratifié). L'adaptation de ce calcul au cas d'un faisceau d'onde d'inertie est présentée dans l'article Cortet *et al.* (2010) [36] (en annexe de ce mémoire), et nous nous contentons d'en donner ici les grandes lignes.

Le point de départ est identique à celui de Thomas & Stevenson (1972) [130] pour les ondes internes, à savoir l'hypothèse d'écoulement quasi-parallèle de type "couche limite" dans le faisceau d'onde. En introduisant l'échelle de longueur visqueuse

$$\ell = \left(\frac{\nu}{\sigma \tan\theta}\right)^{1/2}, \tag{2.6}$$

où $\theta$ est l'angle sélectionné par la relation de dispersion à pulsation $\sigma$ donnée, il est possible d'exprimer les profils de vitesse et de vorticité dans l'épaisseur du faisceau sous la forme autosimilaire

$$u_0(x,\eta) = U_0^* \frac{E_0(\eta)}{E_0(0)} \left(\frac{\ell}{x}\right)^{1/3} \qquad \omega_0(x,\eta) = W_0^* \frac{E_1(\eta)}{E_1(0)} \left(\frac{\ell}{x}\right)^{2/3}, \tag{2.7}$$

où l'on introduit la coordonnée réduite $\eta = z/x^{1/3}\ell^{2/3}$. Ici, un système de coordonnées local $(x,z)$ est utilisé, tel que $x$ est le long du faisceau et $z$ est transverse. On a introduit la famille d'enveloppe $E_m(\eta)$, avec $m = 0$ pour la vitesse et $m = 1$ pour la vorticité, dont les expressions

[5] Le même argument permet de retrouver l'épaississement classique $\delta(x) \simeq (\nu x/U)^{1/2}$ d'une couche limite laminaire sur une plaque plane, en raisonnant sur la vitesse de l'écoulement $U$ au lieu de la vitesse de groupe.

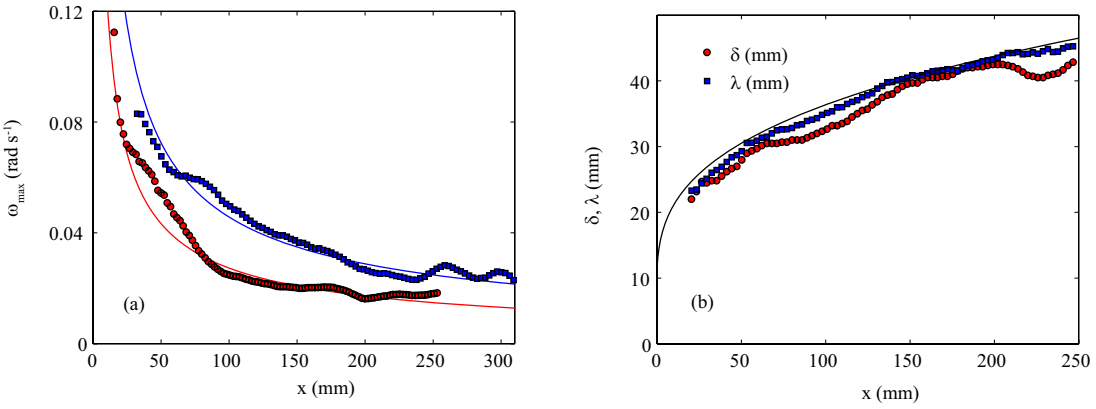


FIG. 2.7 – Diffusion visqueuse d'un faisceau d'onde d'inertie. (a) Déclin du maximum de l'enveloppe de vorticité pour 2 valeurs de la vitesse angulaire $\Omega$, et comparaison avec la prédiction en $x^{-2/3}$. (b) Largeur à mi-hauteur de l'enveloppe de vorticité ($\delta$), longueur d'onde apparente ($\lambda$), et comparaison avec la solution de similitude (2.8) incluant l'effet de taille finie de la source (d'après Cortet *et al.* (2010) [36]).

| $m$ | Décroissance de l'enveloppe | Spectre | Onde interne | Onde d'inertie |
|---|---|---|---|---|
| 0 | $1/\eta$ | $K^0 e^{-K^3}$ | pression | vitesse |
| 1 | $1/\eta^2$ | $K^2 e^{-K^3}$ | vitesse | vorticité |
| 2 | $1/\eta^3$ | $K^4 e^{-K^3}$ | vorticité | - |

TAB. 2.1 – Correspondance entre les solutions de similitude pour le problème des ondes internes et des ondes d'inertie. Le nombre d'onde adimensionné $K$ est donné par $k\ell^{2/3}x^{1/3}$.

analytiques sont données en annexe de l'article [36]. La largeur a mi-hauteur du faisceau suit la loi

$$\delta(x) \simeq 6.84\,\ell \left(\frac{x}{\ell}\right)^{1/3}, \tag{2.8}$$

en accord avec la loi qualitative (2.5). Une correction à cette loi pour tenir compte de la taille finie de la source est également proposée dans l'article.

La figure 2.7 montre les mesures expérimentales des maxima d'enveloppe de vorticité ainsi que de largeur de faisceau. Un excellent accord avec les lois de puissance (2.7) et (2.8) est obtenu ; les oscillations observées autour de la tendance en loi de puissance proviennent de la déformation du faisceau principal due à une interférence avec des faisceaux secondaires réfléchis.

Si l'étalement du faisceau décrit par l'équation (2.8) est le même pour les ondes internes et pour les ondes d'inertie, l'enveloppe des champs physiques est décallée d'un ordre de dérivation (i.e., $m \to m+1$) entre ces deux systèmes d'onde. Le tableau 2.1 résume cette correspondance : on voit que le rôle joué par la pression et la vitesse pour les ondes internes est joué par la vitesse et la vorticité respectivement pour les ondes d'inertie. Cette correspondance montre que le champ de vitesse d'une onde d'inertie est beaucoup plus "large bande" que celui d'une onde interne.

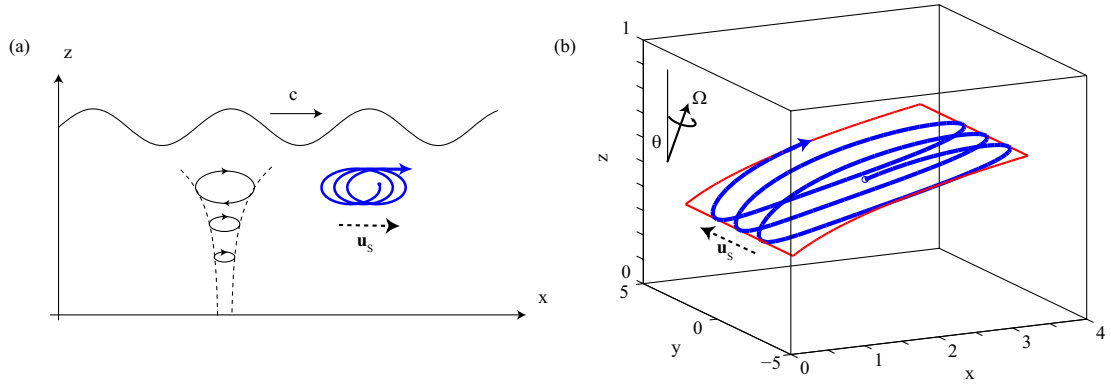


FIG. 2.8 – Phénomène de dérive de Stokes. (a) Situation usuelle de dérive pour une onde de surface. La variation verticale de l'amplitude de vitesse induit une dérive horizontale $\mathbf{u}_s$, dans la direction de la vitesse de phase (selon $x$). (b) Dérive de Stokes dans un faisceau d'onde d'inertie, obtenue par intégration numérique des solutions de similitude [36]. Le système d'axes $(x, y, z)$ est incliné de telle sorte que l'onde est générée par une source linéaire selon $y$, et se propage selon $x$. La trajectoire des particules fluides est comprise dans une surface d'équation $z \propto \ell^{2/3} x^{1/3}$, où $\ell$ est l'épaisseur de diffusion visqueuse, et la dérive $\mathbf{u}_s$ apparait dans la direction $y > 0$.

## 2.4 Perspectives

### 2.4.1 Dérive de Stokes

Une propriété classique commune aux systèmes d'onde présentant une inhomogénéité spatiale est l'existence d'un transport de masse par le mécanisme de "dérive de Stokes" [78]. L'origine de ce mécanisme est une asymétrie, entre un "aller" et un "retour" de l'oscillation, dans la trajectoire d'une particule fluide advectée par un champ d'onde variant spatialement. Bien que présente dans l'approximation linéarisée de l'onde, cette dérive est un phénomène intrinsèquement non-linéaire (la vitesse de dérive varie comme le carré de l'amplitude de l'onde), provenant de l'intégration Lagrangienne du champ d'onde Eulérien oscillant de moyenne nulle.

Le phénomène de dérive de Stokes se manifeste classiquement pour les ondes de surface, par exemple dans le cas de la houle [77]. Dans l'approximation de fluide parfait, l'amplitude de l'onde décroît exponentiellement avec la profondeur, selon une échelle caractéristique donnée par la longueur d'onde. Il en résulte une dérive horizontale, dans la direction donnée par la vitesse de phase (figure 2.8a).

Bien que ce phénomène de dérive soit usuellement de faible amplitude, son existence peut avoir un rôle important. Dans le contexte des ondes internes, ce courant de dérive peut contribuer significativement au transport de traceurs (nutriments par exemple) dans l'océan au voisinage d'un changement de topographie. Dans le cas d'une onde interne monochromatique, aucune dérive ne peut exister, du fait de la nature rectiligne de la trajectoire des particules. En revanche, l'existence d'une telle dérive pour un faisceau d'onde interne localisé, tel que celui décrit par la solution de similitude de Thomas & Stevenson (1972) [130], est encore un problème ouvert [50].

Le problème de la dérive de Stokes pour les ondes d'inertie est en fait beaucoup plus simple, car les trajectoires des particules fluides sont approximativement circulaires, comme dans le cas de la houle. Ainsi, une attenuation de l'amplitude dans une direction doit donner lieu à une dérive dans la direction perpendiculaire (figure 2.8b). Dans la géométrie bidimensionnelle

étudiée ici, l'atténuation de l'onde selon la direction $x$ (direction de la vitesse de groupe) doit s'accompagner d'une dérive selon $y$ (le long du cylindre oscillé). D'une manière générale, la dérive est attendue selon la direction donnée par $\mathbf{\Omega} \times \mathbf{c}_g$, ce qui correspond à un contournement cyclonique de la source de l'onde [36]. De façon remarquable, contrairement au cas de la houle, la dérive ici est normale à la fois à la vitesse de phase et à la vitesse de groupe.

Nos expériences préliminaires destinées à observer ce phénomène dans le cas d'un faisceau d'onde d'inertie localisé n'ont malheureusement pas été concluantes jusqu'à présent. La raison en est probablement la trop faible amplitude de l'onde générée par l'oscillation d'un cyclindre de petite taille. Une autre raison est que le signal de vitesse de cette dérive peut être facilement masqué par celui engendré par des effets de convection thermique résiduelle. En effet, même dans une pièce raisonablement thermalisée, des différences de température de l'ordre du dixième de degré sont très difficiles à éviter sur des volumes d'eau importants, notamment du fait de l'évaporation. Les mouvements de convection thermique qui en résultent sont de l'ordre de la fraction de mm $s^{-1}$, et constituent un bruit de fond difficile à supprimer.

Une telle dérive de Stokes n'est pas sans rappeler le phénomène de "vents zonaux", qui sont des courants à latitude constante dans l'atmosphère terrestre ou dans les planètes gazeuses [83]. Ces vents zonaux peuvent être décrits comme le résultat d'une interaction non-linéaire d'un mode d'inertie avec lui-même, mode excité par un phénomène de marée (interaction de type Terre-Lune) [131, 102], ou bien par la precession de l'axe de rotation. Un tel phénomène est un exemple d'"écoulement redressé" (*steady streaming*) [116], conduisant à une moyenne *eulérienne* non nulle. La possibilité d'une dérive de Stokes (lagrangienne), qui viendrait s'ajouter au phénomène découlement redressé (eulérien), est envisageable dans ce système, et n'a pas été examinée à notre connaissance.

### 2.4.2 Autres effets non linéaires

La dynamique des ondes d'inertie d'amplitude finie est un champ qui reste encore largement à explorer. Les phénomènes en jeu peuvent jouer un rôle important pour le problème de la turbulence en rotation, qui est le sujet du chapitre suivant, en particulier dans les situations de nombres de Rossby "petits mais pas trop".

Les effets non-linéaires peuvent être à l'origine d'une instabilité de cisaillement, similaire à l'instabilité classique de Kelvin-Helmholtz dans une couche de cisaillement [28], pouvant conduire à un déferlement de l'onde d'inertie. Sutherland (2006) [126] a caractérisé ce phénomène numériquement dans le cas d'une onde interne, mais le problème reste ouvert à notre connaissance dans la situation plus complexe du cisaillement tournant engendré par une onde d'inertie.

Le cas d'une couche de cisaillement alternatif unidimensionelle a été beaucoup étudié dans le contexte d'un fluide bi-couche, avec ou sans tension de surface (instabilité dite de *frozen wave*) [113]. Qualitativement, on peut s'attendre à ce qu'une oscillation ait un caractère stabilisant sur une couche de cisaillement. En effet, le temps caractéristique pour qu'un écoulement de cisaillement d'épaisseur $\delta$ devienne instable est $\delta/U$. Si la période d'oscillation est petite comparée à ce temps de croissance, soit $U/\sigma\delta \ll 1$ (ce qui correspond à un nombre de Rossby construit sur l'épaisseur du faisceau petit), alors l'instabilité n'aura pas le temps de se développer et sera inhibée à la demi-période suivante. En revanche, un autre phénomène peut prendre le relai, celui d'une instabilité paramétrique (réponse du système à une fréquence sous-harmonique du forçage ; voir aussi § 4.3.1). La pertinence d'un tel mécanisme pour les ondes d'inertie est un problème qui reste ouvert.

Enfin, un dernier phénomène non-linéaire reste à explorer, celui de l'asymétrie entre vorticité cyclonique et anticyclonique. Dans la limite de faible nombre de Rossby $Ro$ (mais à $Ro_T$ fini), le signe de la vorticité n'intervient pas. En revanche, à $Ro$ fini, le mécanisme non-linéaire d'étirement tourbillonnaire est plus prononcé pour la vorticité cyclonique qu'anticyclonique. En effet, dans un référentiel tournant, c'est la vorticité absolue $2\boldsymbol{\Omega} + \boldsymbol{\omega}$ qui est étirée par le gradient de vitesse, conduisant à un effet plus prononcé lorsque $\Omega$ et $\omega_Z$ sont de même signe (voir également le § 3.4.3). Les plans de phase d'une onde inertielle étant alternativement cycloniques et anticycloniques, une telle asymétrie devrait engendrer une modification de la structure du faisceau d'onde qui, à notre connaissance, n'a jamais été étudiée.

### 2.4.3 Génération d'ondes d'inertie non-linéaires

Une difficulté apparait pour l'étude expérimentale de ces différents effets non-linéaires partant d'un faisceau d'onde émis par une source localisée : étant donné le déclin de l'amplitude par diffusion visqueuse, les effets non-linéaires sont surtout attendus en amont du faisceau, dans la région précisément où la solution de similitude ne s'applique pas. Pour une telle étude, l'approche en similitude s'avère donc inopérante, et le traitement complet de l'écoulement au voisinage de la source devient nécessaire, ce qui complique notablement cette approche.

Une solution pourrait être celle d'un faisceau d'onde excité de façon globale et focalisé par une géométrie d'attracteur, comme exploré récemment par le groupe de L. Maas à l'Université d'Utrecht, à la fois pour les ondes d'inertie [83] et aussi récemment pour les ondes internes [66]. Dans un tel attracteur, la focalisation géométrique est compensée par la diffusion visqueuse, et l'amplitude du faisceau converge vers un état stationnaire après quelques réflexions. Le faisceau ainsi obtenu est d'amplitude homogène, ajustable par l'intensité du forçage, et peut constituer ainsi une configuration intéressante pour l'étude des effets non-linéaires évoqués ici.

Une autre solution, basée sur un générateur d'onde monochromatique localisé, permettrait également d'aborder les différents phénomènes non-linéaires évoqués ci-dessus. Une collaboration avec l'équipe de Thierry Dauxois (ENS Lyon), qui a développé un générateur d'onde monochromatique pour l'étude des ondes internes (Gostiaux *et al.* (2007) [64]), est envisagée. Ce générateur est constitué de plaques superposées, en translation circulaire avec un déphasage d'une plaque à l'autre, induisant ainsi des conditions aux limites proches de celles du champ de vitesse attendu dans l'onde. Un tel générateur, embarqué sur la plateforme Gyroflow, permettrait de générer un faisceau d'onde d'inertie monochromatique d'amplitude importante, et devrait ainsi permettre d'observer et de caractériser les phénomènes de dérive de Stokes, de déferlement et d'asymétrie cyclone-anticyclone dans ce système.

# Viscous spreading of an inertial wave beam in a rotating fluid

Pierre-Philippe Cortet,[a] Cyril Lamriben, and Frédéric Moisy
*Laboratoire FAST, CNRS UMR 7608, Université Paris-Sud, Université Pierre-et-Marie-Curie, Bât. 502, Campus Universitaire, 91405 Orsay, France*

(Received 23 March 2010; accepted 3 August 2010; published online 30 August 2010)

We report experimental measurements of inertial waves generated by an oscillating cylinder in a rotating fluid. The two-dimensional wave takes place in a stationary cross-shaped wavepacket. Velocity and vorticity fields in a vertical plane normal to the wavemaker are measured by a corotating particle image velocimetry system. The viscous spreading of the wave beam and the associated decay of the velocity and vorticity envelopes are characterized. They are found in good agreement with the similarity solution of a linear viscous theory, derived under a quasiparallel assumption similar to the classical analysis of Thomas and Stevenson ["A similarity solution for viscous internal waves," J. Fluid Mech. **54**, 495 (1972)] for internal waves. © *2010 American Institute of Physics*. [doi:10.1063/1.3483468]

## I. INTRODUCTION

Rotating and stratified fluids both support the propagation of waves, referred to as inertial and internal waves, respectively, which share numbers of similar properties.[1,2] These waves are of first importance in the dynamics of the ocean and the atmosphere,[3] and play a key role in the anisotropic energy transfers and in the resulting quasi-two-dimensional nature of turbulence under strong rotation and/or stratification.[4]

More specifically, rotation and stratification both lead to an anisotropic dispersion relation in the form $\sigma=f(k_z/|\mathbf{k}|)$, where $\sigma$ is the pulsation, $\mathbf{k}$ is the wave vector, and the $z$ axis is defined either by the rotation axis or the gravity.[2] This particular form implies that a given excitation frequency $\sigma$ selects a single direction of propagation, whereas the range of excited wavelengths is set by boundary conditions or viscous effects. A number of well-known properties follow from this dispersion relation, such as perpendicular phase velocity and group velocity, and anomalous reflection on solid boundaries.[2,5]

Most of the laboratory experiments on internal waves in stratified fluids have focused on the properties of localized wave beams, of characteristic thickness and wavelength which are much smaller than the size of the container, excited either from local[6–10] or extended[11] sources. On the other hand, most of the experiments in rotating fluids have focused on the inertial modes or wave attractors in closed containers,[12–16] whereas less attention has been paid to localized inertial wave beams in effectively unbounded systems. Inertial modes and attractors are generated either from a disturbance of significant size compared to the container,[12] or more classically from global forcing (precession or modulated angular velocity).[13–16] Localized inertial waves generated by a small disturbance were visualized from numerical simulations by Godeferd and Lollini,[17] and were recently investigated using particle image velocimetry (PIV) by Messio *et al.*[18] In this latter experiment, the geometrical properties of the conical wavepacket emitted from a small oscillating disk was characterized, by means of velocity measurements restricted to a horizontal plane normal to the rotation axis, intersecting the wavepacket along an annulus.

The weaker influence of rotation compared to stratification in most geophysical applications probably explains the limited number of references on inertial waves compared to the abundant literature on internal waves (see Ref. 19 and references therein). Another reason might be that quantitative laboratory experiments on rotating fluids are more delicate to perform than for stratified fluids: Mounting the measurement devices, such as cameras and light sources for PIV, on the rotating frame implies technical issues (connection wiring and mechanical vibrations). Moreover, only PIV is available for quantitative investigation of the wave structure for inertial waves, whereas other optical methods, such as shadowgraphy, or more recently synthetic Schlieren,[8] are also possible for internal waves.

The purpose of this paper is to extend the results of Messio *et al.*,[18] using a newly designed rotating turntable, in which the velocity field can be measured over a large vertical field of view using a corotating PIV system. In the present experiment, the inertial wave is generated by a thin cylindrical wavemaker, producing a two-dimensional cross-shaped wave beam, and special attention is paid to the viscous spreading of the wave beam. The beam thickness and the vorticity decay are found to compare well with a similarity solution, analogous to the one derived by Thomas and Stevenson[7] for internal waves.

## II. THEORETICAL BACKGROUND

### A. Geometry of the wave pattern

A detailed description of the structure of a plane monochromatic inertial wave in an inviscid fluid can be found in Ref. 18 and only the main properties are recalled here. We consider a fluid rotating at constant angular velocity $\mathbf{\Omega}=\Omega\mathbf{e}_Z$, where the direction $\mathbf{e}_Z$ of the reference frame

[a]Electronic mail: ppcortet@fast.u-psud.fr.

 

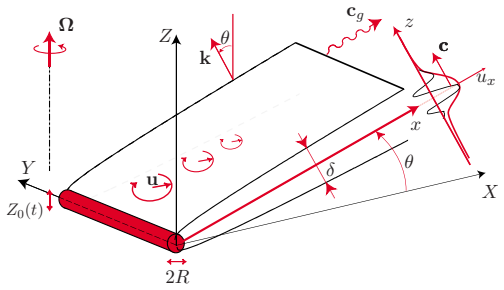


FIG. 1. (Color online) Geometry of an inertial wave beam emitted in an infinite medium from a localized oscillating cylindrical wavemaker invariant in the $Y$-direction.

$(\mathbf{e}_X, \mathbf{e}_Y, \mathbf{e}_Z)$ is vertical (see Fig. 1). Fluid particles forced to oscillate with a pulsation $\sigma < 2\Omega$ describe anticyclonic circular trajectories in tilted planes. A propagating wave defined by a wavevector $\mathbf{k}$ normal to these oscillating planes is a solution of the linearized inviscid equations, satisfying the following dispersion relation:

$$\sigma = 2\mathbf{\Omega} \cdot \mathbf{k}/k = 2\Omega \cos\theta. \tag{1}$$

In this relation, only the angle of $\mathbf{k}$ with respect to the rotation axis is prescribed, whereas its magnitude is set by the boundary conditions. For such anisotropic dispersion relation, the phase velocity, $\mathbf{c} = \sigma\mathbf{k}/k^2$, is normal to the group velocity,[2] $\mathbf{c}_g = \nabla_{\mathbf{k}}\sigma$ (see Fig. 1).

If one now considers a wave forced by a thin horizontal velocity disturbance invariant in the $Y$ direction, although the velocity field still has three components, the wave pattern is two-dimensional, varying only in the $(X,Z)$ vertical plane. The wave pattern consists in four plane beams making angle $\pm\theta$ with respect to the horizontal, drawing the famous *St. Andrew's cross* familiar in the context of internal waves.[6] In the following, we consider only one of those four beams, with $X > 0$ and $Z > 0$, and we define in Fig. 1 the associated local system of coordinates $(\mathbf{e}_x, \mathbf{e}_y, \mathbf{e}_z)$: The axis $\mathbf{e}_x$ is in the direction of the group velocity, $\mathbf{e}_z$ is directed along the wavevector $\mathbf{k}$, and $\mathbf{e}_y = \mathbf{e}_Y$ is along the wavemaker.

Considering the idealized case of an infinitely thin cylinder oscillating with an infinitely small amplitude (a Dirac disturbance), a white spectrum of wavevectors is excited, all aligned with $\mathbf{e}_z$. In an inviscid fluid, the interference of this infinite set of plane waves will cancel out everywhere except in the $z=0$ plane, where all the wave phases coincide, resulting in a single, infinitely thin oscillating sheet of fluid describing circular trajectory normal to $\mathbf{e}_z$. Of course, for a disturbance of finite size, finite amplitude, and in a viscous fluid, the constructive interferences will spread over a layer of finite thickness around the $z=0$ plane, as discussed in the following section.

### B. Viscous spreading

In a viscous fluid, the energy of the wave beam is dissipated because of the shearing motion between oscillating planes. As the energy propagates away from the source, the larger wavenumbers will be damped first so that the spectrum of the wave beam gradually concentrates toward lower wavenumbers, resulting in a spreading of the wave beam away from the source.

Although the viscous attenuation of a single Fourier component yields a purely exponential decay, the attenuation of a localized wave follows a power law with the distance from the source, which originates from the combined exponential attenuation of its Fourier components. A similarity solution for the viscous spreading of a wave beam was derived by Thomas and Stevenson[7] in the case of internal waves, and was extended to the case of coupled internal-inertial waves by Peat.[20] The derivation in the case of a pure inertial wave is detailed in the Appendix, and we provide here only a qualitative argument for the broadening of the wave beam.

During a time $t$, the amplitude of a planar monochromatic wave of wavevector $\mathbf{k}$ is damped by a factor $\epsilon_k = \exp(-\nu k^2 t)$ as it travels a distance $x = c_g t$ along the beam, where $c_g$ is the group velocity. Using $c_g = (2\Omega/k)\sin\theta = (\sigma/k)\tan\theta$, the attenuation factor writes

$$\epsilon_k = \exp(-\ell^2 k^3 x),$$

where we introduce the viscous lengthscale,

$$\ell = \left(\frac{\nu}{\sigma \tan\theta}\right)^{1/2}. \tag{2}$$

For a wave beam emitted from a thin linear source at $x=0$, an infinite set of plane waves is generated, and the energy of the largest wavenumbers will be preferentially attenuated as the wave propagates in the $x$ direction. At a distance $x$ from the source, the largest wavenumber, for which the energy has decayed by less than a given factor $\epsilon^*$, is $k_{\max} = (\ell^2 x)^{-1/3} \ln \epsilon^*$. At distance $x$, the wave beam thus results from the interference of the remaining plane waves of wavenumbers ranging from 0 to $k_{\max}$. Its thickness can be approximated by $\delta(x) \sim k_{\max}^{-1}$, yielding $\delta(x)/\ell \sim (x/\ell)^{1/3}$. Mass conservation across a surface normal to the group velocity implies that the velocity amplitude of the wave must decrease as $x^{-1/3}$.

More specifically, introducing the reduced transverse coordinate $\eta = z/x^{1/3}\ell^{2/3}$, a similarity solution exists for the velocity envelope,

$$u_0(x) = U_0^* \frac{E_0(\eta)}{E_0(0)} \left(\frac{\ell}{x}\right)^{1/3}, \tag{3}$$

where $U_0^*$ is the velocity scale of the wave and the analytical expression of the nondimensional envelope $E_0(\eta)$ is given in the Appendix. Similarly, the vorticity envelope can be written as

$$\omega_0(x) = W_0^* \frac{E_1(\eta)}{E_1(0)} \left(\frac{\ell}{x}\right)^{2/3}, \tag{4}$$

with $W_0^*$ as the vorticity scale. Although the normalized velocity envelope $E_0(\eta)/E_0(0)$ has larger tails than the vorticity one $E_1(\eta)/E_1(0)$, they turn out to be almost equal for $\eta < 4$.

The width at midheight, defined such that $E_m(\eta_{1/2}/2) = E_m(0)/2$, with $m=0,1$, is $\eta_{1/2} \simeq 6.84$ for both envelopes so that the width of the beam in dimensional units is

$$\delta(x) \simeq 6.84\ell\left(\frac{x}{\ell}\right)^{1/3}. \quad (5)$$

### C. Finite size effect of the source

The similarity solution described here applies only in the case of a source of size much smaller than the viscous scale $\ell$. In the case of internal waves, Hurley and Keady[21] (see also Ref. 9) showed that for a source of large extent, vertically vibrated with a small amplitude, the wave could be approximately described as originating from two virtual sources, respectively, located at the top and bottom of the disturbance. Following qualitatively this approach in the case of inertial waves forced by a horizontal cylinder of radius $R$, the boundaries of the upper wave are given by $z^{\pm}_{\text{up}} = R \pm \delta(x)/2$, and those of the lower wave are given by $z^{\pm}_{\text{down}} = -R \pm \delta(x)/2$. The lower boundary of the upper source intersects the upper boundary of the lower source at a distance $x_i$, such that $z^{-}_{\text{up}}(x_i) = z^{+}_{\text{down}}(x_i)$, yielding $\delta(x_i) = 2R$. Using the numerical factor given in Eq. (5), the distance $x_i$ writes

$$\frac{x_i}{R} \simeq 0.025\left(\frac{R}{\ell}\right)^2. \quad (6)$$

For large wavemakers ($R/\ell \gg 0.025^{-1/2} \simeq 6.3$), one has two distinct wave beams for $x \ll x_i$, and one single merged beam for $x \gg x_i$. On the other hand, for smaller wavemakers, the merging of the two wave beams occurs virtually inside the source, which can be effectively considered as a point source. In this case, the effective beam width far from the source may be simply written as

$$\delta_{\text{eff}}(x) \simeq 2R + \delta(x). \quad (7)$$

## III. THE EXPERIMENT

### A. Experimental setup

The experimental setup consists in a cubic glass tank, of 60 cm sides and filled with 54 cm of water (see Fig. 2), mounted on the new precision rotating turntable "Gyroflow," with 2 m diameter. The angular velocity $\Omega$ of the turntable is set in the range of 0.63–2.09 rad s$^{-1}$, with relative fluctuations $\Delta\Omega/\Omega$ less than $5 \times 10^{-4}$. A cover is placed at the free surface, preventing from disturbances due to residual surface waves. The rotation of the fluid is set long before each experiment (at least 1 h) in order to avoid transient spin-up recirculation flows and to achieve a clean solid body rotation.

The wavemaker is a horizontal cylinder of radius $R=4$ mm and length $L=50$ cm, hung at 33.5 cm below the cover by a thin vertical stem with 3 mm diameter. It is off-centered in order to increase the size of the investigated wave beam in the quadrant $X<0$ and $Z<0$. The vertical oscillation $Z_0(t) = A\cos(\sigma_o t)$, with $A=2$ mm, is achieved by a step-motor, coupled to a circular camshaft which converts the rotation into a sinusoidal vertical oscillation. In the present experiments, the wavemaker frequency is kept constant, equal to $\sigma_o = 1.26$ rad s$^{-1}$, and the angular velocity of the turntable is used as the control parameter. This allows the velocity disturbance $\sigma_o A = 2.5$ mm s$^{-1}$ to be fixed, whereas the angle of the inertial wave beam with respect to the horizontal, $\theta = \cos^{-1}(\sigma_o/2\Omega)$, is varied between 0° and 72°. The velocity and vorticity profiles are examined at distances $x$ between 30 and 300 mm from the wavemaker. The three-dimensional effects originating from the finite length $L$ of the cylinder can be safely neglected since $x < 0.6L$. The Reynolds number based on the wavemaker velocity is $\text{Re} = \sigma_o A(2R)/\nu \simeq 20$ so that the flow in the vicinity of the wavemaker is essentially laminar. Except in Sec. IV B, where the transient regime is described, measurements start after several wavemaker periods in order to achieve a steady state.

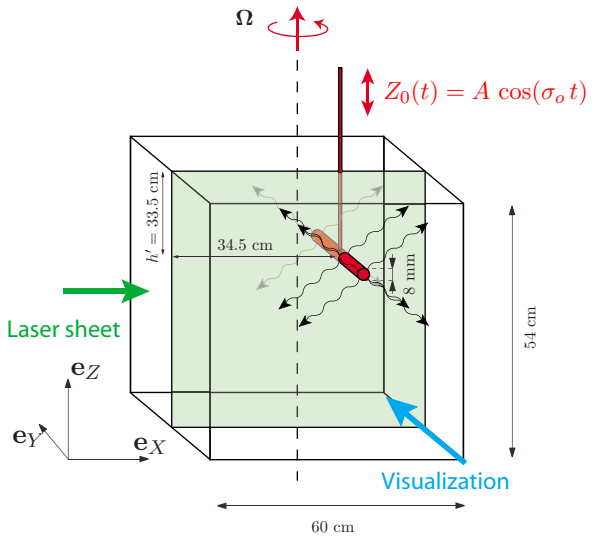


FIG. 2. (Color online) Schematic view of the experimental setup. The horizontal 8 mm diameter cylinder is oscillating vertically according to $Z_0(t) = A\cos(\sigma_o t)$, with $A=2$ mm and $\sigma_o = 0.2$ Hz. PIV measurements in a vertical plane $(X,Z)$ in the rotating frame are achieved by a vertical laser sheet and a camera at 90°.

For the forcing frequency $\sigma_o$ considered here, the characteristic boundary layer thickness is $\delta_S = (\nu/\sigma_o)^{1/2} \simeq 0.9$ mm. This thickness also gives the order of magnitude of the viscous length $\ell = \delta_S/\sqrt{\tan\theta}$ [see Eq. (2)], for angles not too close to 0 and $\pi/2$. The wavemaker radius being chosen such that $R/\ell \simeq 4$, the small source approximation is satisfied according to the criterion discussed in Sec. II C.

### B. PIV measurements

Velocity fields in a vertical plane $(X,Z)$ are measured using a 2D particle image velocimetry system. The flow is seeded by 10 $\mu$m tracer particles, and illuminated by a vertical laser sheet, generated by a 140 mJ Nd:YAG (yttrium aluminum garnet) pulsed laser. A vertical $43 \times 43$ cm$^2$ field of view is acquired by a $2048 \times 2048$ pixel camera synchronized with the laser pulses. The field of view is set on the

lower left wave beam. For each rotation rate, a set of 2000 images is recorded, at a frequency of 2 Hz, representing ten images per wavemaker oscillation period.

PIV computations are performed over successive images, on $32\times32$ pixel interrogation windows with 50% overlap, leading to a spatial resolution of 3.4 mm.[22] In the following, the two quantities of interest are the velocity component $u_x$, obtained from the measured components $u_X$ and $u_Z$ projected along the direction of the wave beam, and the vorticity component $\omega_y$ normal to the measurement plane.

The velocity along the wave beam typically decreases from 1 to 0.1 mm $s^{-1}$, and is measured with a resolution of 0.02 mm $s^{-1}$. Two sources of velocity noise are present, both of the order of 0.2 mm $s^{-1}$, originating from residual modulations of the angular velocity of the turntable, and from thermal convection effects due to a slight difference between the water and the room temperature. The residual velocity modulations, of the order of $L_0\Delta\Omega/2$ (where $L_0$ is the tank size and $\Delta\Omega\simeq5\times10^{-4}$ $\Omega$), are readily removed by computing the phase-averaged velocity fields $\mathbf{u}(x,z,\phi)$ from the instantaneous velocity $\mathbf{u}_{\text{inst}}(x,z,t)$. Here the phase-averaged field at a given phase $\phi\in[0,2\pi]$ is defined as

$$\mathbf{u}(x,z,\phi)=\frac{1}{N}\sum_{n=1}^{N}\mathbf{u}_{\text{inst}}\left[x,z,\left(\frac{\phi}{2\pi}+n\right)T\right], \tag{8}$$

where $T=2\pi/\sigma_o$ is the oscillation period and $N=200$ is the number of recorded periods. Thermal convective motions, in the form of slowly drifting ascending and descending columns, could be reduced but not completely suppressed by this phase-averaging, and represent the main source of uncertainty in these experiments. However, the vorticity level associated to those convective motions appears to be negligible compared to the typical vorticity of the inertial wave. Therefore, the vorticity profiles of the wave could be safely computed from the phase-averaged velocity fields.

## IV. GENERAL PROPERTIES OF THE WAVE PATTERN

### A. Visualization of the wave beams

Figure 3 is a close-up view of the velocity and vorticity fields at $\sigma_o/2\Omega=0.67$, showing velocity vectors almost parallel to the beam direction $\mathbf{e}_x$ and vorticity layers of alternating sign. The angle of the beam with respect to the horizontal (see the black line) accurately follows the prediction of the dispersion relation (1), as shown in Fig. 4. In Figs. 5(a)–5(c), phase-averaged horizontal vorticity fields $\omega_y$ are shown for three equally spaced values of the phase. One can clearly see the location of the inertial wave inside a wavepacket that draws the classical four-ray St. Andrew's cross. The evolution of the vorticity field from Fig. 5(a) to Fig. 5(c) illustrates the propagation of the phase, in directions normal to the beams and toward the rotation axis. Some reflected wave beams of much smaller amplitude may also be distinguished on the background.

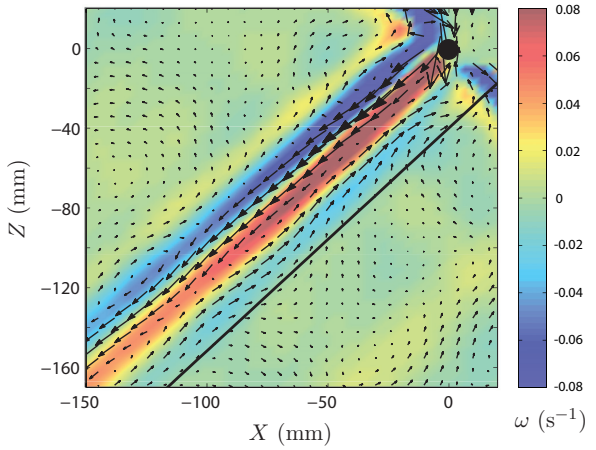


FIG. 3. (Color) Close-up view of the phase-averaged velocity (arrows) and vorticity $\omega_y$ (shade/color mapped) for an experiment performed at $\sigma_o/2\Omega=0.67$. The black line shows the direction predicted by the dispersion relation $\cos\theta=\sigma_o/2\Omega$. The filled black circle represents the oscillating cylinder. The velocity field on the right of the cylinder is not resolved because the particles are not illuminated by the laser sheet originating from the left.

### B. Transient experiments

In order to characterize the formation of the inertial wave pattern as the oscillation is started, a series of transient experiments have been performed. In the case of a pure monochromatic plane wave, the front velocity of the wavepacket would be simply given by the group velocity. However, in the case of a localized wave beam, since each Fourier component $k$ travels with its own group velocity $c_g=(\sigma/k)\tan\theta$, the shape of the wavepacket gradually evolves as the wave propagates. A rough estimate for the front velocity can be readily obtained from $V_f\simeq\sigma(\lambda/2\pi)\tan\theta$, where $\lambda$ is the apparent wavelength of the wave, simply estimated as twice the distance between the locations of two successive vorticity extrema.

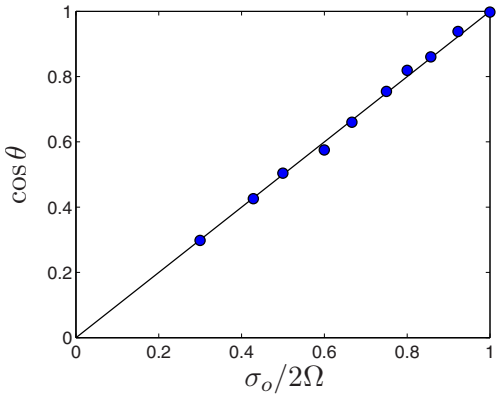


FIG. 4. (Color online) Cosine of the measured average beam angle, $\cos\theta$, as a function of the frequency ratio $\sigma_o/2\Omega$. The angle is determined from the location of the maximum of the vorticity envelope. The line shows the dispersion relation (1). Experimental uncertainties are of the order of the marker size.

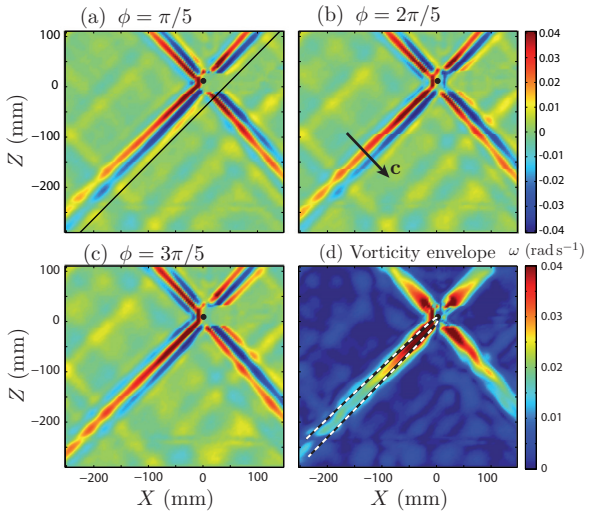


FIG. 5. (Color) Phase-averaged horizontal vorticity field $\omega_y$ for $\sigma_o/2\Omega=0.67$ at different phases: (a) $\phi=\pi/5$, (b) $\phi=2\pi/5$, and (c) $\phi=3\pi/5$. The black line in (a) draws the direction predicted by the dispersion relation. (d) Vorticity envelope field $\omega_0$ (see Sec. V). The dashed black and white lines show the wave beam thickness predicted by the similarity solution [see Eq. (7)].

Figure 6 shows spatiotemporal diagrams of the vorticity $\omega_y(x,z=0,t)$ at the center of the beam as a function of the distance $x$ from the wavemaker, for $\sigma_o/2\Omega$ between 0.85 and 0.50. Superimposed to these spatiotemporal images, we show the front velocity $V_f \simeq \sigma(\lambda/2\pi)\tan\theta$, starting from $x=0$ at $t=0$. Qualitative agreement with the spatiotemporal

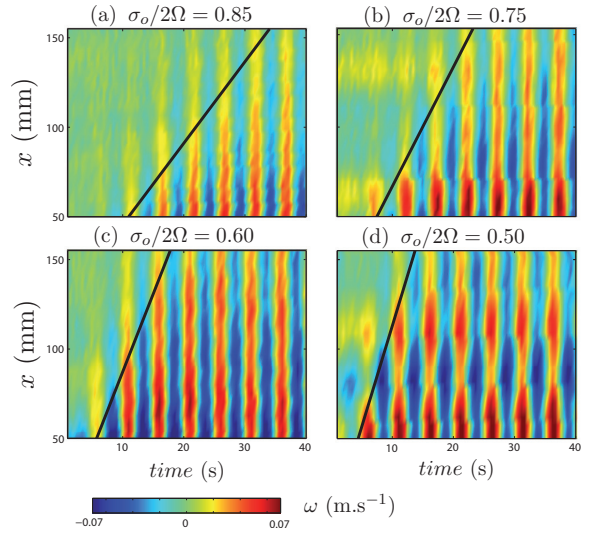


FIG. 6. (Color) Spatiotemporal representation of the vorticity $\omega_y$ along the wave beam, where space is the distance $x$ to the oscillating cylinder, for experiments performed at $\sigma_o/2\Omega=0.85,0.75,0.60,0.50$. Black lines originating at $(x=0,t=0)$ trace the front velocity $V_f=\sigma(\lambda/2\pi)\tan\theta$ estimated from the apparent wavelength (see Sec. V A). $t=0$ corresponds to the start of the oscillation.

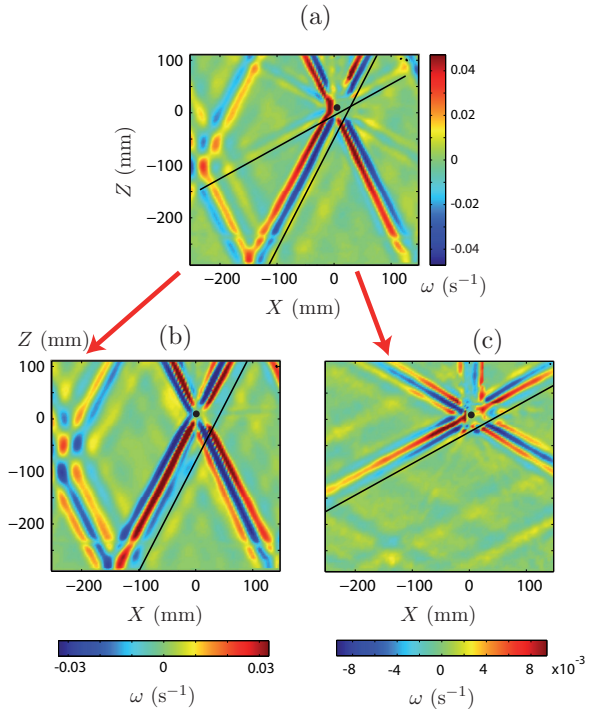


FIG. 7. (Color) (a) Phase-averaged vorticity field $\omega_y$ for an experiment performed at $\sigma_o/2\Omega=0.43$, showing both the fundamental ($n=1$) and the second harmonic ($n=2$) wave beams. The corresponding frequency-filtered vorticity fields are extracted in (b) and (c).

diagrams is obtained, indicating that the propagation of the wave envelope is indeed compatible with this simple estimate of the front velocity.

Further quantitative estimate of the front velocity would require us to extract the instantaneous wave envelope from those spatiotemporal diagrams, which is difficult because the front velocity and the phase velocity are of the same order. This property actually prevents a safe extraction of a longitudinal wavepacket envelope using standard temporal averaging over small time windows.

### C. Generation of harmonics

Returning to steady waves, we now characterize the generation of higher order wave beams that take place at low forcing frequency. According to the dispersion relation, an harmonic wave of order $n \geq 2$ is allowed to develop whenever $n\sigma_o/2\Omega < 1$. Such harmonic waves of order $n \geq 2$ may originate either from a residual nonharmonic component of the wavemaker oscillation profile $Z_0(t)$, or from inertial nonlinear effects in the flow in the vicinity of the wavemaker, which may exist at the Reynolds number $\mathrm{Re} \simeq 20$ considered here.

In Fig. 5, for $\sigma_o/2\Omega=0.67$, only the fundamental wave ($n=1$) can be seen. On the other hand, in Fig. 7(a), for $\sigma_o/2\Omega=0.43$, a second harmonic wave beam is clearly present, propagating at an angle closer to the horizontal, as expected from the dispersion relation. This is confirmed by Figs. 7(b) and 7(c), showing the corresponding frequency-

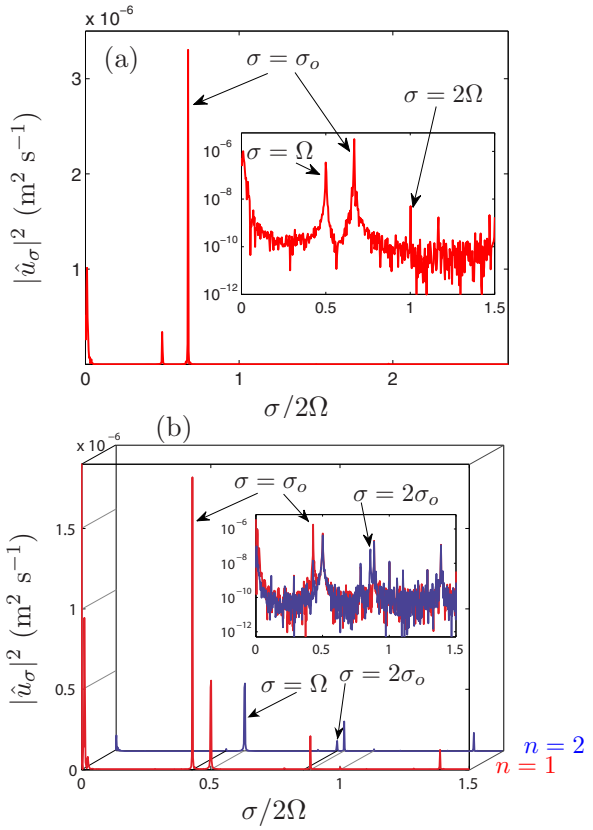


FIG. 8. (Color online) Energy spectrum of the velocity time series measured at the center of the wave beam of interest, at a fixed distance $x_0=100$ mm from the wavemaker. (a) $\sigma_o/2\Omega=0.67$, showing a single peak at the forcing frequency. (b) $\sigma_o/2\Omega=0.43$, showing measurements performed in the fundamental beam $n=1$ (light gray in print, red online) and in the second harmonic beam $n=2$ (dark gray in print, blue online). In (a) and (b), the inset shows the same spectrum in semilogarithmic coordinates. Additional peaks are present at $\sigma/2\Omega=0.5$ and 1, originating from mechanical noise of the rotating platform.

filtered phase-averaged vorticity fields, in (b) for the fundamental $n=1$ and in (c) for the second harmonics $n=2$.

In order to further characterize this generation of harmonics, we have performed a spectral analysis of the time series of the longitudinal velocity $u_x(t)$, measured at a given distance $x_0=100$ mm from the source, at the center of each wave beam. The energy spectrum $|\hat{u}_\sigma|^2$, where $\hat{u}_\sigma$ is the temporal Fourier transform of $u_x(t)$, is shown in Fig. 8 for the two cases $\sigma_o/2\Omega=0.67$ and 0.43. In both cases, the spectra are clearly dominated by the fundamental forcing frequency $\sigma_o$. Two other peaks are also found, at $\sigma=\Omega$ and $\sigma=2\Omega$, originating from the residual modulation of the angular velocity of the platform, as discussed in Sec. III B (the energy of those peaks is typically three to ten times smaller than the fundamental one). It has been checked that these two peaks are also present when the cylinder is not oscillating, confirming that they are not linked to the inertial wave beam. Computing the velocity field bandpass filtered at $\sigma=\Omega$ actually shows that the mechanical noise at $\Omega$ excites a high order spatial structure characteristic of a resonating inertial mode of the container.[23] This is not the case for the peak at $\sigma=2\Omega$, which theoretically cannot be associated to an inertial mode. One can also see a peak at $\sigma\simeq 0$, probably originating from the slowly drifting thermal convection columns discussed in Sec. III B, which are of significant amplitude compared to the inertial waves.

As expected, no harmonic frequency $n\sigma_o$ $(n\geq 2)$ is found in the spectrum for $\sigma_o/2\Omega=0.67$ [see Fig. 8(a)], but a second harmonic $n=2$ is indeed present for $\sigma_o/2\Omega=0.43$ [see Fig. 8(b)]. In this case, the energy ratio of the first to the second harmonics, each of them being measured at a distance $x_0=100$ mm from the source on the corresponding beam, is $|\hat{u}_{2\sigma}|^2/|\hat{u}_\sigma|^2\simeq 0.036$. (Note that the additional peak at $\sigma/2\Omega=0.89$, immediately to the right of the second harmonic peak at $2\sigma_o/2\Omega=0.86$, originates from a residual vibration of the camera with respect to the water tank at this particular angular velocity $\Omega$). As $\sigma_o/2\Omega$ is further decreased, the ratio $|\hat{u}_{2\sigma}|^2/|\hat{u}_\sigma|^2$ increases, reaching 0.05 for $\sigma_o/2\Omega=0.30$, and even higher order harmonics emerge, although with very weak amplitude.

## V. TEST OF THE SIMILARITY SOLUTION

### A. Velocity and vorticity envelopes

We now focus on the dependence of the wavepacket shape and the viscous spreading of the wave beam with the distance $x$ from the source. Figures 9(a) and 9(b) illustrate the shape of the phase-averaged velocity and vorticity profiles, respectively, for two values of the phase $\phi_0$ and $\phi_0+2\pi/5$. The wavepacket envelopes are defined as

$$u_0(x,z)=\sqrt{2\langle u_x(x,z,\phi)^2\rangle_\phi}$$

(and similarly for $\omega_0$), where $\langle\cdot\rangle_\phi$ is the average over all phases $\phi$. Although the measured normalized envelopes compare well with the normalized envelopes predicted from the similarity solutions $[E_m(\eta)/E_m(0)$, with $m=0$ for the velocity and $m=1$ for the vorticity], the agreement is actually better for the vorticity. This is probably due to the velocity contamination originating from the residual angular velocity modulation of the platform and the slight thermal convection effects discussed in Sec. III B. The better defined vorticity envelopes actually confirm that those velocity contaminations have a negligible vorticity contribution. For this reason, we will concentrate only on the vorticity field in the following.

It is worth to examine here the singular situation $\sigma_o/2\Omega=1$, in which the similarity solution is no longer valid. In this situation, the phase velocity is strictly vertical and the group velocity vanishes. The upward and downward beams are expected to superimpose and generate a stationary wave pattern in the horizontal plane $Z=z=0$. Figure 10 shows the velocity envelope $u_0(x_0,z)$ and three phase-averaged profiles as a function of the transverse coordinate $z$. The observed wave is actually stationary at the center of the wavepacket (see the velocity node and vorticity maximum for $z=0$), and shows outward propagation on each side of the wavepacket.

Returning to the standard situation $\sigma_o/2\Omega<1$, the vorticity amplitude at a given location $x$ is defined as the maximum of the vorticity envelope at the center of the beam,

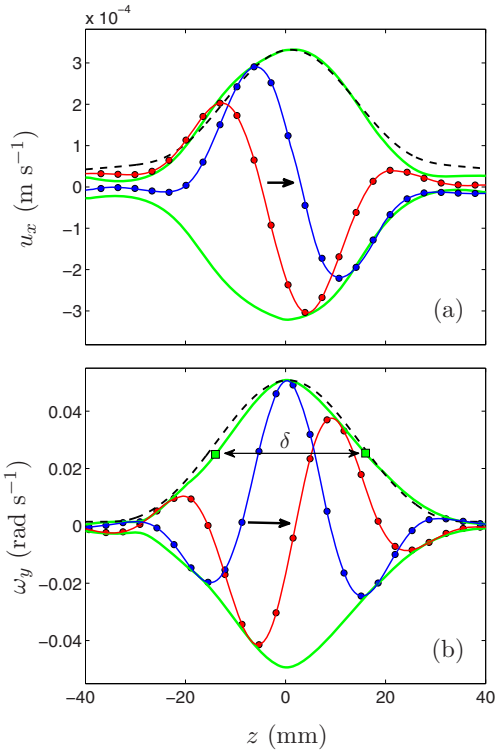


FIG. 9. (Color online) (a) Velocity envelope $u_0(x_0,z)$ and two velocity profiles $u_x(x_o,z,\phi)$ for two values of the phase $\phi$, as a function of the transverse coordinate $z$ at a fixed distance $x_o$=100 mm from the wavemaker for $\sigma_o/2\Omega$=0.67. (b) Corresponding vorticity envelope $\omega_0(x_0,z)$ and vorticity profiles $\omega_y(x_0,z,\phi)$. (●) Data points with spline interpolations of the profiles in continuous lines. Light gray (green online) continuous lines: Envelopes computed from the interpolated profiles. Dashed curves: similarity solution normalized by the measured maximum. Both profiles are averaged over a distance range $90<x<110$ mm from the wavemaker. $\delta$ is the envelope thickness at midheight.

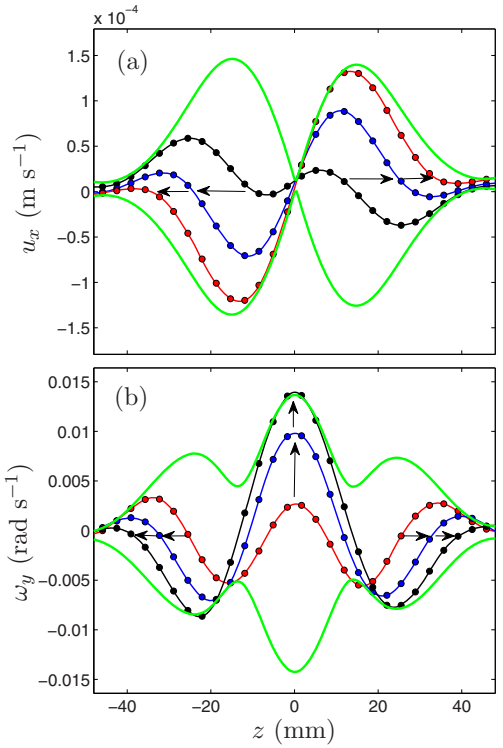


FIG. 10. (Color online) (a) Velocity envelope $u_0(x_0,z)$ and three velocity profiles $u_x(x_0,z,\phi)$ as a function of the transverse coordinate $z$ at a fixed distance $x_o$=70 mm (average over $50<x<90$ mm) from the wavemaker for $\sigma_o/2\Omega$=1. (b) Corresponding vorticity envelope and vorticity profiles. The arrows indicate the time evolution of the profiles. The interference of the upward and downward wave beams produces a stationary wave pattern at $z$=0 with a velocity node and a vorticity maximum. Same data representations as in Fig. 9.

$\omega_{\max}(x)=\omega_0(x,z=0)$. The thickness of the wavepacket $\delta(x)$ is defined from the width at midheight of the envelope, such that

$$\omega_0[x,\delta(x)/2]=\omega_{\max}(x)/2.$$

This beam thickness $\delta$ depends both on the distance $x$ from the source and on the viscous length $\ell$ [see Eqs. (5) and (7)]. In order to check those two dependencies, $\delta$ is plotted in Fig. 11(a) as a function of $x$ at fixed $\sigma_o/2\Omega$, and in Fig. 11(b) as a function of $\sigma_o/2\Omega$ at fixed $x_0$. The agreement with the effective wave beam thickness $\delta_{\text{eff}}=2R+6.84\ell(x/\ell)^{1/3}$ is correct, to within 10%, which justifies the simple analysis of merged beams originating from the two virtual sources located at the top and bottom of the wavemaker. The oscillations of $\delta$ probably originate from the interaction of the principal wave beam with reflected ones. Figure 11(a) also shows the apparent wavelength $\lambda(x)$ of the wave, simply defined as twice the distance between a maximum and a minimum of the phase-averaged vorticity profiles. This apparent wavelength turns out to be even closer to the expected lengthscale $\delta_{\text{eff}}$ of Eq. (7), to within 4%, suggesting that $\lambda$ is less affected by the background noise than the beam thickness. A good agreement between both $\delta$ and $\lambda$ and prediction (7) is also obtained as $\sigma_o/2\Omega$ (and hence $\ell$) is varied at fixed $x_0$, as shown in Fig. 11(b). Here again, the interaction with reflected wave beams is probably responsible for the significant scatter in this figure.

### B. Decay of the vorticity envelope

The decay of the vorticity amplitude $\omega_{\max}(x)$ as a function of the distance $x$ from the source is shown in Fig. 12. Taking the similarity solution (4) at the center of the wave beam $z$=0 yields

$$\omega_{\max}(x)=W_0^*\left(\frac{\ell}{x}\right)^{2/3}. \tag{9}$$

Letting the vorticity scale $W_0^*$ as a free parameter, a power law $x^{-2/3}$ is found to provide a good fit for the overall decay of $\omega_{\max}(x)$. Some marked oscillations are however clearly visible, e.g., at $x$ between 220 and 320 mm for $\sigma_o/2\Omega$ =0.85. Those oscillations appear at locations where reflected wave beams interact with the principal one, inducing modulations of the wave amplitude. This interpretation is confirmed by the fact that (i) the observed modulation has a wavelength of 45 mm, which corresponds to the apparent wavelength of the wave, and that (ii) in Fig. 5, corresponding

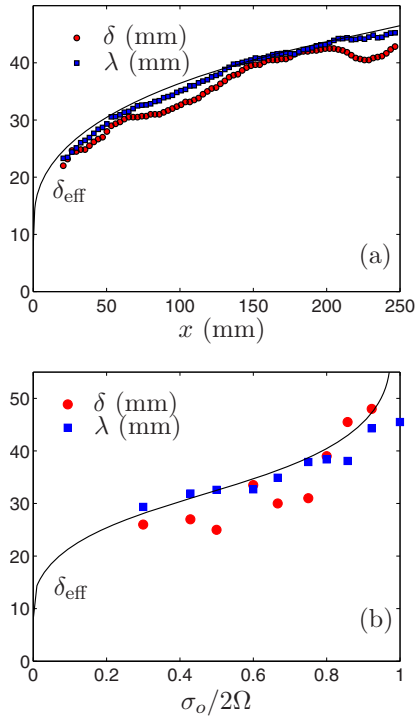


FIG. 11. (Color online) (●) Wave beam thickness $\delta$ and (■) apparent wavelength $\lambda$; (a) as a function of the distance $x$ from the wavemaker for $\sigma_o/2\Omega=0.67$; (b) as a function of $\sigma_o/2\Omega$ at a distance $x_o=100$ mm from the wavemaker. In both plots, the line shows the predicted effective wave beam thickness $\delta_{\text{eff}}$ (7).

to $\sigma_o/2\Omega=0.67$, a modulation of the principal wave beam by a reflected one can be clearly seen at a distance of about 250 mm from the source.

The vorticity scale $W_0^*$ is theoretically related to the velocity scale $U_0^*$ through the relation $W_0^*=[E_1(0)/E_0(0)]U_0^*/\ell \simeq 0.506U_0^*/\ell$ (see the Appendix). Since the wavemaker velocity is $\sigma_o A$, the velocity scale $U_0^*$ is expected to write in the form $\sigma_o A g(\theta)$, where the unknown function $g(\theta)$ describes the forcing efficiency of the wavemaker. Accordingly, the forcing efficiency can be deduced from the vorticity data, by computing

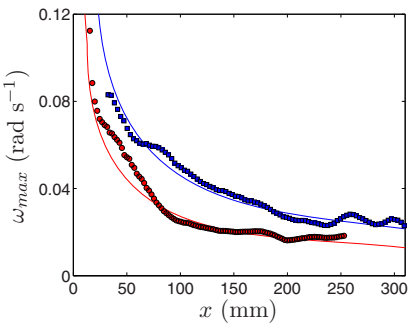


FIG. 12. (Color online) Vorticity amplitude $\omega_{\max}(x)$ as a function of the distance $x$ from the wavemaker, and best fit with the law $W_0^*(x/\ell)^{-2/3}$. (■) $\sigma_o/2\Omega=0.67$. (●) $\sigma_o/2\Omega=0.85$.

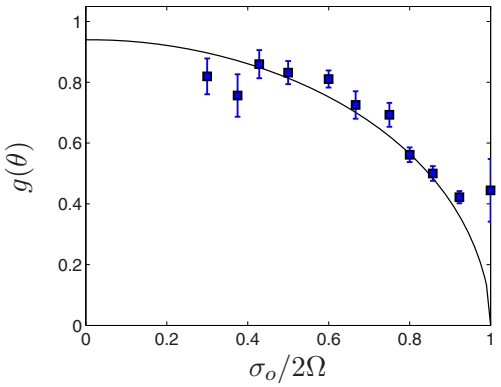


FIG. 13. (Color online) Forcing efficiency $g(\theta)$ defined from Eq. (10) as a function of $\sigma_o/2\Omega$. Squares and errorbars represent the mean and the standard deviation for each $\sigma_o/2\Omega$, respectively, reflecting the variability of $\omega_{\max}$ along $x$. The line shows the best fit according to Eq. (11), with $g_0=0.94\pm0.10$.

$$g(\theta)=\frac{W_0^*}{0.506\sigma_o A/\ell}=\frac{\omega_{\max}(x/\ell)^{2/3}}{0.506\sigma_o A/\ell} \tag{10}$$

for each value of $\sigma_o/2\Omega$. Measurements of $g(\theta)$ are plotted as a function of $\sigma_o/2\Omega$ in Fig. 13. As expected, this forcing efficiency decreases as $\sigma_o/2\Omega$ is increased, i.e., as the wave beam becomes closer to the horizontal. In the limit $\sigma_o/2\Omega\to1$, the vertically oscillating wavemaker becomes indeed very inefficient to force the quasihorizontal velocities of the wave.

An analytical expression for the function $g(\theta)$ would require us to solve exactly the velocity field in the vicinity of the wavemaker and, in particular, the coupling between the oscillating boundary layer and the wave far from the source, which is beyond the scope of this paper. In the case of a cylinder, a naive estimate of $g(\theta)$ could however be obtained, assuming that the effective velocity forcing is simply given by the projection of the wavemaker velocity along the wave beam direction, yielding

$$g(\theta)=g_0\sin\theta=g_0\sqrt{1-\left(\frac{\sigma_o}{2\Omega}\right)^2}, \tag{11}$$

with $g_0$ a constant to be determined. A best fit of the experimental values of $g(\theta)$ with this law leads to $g_0\simeq0.94\pm0.10$ (see Fig. 13), and reproduces well the decrease of $g(\theta)$ as $\sigma_o/2\Omega$ is increased. The fact that $g_0$ is found close to 1 indicates that the inertial wave beam is essentially fed by the oscillating velocity field in the close vicinity of the wavemaker. The discrepancy at large forcing frequency may be due to the breakdown of the similarity solution as the angle $\theta$ approaches 0.

## VI. STOKES DRIFT

We finally consider the possibility of Stokes drifts which may take place in a localized inertial wave beam. Two drift mechanisms may be expected in this geometry: a first one in the vertical plane $(x,z)$ and a second one along the invariant direction $y$. The first drift mechanism is similar to the one

discussed by Kistovich and Chashechkin[24] in the case of a two-dimensional internal wave beam, leading to a mass transport of different signs on each side of the wave beam. The second drift mechanism is specific to the inertial wave and originates from the circular motion in the $(x,y)$ plane of the wave.

The physical mechanism for this second drift is as follows. A fluid particle in the inertial wave approximately describes a circular orbit. During this orbit, the particle experiences a larger velocity along $y$ when it is closer than when it is further from the wavemaker (see Fig. 1), resulting in a net mass transport along $y$. This is similar to the classical Stokes drift for surface waves, which is horizontal because of the decay of the velocity magnitude with depth.[25] Here the drift is due to the viscous decay of the wave which takes place along the direction of propagation and is expected, in general, in the direction given by $\mathbf{\Omega}\times\mathbf{c}_g$.

Attempts to detect this effect have been carried out from PIV measurements in vertical planes $(Y,Z)$. Because of the weakness of the considered drift, the measurements have been performed very close to the wavemaker, for $X$ between 5 and 30 mm, where a stronger effect is expected. However, those attempts were not successful, probably because the drift, if present, is hidden by the stronger fluid motions induced by the residual thermal convection columns, as discussed in Sec. III B.

The magnitude of the expected Stokes drift cannot be easily inferred from the complex motion of the fluid particles close to the wavemaker. An estimate could however be obtained in the far field, from the similarity solution of the wave beam. We consider, for simplicity, a particle lying at the center of the wave beam $(z=0)$, at a mean distance $x_0$ from the source, describing approximate circles of gyration radius $a\simeq|\mathbf{u}(x_0)|/\sigma$ in the tilted plan $(x,y)$. The expected drift velocity $\bar{\mathbf{v}}_S$ can be approximated by computing the velocity difference between the two extreme points $x_0-a$ and $x_0+a$ of the orbit, yielding, to first order in $a/x_0$, to[26]

$$\bar{v}_{Sy}(x_0)\simeq\frac{2}{3}\frac{U_0^{*2}\ell^{2/3}}{\sigma x_0^{5/3}}. \tag{12}$$

The steep decrease as $x_0^{-5/3}$ confirms that the drift should be essentially present close to the wavemaker. Although this formula is expected to apply only in the far-field wave (typically for $x_0>40\ell$, see the Appendix), its extrapolation close to the wavemaker, for $x_0\simeq 10\ell\simeq 2R$, gives $\bar{v}_{Sy}\simeq 0.1$ mm s$^{-1}$. This expected drift velocity is about 10% of the wave velocity at the same location, but it turns out to remain smaller than the velocity contamination due to the thermal convection columns. Although the phase-averaging proved to be efficient to extract the inertial wave field from the measured velocity field because of a sufficient frequency separation between convection effects and the inertial wave, it fails here to extract the much weaker velocity signal expected from this drift since it is of zero frequency and hence mixed with the very low frequency of those convective motions.

## VII. CONCLUSION

In this paper, particle image velocimetry measurements have been used to provide quantitative insight into the structure of the inertial wave emitted by a vertically oscillating horizontal cylinder in a rotating fluid. Large vertical fields of view could be achieved, thanks to a new rotating platform, allowing for direct visualization of the cross-shaped St. Andrew's wave pattern.

It must be noted that performing accurate PIV measurements of the very weak signal of an inertial wave is a challenging task. In spite of the high stability of the angular velocity of the platform $(\Delta\Omega/\Omega<5\times10^{-4})$, the velocity signal-to-noise ratio remains moderate here. Additionally, slowly drifting vertical columns are present because of residual thermal convection effects, and are found to account for most of velocity noise in these experiments. Those thermal convection effects are very difficult to avoid in large containers, even in an approximately thermalized room. However, this noise can be significantly reduced by a phase-averaging over a large number of oscillation periods. This concern is not present for internal waves in stratified fluids because residual thermal motions are inhibited by the stable stratification. This emphasizes the intrinsic difficulty of experimental investigation of inertial waves, in contrast to internal waves which have been the subject of a number of studies (although it must be noted that achieving a strictly linear stratification through the whole fluid volume, and hence a strictly homogeneous Brunt–Väsäilä frequency, is also a delicate issue).

In this article, emphasis has been given on the spreading of the inertial wave beam induced by viscous dissipation. The attenuation of a two-dimensional wave beam emitted from a linear source is purely viscous, whereas it combines viscous and geometrical effects in the case of a conical wave emitted from a point source. The linear theory presented in this paper is derived under the classical boundary layer assumption first introduced by Thomas and Stevenson[7] for two-dimensional internal waves in stratified fluids. The measured thickening of the wave beam and the decay of the vorticity envelope are quantitatively fitted by the scaling laws of the similarity solutions of this linear theory, $\delta(x)\sim x^{1/3}$ and $\omega_{\max}(x)\sim x^{-2/3}$, where $x$ is the distance from the source. More precisely, we have shown that the amplitude of the vorticity envelope could be correctly predicted from the velocity disturbance induced by the wavemaker, by introducing a simple forcing efficiency function $g(\theta)$, where $\theta$ is the angle of the wave beam.

Finally, it is shown that an attenuated inertial wave beam should, in principle, generate a Stokes drift along the wavemaker, in the direction given by $\mathbf{\Omega}\times\mathbf{c}_g$, where $\mathbf{c}_g$ is the group velocity. However, in spite of the high precision of the rotating platform and the PIV measurements, attempts to detect this drift were not successful in the present configuration. Velocity fluctuations induced by thermal convection effects probably hide this slight mean drift velocity, suggesting that an improved experiment with a very carefully controlled temperature stability would be necessary to detect this very weak effect.

## ACKNOWLEDGMENTS

We acknowledge A. Aubertin, L. Auffray, C. Borget, G.-J. Michon, and R. Pidoux for experimental help, and T. Dauxois, L. Gostiaux, M. Mercier, C. Morize, M. Rabaud, and B. Voisin for fruitful discussions. The new rotating platform Gyroflow was funded by the ANR (Grant No. 06-BLAN-0363-01 "HiSpeedPIV") and the "Triangle de la Physique."


## APPENDIX: SIMILARITY SOLUTION FOR A VISCOUS PLANAR INERTIAL WAVE

In this appendix, we derive the similarity solution for a viscous planar inertial wave, following the procedure first described by Thomas and Stevenson[7] for internal waves.

We consider the inertial wave emitted from a thin linear disturbance invariant along the $Y$ axis and oscillating along $Z$ with a pulsation $\sigma$ in a viscous fluid rotating at angular velocity $\mathbf{\Omega}=\Omega\mathbf{e}_Z$. Since the linear source is invariant along $Y$, so will the wave beams, and the energy propagates in the $(X,Z)$ plan. In the following, we consider only the wave beam propagating along $X>0$ and $Z>0$.

The linearized vorticity equation is

$$\partial_t\boldsymbol{\omega}=(2\mathbf{\Omega}\cdot\nabla)\mathbf{u}+\nu\nabla^2\boldsymbol{\omega}.$$

Recasting the problem in the tilted frame of the wave, $(\mathbf{e}_x,\mathbf{e}_y,\mathbf{e}_z)$, with $\mathbf{e}_y=\mathbf{e}_Y$ and $\mathbf{e}_x$ tilted of an angle $\theta=\cos^{-1}(\sigma/2\Omega)$ with the horizontal, one has $\mathbf{\Omega}=\Omega(\sin\theta\mathbf{e}_x+\cos\theta\mathbf{e}_z)$ so that $(2\mathbf{\Omega}\cdot\nabla)=2\Omega(\sin\theta\partial_x+\cos\theta\partial_z)=\sigma(\tan\theta\partial_x+\partial_z)$. Assuming that the flow inside the wave beam is quasiparallel (boundary layer approximation), i.e., such that $|u_x|,|u_y|\gg|u_z|$, $|\omega_x|,|\omega_y|\gg|\omega_z|$, and $\nabla^2\simeq\partial_z^2$, the linearized vorticity equation reduces to

$$\partial_t\omega_x=\sigma(\tan\theta\partial_x+\partial_z)u_x+\nu\partial_z^2\omega_x, \tag{A1}$$

$$\partial_t\omega_y=\sigma(\tan\theta\partial_x+\partial_z)u_y+\nu\partial_z^2\omega_y. \tag{A2}$$

We introduce the complex velocity and vorticity fields in the $(x,y)$ plan as

$$U=u_x+iu_y,\quad W=\omega_x+i\omega_y.$$

Since, within the quasiparallel approximation, one has $W=i\partial_z U$, the combination (A1)+$i$(A2) yields

$$i\partial_t\partial_z U=\sigma(\tan\theta\partial_x+\partial_z)U+i\nu\partial_z^3U. \tag{A3}$$

Searching solutions in the form $U=U_0e^{-i\sigma t}$, Eq. (A3) becomes

$$\partial_x U_0+i\ell^2\partial_z^3U_0=0, \tag{A4}$$

where we have introduced the viscous scale $\ell$ (2). Equation (A4) admits similarity solutions as a function of the variable

$$\eta=\frac{z}{x^{1/3}\ell^{2/3}}, \tag{A5}$$

which are of the form

$$U_0(x,z)=\widetilde{U}_0\left(\frac{\ell}{x}\right)^{1/3}f(\eta), \tag{A6}$$

where $\widetilde{U}_0$ is a velocity scale and $f(\eta)$ is a nondimensional complex function of the reduced transverse coordinate $\eta$. Plugging such similarity solution (A6) into Eq. (A4) shows that $f(\eta)$ is a solution of the ordinary differential equation

$$3f'''+i(f+\eta f')=0, \tag{A7}$$

which is identical to Eq. (16) derived by Thomas and Stevenson[7] for the pressure field of internal waves. Following their development, we introduce the family of functions $f_m$ defined through

$$f_m(\eta)=c_m+is_m=\int_0^\infty K^m e^{-K^3}e^{iK\eta}dK, \tag{A8}$$

where $c_m$ and $s_m$ are real, and such that $f_0(\eta)$ is a solution of Eq. (A7).

The velocity in the plan of the wave beam is therefore given by $u_x=\Re\{U\}$ and $u_y=\Im\{U\}$, leading to

$$u_x=\frac{U_0^*}{E_0(0)}\left(\frac{\ell}{x}\right)^{1/3}[c_0(\eta)\cos(\sigma t)+s_0(\eta)\sin(\sigma t)],$$

$$u_y=\frac{U_0^*}{E_0(0)}\left(\frac{\ell}{x}\right)^{1/3}[s_0(\eta)\cos(\sigma t)-c_0(\eta)\sin(\sigma t)],$$

with $U_0^*=E_0(0)\widetilde{U}_0\simeq0.893\widetilde{U}_0$, where we introduce the family of envelopes $E_m(\eta)=|f_m(\eta)|=(c_m^2+s_m^2)^{1/2}$ for $m=0,1$.

Similarly, the vorticities in the plan of the wave beam are $\omega_x=\Re\{W\}$ and $\omega_y=\Im\{W\}$ so that

$$\omega_x=\frac{W_0^*}{E_1(0)}\left(\frac{\ell}{x}\right)^{2/3}[-c_1(\eta)\cos(\sigma t)-s_1(\eta)\sin(\sigma t)],$$

$$\omega_y=\frac{W_0^*}{E_1(0)}\left(\frac{\ell}{x}\right)^{2/3}[-s_1(\eta)\cos(\sigma t)+c_1(\eta)\sin(\sigma t)],$$

with $W_0^*=[E_1(0)/E_0(0)]U_0^*/\ell\simeq0.506U_0^*/\ell$.

The velocity and vorticity envelopes, defined as $u_0=(\langle u_x^2\rangle+\langle u_y^2\rangle)^{1/2}$ and $\omega_0=(\langle\omega_x^2\rangle+\langle\omega_y^2\rangle)^{1/2}$, where $\langle\cdot\rangle$ is the time-average over one wave period, are given by

$$u_0=U_0^*\left(\frac{\ell}{x}\right)^{1/3}\frac{E_0(\eta)}{E_0(0)},$$

$$\omega_0=W_0^*\left(\frac{\ell}{x}\right)^{2/3}\frac{E_1(\eta)}{E_1(0)}.$$

The two normalized envelopes $E_m(\eta)/E_m(0)$ are compared in Fig. 14. Interestingly, they closely coincide up to $\eta\simeq4$, but the vorticity envelope decreases much more rapidly than the velocity envelope as $\eta\to\infty$ (one has $E_m\propto1/\eta^{m+1}$ for $\eta\gg1$). The thickness $\eta_{1/2}$ of the two envelopes, defined such that

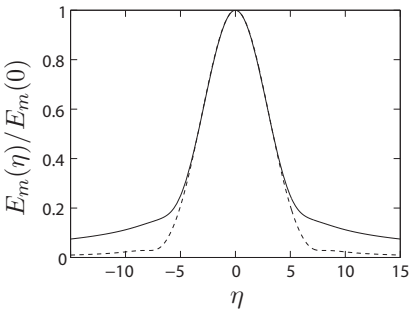


FIG. 14. Normalized velocity [(—) $m=0$] and vorticity [(- -) $m=1$] envelopes of the similarity solutions.

$E_m(\eta_{1/2}/2)=E_m(0)/2$, turns out to be almost equal: $\eta_{1/2}\simeq 6.841$ for $m=0$ and $\eta_{1/2}\simeq 6.834$ for $m=1$. In dimensional units, the wave thickness is thus given by Eq. (5).

It is interesting to note that velocity and vorticity in the present analysis are analogous to the pressure and velocity in the analysis of Thomas and Stevenson.[7] One consequence is that the lateral decay of the velocity envelope is sharper for an internal wave (as $1/\eta^2$) than for an inertial wave (as $1/\eta$).

Finally, the $z$ component of the velocity is obtained using incompressibility $(\partial_x u_x+\partial_z u_z=0)$,

$$u_z=\frac{1}{3}\frac{U_0^*}{E_0(0)}\left(\frac{\ell}{x}\right)\eta[c_0(\eta)\cos(\sigma t)+s_0(\eta)\sin(\sigma t)], \qquad \text{(A9)}$$

which is zero in the center of the wave beam $(\eta=0)$. Interestingly, the envelope of $u_z$ is given by $\eta E_0(\eta)$, which tends toward 1 as $\eta\to\infty$ so that no thickness could be defined for $u_z$.

The streamlines projected in the vertical plane $(x,z)$ can be deduced from the ratio of the velocity components,

$$\frac{u_z}{u_x}=\frac{1}{3}\frac{z}{x}, \qquad \text{(A10)}$$

which integrates to $x=cz^{1/3}$. This result shows that the streamlines lie in surfaces of constant $\eta$, invariant along $y$. As a consequence, a particle trajectory is an approximate circle wrapped on a curved surface, such that $z=\eta^*\ell^{2/3}x^{1/3}$, with $\eta^*$ given by the initial location of the particle.

Finally, we note that the quasiparallel approximation used in the present analysis is satisfied for $|u_z|/|u_x|\ll 1$. Using $|u_z|/|u_x|=\eta^{1/3}(\ell/x)^{1/3}/3$, and evaluating the envelope ratio at the boundary of the wave, i.e., for $\eta=\eta_{1/2}/2\simeq 3.42$, this criterion is satisfied within 10% for $x>38\ell$.

[1] H. Greenspan, *The Theory of Rotating Fluids* (Cambridge University Press, London, 1968).
[2] J. Lighthill, *Waves in Fluids* (Cambridge University Press, London, 1978).
[3] J. Pedlosky, *Geophysical Fluid Dynamics* (Springer-Verlag, Heidelberg, 1987).
[4] C. Cambon, "Turbulence and vortex structures in rotating and stratified flows," Eur. J. Mech. B/Fluids **20**, 489 (2001).
[5] O. M. Phillips, "Energy transfer in rotating fluids by reflection of inertial waves," Phys. Fluids **6**, 513 (1963).
[6] D. E. Mowbray and B. S. H. Rarity, "A theoretical and experimental investigation of the phase configuration of internal waves of small amplitude in a density stratified liquid," J. Fluid Mech. **28**, 1 (1967).
[7] N. H. Thomas and T. N. Stevenson, "A similarity solution for viscous internal waves," J. Fluid Mech. **54**, 495 (1972).
[8] B. R. Sutherland, S. B. Dalziel, G. O. Hughes, and P. F. Linden, "Visualization and measurement of internal waves by 'synthetic Schlieren.' Part 1. Vertically oscillating cylinder," J. Fluid Mech. **390**, 93 (1999).
[9] M. R. Flynn, K. Onu, and B. R. Sutherland, "Internal wave excitation by a vertically oscillating sphere," J. Fluid Mech. **494**, 65 (2003).
[10] L. Gostiaux, T. Dauxois, H. Didelle, J. Sommeria, and S. Viboud, "Quantitative laboratory observations of internal wave reflection on ascending slopes," Phys. Fluids **18**, 056602 (2006).
[11] L. Gostiaux, H. Didelle, S. Mercier, and T. Dauxois, "A novel internal waves generator," Exp. Fluids **42**, 123 (2007).
[12] D. Fultz, "A note on overstability and the elastoid-inertia oscillations of Kelvin, Soldberg, and Bjerknes," J. Meteorol. **16**, 199 (1959).
[13] A. D. McEwan, "Inertial oscillations in a rotating fluid cylinder," J. Fluid Mech. **40**, 603 (1970).
[14] R. Manasseh, "Distortions of inertia waves in a rotating fluid cylinder forced near its fundamental mode resonance," J. Fluid Mech. **265**, 345 (1994).
[15] L. R. M. Maas, "Wave focusing and ensuing mean flow due to symmetry breaking in rotating fluids," J. Fluid Mech. **437**, 13 (2001).
[16] P. Meunier, C. Eloy, R. Lagrange, and F. Nadal, "A rotating fluid cylinder subject to weak precession," J. Fluid Mech. **599**, 405 (2008).
[17] F. S. Godeferd and L. Lollini, "Direct numerical simulations of turbulence with confinement and rotation," J. Fluid Mech. **393**, 257 (1999).
[18] L. Messio, C. Morize, M. Rabaud, and F. Moisy, "Experimental observation using particle image velocimetry of inertial waves in a rotating fluid," Exp. Fluids **44**, 519 (2008).
[19] B. Voisin, "Limit states of internal wave beams," J. Fluid Mech. **496**, 243 (2003).
[20] K. S. Peat, "Internal and inertial waves in a viscous rotating stratified fluid," Appl. Sci. Res. **33**, 481 (1978).
[21] D. G. Hurley and G. Keady, "The generation of internal waves by vibrating elliptic cylinders. Part 2. Approximate viscous solution," J. Fluid Mech. **351**, 119 (1997).
[22] DAVIS, LaVision GmbH, Anna-Vandenhoeck-Ring 19, 37081 Goettingen, Germany, complemented with the PIVMat toolbox for MATLAB, http://www.fast.u-psud.fr/pivmat.
[23] L. R. M. Maas, "On the amphidromic structure of inertial waves in a rectangular parallelepiped," Fluid Dyn. Res. **33**, 373 (2003).
[24] Y. V. Kistovich and Y. D. Chashechkin, "Mass transport and the force of a beam of two-dimensional periodic internal waves," J. Appl. Math. Mech. **65**, 237 (2001).
[25] M. S. Longuet-Higgins, "Mass transport in water waves," Philos. Trans. R. Soc. London, Ser. A **245**, 535 (1953).
[26] A numerical integration of the particle trajectory in the center of the beam ($z=0$) actually shows that the numerical prefactor in Eq. (12) is 1.047 instead of 2/3.

# Chapitre 3

# Turbulence en rotation

## 3.1 Introduction

Pour qui vient de la "turbulence tout court" (entendez, la turbulence homogène et isotrope), la turbulence en rotation apparaîtra assurément comme un problème difficile. Les concepts issus de la dynamique des fluides géophysiques, de la turbulence d'onde, et les connections avec la turbulence stratifiée et la turbulence magnétohydrodynamique, en font un sujet vaste et ramifié. L'importance considérable de ce problème, tant pour les applications géophysiques qu'industrielles, et ses liens avec d'autres problèmes ouverts, comme la génération d'un champ magnétique par effet dynamo, en font un sujet de recherche extrêmement actif aujourd'hui, tant sur les fronts théoriques que numériques et expérimentaux.

Le problème de l'influence d'une rotation d'ensemble sur un écoulement turbulent est un problème ancien, dont l'étude a débuté à la fin des années 1950 [132]. Malgré cet âge honorable, il peut être surprenant de constater que certaines questions apparamment simples, telles que la direction de la cascade d'énergie, l'origine physique de la formation de structures colonnaires ou encore l'asymétrie entre cyclones et anticyclones, soient toujours ouvertes. Si les progrès semblent si lents sur ces sujets, c'est que les difficultés sont nombreuses :

(i) L'approche théorique est confrontée, en plus des difficultés "classiques" inhérentes au problème de la turbulence isotrope (non-localité, caractère multi-échelle, fermetures), à la difficulté supplémentaire de manipuler des quantités anisotropes, ne se réduisant pas à de simples champs scalaires. Des approches asymptotiques, valables en milieu infini et dans la limite où $Ro \ll 1$ et $Re \gg 1$, sont accessibles sous certaines conditions (théorie de la distortion rapide, turbulence d'onde), mais le monde réel du $Ro \simeq O(1)$ avec confinement constitue encore un problème non résolu.

(ii) L'approche numérique est confrontée à deux difficultés : Outre le besoin d'une résolution spatiale très élevée lorsque $Re \gg 1$, la grande disparité des échelles de temps (linéaire et non linéaire) dans la limite $Ro \ll 1$ implique des temps de simulation très élevés. En outre, les conditions aux limites, le plus souvent périodiques, peuvent introduire des biais importants lorsque les échelles de corrélation axiale atteignent la taille du domaine.

(iii) Enfin, les expériences ne sont pas en reste, et l'on peut identifier deux grandes difficultés. La première réside dans l'obtention en laboratoire de petits nombres de Rossby, qui nécessitent d'une part une vitesse de rotation élevée ou une expérience de grande taille, et d'autre part des vitesses relatives modérées dans le référentiel tournant, venant contredire l'exigence de grands nombres de Reynolds. La seconde difficulté est de nature instrumentale :

les mesures doivent être effectuées dans le référentiel tournant, et doivent permettre d'accéder à 2 voire 3 composantes de vitesse.

Mes travaux dans ce domaine ont débuté en 2003, avec M. Rabaud et C. Morize, avec une première expérience de turbulence de grille utilisant la "petite" plateforme tournante du FAST. Ces travaux se concentrent sur la configuration modèle que constitue le déclin d'une turbulence en rotation "initialisée" dans un état 3D approximativement homogène et isotrope. La nécessité d'appréhender la structuration anisotrope de l'écoulement a motivé une collaboration avec J. Sommeria (LEGI) pour une campagne de mesure sur la "grande" plateforme Coriolis, à Grenoble en 2005. Enfin, ces travaux se poursuivent depuis 2009 avec P.-P. Cortet et C. Lamriben, grâce à l'installation au FAST de la nouvelle plateforme tournante de taille intermédiaire "Gyroflow".

Dans ce chapitre nous tenterons de décrire certains aspects du "problème de la turbulence en rotation", puis de présenter brièvement les approches expérimentales qui ont précédées nos travaux. Dans un second temps, en prenant comme fil conducteur nos résultats expérimentaux, nous tenterons de pointer quelques idées clefs et questions encore ouvertes sur ce sujet. Enfin, nous conclurons sur quelques directions d'études pour le futur, et plus précisément sur quelques projets d'expériences qui pourront être réalisés sur la nouvelle plateforme "Gyroflow".

## 3.2 Position du problème

### 3.2.1 Phénoménologie

Afin de décrire la turbulence en rotation, deux approches extrèmes sont envisageables :

(1) **Rotation modérée, nombre de Rossby grand ou d'ordre 1** : Le problème est celui d'une turbulence "classique" (classiquement homogène et isotrope), que l'on vient perturber par une "horloge extérieure", dont le temps $T_\Omega$ est grand ou comparable au temps de retournement à grande échelle $L/U$. La turbulence est faiblement anisotrope dans ce cas.

(2) **Rotation forte, nombres de Rossby très inférieurs à 1** : Le problème peut être vu comme une superposition d'ondes d'inertie rapides, dont les interactions non-linéaires régissent le comportement à temps long ("dérives séculières") de l'écoulement. La turbulence est alors fortement anisotrope.

La situation se complique entre ces deux situations extrèmes, pour des nombres de Rossby intermédiaires, qui sont ceux rencontrés le plus souvent dans les expériences ou les écoulements naturels, et qui sont ceux accessibles aux simulations numériques directes. En effet, la large gamme de temps caractéristiques présente en turbulence fait que, selon les échelles considérées, le système peut se trouver simultanément dans les situations de nombres de Rossby petits et grands.

Concernant le cas extrème de rotation forte (2), notons que la limite triviale $Ro = 0$ (pas de non-linéarité) n'est d'aucune utilité : l'écoulement se réduit alors à une simple superposition (interférence) d'ondes d'inertie purement linéaires, sans interaction. Aucun transfert d'énergie n'étant possible dans cette situation, alors si la distribution d'énergie initiale est isotrope, elle le reste à tout temps[1].

[1]Dans cette situation, l'évolution temporelle d'une structure donnée à un instant initial s'obtient selon la démarche classique pour un système d'ondes dispersives : On décompose la structure initiale $\mathbf{u}(\mathbf{x}, 0)$ dans

Après quelques 30 ans d'efforts expérimentaux, théoriques et numériques, un certain nombre de propriétés de la turbulence en rotation sont maintenant bien établies. Nous pouvons mentionner 3 résultats clefs dans ce domaine :

1. La rotation d'ensemble induit une anisotropie de l'écoulement, compatible avec une tendance à la bi-dimensionalisation [22].
2. La cascade d'énergie vers les petites échelles est inhibée. Dans le cas d'une turbulence en déclin, cette inhibition conduit à un ralentissement de la décroissance de l'énergie [70].
3. L'écoulement s'organise en structures tourbillonnaires colonnaires relativement stables, présentant une brisure de symétrie en faveur des tourbillons cycloniques [5].

Les deux premiers résultats ne sont pas indépendants : en particulier, le ralentissement du déclin de l'énergie n'est pas une conséquence directe de l'action de la force de Coriolis (cette force ne travaille pas : $\mathbf{u} \cdot (\mathbf{\Omega} \times \mathbf{u}) = 0$), mais résulte de l'anisotropisation de l'écoulement. Le troisième résultat est plus subtil, et ne fait pas encore l'objet d'un consensus ; nous y reviendrons en Section 3.4.3.

Ces résultats sont brièvement décrits ci-après, et le lecteur est renvoyé au chapitre 4 du livre de Sagaut & Cambon (2008) [119] pour une revue plus détaillée.

#### Cas particulier de la turbulence en déclin

Le cas d'une turbulence en déclin dans un référentiel en rotation est celui qui nous interessera plus particulièrement dans la suite. Dans ce cas, les nombres de Reynolds et de Rossby instantannés,

$$Re(t) = \frac{u'L}{\nu}, \qquad Ro(t) = \frac{u'}{2\Omega L},$$

où $u'(t)$ est l'échelle de vitesse turbulente et $L(t)$ l'échelle intégrale (horizontale par exemple), sont des fonctions décroissantes du temps, comme représenté sur la figure 3.1(a). Si l'on part d'une situation initiale homogène et isotrope, caractérisée par $Re \gg 1$ et $Ro \gg 1$, alors la situation intermédiaire telle que $Ro(t^*) \simeq O(1)$ sera atteinte lors du déclin. C'est à ce moment que le couplage entre effets linéaires (force de Coriolis) et non linéaires est maximum, se traduisant notamment par des transferts d'énergie anisotropes, ainsi que par la naissance d'une asymétrie cyclone-anticyclone [13]. A temps plus long, le couplage diminue, mais le système "hérite" des propriétés acquises lors de son passage à $Ro \simeq O(1)$, suggérant que l'état asymptotique résulte de l'histoire de la turbulence intégrée le long de sa trajectoire.

### 3.2.2 Les approches expérimentales

Une difficulté importante pour aborder le problème de la turbulence en rotation d'un point de vue expérimental est l'impossibilité de concilier les critères d'*homogénéité* et de *stationarité*. La situation idéalisée de Turbulence en Rotation Homogène et Stationnaire est donc une situation académique très artificielle, accessible uniquement au moyen de simulations numériques.

---

l'espace de Fourier, $\sum_{\mathbf{k}} \hat{\mathbf{u}}_{\mathbf{k}}(0) e^{i\mathbf{k}\cdot\mathbf{x}}$, puis l'on fait évoluer la phase de chaque composante $\mathbf{k}$ selon la relation de dispersion (i.e., $\hat{\mathbf{u}}_{\mathbf{k}}(t) = \hat{\mathbf{u}}_{\mathbf{k}}(0) e^{i\sigma(\mathbf{k})t}$), enfin on resomme dans l'espace physique pour obtenir $\mathbf{u}(\mathbf{x}, t)$. Dans ce processus, on voit que seule la phase des ondes évolue, mais que leurs amplitudes, et donc le spectre d'énergie $|\hat{\mathbf{u}}_{\mathbf{k}}(t)|^2$, n'évoluent pas : elles sont fixées par le spectre initial $|\hat{\mathbf{u}}_{\mathbf{k}}(0)|^2$. Ainsi, si la distribution d'énergie initiale est isotrope, elle le reste à tout temps : une anisotropie ne peut pas naître dans la limite linéaire.

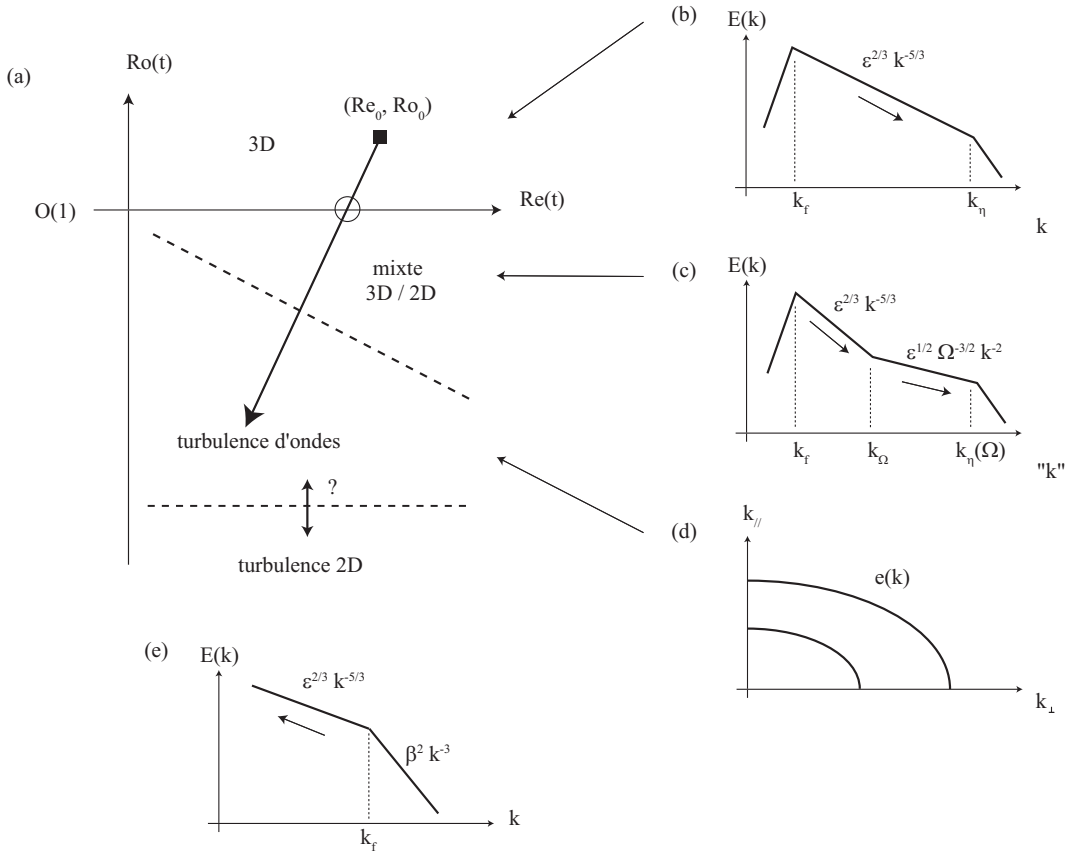


FIG. 3.1 – Synthèse des différents "états" d'une turbulence en rotation en déclin. (a) Le système suit une trajectoire dans l'espace des nombres de Reynolds et Rossby turbulents. Les spectres schématisés en (b)-(e) sont ceux de systèmes stationnaires, en faisant l'hypothèse qu'ils restent pertinents de façon instantanée lors du déclin. (b) Spectre de Kolmogorov (1941) de la turbulence 3D, dans le cas $Re \gg 1$, $Ro \gg 1$. (c) Spectre phénoménologique isotrope de Zhou (1995) [144]. (d) Spectre anisotrope dans l'espace $(k_\perp, k_\parallel)$. (e) Spectre de Kraichnan de la turbulence 2D (pour référence).

Dès lors, deux stratégies sont possibles, illustrées en figure 3.2 par quelques expériences modèles :

1. **Turbulence en déclin en rotation** : *homogène* mais *instationnaire*. On peut distinguer deux situations :
   (i) *Déclin spatial*, en soufflerie avec écoulement axial moyen (fig. 3.2a).
   (ii) *Déclin temporel*, en cuve tournante (fig. 3.2b).
2. **Turbulence forcée en rotation** : *stationnaire* mais *inhomogène*, en cuve tournante (fig. 3.2c).

Jusqu'à il y a peu, les études expérimentales devaient se contenter de mesures en un point, au moyen d'anémométrie à fil chaud : Ibbetson & Tritton (1975) [69], dans une expérience de grille translatée en cuve fermée, ou encore Wigeland & Nagib (1978) [139] et Jacquin *et al.* (1990) [70], dans des expériences de turbulence de grille en soufflerie en aval d'une section de conduite en rotation. Ces dernières mesures [70] constituent encore des résultats de référence sur le sujet.

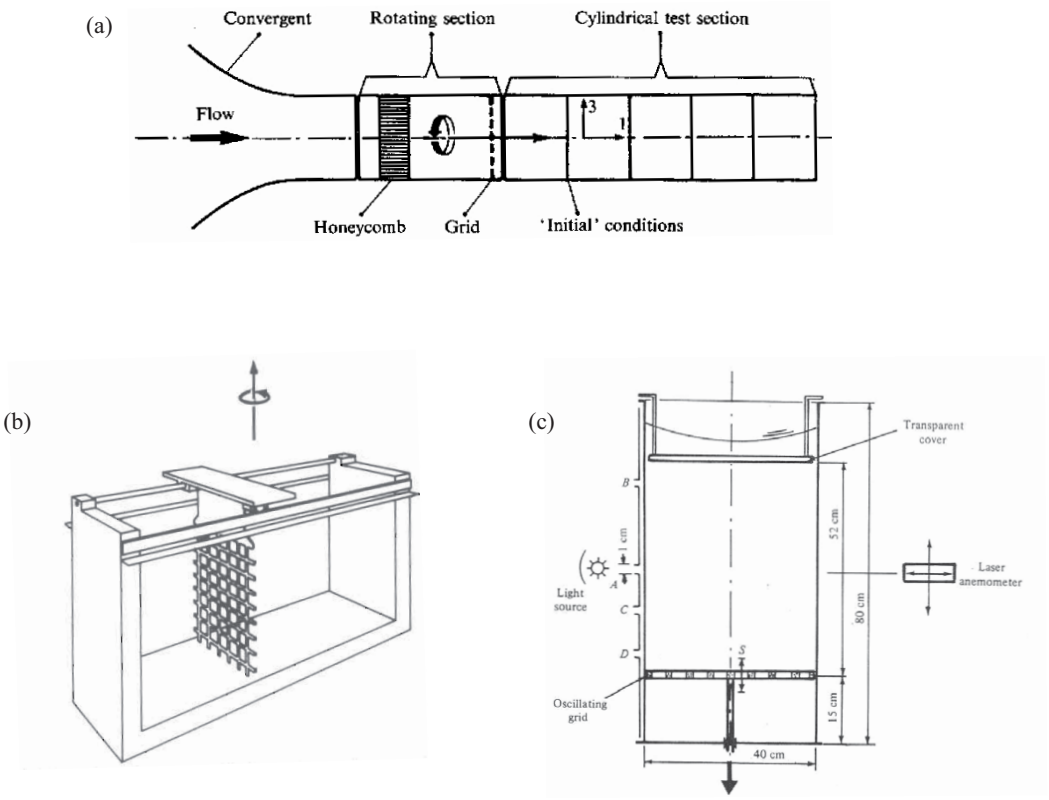


FIG. 3.2 – Revue de quelques expériences de turbulence en rotation. (a), Turbulence en déclin spatial, en soufflerie ; d'après Jacquin *et al.* (1990) [70]. (b), Turbulence en déclin temporel, en cuve tournante ; d'après Dalziel (1992) [40]. (c), Turbulence forcée, en cuve tournante ; d'après Hopfinger *et al.* (1982) [68].

Concernant la structuration spatiale de la turbulence en rotation, cet aspect n'a pu être abordé que de manière qualitative dans un premier temps, au moyen de visualisations (Hopfinger *et al.* (1982) [68] ; Dickinson & Long (1983) [44]). Les expériences de Hopfinger *et al.* (1982) [68] ont été en particulier les premières à mettre en évidence la brise de symétrie cyclone-anticyclone, sur laquelle nous reviendrons en Section 3.4.3.

Depuis quelques années, l'arrivée de méthodes optiques quantitatives, en premier lieu la PIV (Particle Image Velocimetry) mais aussi la PTV (Particle Tracking Velocimetry), avec la possibilité de les embarquer dans le référentiel tournant, a considérablement transformé l'approche expérimentale de ce problème. Ces méthodes optiques ont permis de concilier les aspects *structurels* (organisation spatiale), qui n'étaient accessibles que par des visualisations, et *statistiques* (moments, spectres), qui n'étaient eux accessibles que par des mesures en un point (ou en deux points, avec l'utilisation de l'hypothèse de Taylor en présence d'un écoulement moyen).

Une étude pionnière dans ce domaine est celle de S. Dalziel (1992) [40] à Cambridge, qui le premier a mis en œuvre des mesures de PIV en référentiel tournant, dans une expérience de turbulence de grille translatée dans un canal en rotation. Cet auteur a en outre été le premier à décrire en détail les problèmes liés à la génération de modes d'inertie en géométrie fermée, sur lesquels nous reviendrons en Section 3.5.1.

Etant donnée la difficulté de mise en œuvre d'un système de PIV en référentiel tournant, il faut attendre 2002, avec les expériences du groupe de H. Swinney à l'Université du Texas,

pour que cette approche expérimentale prenne son véritable essor [3, 117]. Ces expériences ont été rapidement suivies à partir de 2005 par nos travaux [104, 103, 120, 95], ainsi que ceux des équipes de P. Davidson et S. Dalziel au DAMTP Cambridge [123]. Enfin, très récemment, deux équipes mettent en oeuvre des méthodes de PIV stéréoscopiques et de PTV 3D dans des écoulements forcés en référentiel tournant : l'équipe de H. Clercx à l'Université de Technologie d'Eindhoven [133, 134], et celle de B. Lüthi à l'Ecole Polytechnique de Zürich.

Ce rapide tour d'horizon d'expériences n'est pas exhaustif, et fait en particulier l'impasse sur les nombreuses études de turbulence stratifiée en rotation. Pour une revue récente et une comparaison de ces différentes expériences, on pourra se reporter à l'article de van Bokhoven *et al.* (2009) [134].

## 3.3 Approches théoriques

### 3.3.1 Description spectrale

L'influence première de la rotation sur un écoulement turbulent est d'induire une direction privilégiée le long de l'axe de rotation, et par conséquence une tendance à la bi-dimensionalisation. Cette tendance est toutefois subtile : elle est clairement visible sur certaines quantités, comme les échelles intégrales, tandis qu'elle est très peu marquée sur d'autres, comme les rapports des composantes de vitesse (ou, de manière équivalente, sur le tenseur de Reynolds $\langle u_i' u_j' \rangle$). Cette subtilité tient notamment à la distinction cruciale entre *dimensionalité* et *componentalité* [22] : comme déjà vu au chapitre 2, dans le cas limite d'un écoulement très lent comparé à la rotation d'ensemble, le champ de vitesse est 2D-3C (2 dimensions et 3 composantes). Par opposition, un écoulement stratifié très lent comparé à la fréquence de Brunt-Väisälä sera, lui, 3D-2C (3 dimensions et 2 composantes), comme illustré en figure 3.3. Il resulte de la nature 2D-3C de la turbulence en rotation que la vitesse ne peut constituer un indicateur robuste de bidimensionalisation.

L'origine de cette tendance à la bi-dimensionalisation sous l'effet de la rotation tient aux propriétés anisotropes des ondes d'inertie : l'énergie des structures turbulentes sera rayonnée selon une direction d'autant plus proche de la verticale que celles-ci seront "lentes", conduisant ainsi à une organisation de la turbulence en structures colonnaires.

En supposant l'homogénéité de l'écoulement, cette structuration anisotrope se décrit très bien dans l'espace de Fourier. Les demi-sphères de la figure 3.3 représentent l'espace de Fourier axisymétrique, dans lequel un vecteur d'onde $\mathbf{k}$ est paramétré par sa norme, $k$, et l'angle qu'il fait avec la direction verticale, $\theta$. La tendance à la bi-dimensionalisation se traduit alors par un transfert angulaire d'énergie selon $\theta$ croissant et, *in fine*, par une concentration de l'énergie dans le plan horizontal $k_z = 0$.

La description complète de la turbulence en rotation repose sur l'introduction de 3 spectres : énergie, hélicité et polarisation [21, 119]. Pour simplifier le propos, nous n'examinerons ici que le spectre d'énergie tri-dimensionnel $e(\mathbf{k}) = e(k_\perp, k_\parallel)$, avec $k_\parallel = k_z$ ici. Un écoulement purement 2D doit satisfaire

$$e(k_\perp, k_\parallel) = \frac{E(k_\perp)}{2\pi k_\perp} \delta(k_\parallel), \tag{3.1}$$

où $E(k_\perp)$ est le spectre unidimensionnel et $\delta$ la distribution de Dirac. La concentration singulière d'énergie en $k_\parallel = 0$ traduit bien l'invariance par translation verticale ($\partial/\partial x_\parallel = 0$) d'un écoulement 2D, sans rien impliquer sur la composante verticale $u_z$, non affectée par la

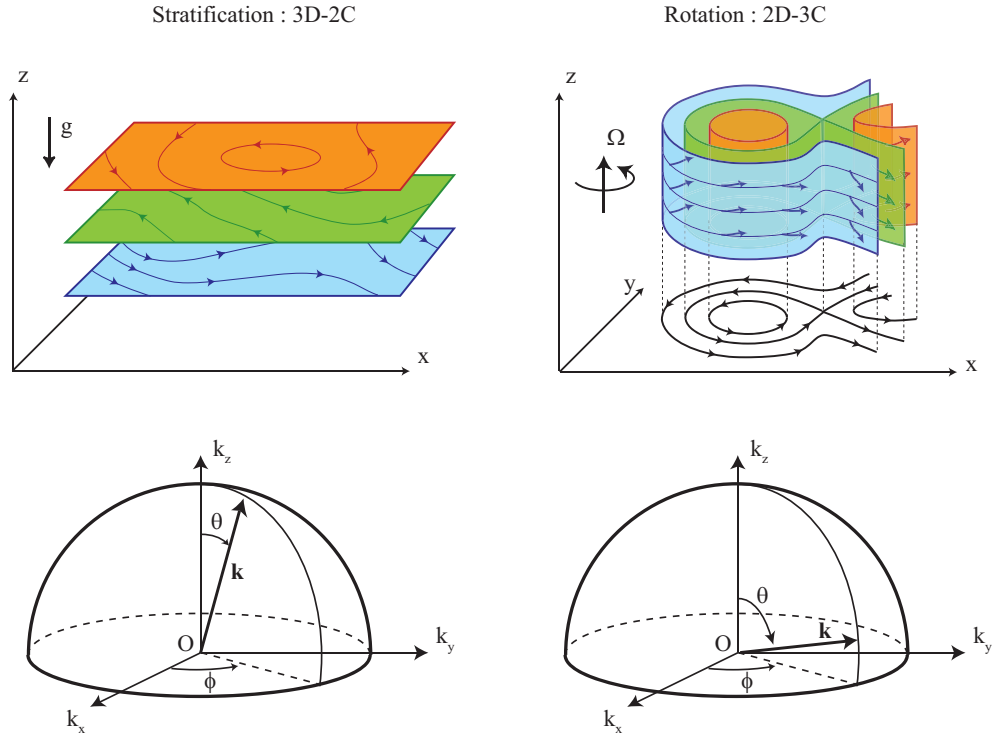


FIG. 3.3 – Vue dans l'espace physique et spectral de la structure d'un écoulement dominé par les effets de stratification (à gauche) et de rotation (à droite). Cette figure illustre la différente entre *dimensionalité* et *componentalité* : la turbulence stratifiée est 3D-2C, tandis que la turbulence en rotation en 2D-3C.

force de Coriolis[2] : l'écoulement est bien 2D-3C. Ce mode 2D-3C est appelé *variété lente* (ou *géostrophique*), car il est associé à une fréquence nulle selon la relation de dispersion des ondes d'inertie (2.3), en accord avec le théorème de Taylor-Proudman. Cependant, il est important de remarquer que ce théorème ne permet aucunement d'expliquer la transition 3D → 2D elle-même. En effet, ce théorème ne s'applique que dans la limite de non-linéarités négligeables, et ce sont précisément les non-linéarités, modifiées par la force de Coriolis, qui sont responsables d'un transfert préférentiel de l'énergie vers les modes horizontaux [21, 138, 22].

### 3.3.2 Phénoménologie quasi-isotrope (rotation modérée)

La situation pour laquelle le nombre de Rossby est d'ordre 1 est délicate du fait que les temps caractéristiques linéaire $T_\Omega$ et non linéaire $T = L/U$ sont du même ordre de grandeur. Une approche simplifiée de cette situation, proposée par Zhou (1995) [144] (voir aussi Canuto & Dubovikov (1997) [24]), consiste à reprendre l'analyse classique "à la Kolmogorov" de la turbulence homogène et isotrope, basée sur un transfert d'énergie échelle-à-échelle régi par un temps caractéristique $\tau(r) = r/u'_r$ (où $u'_r$ note la fluctuation typique de vitesse à une échelle $r$), et d'y incorporer le temps additionel $T_\Omega$ comme unique signature de la rotation d'ensemble.

Dans cette approche on postule que, bien que la rotation affecte les grandes échelles, il reste la possibilité que les échelles $r \ll L$, plus rapides, "échappent" à l'effet de la rotation si

[2]Par incompressibilité, la transformée de Fourier de la vitesse est perpendiculaire au vecteur d'onde, $\mathbf{k}\cdot\hat{\mathbf{u}}_\mathbf{k} = 0$. Les modes tels que $k_z = 0$ peuvent donc être associés à des composantes de vitesse *a priori* quelconques.

leur "nombre de Rossby local" $Ro(r) = T_\Omega/\tau(r) = u'_r/2\Omega r$ reste supérieur à 1. Il existe alors une échelle de transition,

$$r_\Omega = \epsilon^{1/2}(2\Omega)^{-3/2} = LRo^{-3/2}, \tag{3.2}$$

telle que $Ro(r_\Omega) \simeq 1$. Cette échelle joue un rôle analogue à l'échelle d'Ozmidov pour les écoulements stratifiés, et a été introduite dans le contexte de la turbulence en rotation par Zeman (1994) [143]. Pour $r \ll r_\Omega$ on retrouve la cascade de Kolmogorov classique, caractérisée par un spectre d'énergie $E(k) \simeq \epsilon^{2/3}k^{-5/3}$ (fig. 3.1b). Pour $r_\Omega \ll r \ll L$, la dynamique est dominée par le temps caractéristique $T_\Omega$, et une analyse dimensionelle [144, 24] montre que le spectre prend la forme (fig. 3.1c) :

$$E(k) \simeq (\epsilon\Omega)^{1/2}k^{-2}. \tag{3.3}$$

Il est important de noter que ce raisonnement, uniquement basé sur des comparaisons de temps ou d'échelles caractéristiques, reste intrinsèquement isotrope, et ne peut prédire ni la direction des transferts d'énergie, ni la structuration anisotrope induite par la rotation. En particulier, dans l'expression (3.3), la direction du vecteur d'onde $\mathbf{k}$ n'est pas spécifiée, et le nombre d'onde $k$ n'est assimilable qualitativement à la composante $k_\perp$ que pour $Ro$ suffisament petit.

### 3.3.3 Transferts d'énergie

#### Cas isotrope

D'une manière générale, les transferts d'énergie peuvent être caractérisés à partir des corrélations triples de la vitesse, exprimées soit dans l'espace physique (équation de von Kármán-Howarth), soit dans l'espace spectral (équation de Lin). Le lien entre ces 2 approches a été discuté récemment dans Cambon *et al.* (2010) [20]. A noter que, bien que la description des transferts soit plus délicate à manipuler dans l'espace physique, du fait du couplage non trivial entre vitesse et gradient de pression, ceux-ci sont beaucoup plus accessibles aux mesures expérimentales (en particulier, l'existence de "trous" de mesures ou de vecteurs aberrants dans les champs de PIV n'empêche pas le calcul de ces corrélations en deux points à partir des seuls vecteurs mesurés). Dans la formulation spectrale, une grande simplification provient de l'élimination du terme de pression par la condition d'incompressibilité, mais nécessite l'hypothèse d'homogénéité ; c'est la formulation la plus naturelle pour les simulations numériques avec conditions aux limites périodiques.

Dans le cas homogène et isotrope (sans rotation), les corrélations triples de vitesse peuvent s'exprimer simplement à partir d'une quantité scalaire, $S_3(r)$, la fonction de structure d'ordre 3, avec $S_n = \langle(\delta_r u_L)^n\rangle$ et $\delta_r u_L = [\mathbf{u}(\mathbf{x}+\mathbf{r}) - \mathbf{u}(\mathbf{x})] \cdot \mathbf{r}/|\mathbf{r}|$ l'incrément de vitesse longitudinale selon la direction $\mathbf{r}$. L'équation de von Kármán-Howarth s'écrit alors [57, 96]

$$-\frac{4}{5}\epsilon r = S_3(r) - 6\nu\frac{\partial S_2(r)}{\partial r}, \tag{3.4}$$

qui se réduit à la fameuse loi des 4/5, $S_3(r) = -(4/5)\epsilon r$, dans la limite des grands nombres de Reynolds. Le signe négatif de $S_3$ traduit la direction de la cascade d'énergie, des grandes vers les petites échelles (dans le cas de la turbulence 2D, on montre que $S_3 = (3/2)\epsilon r > 0$ dans la cascade inverse [127]).

L'équation d'évolution pour le spectre d'énergie $E(k)$, toujours dans le cas isotrope, s'exprime par l'équation de Lin [119]

$$\partial_t E(k) = T(k) - 2\nu k^2 E(k),$$

qui a la même structure que l'équation de von Kármán-Howarth (3.4). Dans cette équation, le transfert spectral d'énergie $T(k)$ est lié au flux d'énergie par $F(k) = -\partial T/\partial k$. De manière équivalente à la formulation dans l'espace des échelles, le signe de $F(k)$ indique la direction de la cascade d'énergie.

Le transfert d'énergie $T(k)$ provient de l'intéraction non-linéaire entre vecteurs d'ondes. Il s'exprime comme une somme sur tous les vecteurs d'onde $\mathbf{p}, \mathbf{q}$ formant un triangle avec $\mathbf{k}$ :

$$\mathbf{k} + \mathbf{p} + \mathbf{q} = 0. \tag{3.5}$$

L'examen des différentes géométries de triades $(\mathbf{k}, \mathbf{p}, \mathbf{q})$, en particulier leur nature "locale" ($|\mathbf{k}| \simeq |\mathbf{p}| \simeq |\mathbf{q}|$) ou "non-locale" ($|\mathbf{k}|, |\mathbf{p}| \gg |\mathbf{q}|$ par exemple) permet d'estimer quelles sont celles qui contribuent en moyenne à une cascade directe ou inverse.

Parmi les différentes formulations possibles de ce problème, en particulier parmi les différentes bases de projection de la vitesse dans l'espace de Fourier [119], celle reposant sur les modes hélicaux, décrits dans Cambon & Jacquin (1989) [21], s'avère particulièrement fructueuse. Un argument élégant de stabilité[3] proposé par Waleffe (1992) [137] permet de montrer que, dans le cas isotrope, le transfert d'énergie est principalement le résultat d'intéractions non-locales, conduisant à un transfert préférentiel vers les grands nombres d'onde.

**Cas avec rotation**

En présence de rotation, les transferts d'énergie sont anisotropes, et peuvent avoir une contribution à la fois en échelle ("cascade") et angulaire (tendance 3D → 2D) [138, 21, 22]. Dans la prise en compte des triades (3.5), la relation de dispersion des ondes d'inertie, $\sigma(\mathbf{k}) = 2\mathbf{\Omega}\cdot\mathbf{k}/k$ (2.3), fait apparaître un terme oscillant dans le transfert $T(\mathbf{k})$, de la forme

$$e^{i(\pm\sigma(\mathbf{k})\pm\sigma(\mathbf{p})\pm\sigma(\mathbf{q}))t}. \tag{3.6}$$

Ce terme oscillant est présent dans toute corrélation triple (vitesse, mais aussi vorticité par exemple), et affecte donc la dynamique de toutes les corrélations doubles (spectre d'énergie, d'enstrophie, etc.)

Si cette approche reste valide à tout nombre de Rossby, il est toutefois instructif de considérer la limite de grande rotation ($Ro \ll 1$) pour comprendre l'effet de ce terme oscillant (3.6) dans la dynamique de la turbulence en rotation. Les oscillations de (3.6) deviennent alors très rapides (d'ordre $Ro^{-1}$ en temps adimensionné $\Omega t$), conduisant à un amortissement des transferts par mélange de phase, à l'exception du cas singulier où

$$\pm\sigma(\mathbf{k}) \pm \sigma(\mathbf{p}) \pm \sigma(\mathbf{q}) = 0. \tag{3.7}$$

Les triades (3.5) satisfaisant la relation (3.7) sont appellées *triades résonnantes* : ce sont les seules qui peuvent contribuer aux transferts d'énergie dans la limite $Ro \ll 1$.

L'utilisation de la base de modes hélicaux, introduite plus haut pour la turbulence isotrope, est particulièrement adaptée à la turbulence en rotation, car la structure des ondes d'inertie coïncide précisément avec ces modes hélicaux. L'application de l'argument de stabilité de Waleffe (1992) [137] à ces triades résonnantes (3.5)-(3.7) indique de fait l'existence d'un transfert angulaire préférentiel vers le mode horizontal [138] mais à une vitesse qui diminue à

[3]Le terme de stabilité est employé ici par analogie avec la dynamique d'un solide en rotation, dont on sait que la rotation autour de l'axe de moment d'inertie intermédiaire est instable au profit des deux autres axes.

mesure que l'on s'en approche. Cette conclusion est conforme aux simulations basées sur des hypothèses de fermeture de type EDQNM (Eddy-damped quasi-normal Markovian) [21, 22]. Le transfert d'énergie s'annule exactement lorsque l'un des vecteurs d'onde de la triade résonnante est strictement horizontal (variété lente) : le mode 2D ne peut être alimenté directement en énergie, et est donc découplé des modes 3D. Ce découplage a lieu dans une région proche de $k_z = 0$, d'"épaisseur" $\delta k_z \sim k/Ro$, qui coïncide bien avec le mode 2D dans la limite $Ro \ll 1$.

### 3.3.4 Cas limite : turbulence d'ondes (rotation très rapide)

Comme on l'a vu en Sec. 3.2.1, le cas trivial $Ro = 0$ exclut la possibilité de transferts d'énergie, et donc de turbulence. Si l'on considère en revanche la limite $Ro \to 0$, l'amplitude des ondes d'inertie ne peut plus être négligée, et les (faibles) non-linéarités induisent un couplage entre elles. Le formalisme de la "turbulence d'onde" (ou "turbulence faible") vise à décrire statistiquement un tel système d'ondes non-linéaires dispersives en faible interaction. Ce formalisme a été développé à partir des années 1960 [141], et a pu être appliqué à un grand nombre de situations physiques, incluant les ondes gravito-capillaires (nous y reviendrons au chapitre 4) ou la MHD (ondes d'Alfvén).

L'approche précédente a permi de mettre en évidence l'existence de transferts angulaires d'énergie en présence de rotation, mais sans pouvoir conduire à l'expression d'un spectre anisotrope. L'application du formalisme de turbulence d'onde au cas de la turbulence en rotation, réalisée indépendamment par Galtier (2003) [58] et Cambon *et al.* (2004) [23, 8] (modèle AQNM, Asymptotic Quasi-Normal Markovian), permet d'obtenir ce spectre :

$$e(k_\perp, k_\parallel) \simeq k_\perp^{-7/2} k_\parallel^{-1/2} \simeq (\cos\theta)^{-1/2} k^{-4}, \tag{3.8}$$

avec $\cos\theta = k_\parallel/k \simeq k_\parallel/k_\perp$ (figures 3.1d et 3.3). A noter que, après intégration sphérique pour $\cos\theta \ll 1$, le spectre unidimensionnel $E(k) \sim k^2 e(k)$ est compatible avec le spectre phénoménologique (3.3) proposé par Zhou [144].

Ce spectre (3.8) montre comme attendu une concentration de l'énergie vers le plan 2D, mais il ne coïncide pas avec un spectre bi-dimensionnel de la forme (3.1) : la turbulence d'ondes d'inerties ne décrit pas un état de turbulence 2D. Ce résultat n'est pas surprenant pour deux raisons : (i) le mode strictement 2D correspond au cas $k_\parallel = k_z = 0$, qui n'est pas décrit par définition pour $Ro \neq 0$ ; (ii) l'existence d'un flux d'énergie constant, et en particulier le *sens* de la cascade (ici vers les petites échelles), est un ingrédient de la théorie : celle-ci ne peut donc être compatible avec la turbulence 2D qui, elle, présente une cascade *inverse* d'énergie.

### 3.3.5 Discussion

Nous avons vu dans cette section comment, pour une turbulence en rotation *homogène* (et donc en milieu infini), une approche spectrale permettait de prédire une bi-dimensionalisation partielle de l'écoulement. La validité de cette tendance pour des réalisations expérimentales ou numériques de turbulence peut toutefois être questionnée, et ce pour plusieurs raisons :

- Dans le cas d'une turbulence forcée, l'existence d'un forçage implique une inhomogénéité, rendant l'approche spectrale problématique.
- Dans le cas d'une turbulence en déclin, possiblement homogène, la tendance à la bi-dimensionalisation ne peut être observée que si celle-ci intervient suffisamment rapidement par rapport au temps de déclin.

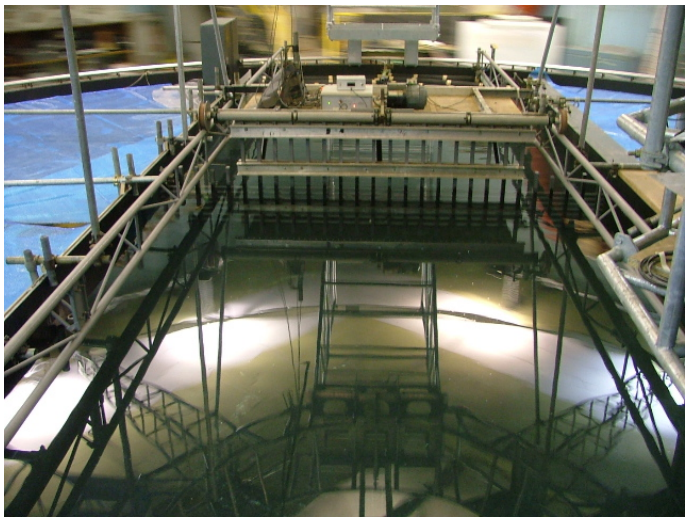

FIG. 3.4 – Expérience de turbulence de grille réalisée sur la plateforme Coriolis, à Grenoble. Un canal, de 4 m de large et 11 m de long, a été disposé sur la plateforme de 13 m de diamètre, en rotation avec une période $T_\Omega$ variant entre 30 et 120 s. La grille, que l'on distingue au fond, à une maille carrée de 17 cm, et est translatée le long du canal à une vitesse de 30 cm/s.

– La prise en compte de conditions aux limites, de type paroi fixe dans les expériences ou périodiques dans les simulations, introduit une discrétisation de l'espace de Fourier : on parle alors de *modes* d'inertie confinés (nous y reviendons en Section 3.5.1). Le mode 2D ne peut donc plus être approché continûment : il doit exister un nombre de Rossby limite pour lequel le mode 3D le plus proche de l'horizontal n'est plus distinguable du vrai mode 2D.
– Enfin, la présence de parois fixes perpendiculaires à l'axe de rotation, naturelles dans une expérience en cuve tournante, peut contraindre l'écoulement $2D-3C$ à devenir $2D-2C$ (vitesse purement horizontale), du moins pour des temps suffisament longs pour que les conditions aux limites influent tout le volume de l'écoulement.

On le voit, l'écart entre prédictions théoriques de turbulence homogène anisotrope et réalisation pratique (expérimentale ou numérique), reste important. En particulier, l'excitation d'un mode 2D avec cascade inverse, impossible dans le cadre d'une théorie homogène en milieu infini, n'est plus nécessairement exclu dans ce cas confiné ou périodique. Ces problèmes encore ouverts continuent de susciter d'importants travaux, dont nous présentons quelques contributions personnelles en § 3.4.

## 3.4 Résultats expérimentaux

### 3.4.1 Expériences

Les résulats que nous présentons dans la suite de ce chapitre ont été obtenus à partir de deux dispositifs expérimentaux : la "petite" plateforme tournante du FAST, déjà décrite au § 2.3.1, et la "grande" plateforme Coriolis à Grenoble (figure 3.4). La "petite" plateforme est décrite en détail dans le manuscrit de thèse Morize (2006) [101], ainsi que dans l'article Morize *et al.* (2005) [104] reproduit en annexe de ce chapitre. La "grande" plateforme est décrite quant à elle dans l'article Moisy *et al.* (2010) [95], également reproduit en annexe.

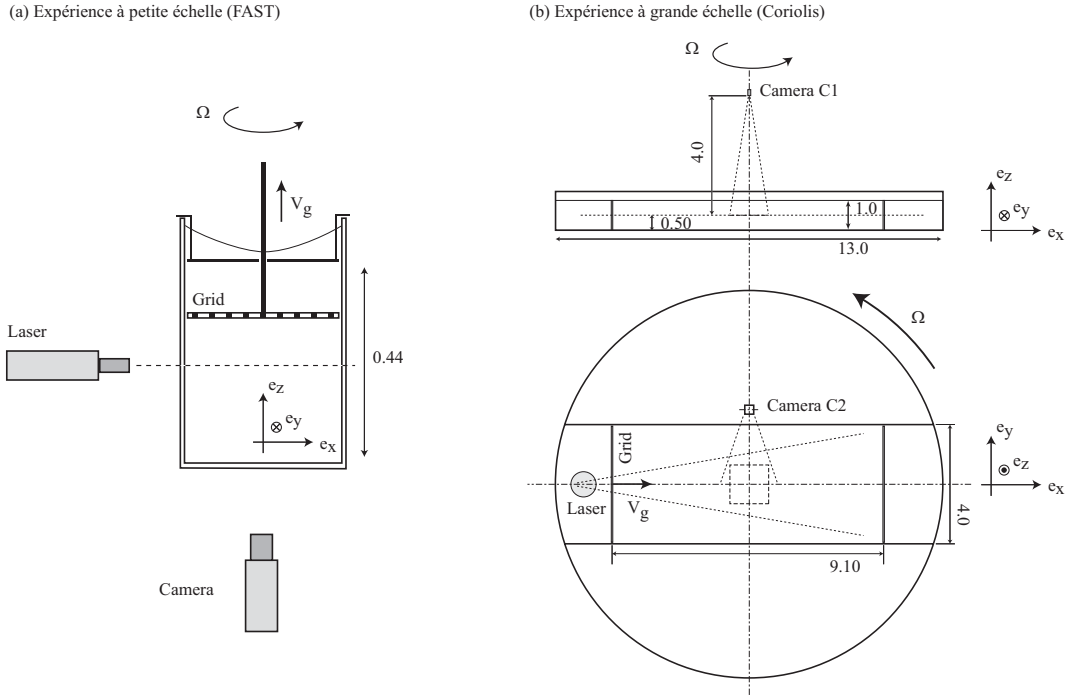


FIG. 3.5 – Schéma des 2 expériences de turbulence en rotation. Toutes les dimensions sont en mètres. (a) Expérience du FAST. La caméra est embarquée dans le référentiel tournant tandis que le laser est fixe. La vitesse de grille et l'axe de corotation sont colinéaires. (b) Expérience Coriolis. Les 2 caméras et le laser sont embarqués. La vitesse de grille est perpendiculaire à l'axe de rotation. D'après Morize *et al.* (2005) [104] et Moisy *et al.* (2010) [95].

La figure 3.5 compare les deux dispositifs expérimentaux. Dans les deux cas, la turbulence est générée par la translation d'une grille de maille $M$ à la vitesse $\mathbf{V}_g$ dans un volume d'eau en rotation solide (avec $\mathbf{V}_g$ parallèle ou perpendiculaire à $\mathbf{\Omega}$ dans la petite et la grande plateforme respectivement). La durée d'un déclin dans la petite plateforme (quelques minutes) permet d'effectuer un grand nombre de réalisations, et donc d'assurer une bonne convergence des moyennes d'ensemble. En revanche, les expériences dans la grande plateforme sont moins bien convergées (6 réalisations au plus dans chaque configuration), mais permettent un bon suivi temporel des structures turbulentes. Le nombre de Reynolds de grille, $Re_g = V_g M/\nu$, est supérieur à $3\ 10^4$, tandis que le nombre de Rossby de grille, $Ro_g = V_g/2\Omega M$, est compris entre 2 et 60. Ces valeurs montrent que l'écoulement initial est dans un état de turbulence pleinement développée, peu ou pas affectée par la rotation d'ensemble. Les paramètres expérimentaux des deux expériences sont résumés dans le tableau 3.1.

### 3.4.2 Structuration de l'écoulement et déclin d'énergie

Des champs de vorticité dans le plan horizontal et vertical, obtenus par PIV sur la grande plateforme, sont montrés en figure 3.6. Le champ de vorticité verticale, $\omega_z$ (fig. 3.6a), fait d'emblée apparaître la propriété la plus remarquable de la turbulence en rotation : l'emergence de grandes structures tourbillonnaires, majoritairement cycloniques, entourées de couches de cisaillement spiralées.

Sur la composante horizontale de la vorticité, $\omega_y$ (fig. 3.6b), une structuration verticale ap-

| | FAST | Coriolis |
|---|---|---|
| | Moyennes d'ensemble | Suivi temporel |
| Configuration | $V_g \parallel \Omega$ | $V_g \perp \Omega$ |
| Dimensions $(x, y, z)$ (m) | $0.35, 0.35, 0.44$ | $9.1, 4.0, 1.0$ |
| Rapports d'aspects $(x/z, y/z)$ | $0.8, 0.8$ | $9.1, 4.0$ |
| Période $T_\Omega$ (s) | 1.5 - 45 | 30, 60, 120 |
| $Re_g = V_g M/\nu$ | $(3-6)10^4$ | $4.2\ 10^4$ |
| $Ro_g = V_g/2\Omega M$ | $2-60$ | $5, 10, 20$ |
| Plans de mesure PIV | horizontal | horizontal et vertical |

TAB. 3.1 – Principaux paramètres des deux expériences de turbulence en rotation.

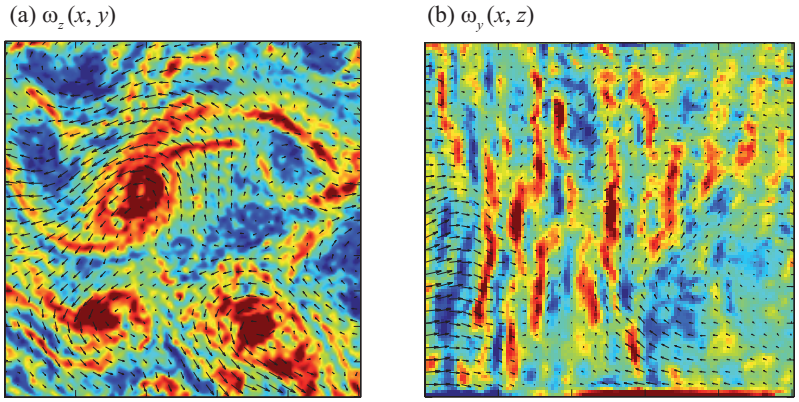


FIG. 3.6 – Champs de vorticité dans le plan horizontal (a) et vertical (b), obtenus sur la plateforme Coriolis. Vitesse angulaire $\Omega = 0.10$ rad s$^{-1}$, $tV_g/M \simeq 770$. D'après Moisy *et al.* (2010) [95].

paraît clairement, évoquant l'invariance verticale prédite par le théorème de Taylor-Proudman. Cependant, cette structuration n'est pas liée à un champ de vitesse purement horizontal : le rapport $u'_z/u'_x$, (où la prime ' désigne l'écart-type des fluctuations turbulentes) prend des valeurs modérées, de l'ordre de $0.5 \pm 0.1$ seulement, indiquant que la composante verticale est loin d'être négligeable. Cette structuration 3C-2D de la turbulence, déjà évoquée au § 2.2.3, est un des effets remarquables de la rotation d'ensemble sur le déclin d'une turbulence initialement isotrope.

D'après la figure 3.1, lorsque le nombre de Rossby instantané franchit une valeur critique de l'ordre de l'unité, la turbulence doit entrer dans un régime dominé par la rotation. C'est ce que confirme la figure 3.7, qui montre l'évolution de l'énergie cinétique turbulente en fonction du temps, pour 3 valeurs de la vitesse angulaire : à temps court, l'énergie $u'^2(t)$ (c'est-à-dire la variance des fluctuations de vitesse turbulentes) décroît selon une loi proche de $t^{-6/5}$, comme attendu en turbulence 3D isotrope [42]. Après une transition à un temps $t = t^*$, un déclin moins prononcé apparaît, confirmant que la rotation d'ensemble inhibe les transferts d'énergie vers les petites échelles, et relentit donc la dissipation d'énergie. Il est intéressant de remarquer que la loi de déclin pour $t > t^*$ est compatible avec une prédiction faite par Squires *et al.* (1994) [122], basée sur l'hypothèse d'un temps de transferts d'énergie contrôlé par la période de rotation. Cette hypothèse, dont on peut montrer qu'elle est essentiellement équivalente au spectre en $k^{-2}$ proposé par Zhou (1995) [144] (équation (3.3), conduit en effet à un exposant de déclin 2 fois moindre que celui obtenu en l'absence de rotation, soit ici

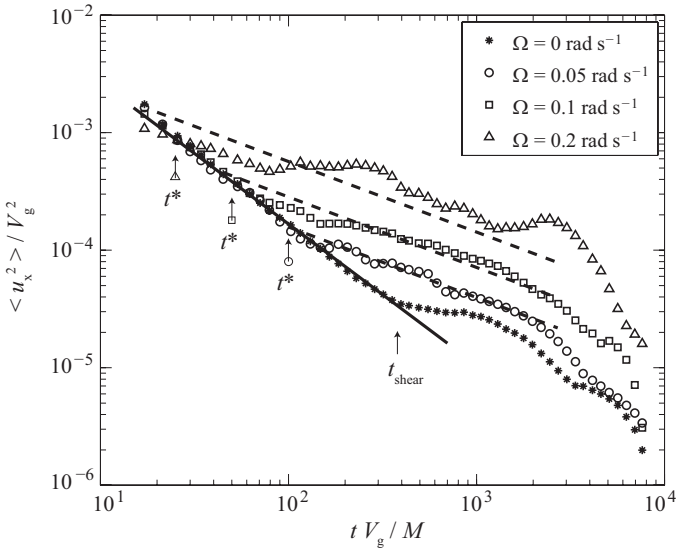


FIG. 3.7 – Déclin d'énergie pour différentes valeurs de la vitesse angulaire de la cuve. Le temps $t^*$ marque la transition entre un déclin isotrope 3D, tel que $u^2(t) \simeq t^{-6/5}$, et un déclin dominé par la rotation, tel que $u'^2(t) \simeq t^{-3/5}$. D'après Moisy *et al.* (2010) [95].

$t^{-3/5}$ [103]. A noter qu'un résultat analogue, avec une transition $t^{-10/7} \to t^{-5/7}$, a été obtenu récemment à partir de simulations numériques directes [133][4].

A la transition $t = t^*$, on observe que le nombre de Rossby critique vaut 0.25. De façon remarquable, ce nombre de Rossby est atteint après un nombre de tours de cuve constant, indépendant de la vitesse angulaire. En effet, on peut montrer que, pour le déclin d'une turbulence isotrope, le temps caractéristique turbulent, $\tau \simeq L/u'$, est simplement proportionnel au temps écoulé depuis le passage de la grille. Ainsi le nombre de Rossby, qui s'exprime comme le rapport $T_\Omega/\tau$, franchit la valeur seuil lorsque $\tau$ est de l'ordre de la période de rotation $T_\Omega$, ce qui est réalisé après un nombre fixe de tours — en l'occurrence, la transition s'opère après 0.4 tour de cuve environ. Ce résultat, d'une remarquable simplicité, n'est valable que lorsque l'état initial est caractérisé par des nombres de Reynolds et de Rossby suffisamment grands.

### 3.4.3 L'asymétrie cyclone-anticyclone

#### Origine physique de l'asymétrie

Une des propriétés remarquables de la figure 3.6(a) est la brisure de symétrie entre cyclones et anticyclones pour $Ro \simeq O(1)$. Une telle discrimination entre vorticité cyclonique et anticyclonique est une propriété générique des écoulements en rotation, comme l'illustre l'expérience de lâchers tourbillonnaires en référentiel tournant reproduite en figure 3.8(a) [124].

Cette brisure de symétrie a été décrite pour la première fois en turbulence en rotation par Hopfinger *et al.* (1982) [68]. Sur la figure 3.8(b), on voit que la surface libre supérieure, de forme paraboloïdale, présente un certain nombre de creux, signature d'une dépression relative venant

[4]En l'absence de rotation, il existe deux prédictions classiques pour le déclin de l'énergie, en fonction des propriétés de la turbulence à grande échelle : soit en $t^{-6/5}$ pour un spectre $E(k) \simeq k^2$ à petit $k$ (Saffman 1967 [118]), soit en $t^{-10/7}$ pour un spectre $E(k) \simeq k^4$ (Loitsanskii). Le point important ici est le facteur 2 dans l'exposant lors de la transition, $t^{-6/5} \to t^{-3/5}$ ou $t^{-10/7} \to t^{-5/7}$ respectivement.

(a) 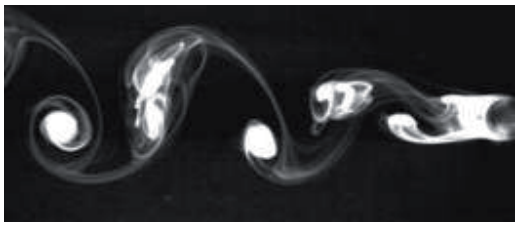 (b) 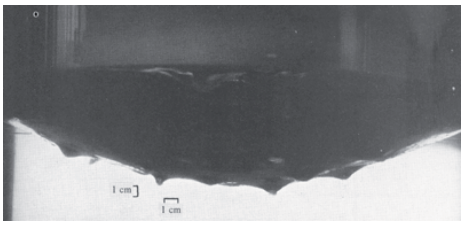

FIG. 3.8 – Deux illustrations de l'asymétrie cyclone-anticyclone dans un référentiel tournant. (a) Géométrie du lâcher tourbillonnaire de Bénard - von Kármán : les tourbillons inférieurs, cycloniques, sont plus stables que les tourbillons supérieurs, anticycloniques. D'après Stegner *et al.* (2005) [124]. (b) Surface libre de l'expérience de Hopfinger *et al.* (1982) [68] (voir la figure 3.2c), montrant des creux à l'endroit des cyclones, dépressionnaires — et pas d'anticyclones, "surpressionnaires".

s'ajouter à la dépression globale liée à la rotation d'ensemble. Les tourbillons produisant ces dépressions tournent donc plus vite que le référentiel : ce sont des cyclones. Des anticyclones, qui conduiraient au contraire à des surpressions relatives et donc à des bosses par rapport à la paraboïde, ne sont pas observés.

Cette brisure de symétrie est un phénomène intrinsèquement non linéaire. Deux mécanismes sont candidats pour expliquer cette dissymétrie. Tout d'abord, dans un référentiel tournant, c'est la vorticité absolue qui est sujette à l'amplification (ou l'amortissement) par étirement (ou contraction) tourbillonnaire. En effet, l'équation pour la composante verticale de la vorticité s'écrit :

$$\frac{\partial \omega_z}{\partial t} + \mathbf{u} \cdot \nabla \omega_z = (\boldsymbol{\omega} + 2\Omega \mathbf{e}_z) \nabla u_z + \nu \nabla^2 \omega_z.$$

Ainsi, dans un champ de déformation vertical $\partial u_z/\partial z$ donné, la vorticité $\omega_z$ sera amplifiée ou amortie à un taux $(\omega_z + 2\Omega)\partial u_z/\partial z$, qui sera d'autant plus élevé que les signes de $\omega_z$ et de $\Omega$ coïncident. En turbulence isotrope, il est connu que c'est l'amplification qui domine statistiquement : le vecteur vorticité a tendance à s'aligner avec la valeur propre intermédiaire du tenseur de gradient de vitesse, qui est positive en moyenne [42]. Ainsi, pour des nombres de Rossby modérés, si cette propriété d'alignement reste valable, la vorticité cyclonique sera plus étirée que la vorticité anticyclonique. Cet argument ne s'applique plus si l'écoulement devient bi-dimensionel (état asymptotique supposé dans la limite $Ro \ll 1$), puisque $\partial u_z/\partial z = 0$.

Un second mécanisme provient de l'instabilité de la vorticité anticyclonique. Pour l'illustrer, le mécanisme d'instabilité le plus simple est obtenu pour un tourbillon axisymétrique. Dans un referentiel non tournant, la stabilité d'un tel écoulement peut s'exprimer par le critère de Rayleigh, stipulant que le moment cinétique doit être une fonction croissante de la distance à l'axe de rotation. L'écoulement sera potentiellement instable (aux effets de viscosité près) s'il existe une région telle que $\phi(r) = \omega_z u_\theta / r < 0$. Une généralisation simple de ce critère peut s'obtenir dans un référentiel tournant :

$$\phi(r) = (\omega_z + 2\Omega)(u_\theta/r + \Omega) < 0.$$

On voit donc que $\phi(r)$ sera augmenté lorsque lorsque les signes de $\omega_z$ et $\Omega$ coïncident. Bien que, formulé ainsi, cet argument ne s'applique qu'au cas axisymétrique, le résultat reste néanmoins qualitativement correct pour des perturbations plus générales (on peut montrer en particulier que le seuil d'instabilité de perturbations hélicoïdales est toujours supérieur à celui de perturbations axisymétriques). Ainsi, les anticyclones seront donc potentiellement instables lorsque typiquement $\omega_z \simeq -2\Omega$ (vorticité absolue nulle), tandis que les cyclones resteront stables.

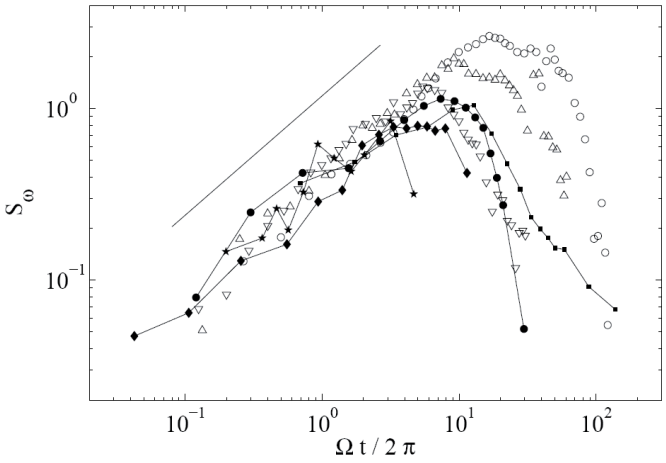


FIG. 3.9 – Evolution du coefficient d'asymétrie (*skewness*) de la vorticité en fonction du temps, mesurées sur la "petite" plateforme en symboles pleins [104], et sur la "grande" plateforme en symboles ouverts [95]. La droite montre une loi de puissance en $(\Omega t)^{0.7}$. D'après Morize *et al.* (2006b) [105].

### Croissance et décroissance de l'asymétrie

Nous avons quantifié l'asymétrie cyclone-anticyclone à partir du coefficient d'asymétrie de la vorticité [5], $S_\omega = \langle\omega_z^3\rangle/\langle\omega_z^2\rangle^{3/2}$ (cette quantité est nulle pour une distribution symétrique de vorticité). Dans nos deux expériences, nous observons une croissance autosimilaire, suivant la loi de puissance suivante pour $t > t^*$,

$$S_\omega \simeq 0.45(\Omega t/2\pi)^{0.7}$$

(voir la figure 3.9). La coïncidence des préfacteurs entre les deux expériences est remarquable, malgré les différences géométriques importantes, suggérant un caractère universel de cette croissance. Par ailleurs, la visualisation des champs de vorticité indique que c'est le premier mécanisme évoqué plus haut qui est responsable de cette croissance de $S_\omega$, à savoir l'étirement tourbillonnaire privilégié de la vorticité cyclonique. En effet, très peu d'anticyclones sont observés, indiquant que ceux-ci ne sont presque pas produits dans cette phase d'étirement, et il n'est donc pas utile d'invoquer un argument d'instabilité *a posteriori*.

A temps plus long, les tourbillons se séparent du fond turbulent, et l'écoulement consiste alors en une population diluée de tourbillons, majoritairement cycloniques, en interaction. Des appariements de tourbillons de même signe, en l'occurrence essentiellement des cyclones, sont observés dans cette phase finale, similaires à ce qui est observé classiquement en turbulence bidimensionelle [127].

Un tel mécanisme d'appariement devrait s'accompagner d'une augmentation de l'intermittence de la vorticité, définie usuellement sur le facteur d'applatissement, ou *flatness*, $F_\omega = \langle\omega_z^4\rangle/\langle\omega_z^2\rangle^2$, mais devant également être présente sur $S_\omega$ si tous les tourbillons sont tous de même signe. Or, c'est paradoxalement une décroissance de $S_\omega$ qui est observée à temps long. Deux explications physiques peuvent être proposées pour cette décroissance :

(i) la diffusion de vorticité (par friction visqueuse "interne" ou par friction d'Ekman sur les parois horizontales) ;

(ii) la production de petites échelles turbulentes de vorticité symétrique.

L'origine de cette deuxième contribution, caractérisée en détail dans l'article Moisy *et al.* (2010) [95], est la destabilisation des couches de cisaillement verticales que l'on peut deviner sur la figure 3.6(b). En effet, à temps long, les fluctuations de vitesse verticales, fossiles de la turbulence initialement isotrope, sont advectées, étirées et repliées, par l'écoulement horizontal, à la manière d'un champ scalaire passif en turbulence 2D. Les fines couches verticales ainsi générées s'intensifient par compression, et peuvent devenir instables : Ces instabilités réinjectent des fluctuations de vitesse horizontale à petite échelle, et donc de la vorticité verticale de signe aléatoire, ce qui a pour conséquence une diminution de $S_\omega$.

La croissance autosimilaire de l'asymétrie cyclone-anticyclone a reçu récemment un certain nombre de confirmations qualitatives, expérimentales (Staplehurst *et al.* (2008) [123]) et numériques (van Bokhoven *et al.* (2008) [133]). L'origine de la décroissance à temps long, en revanche, est un sujet encore débattu à ce jour. En particulier, une explication purement basée sur les interférences d'ondes d'inertie peut également être invoquée [133] : Comme nous l'avons vu en Section 3.3.3, dans la limite $Ro \to 0$, les corrélations triples de vorticité verticale (ou de tout autre champ turbulent) sont des fonctions rapidement oscillantes du temps qui, en dehors des interactions résonnantes, interfèrent de manière destructive (mélange de phase). Cette explication suggère que la vorticité du mode bidimensionel (i.e. moyennée selon l'axe de rotation) pourrait continuer à montrer une asymétrie cyclone-anticyclone, tandis que la vorticité totale (incluant les fluctuations 3D), elle, redeviendrait symétrique à temps long.

Des travaux complémentaires sont nécessaires afin de trancher entre les différentes contributions en jeu pour expliquer cette re-symétrisation de la vorticité à temps long. La vorticité moyennée selon l'axe de rotation n'étant pas accessible expérimentalement, il semble nécessaire d'introduire d'autres quantités à plus grande échelle, basées sur la vitesse et non la vorticité, telles que les incréments de vitesse transverses ou le moment angulaire normalisé [62]. Une autre approche possible pourrait être basée sur l'étude statistique de l'évolution de la population de tourbillons, par une approche de type *recensement de tourbillons* (*vortex census*) introduite en turbulence 2D [25].

### 3.4.4 Transferts d'énergie

Dans l'espace physique, les transferts d'énergie sont décrits par le tenseur de corrélation triple de vitesse en deux points, $\langle u_i(\mathbf{x})u_j(\mathbf{x}+\mathbf{r})u_k(\mathbf{x}+\mathbf{r})\rangle_\mathbf{x}$ [57]. Comme nous l'avons vu en Section 3.3.3, dans le cas isotrope, cette corrélation se ramène à un simple scalaire : la fonction de structure d'ordre 3, $S_3 = \langle(\delta_r u_L)^3\rangle$. Une question ouverte est l'origine d'un possible changement de signe de $S_3(r)$ en présence de rotation, et son lien éventuel avec une cascade inverse d'énergie. Un tel changement de signe a été observé dans la configuration de turbulence forcée par Baroud *et al.* (2002) [3], mais dans une situation où une échelle d'injection bien définie sépare deux gammes d'échelles distinctes dans lesquelles une cascade directe (3D) ou inverse (2D) prennent place séparément.

Nos mesures dans le cas d'une turbulence en déclin [104, 89] montrent l'existence d'un tel changement de signe (fig. 3.10). L'échelle $r_0$ de changement de signe diminue au cours du temps, suggérant un état de turbulence 2D "envahissant" progressivement les grandes échelles du domaine inertiel, en accord qualitatif avec la loi (3.2). L'interprétation physique de ce phénomène est toutefois délicate dans le cas d'une turbulence en déclin, étant donné qu'il n'existe pas d'injection d'énergie à cette échelle intermédiaire $r_0$. En outre, les mesures de fonctions de structure d'ordre 2, $S_2(r)$, suggèrent que l'énergie cinétique est une fonction strictement décroissante du temps, et ce pour toutes les échelles $r$, venant contredire l'hypothèse d'une

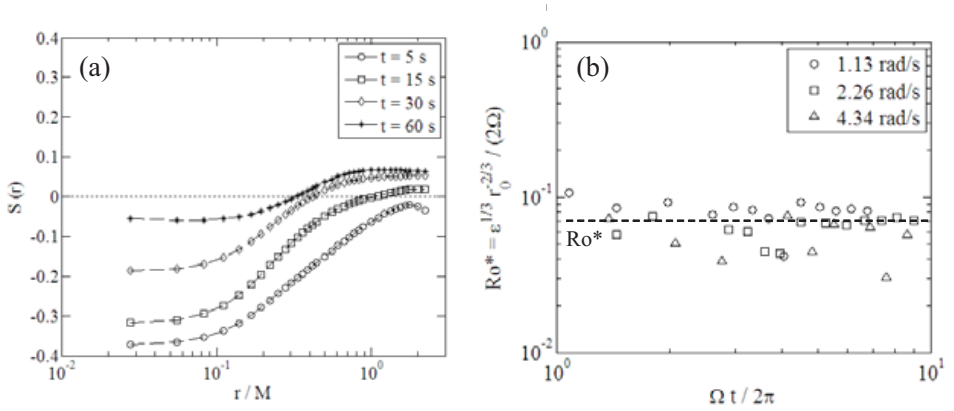


FIG. 3.10 – (a) Coefficient d'asymétrie (*skewness*) des incréments de vitesse longitudinaux, $S(r) = S_3(r)/S_2(r)^{3/2}$, mesurés dans le plan horizontal, à 4 instants durant le déclin. L'échelle $r_0$ à laquelle $S(r)$ change de signe est une fonction décroissante du temps. (b) Nombre de Rossby local calculé à l'échelle $r_0$ pour différentes vitesses angulaires. D'après Moisy *et al.* (2009) [89].

cascade inverse. Il n'est pas clair aujourd'hui si ce changement de signe de $S_3$ est une véritable signature d'une cascade inverse, dont les effets sont éventuellement masqués par les effets visqueux [89], ou bien un artefact de projection lié au fait que seules les composantes normales à l'axe de rotation sont mesurées. Afin de lever cette ambiguité, des mesures de fonctions de structures anisotropes, dans le plan vertical $(x, z)$, sont nécessaires : quelques pistes sont données au § 3.5.2 à ce sujet.

## 3.5 Perspectives

La mise en place de la nouvelle plateforme "Gyroflow" au FAST en 2009 ouvre de nouvelles perspectives expérimentales pour l'étude de la turbulence en rotation et, au-delà, pour l'étude des écoulements géophysiques (couplage rotation-stratification, ou rotation-convection thermique). Les quelques pistes de recherche proposées ci-après sont limitées à la turbulence en rotation uniquement, dans le prolongement des résultats présentés dans ce chapitre.

La possibilité d'explorer la structure verticale de l'écoulement, et à terme d'embarquer sur la plateforme un système de PIV stéréoscopique pour accéder aux 3 composantes de la vitesse, constituent les atouts principaux de cette nouvelle plateforme. Dans un tel système, la composante de la vitesse normale au plan de la nappe laser est reconstruite à partir des images obtenues par 2 caméras filmant la zone d'intérêt sous des incidences différentes. Les quelques pistes de recherche qui suivent tirent profit d'une telle possibilité.

### 3.5.1 Couplage turbulence - modes d'inertie

Une difficulté majeure dans l'étude expérimentale du déclin de l'énergie turbulente, qu'il s'agisse d'expériences avec ou sans rotation, est le couplage possible avec un écoulement moyen résiduel, qui peut venir alimenter la composante turbulente. En présence de rotation et de confinement, cet écoulement grande échelle prend la forme de modes d'inertie, qui sont des ondes d'inertie piégées dans la cuve [40]. Le spectre discret de ces modes d'inertie dépend du détail de la géométrie du volume fluide, et a été caractérisé en détail dans le cas d'un

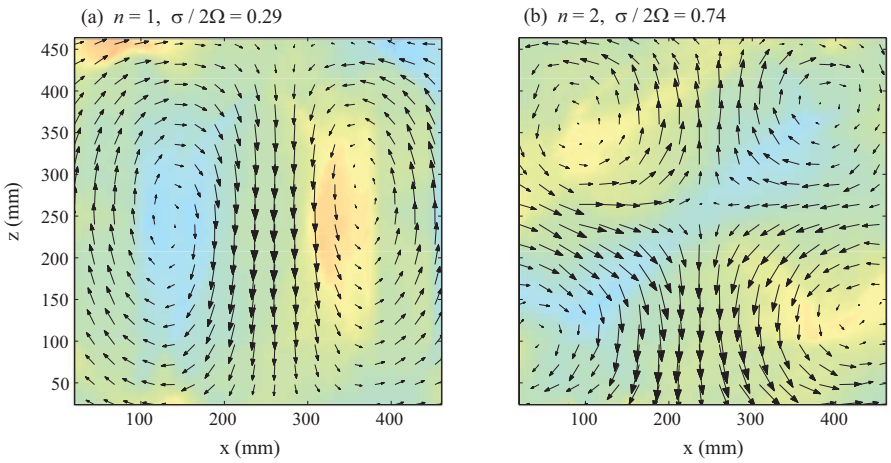


FIG. 3.11 – Deux modes d'inertie, de nombre d'onde vertical $n = 1$ et $n = 2$, excités dans l'expérience de turbulence de grille en rotation sur la plateforme Gyroflow. Ces champs sont obtenus par filtrage passe-bande, aux pulsations $\sigma/2\Omega = 0.29$ et 0.74, de la moyenne d'ensemble des champs de vitesse à temps fixé sur plusieures réalisations indépendantes. Une partie significative de l'énergie cinétique injectée par la grille est stockée dans ces modes d'inertie, qui peuvent affecter la dynamique de la "vraie turbulence" en rotation.

parallélépipède par Maas (2003) [82]. L'existence de ce couplage peut affecter significativement les lois de déclin de l'énergie turbulente, comme suggéré par les récentes expériences de Bewley *et al.* (2007) [11] : en effet, l'énergie stockée dans les modes d'inertie peut être restituée à la composante turbulente de l'écoulement au fur et à mesure du déclin.

Le couplage turbulence - modes d'inertie peut être décrit par une approche classique de type "décomposition de Reynolds". Cette décomposition doit être appliquée sur la moyenne d'ensemble et non sur la moyenne temporelle afin d'extraire les modes d'inertie oscillants reproductibles et de les découpler de la contribution turbulente non reproductible. La figure 3.11 illustre 2 des modes d'inertie excités par la translation de la grille, de nombre d'onde vertical $n = 1$ et $n = 2$.

La difficulté de cette étude tient à la fois à la bonne convergence des statistiques nécessaire à une extraction correcte des modes d'inertie, et aussi à la détermination expérimentale du terme de couplage turbulence-mode,

$$T = -\langle u_i' u_j' \rangle \langle \partial u_i / \partial x_j \rangle.$$

Mesurer ce terme, construit sur une corrélation de tenseurs tri-dimensionnels des fluctuations de vitesse, nécessite la mise en place d'un système de PIV stéréoscopique pour la mesure des 3 composantes de la vitesse. L'étude fine d'un tel couplage permettrait d'expliquer certaines différences observées entre nos deux expériences réalisées dans différentes géométries [103, 95], et les prédictions théoriques en milieu non confiné.

Dans une configuration idéalisée où de tels modes ne seraient pas excités, on aurait $T = 0$, et le declin de la turbulence serait un vrai déclin "libre". Des expériences préliminaires menées actuellement, inspirées de la configuration récemment introduite par Staplehurst *et al.* (2008) [123], semblent montrer qu'une diminution de l'énergie injectée dans ces modes est possible par des modifications de la géométrie de la grille. Une collaboration avec L. Maas (Université d'Utrecht) a été démarrée en 2010 sur ce sujet [74]. Cependant, la configuration avec modes d'inertie est un sujet d'étude fondamental en soi : elle constitue un cadre original d'étude

de couplage entre ondes et turbulence, qui possède de nombreuses connections au-delà du problème de la turbulence en rotation exploré ici.

### 3.5.2 Transferts d'énergie anisotropes

Les mesures de transfert d'énergie étaient limitées jusqu'à présent aux mesures au plan horizontal, sur la "petite" plateforme tournante (§ 3.4.4). Il s'agit ici de transferts turbulence-turbulence, et non de transferts turbulence-mode comme au paragraphe précédent. Une perspective intéressante pour le futur sera d'étendre ces mesures dans le plan vertical, afin de caractériser directement l'anisotropie des transferts d'énergie, et découpler en particulier les aspects de transferts *angulaires* (i.e. vers les angles proches de l'horizontale) et *en échelle* $|\mathbf{r}|$ (cascade, directe ou inverse).

Une telle étude nécessite une généralisation anisotrope de la loi de von Kármán-Howarth (3.4) au cas en rotation. Cette généralisation fait actuellement l'objet d'efforts théoriques soutenus [59, 20]. Une première adaptation de la loi au cas quasi-isotrope sous l'effet d'une faible rotation a été proposée par Chakraborty & Bhattacharjee (2007) [27]. Une avancée significative sur ce sujet est celle de Galtier (2009) [59], qui propose une généralisation de cette loi basée sur le moment d'ordre 3 des projections des incréments de vitesse selon un angle dépendent de la vitesse de rotation du référentiel (et donc du nombre de Rossby). Au stade actuel de développement de cette approche, la paramétrisation de cet angle est effectuée de façon phénoménologique, à partir de la relation de dispersion des ondes d'inertie.

Des mesures de PIV stéréoscopique dans le plan vertical devraient permettre d'accéder expérimentalement à ces transferts d'énergie anisotropes. Une première approche peut consister à étudier le terme de flux d'énergie dans l'espace des échelle, exprimé par la fonction de structure d'ordre 3 anisotrope :

$$\mathbf{F}(\mathbf{r}) = \langle \delta\mathbf{u}(\mathbf{r})[\delta\mathbf{u}(\mathbf{r})]^2 \rangle,$$

où $\delta\mathbf{u}(\mathbf{r}) = \mathbf{u}(\mathbf{x}+\mathbf{r}) - \mathbf{u}(\mathbf{r})$ est l'incrément vectoriel de vitesse. La composante radiale de ce flux, $F_r = \mathbf{F} \cdot \mathbf{e}_r$, caractérise la "cascade" en échelle, tandis que la composante orthoradiale, $F_\theta = \mathbf{F} \cdot \mathbf{e}_\theta$, les transferts angulaires. Dans le cas isotrope, on a $F_\theta = 0$, et le flux vérifie la relation

$$\nabla_\mathbf{r} \cdot \mathbf{F}(\mathbf{r}) = -4\epsilon,$$

équivalent à la loi des $4/5$ pour la fonction de structure longitudinale d'ordre 3, $S_3(r)$.

La mesure directe par PIV du terme de flux $\mathbf{F}(\mathbf{r})$ devrait permettre de caractériser pour la première fois expérimentalement les transferts anisotropes dans l'espace des échelles. Elles devraient constituer une alternative intéressante à la détermination du terme de transfert $T(\mathbf{k})$ dans l'espace de Fourier, plus naturelle pour les simulations mais trop délicate à partir de mesures expérimentales. Ces mesures devraient en outre permettre d'élucider l'origine du changement de signe de $S_3(r)$ que nous avons identifiée pour les incréments purement horizontaux (§ 3.4.4).

### 3.5.3 Intermittence

Enfin, une dernière piste intéressante, et encore inexplorée, serait de caractériser l'influence de la rotation sur les propriétés d'intermittence de la turbulence. L'intermittence est définie ici dans le domaine inertiel, par l'existence de lois d'échelles anormales des fonctions de structure

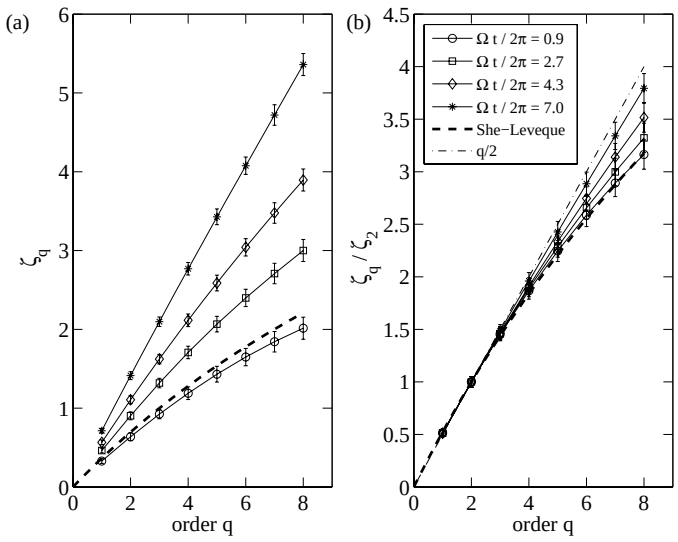


FIG. 3.12 – Exposants de fonction de structures mesurées dans le plan normal à l'axe de rotation, au cours du déclin. (a), Exposants bruts $\zeta_q$, mesurés à partir de la relation $\langle|\delta u(r)|^q\rangle \sim r^{\zeta_q}$. (b), Exposants relatifs $\zeta_q/\zeta_2$, mesurés par la méthode *Extended Self Similarity* [10]. D'après Seiwert *et al.* (2008) [120].

d'ordre élevé, $\langle|\delta u(r)|^q\rangle \sim r^{\zeta_q}$ avec $\zeta_q \neq q/3$ [57]. Ces lois d'échelles anormales sont la signature de densités de probabilités des incréments de vitesse non autosimilaires à travers les échelles, et ont fait l'object d'une littérature abondante ces dernières années en turbulence 3D.

Des premiers résultats prometteurs ont été obtenus sur les fonctions de structure restreintes au plan normal à l'axe de rotation (voir la figure 3.12) [120]. Nous avons observé que l'évolution temporelle des exposants d'ordre élevé est essentiellement asservie à l'évolution de l'exposant d'ordre 2, qui est lié au "raidissement" du spectre d'énergie (grandes échelles contenant relativement plus d'énergie en présence de rotation). En revanche, les exposants relatifs, $\zeta_q/\zeta_2$, montrent une évolution claire entre une situation d'intermittence 3D à temps court et une situation d'intermittence réduite à temps long (i.e. $\zeta_q/\zeta_2 \to q/2$), en accord qualitatif avec la turbulence 2D. Ces résultats ont été confirmés par des simulations numériques récentes en turbulence en rotation forcée (Thiele & Müller (2009) [129]).

L'extension de ces résultats aux fonctions de structure anisotropes devrait constituer une percée importante dans ce domaine. La possibilité notamment d'extraire le mode 2D (par moyennage vertical de la vitesse horizontale) devrait permettre d'étudier séparément les différentes contributions des fonctions de structure, et de caractériser en particulier les propriétés d'intermittence de la composante 2D et de la composante résiduelle.

# Decaying grid-generated turbulence in a rotating tank

C. Morize, F. Moisy,[a] and M. Rabaud
*Fluides, Automatique et Systèmes Thermiques, Bâtiment 502, Campus Universitaire, 91405 Orsay Cedex, France*

(Received 17 December 2004; accepted 19 July 2005; published online 16 September 2005)

The decay of initially three-dimensional homogeneous turbulence in a rotating frame is experimentally investigated. Turbulence is generated by rapidly towing a grid in a rotating water tank, and the velocity field in a plane perpendicular to the rotation axis is measured by means of particle image velocimetry. During the decay, strong cyclonic coherent vortices emerge, as the result of enhanced stretching of the cyclonic vorticity by the background rotation, and the selective instability of the anticyclonic vorticity by the Coriolis force. This asymmetry towards cyclonic vorticity grows on a time scale $\Omega^{-1}$ ($\Omega$ is the rotation rate), until the friction from the Ekman layers becomes dominant. The energy spectrum perpendicular to the rotation axis becomes steeper as the instantaneous Rossby number $\mathrm{Ro}_\omega=\omega'/2\Omega$ decreases below the value $2\pm0.5$ ($\omega'$ is the root-mean square of the vertical vorticity). The spectral exponent increases in time from its classical Kolmogorov value 5/3 up to values larger than 2. Below the threshold $\mathrm{Ro}_\omega<2$, the velocity derivative skewness decreases as $|S|\propto\mathrm{Ro}_\omega$, reflecting the inhibition of the energy transfers by the background rotation, with a net inverse energy cascade that develops at large scales. © *2005 American Institute of Physics*. [DOI: 10.1063/1.2046710]

## I. INTRODUCTION

Turbulence subjected to system rotation is present in a wide range of applications, from engineering to geophysics and astrophysics.[1–3] Although often coupled to other effects, such as stratification or confinement, rotating turbulence in itself is a delicate issue that is not completely understood. Rotation considerably affects the dynamics and the structure of turbulence through the Coriolis force, which tends to two-dimensionalize the flow. The importance of rotation is usually measured from the Rossby number, $\mathrm{Ro}=U/\Omega L$, where $U$ is a typical velocity, $L$ is a typical length scale, and $\Omega$ is the rotation rate. While the two-dimensional (2D) state is expected in the limit $\mathrm{Ro}\to0$, according to the Taylor-Proudman theorem, the two-dimensionalization process itself, being driven by the nonlinear interactions, requires moderate Rossby numbers or asymptotically large times to take place. Such asymptotic may however never be reached in laboratory experiments, for which a much shorter time scale associated to the dissipation in the Ekman layers is present,[1] which may prevent this slow trend towards two-dimensionality.

Early experiments, either from an oscillating grid or source-sink forcing in a rotating frame,[4–7] or from a wind tunnel with a rotating honeycomb,[8] have led to a base of commonly accepted features for rotating turbulence. First, the flow develops a strong anisotropy, which may be characterized from increased correlation lengths along the axis of rotation.[8] This first observation is in qualitative agreement with a trend towards 2D turbulence, except that the flow is found to become dominated by a population of large-scale coherent cyclonic vortices,[5,6] while symmetric vorticity fluctuations are expected for strictly 2D turbulence. Second, the energy transfer from large to small scales is reduced, leading to reduced energy dissipation and a slower decay.[8] This inhibition of the energy transfer may however be hidden for bounded flows, for which the Ekman friction leads to an extra dissipation.[4,9]

The asymmetry between cyclonic and anticyclonic vorticity is a generic property of rotating systems, which originates from a selective destabilization of the anticyclonic vorticity by the Coriolis force when $\mathrm{Ro}\simeq O(1)$.[10–12] The statistical signature of this asymmetry has been first characterized for decaying rotating turbulence by Bartello *et al.*[13] from large-eddy simulations (LES), showing that the vorticity skewness at a fixed time during the decay was maximum for an initial Rossby number $\sim O(1)$. As a consequence, the vorticity distribution in the two-dimensionalization process is expected to be strongly affected by the initial conditions in the decaying case, or the forcing scheme in the stationary case, and should not be universal.

The trend towards two-dimensionality may be characterized in the spectral space by a net energy transfer toward wave vectors $\mathbf{k}$ normal to the rotation axis.[14,15] This trend towards two-dimensionality is not directly related to a trend towards a two-component flow, as may be traced by the anisotropy of the Reynolds stress tensor.[14,16,17] Despite much theoretical and numerical efforts, the issues of the direction of the energy transfers towards smaller or larger wavenumber magnitude $k=|\mathbf{k}|$, and the shape of the energy spectrum, remain controversial. First, a simple dimensional analysis, assuming that $\Omega^{-1}$ is the only relevant time scale in the problem and no energy transfer takes place, yields a spectrum $E(k)\sim\Omega^2k^{-3}$ (e.g., Smith and Waleffe[18]). Although similar to that of geostrophic turbulence (Charney[19]) and strictly 2D turbulence in the enstrophy cascade regime,[20] this

[a]Electronic mail: moisy@fast.u-psud.fr

 

$k^{-3}$ spectrum in itself does not prove that rapidly rotating turbulence actually tends towards a purely 2D state. On the other hand, assuming local energy transfers and taking $\Omega^{-1}$ as the time scale for those transfers, but ignoring anisotropic effects, a $k^{-2}$ spectrum has been derived by Zhou[21] and Canuto and Dubovikov,[22] with some support from simulations[23,24] and experiments at a moderate Rossby number.[25] Attempts to derive the three-dimensional (3D) anisotropic spectrum have been recently carried out by Galtier[26] and Cambon *et al.*[27] in the limit of a quasizero Rossby number. Steeper slopes, $k^{-5/2}$ to $k^{-3}$, are obtained by these authors, which are in qualitative agreement with direct numerical simulation (DNS),[18,28] LES,[29] and numerical integration of an asymptotic quasinormal Markovian (QNM) closure model.[30]

Recently, particle image velocimetry (PIV), by offering the possibility to study the spatial structure of the flow as well as multipoint statistics, renewed the interest for rotating turbulence experiments.[25,31,32] In particular, the flow field in the plane normal to the rotation axis can be obtained from this measurement technique, in contrast with more conventional one-point probes that are usually restricted to measurements along the rotation axis. Baroud *et al.*[25] observed a transition towards quasi-2D turbulence in an experiment where forcing was applied at small scale through a circular set of 120 jets in a rotating annulus. These authors observed a flow dominated by large-scale coherent vortices, which was interpreted in terms of an inverse energy cascade associated to a $k^{-2}$ spectrum, different from the Kolmogorov-Kraichnan scaling $k^{-5/3}$ for exact 2D turbulence.[33] In recent experiments using the large-scale "Coriolis" rotating platform, Praud *et al.*[32] have investigated the decaying 2D turbulence in the presence of rotation and stratification. In these experiments, turbulence was generated by towing a rake in the direction perpendicular to the rotation, thus preferentially forcing the horizontal modes of the flow. Energy spectra $k^{-3}$ were obtained, in agreement with the expected 2D state in the enstrophy cascade regime. These experiments gave evidence of the existence and stability of a suitably forced 2D turbulence state in a rotating and stratified system, but do not address the issue of the convergence towards this 2D state from a 3D isotropic forcing.

The present experiment has been specially designed to investigate the influence of background rotation during the free decay of an otherwise initially 3D homogeneous and isotropic turbulence. Turbulence is generated by rapidly towing a grid in a rotating water tank, providing an initial state that is close to the ideal situation of homogeneity and isotropy. The setup is similar to the ones proposed by Hopfinger *et al.*[6] or Dickinson and Long,[7] which made use of an oscillating grid in a rotating tank. The advantage of their system was to provide a stationary forcing, but its main drawback was to produce a strongly inhomogeneous flow, with essentially 3D turbulence close to the grid and quasi-2D turbulence at the other end of the tank. In our experiment, close to the one originally proposed by Ibbetson and Tritton,[4] the grid is initially towed through the whole height of the tank and the turbulence freely decays, so that the background rotation gradually affects the entire flow in an homogeneous way. In that sense, the present experiment is closer to the theoretical and numerical approaches, for which homogeneity is generally required while stationarity is not.

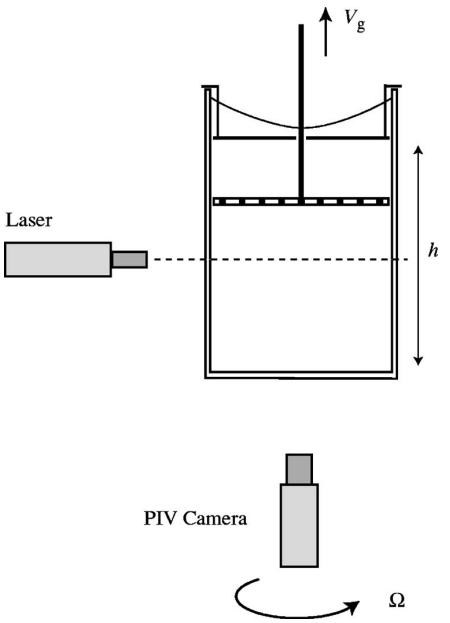


FIG. 1. Schematic of the experimental setup. The water tank, the grid, and the camera are in the rotating frame, while the laser is in the laboratory frame.

The paper is organized as follows: In Sec. II the experimental setup and the particle image velocimetry is presented. Statistics of the vorticity field are presented in Sec. III, with particular attention paid to the asymmetry between cyclonic and anticyclonic vorticity in the course of the decay. Power spectra are investigated in Sec. IV, and the influence of the Rossby number on the energy transfers is characterized from the velocity derivative skewness in Sec. V. Finally, some concluding remarks are offered in Sec. VI.

## II. EXPERIMENTAL SETUP

### A. Experimental apparatus

The experimental setup is sketched in Fig. 1. It consists of a water-filled square glass tank, 55 cm in height and 35 cm in side length, mounted on a rotating turntable, whose angular velocity $\Omega$ has been varied between 0.13 and 4.3 rad $s^{-1}$ (see Table I for a summary of the flow parameters). By convention the rotation axis is directed upward, $\mathbf{\Omega}=\Omega\hat{\mathbf{e}}_z$ with $\Omega>0$, so that the rotation is clockwise when seen from below. The rotation of the fluid is set long before an experiment, in order to avoid transient spin-up recirculation flows and to achieve a solid body rotation regime. A cover is placed below the free surface at a distance $h=44$ cm from the bottom, defining a volume of working fluid of 54 l. This cover prevents surface waves and $\beta$ effects due to the parabolic shape of the free surface.

Turbulence is generated by rapidly towing a corotating square grid at constant velocity $V_g$ from the bottom to the top of the tank. During the subsequent decay of turbulence, the

TABLE I. Summary of experimental conditions. $\Omega$ is the turntable angular velocity, $V_g$ the maximum grid velocity at midheight, $\mathrm{Re}_g = V_g M/\nu$ and $\mathrm{Ro}_g = V_g/2\Omega M$ the initial Reynolds and Rossby numbers based on the grid velocity and the mesh size, $M = 39$ mm. $\Omega t_E = h(\Omega/\nu)^{1/2}$ is the nondimensional Ekman time.

| Symbol | $\Omega$ (rad s$^{-1}$) | $V_g$ (m s$^{-1}$) | $\mathrm{Re}_g$ | $\mathrm{Ro}_g$ | $\Omega t_E$ |
|---|---|---|---|---|---|
| * | 0.13 | 1.17 | $4.7\times10^4$ | 120 | 140 |
| ◇ | 0.53 | 0.82 | $3.1\times10^4$ | 19 | 310 |
| ○ | 1.5 | 0.82 | $3.1\times10^4$ | 6.8 | 540 |
| ● | 1.5 | 1.63 | $6.2\times10^4$ | 14 | 540 |
| □ | 4.3 | 0.82 | $3.1\times10^4$ | 2.4 | 930 |

grid is kept fixed close to the top of the tank. The grid consists of 1-cm-square bars with a mesh $M = 39$ mm, and has a solidity ratio (solid to total area) of 0.45. It is rigidly attached at its center point to a stainless-steel shaft that passes through a hole in the cover. The vertical translation of the grid is achieved by a 5-kW servo-controlled brushless motor. Grid velocities from $V_g = 0.82$ to 1.63 m s$^{-1}$ have been used for the present experiments (see Table I). The grid velocity is constant throughout the height of the tank, except for the case $V_g = 1.63$ m s$^{-1}$, for which the accelerations and decelerations phases near the bottom and the top of the tank restrict the range of constant velocity to approximately $0.3h$.

A number of grid-generated turbulence experiments in a wind tunnel are shown to produce nearly isotropic fluctuations for a downstream distance larger than about $20-40M$.[34] Although this idealized situation cannot be achieved in our closed geometry, for which the height of the tank is only of about $10M$, one may however expect the turbulent velocity field to be approximately isotropic for times $t > (20-40)M/V_g$ after the grid translation. After this time, the velocity fluctuations have decreased down to about $u' \simeq 0.05 V_g$ (velocity measurements are described in Sec. II B), and the turbulence enters into an inertial decay regime. This regime longs for typically 40 s, which is approximately 1000 inertial time scales $M/V_g$, after which the flow undergoes its final period of decay, where the friction from the Ekman layers becomes dominant.

### B. Velocity measurements

Instantaneous velocity fields in the horizontal plane $(x,y)$ at midheight of the tank are obtained from particle image velocimetry (PIV).[35] The water is seeded by borosilicate spheres, 11 $\mu$m in diameter, and illuminated by a horizontal laser sheet of thickness $b \simeq 1$ mm, located at midheight $h/2$, produced by a double-pulsed Nd:YAG laser (25 mJ/pulse). The flow is imaged through the transparent bottom of the tank with a double-buffer high-resolution camera ($1280\times1024$ pixels, 4096 gray levels), located 50 cm below the laser sheet and corotating with the tank. Only a central region of $16\times13$ cm$^2$ of the flow is imaged, where negligible wall effects are expected. For practical reasons, the laser source is kept in the laboratory frame. The laser sheet being invariant under rotation about the vertical axis, accurate tracking of the particles is possible between the two successive images, assuming a time separation much lower than the rotation period of the turntable.

A set of 100 image pairs are acquired during the decay of turbulence. Since the rms velocity decreases in time, the delay between the two successive images of a pair is made to gradually increase during the acquisition sequence, from about 1 to 100 ms, so that the typical particles displacement remains constant, of order of 5–10 pixels, during all the decay. It has been checked than the time delay between the images of a pair remains well below the small-scale turnover time $1/\omega'$ throughout the decay. A careful calibration of this delay is a critical requirement for accurate PIV computations of the velocity fields.

For the PIV computations, interrogation windows of size $16\times16$ pixels, with an overlap of 8 pixels, were used. The final velocity fields are defined on a $160\times128$ grid, with a resulting spatial resolution of 1 mm, which is close to the laser sheet thickness. This allows us to accurately resolve the inertial scales of the flow, but may fail to resolve the dissipative scales when the Reynolds number is very large, in the first period of the decay, for which the Kolmogorov scale can be as low as $\eta \simeq 0.2$ mm. Here $\eta = (\nu^3/\epsilon)^{1/4}$, where $\nu$ is the kinematic viscosity and $\epsilon$ the instantaneous energy dissipation rate. A velocity resolution of 0.1 pixel can be achieved using a classical subpixel interpolation scheme for the correlation function. The resulting velocity signal-to-noise ratio is about $2\times10^{-2}$, allowing us to compute power spectra with more than three decades in energy. A Gaussian filter is applied when spatial derivatives, such as vorticity (Sec. III) or longitudinal velocity derivative (Sec. V), are needed. The error on the spatial derivatives can be estimated to about 5% at moderate Reynolds numbers, and up to 10%–20% at larger Reynolds numbers due to the insufficiently resolved Kolmogorov scale.

Since each realization of the decay is highly fluctuating, convergence of the statistics is achieved by computing ensemble averages for the same time delay $t$ after the grid translation over several independent realizations of the decay. About 50 decays are recorded for each flow parameters, with a delay of at least 3 min (typically $5000M/V_g$) between two grid translations. It is worth noting that true ensemble averages are usually not achievable in most turbulence experiments, which usually make use of spatial or temporal averages instead.

### C. Nondimensional numbers

Three parameters are needed to fully characterize the flow states during the decay: the grid velocity $V_g$, the back-

ground angular velocity $\Omega$, and the time delay after the grid translation, $t$. From the first two parameters, $V_g$ and $\Omega$, which specify the initial conditions, the grid Reynolds and Rossby numbers are defined, $\mathrm{Re}_g = MV_g/\nu$ and $\mathrm{Ro}_g = V_g/2\Omega M$, respectively. For the present experiments, $\mathrm{Re}_g$ lies in the range $3\times10^4 - 6\times10^4$ (see Table I), insuring a fully developed turbulence in the wake of the grid. The Rossby number $\mathrm{Ro}_g$ is relatively large even for high rotation rate, between 2.4 and 120, so that the turbulent energy production in the near wake of the grid is essentially unaffected by the rotation. As a consequence, the early stage of the turbulence decay is expected to be nearly isotropic, and the background rotation gradually affects the flow in the course of the decay. For the third parameter, the time delay $t$ after the grid translation, two nondimensionalizations are of interest depending on which physical effect is being investigated. The nondimensional time based on the grid time scale, $\tau = tV_g/M$, is useful to compare the decay in the presence of rotation with that without rotation, while the nondimensional time based on the background rotation, $\Omega t = \tau/(2\mathrm{Ro}_g)$, is useful for situations dominated by the Coriolis force (e.g., for the buildup of the vorticity skewness, Sec. III B).

It may also be of interest to introduce the turbulent *macro* Reynolds and Rossby numbers, based on the instantaneous horizontal velocity rms $u' = \langle u_x^2 + u_y^2 \rangle^{1/2}/2$ and the mesh size $M$,

$$\mathrm{Re}_M = u'M/\nu, \quad \mathrm{Ro}_M = u'/2\Omega M \tag{1}$$

(the brackets $\langle\cdot\rangle$ denote spatial and ensemble average). These numbers are usually defined from the integral length scales,[8] which are increasing functions of time in decaying turbulence, starting from values of order of the mesh size $M$ at early times. However, our measurements being restricted to a central rectangular area of size $4.0M \times 3.2M$, the large scale limit of the velocity correlation function could not be accurately defined, and we had to make use of macro Reynolds and Rossby numbers based on the mesh size $M$ instead, which systematically underestimate the actual ones. As the turbulence decays, both $\mathrm{Re}_M$ and $\mathrm{Ro}_M$ decrease in time, with the ratio $\mathrm{Ro}_M/\mathrm{Re}_M$ remaining constant. This ratio only depends on the angular velocity of the turntable and is given by $\mathrm{Ro}_g/\mathrm{Re}_g = (h/M)^2\mathrm{Ek}$, where $\mathrm{Ek} = \nu/2\Omega h^2$ is the Ekman number based on the tank height $h$, which lies in the range $3\times10^{-5} - 6\times10^{-7}$ for the present experiments.

Finally, since large Reynolds number turbulence gives rise to vorticity levels much larger than the inverse turnover time $u'/M$, small scales may escape from the influence of the background rotation even for large $\Omega$. It is therefore of interest to introduce a *micro*-Rossby number,

$$\mathrm{Ro}_\omega = \omega'/2\Omega,$$

where $\omega' = \langle \omega_z^2 \rangle^{1/2}$ is the instantaneous rms of the vertical vorticity, that compares the small scale vorticity to the background vorticity. The error on $\omega'$ from the PIV measurement leads to an uncertainty of about 10%–20% on $\mathrm{Ro}_\omega$. The difference between the micro- and macro-Rossby numbers may vanish for asymptotically large rotation rates, for which the vorticity may become a large-scale quantity. However, for sufficiently large Reynolds numbers and moderate rotation rates, an intermediate range may exist, for which $\mathrm{Ro}_M \ll 1$ and $\mathrm{Ro}_\omega \gg 1$ simultaneously. In that range, the large scales are expected to be affected by the rotation whereas the small scales are not.[8] It is in that intermediate range that we are mainly interested, for which interactions between turbulence and inertial waves leads to a nontrivial dynamics, with possible energy transfers towards the 2D mode.

## III. CYCLONIC/ANTICYCLONIC ASYMMETRY

### A. Vorticity distributions

Figure 2 shows four snapshots of the vertical component of the vorticity fields, $\omega_z = \partial u_y/\partial x - \partial u_x/\partial y$, taken at four times during the decay, for $\Omega = 1.5$ rad s$^{-1}$ and $V_g = 1.63$ m s$^{-1}$ (data set ● in Table I). Each field is normalized by its instantaneous vorticity rms $\omega'$. Since the pictures are taken from below, the system rotation is clockwise, so that cyclonic vorticity (in red) is associated with clockwise rotation and anticyclonic vorticity (in blue) with anticlockwise rotation.

Just after the grid translation, $\tau = tV_g/M \simeq 20$ [Fig. 2(a)], the vorticity field shows nearly symmetric small-scale disordered fluctuations. As time proceeds [$\tau \simeq 660$ and 1400, Fig. 2(b) and 2(c)], intense large-scale coherent vortices gradually appear, as the result of the increasing influence of the background rotation. These coherent vortices are essentially cyclonic (their vorticity is of the same sign than the background vorticity), as classically observed from experiments[5,6,31] and numerical simulations.[13,18] Anticyclonic vorticity is also present, but it is much weaker and does not show vortices as coherent as for cyclonic vorticity. Vortex sheets of moderate vorticity, of either cyclonic or anticyclonic sign, can be seen, surrounding the vortices and strained in the horizontal direction. These strained shear layers are visually similar to the filamentation of vorticity observed in the enstrophy cascade of 2D turbulence.[20] The prevalence of corotating cyclonic vortices probably enhances the horizontal straining of these shear layers, compared to the case of usual 2D turbulence, where vortices of both positive and negative signs are present. In the neighborhood of the intense cyclones, vortex sheets spiraling in the clockwise direction are frequently encountered, indicating the presence of axial stretching in the core of the vortices. For the last image, $\tau \simeq 2800$ [Fig. 2(d)], only a strong cylonic vortex with nearly circular cross section, surrounded by a weak turbulent background, is present in the field. Expressed in units of the rotation time scale, the corresponding time is $\Omega t \simeq 100$ in this case. As will be shown in Sec. III B, the effect of the Ekman friction is dominant at that time, and the last isolated cyclonic vortices are eventually damped by Ekman friction.

The asymmetry between cyclonic and anticyclonic vorticity clearly appears from the vorticity distributions shown in Fig. 3, taken at three times during the decay. The same probability density functions (pdf), $p(\omega_z)$, are shown normalized either by the background vorticity $2\Omega$ [Fig. 3(a)] or by the instantaneous vorticity rms $\omega'$ [Fig. 3(b)]. Just after the grid translation, $p(\omega_z)$ is nearly symmetric, but as time evolves it becomes strongly positively skewed, confirming

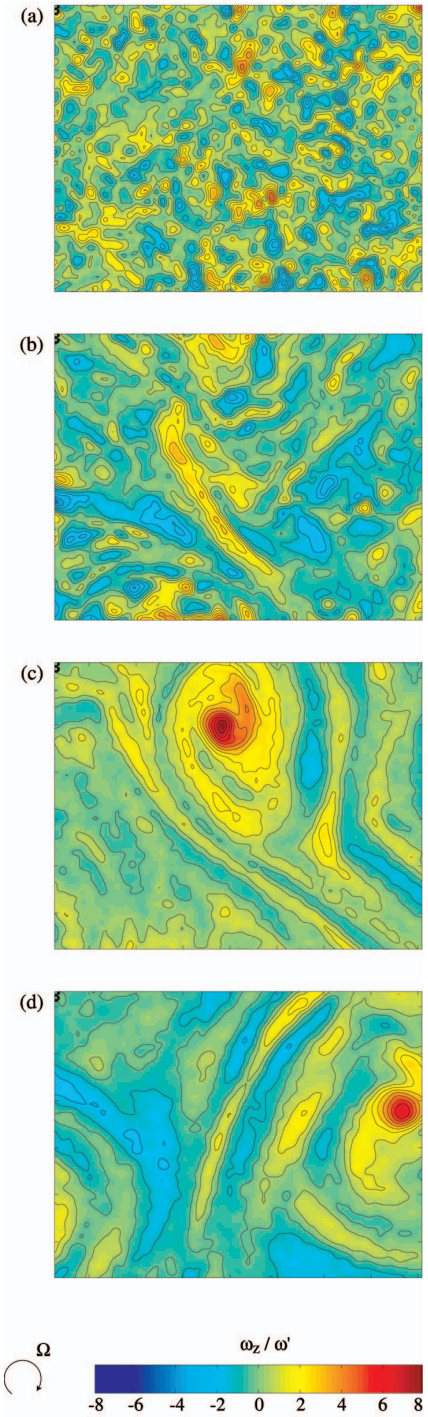


FIG. 2. (Color). Normalized vertical vorticity fields $\omega_z/\omega'$ at four successive times for $\Omega=1.5$ rad s$^{-1}$ and $V_g=1.63$ m s$^{-1}$ (data set ● in Table I). The imaged rectangle represents 16 cm × 13 cm, i.e., about 17% of the section of tank. Twenty-two equally spaced contour levels are shown in the range $[-8\omega', 8\omega']$. (a) $(\tau, \mathrm{Re}_M, \mathrm{Ro}_\omega) \simeq (20, 4400, 6.4)$. (b) (660, 855, 0.61). (c) (1400, 520, 0.27). (d) (2800, 210, 0.11).

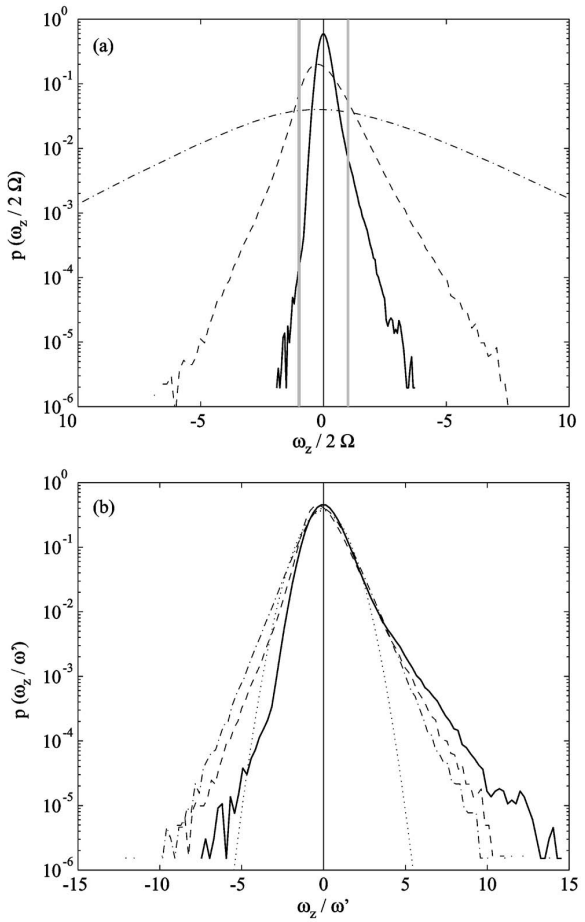


FIG. 3. Probability density function of the axial vorticity $\omega_z$ at three times during the decay, for $\Omega=1.5$ rad s$^{-1}$ and $V_g=0.82$ m s$^{-1}$ (data set ○ in Table I), (a) normalized by the background vorticity $2\Omega$; (b) normalized by the instantaneous vorticity rms $\omega'$. - · -, $(\tau, \mathrm{Re}_M, \mathrm{Ro}_\omega)=(20, 1990, 3.9)$; - -, (230, 780, 0.8); —, (660, 440, 0.26). In (a), the vertical gray lines indicate $\omega_z=\pm 2\Omega$. In (b), the dotted curve shows a Gaussian distribution.

the visual evidence of the cyclonic vorticity prevalence. For $\tau \simeq 230$, the pdf shows an approximately exponential tail for $\omega_z > 3\omega'$, while the negative vorticity fluctuations show a slightly sub-Gaussian distribution. It may be noted that this asymmetry is more pronounced when the extreme fluctuations are of the order of the background vorticity $2\Omega$ [indicated by the vertical gray lines in Fig. 3(a)], i.e., when the associated micro-Rossby number $\omega_z/2\Omega$ is of order of 1. For this pdf, the cyclonic versus anticyclonic probability ratio taken at $|\omega_z|=2\Omega$, $p(2\Omega)/p(-2\Omega)$, is of order of 100.

The prevalence towards cyclonic vorticity is a generic feature of rotating systems, which has received a number of experimental and theoretical characterizations.[10–12,36,37] Two mechanisms may explain this asymmetry. First, since the vortex stretching and tilting by the turbulent strain act on the absolute vorticity $\boldsymbol{\omega}+2\Omega\hat{\mathbf{e}}_z$, vorticity with a positive component along $\hat{\mathbf{e}}_z$, i.e., cyclonic vorticity, is more amplified in average. Shear layers of cyclonic vorticity are thus more likely to be strengthened and to roll up into cyclonic vortices, while those of anticyclonic vorticity remain weak and are destabilized by the surrounding turbulence. This amplification mechanism is essentially present at the early time of the decay, for a moderate Rossby number, since for longer times

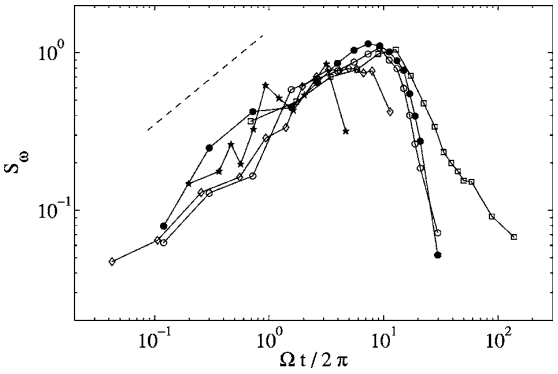


FIG. 4. Vorticity skewness $S_\omega$ as a function of the number of tank rotation $\Omega t/2\pi$, for the five data sets (see the symbols in Table I). The dashed line shows a power law $(\Omega t)^{0.6}$.

the flow may become quasi-2D and the vertical strain should consequently become much weaker. The second reason for the cyclonic vorticity prevalence is an inertial instability modified by the Coriolis force, which leads to a selective destabilization of the anticyclonic regions.[11] For idealized axisymmetric vortices, this instability may be described in terms of a generalized Rayleigh criterion,[36,37] which includes the effect of the background rotation. This criterion predicts that cyclonic regions are stabilized by the background rotation, while anticyclonic regions of negative absolute vorticity, i.e., having $\omega_z < -2\Omega$, may be unstable with respect to axisymmetric disturbances. This is consistent with the pdfs of Fig. 3(a), which show a maximum asymmetry when the tails are of order of the background vorticity $2\Omega$.

### B. Vorticity skewness

A useful quantity to further quantify the prevalence towards cyclonic vorticity as time evolves is the vorticity skewness factor, first introduced by Bartello *et al.*,[13]

$$S_\omega = \frac{\langle \omega_z^3 \rangle}{\langle \omega_z^2 \rangle^{3/2}},$$

where the brackets $\langle \cdot \rangle$ denote spatial and ensemble average. $S_\omega$ is zero for symmetric vorticity fluctuations. A generic behavior for the buildup of $S_\omega$ in decaying rotating turbulence should only be expected if the decay starts from an initial homogeneous 3D turbulence, i.e., for large initial Reynolds and Rossby numbers, which is the case for the present experiment.

The time histories for $S_\omega$ are shown in Fig. 4 as a function of the number of tank rotations $\Omega t/2\pi$. The curves for the different data sets follow the same trend for approximately the first five rotations, showing an approximate power law

$$S_\omega \sim (\Omega t)^{0.6\pm0.1}. \tag{2}$$

Using $\Omega t$ as the nondimensional time shows no significant influence of $V_g$ and $\Omega$ in that range, indicating that $\Omega^{-1}$ is the relevant time scale for the buildup of the vorticity asymmetry. This observation suggests that this growing asymmetry is supported by inertial waves, of maximum frequency given by $2\Omega$. From heuristic statistical arguments, Gence and Frick[39] indeed showed that the time scale for the buildup of the vorticity triple correlation in rotating homogeneous turbulence is $\Omega^{-1}$. However, the power-law behavior (2) observed here is a long-time nonlinear effect, which cannot be inferred from their short-time analysis.

At larger times, $S_\omega$ saturates to a value $\simeq O(1)$, and then sharply decreases, at a time $t_c$ that depends on $\Omega$. This decay probably results from the effect of the confinement. As the characteristic length of the coherent cyclonic vortices reaches the height of the tank, $h$, the Ekman layers on the top and bottom walls induce a vertical pumping of the fluid, from the boundary layers into the core of the vortices for the cyclonic vorticity and inversely for the anticyclonic vorticity.[1,9] In the case of the cyclonic vortices, which are more abundant, this Ekman pumping induces a vortex compression that weakens the circulation of the vortices, on a time scale given by $t_E = h(\nu\Omega)^{-1/2}$, which represents the characteristic time for a fluid particle to travel along the tank height at the vertical velocity of this secondary flow. Although the moderate range for $\Omega$ does not allow to accurately verify the scaling of this time scale, the times $t_c$ for which $S_\omega$ is maximum are found to be

$$t_c \simeq (0.10 \pm 0.02) h(\nu\Omega)^{-1/2} \tag{3}$$

[the values for the Ekman time scale $t_E = h(\nu\Omega)^{-1/2}$ are given in Table I], indicating that the confinement is indeed responsible for the decrease of $S_\omega$ for $t > t_c$. It must be noted that the instantaneous Reynolds number $\mathrm{Re}_M$ for the different data sets is not constant at that time $t_c$, taking values ranging from 350 to 850, ruling out a possible low Reynolds number effect for the decrease of $S_\omega$ at $t > t_c$. The two curves for the data sets at $\Omega = 1.5$ rad s$^{-1}$ (symbols ○ and ● in Table I) approximately coincide, confirming that $V_g$ has no direct influence on the maximum of $S_\omega$ (provided that $\mathrm{Re}_M$ remains sufficiently large at $t \simeq t_c$).

Although the above argument correctly explains the cutoff (3) for the growth of the vorticity skewness, it must be noted however that the *decrease* of $S_\omega$ for $t > t_c$ cannot be explained within the classical linear Ekman theory. A purely linear Ekman pumping, which is valid only for $\mathrm{Ro}_\omega \ll 1$, should equally affect the cyclonic and the anticyclonic vorticity,[1] leading to exponentially decreasing vorticity of both sign, and should therefore let $S_\omega$ unchanged. On the other hand, if the limit $\mathrm{Ro}_\omega \ll 1$ does not hold, as is the case in our experiment ($\mathrm{Ro}_\omega = 0.1-0.4$ for $t \simeq t_c$), nonlinear corrections to the Ekman pumping should be considered, which are shown to enhance the damping of the cyclonic vortices (e.g., Zavala Sansón and van Heijst[38]). As a result, a gradual resymmetrization of the vorticity distribution should be expected on a time scale $O(t_E)$, and may explain the observed decay of $S_\omega$. Accordingly, the self-similar growth (3) may be considered as a generic feature of decaying rotating turbulence, while the maximum of $S_\omega$ is constrained by the finite size effects.

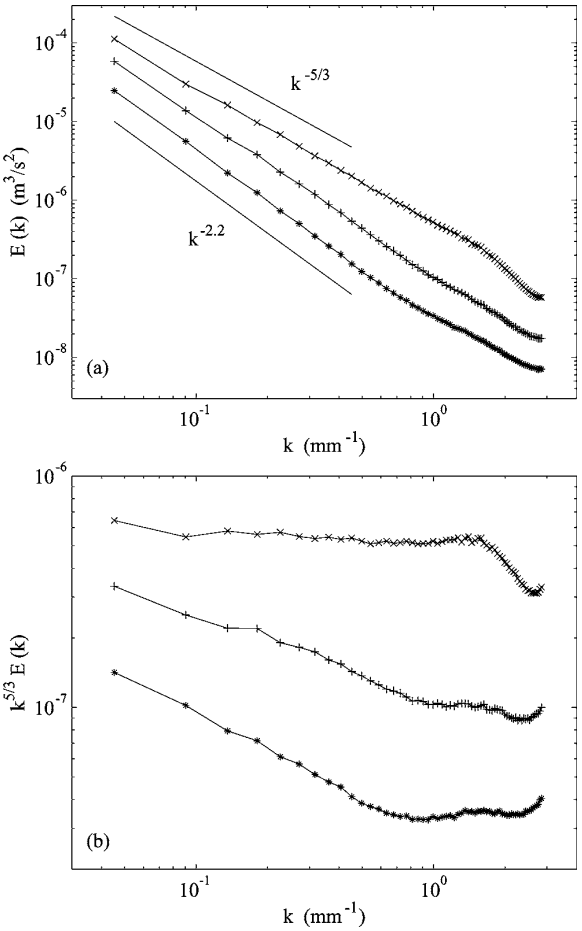


FIG. 5. (a) Energy spectra for different Rossby numbers at three times during the decay, for $\Omega=1.5$ rad s$^{-1}$ and $V_g=1.63$ m s$^{-1}$ (data set ● in Table I). ×, $(\tau, \mathrm{Re}_M, \mathrm{Ro}_\omega)=(50, 3400, 5.5)$; +, (230, 1200, 1.2); *, (700, 600, 0.35). (b) Same spectra compensated by $k^{5/3}$.

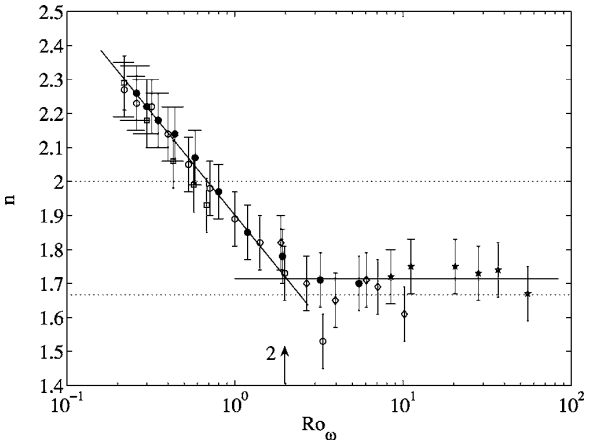


FIG. 6. Exponent $n$ of the power spectrum as a function of the instantaneous micro-Rossby number $\mathrm{Ro}_\omega$, for the five data sets (see the symbols in Table I). Time proceeds from large to small $\mathrm{Ro}_\omega$. The lower dotted line corresponds to the exponent 5/3 of the Kolmogorov spectrum, and the upper one shows the exponent 2 (see the text). The solid lines are guide for the eye.

## IV. ENERGY SPECTRUM

We now turn to the influence of the background rotation on the scaling of the energy spectrum. The 1D energy spectrum $E(k)$, where $k$ is the horizontal wave number, is computed from the 2D Fourier transform of the velocity field truncated to a central $13\times13$ cm$^2$ square, and ensemble averaged over 50 statistically independent realizations at a fixed delay $t$ after the grid translation.

Figure 5(a) shows three energy spectra, obtained at three times during the decay. Just after the grid translation, for $\tau=50$, the energy spectrum shows a well-defined scaling range over more than one decade, with a power law close to $k^{-5/3}$, as expected for 3D isotropic turbulence without significant rotation effect. It must be noted that the power laws extend to wave numbers significantly smaller than the forcing wave number $k_f=2\pi/M\simeq0.16$ mm$^{-1}$ (where $M$ is the mesh size), at which energy is initially injected. This generic feature of decaying turbulence, even in the absence of rotation, is related to the increase of the integral length scale, and does not necessarily imply the existence of a net inverse energy cascade at low wave numbers. No resolved dissipative range can be seen for large wave numbers, due to the limited resolution of the PIV. The spectral behavior of the PIV noise for large wave numbers is possibly due to nontrivial biases in the computation of the image correlations,[40] and we therefore focus on small wave numbers, $k<1$ mm$^{-1}$. Later on, for $\tau=230$ and 700, an inertial range is still present, but the power law becomes steeper, with a slope that gradually increases as time proceeds, reflecting the growing importance of the large scales compared to the small ones. This may be further seen in Fig. 5(b), showing the same three spectra compensated by $k^{5/3}$. While a well-defined plateau is observed at short time, about one decade of power laws with negative slopes is obtained for $\tau=230$ and 700. For even larger times, no clear scaling can be defined from the energy spectrum over a reasonable range of wave numbers, and exponents larger than 2.3 are not found. This lack of scaling occurs for times that approach the Ekman cutoff (3), i.e., it probably results from a confinement effect.

The spectral exponent $n$ is shown for the five data sets in Fig. 6. This exponent is determined by plotting the compensated spectrum $k^nE(k)$ and adjusting the value of $n$ in order to obtain a well-defined plateau for the first decade of wave numbers. An error bar for $n$ can be estimated from this procedure, of about 0.1, as the acceptable range for which a plateau may be defined. Although the scatter is important, a clear trend for $n$ appears when plotted as a function of the instantaneous micro-Rossby number $\mathrm{Ro}_\omega$. For large $\mathrm{Ro}_\omega$, $n$ takes values $\simeq1.7\pm0.1$, close to the expected 5/3 for the Kolmogorov spectrum in the absence of rotation. This slight systematic departure from 5/3 is indeed a well-known intermittency effect, and values close to 1.7 are classically obtained in other experimental configurations.[41] As $\mathrm{Ro}_\omega$ decreases in time, $n$ is found to gradually increase from 1.7 up to $2.3\pm0.1$, with a crossover that takes place at $\mathrm{Ro}_\omega\simeq2\pm0.5$. At the location of this crossover, the Ekman layers

effects are not present yet, and the Reynolds number covers a significant range, from 200 to 2000, so that the steepening of the spectral slope is presumably a true effect of the background rotation. Moreover, the macro-Rossby number $\mathrm{Ro}_M$ lies in the range 0.2–0.7 at the crossover, confirming that the micro-Rossby number $\mathrm{Ro}_\omega$ is the most relevant instantaneous control parameter that governs the scaling of the energy spectrum (plotting the slope $n$ as a function of $\mathrm{Ro}_M$ would increase the horizontal scatter by a factor of 3). This conclusion is actually not straightforward, since the effects of the rotation may be first expected at large scales, and should therefore be governed by the macro-Rossby number $\mathrm{Ro}_M$, with a gradual steepening of the energy spectrum at low wave numbers. However, a $\mathrm{Ro}_M$ dependence of the spectral slope cannot be totally ruled out from the present experiment, because of the restricted range for which $\mathrm{Ro}_\omega > 1$ and $\mathrm{Ro}_M < 1$ simultaneously.

It is worth pointing out that a $k^{-2}$ regime is not supported by our data, except as a transient state for $\mathrm{Ro}_\omega \simeq 0.5$. Spectrum $E(k) \simeq k^{-2}$ for rotating turbulence was predicted by Zhou[21] and Canuto and Dubovikov[22] on phenomenological grounds, assuming that the time scale for energy transfers is given by the rotation time scale $\Omega^{-1}$ instead of the classical nonlinear time scale, but without explicitly taking account of the anisotropy of the flow. In their analysis, the $k^{-2}$ spectrum is limited to low wave numbers, $k \ll \Omega^{3/2}\epsilon^{-1/2}$, for which the *local* Rossby number is $\ll 1$, whereas the classical $k^{-5/3}$ is recovered for larger wave numbers. Although some evidence of a $k^{-2}$ law can be found in experiments[25] and simulations,[23,24] it may be an effect of a moderate Rossby number, for which the anisotropy is indeed weak. This conclusion agrees with the recent LES results of Yang and Domaradski,[29] who do observe a $k^{-2}$ as a transient state for moderate Rossby number as well, but a steeper spectrum for smaller Rossby numbers.

An asymptotic analysis, in the limit of quasi-infinite Reynolds number and quasizero Rossby number, has been recently carried out using the formalism of wave turbulence theory by Galtier,[26] leading to a 3D anisotropic spectrum $e(\mathbf{k}) \sim k_\parallel^{-1/2} k_\perp^{-7/2}$, where $k_\parallel$ and $k_\perp$ are the wave-number components along the rotation axis and normal to it, respectively. In a similar approach, starting from a generalized eddy-damped quasinormal Markovian (EDQNM) model, Cambon, Rubinstein, and Godeferd[27] derived a 3D spectrum $e(\mathbf{k}) \sim k_0^{-1/2} k_\parallel^{-1/2} k_\perp^{-3}$, where $k_0$ is a cutoff in the horizontal plane. Numerical integration of this model[30] yields a $E(k) \simeq k^{-3}$ form for the one-dimensional (1D) spherically averaged spectrum, this scaling being the result of a combination of a $k^{-2}$ scaling for nearly horizonal wave numbers and a steeper scaling for nearly vertical ones. Although direct comparison between these predictions and our spectra is not straightforward, because only two components of the velocity in the plane normal to the rotation axis are experimentally measurable, these two predictions are expected to give 1D spectra steeper than $k^{-2}$, which is consistent with our observations.

## V. ENERGY TRANSFERS

### A. Velocity increments skewness

Further insight into the steepening of the energy spectrum for $\mathrm{Ro}_\omega < 2$ may be obtained by inspecting the influence of the background rotation on the energy transfers in physical space. Using the assumption of isotropy, the scale-to-scale energy transfers may be characterized by the statistics of the longitudinal velocity increment $\delta_r u = [\mathbf{u}(\mathbf{x}+\mathbf{r}) - \mathbf{u}(\mathbf{x})] \cdot \mathbf{r}/r$ across the separation $r = |\mathbf{r}|$. The second-order moment of this quantity, $\langle \delta_r u^2 \rangle$, is a measure of the kinetic energy at scale $r$, while the third-order moment, $\langle \delta_r u^3 \rangle$, is related to the mean energy flux at that scale. In particular, the sign of $\langle \delta_r u^3 \rangle$ gives the direction of the energy flux through that scale: positive for transfers towards larger scales, and negative for transfers towards smaller scales.

For high-Reynolds number nonrotating isotropic turbulence, energy is transferred at a constant rate for all scales in the inertial range, and $\langle \delta_r u^3 \rangle$ satisfies Kolmogorov's 4/5th law:[41]

$$\langle \delta_r u^3 \rangle = -\tfrac{4}{5}\epsilon r, \tag{4}$$

where $\epsilon$ is the mean energy dissipation. The energy proceeds, in average, from large to small scales. This law still applies for decaying turbulence, where $\epsilon$ must be interpreted as the instantaneous energy dissipation rate.[42] This relation indicates that longitudinal velocity increments are negatively skewed, i.e., compressive strain is less likely but more intense than extensional strain.[3] For strictly 2D turbulence, one has to distinguish between the two possible cascade regimes. For $r$ larger than the injection scale, in the inverse energy cascade, the transfers proceed from small to large scale, and $\langle \delta_r u^3 \rangle$ is positive.[20] On the other hand, for $r$ smaller than the injection scale, in the enstrophy cascade, there is no energy transfer and $\langle \delta_r u^3 \rangle$ should be zero.[43]

In Fig. 7(a) is plotted $\langle \delta_r u^3 \rangle$ as a function of $r$, where $\delta_r u$ denotes here the longitudinal velocity increments in the plane normal to the rotation axis, at three times during the decay, for $\Omega = 1.5$ rad s$^{-1}$ and $V_g = 1.63$ m s$^{-1}$ (data set ● in Table I). At early time, $\tau \simeq 80$, $\langle \delta_r u^3 \rangle$ is negative for all $r$ and approximately proportional to $r$ for 1.5 cm $< r <$ 6 cm, in agreement with the 4/5th law (4) for the nonrotating case. This behavior holds for scales slightly larger than the mesh size, $M = 3.9$ cm, which is consistent with the scaling range on the energy spectrum that begins for $k < 2\pi/M$. As time proceeds, the magnitude of $\langle \delta_r u^3 \rangle$ strongly decreases, essentially due to the decay of the energy dissipation rate $\epsilon$. While $\langle \delta_r u^3 \rangle$ remains negative at small scales, its sign changes for $r \simeq 1-2$ cm and becomes positive for larger $r$, suggesting that a net inverse energy cascade begins to develop at large scales. Similar observations were reported by Simand *et al.*[44] from one-point measurements in the vicinity of a strong localized vortex. The scale at which the flux vanishes is found to decrease in time, in agreement with the expected picture of a direct energy cascade confined to smaller scales as the influence of the rotation increases. However, since no energy supply is present, this double cascade regime can only take place as a transient state during the decay.

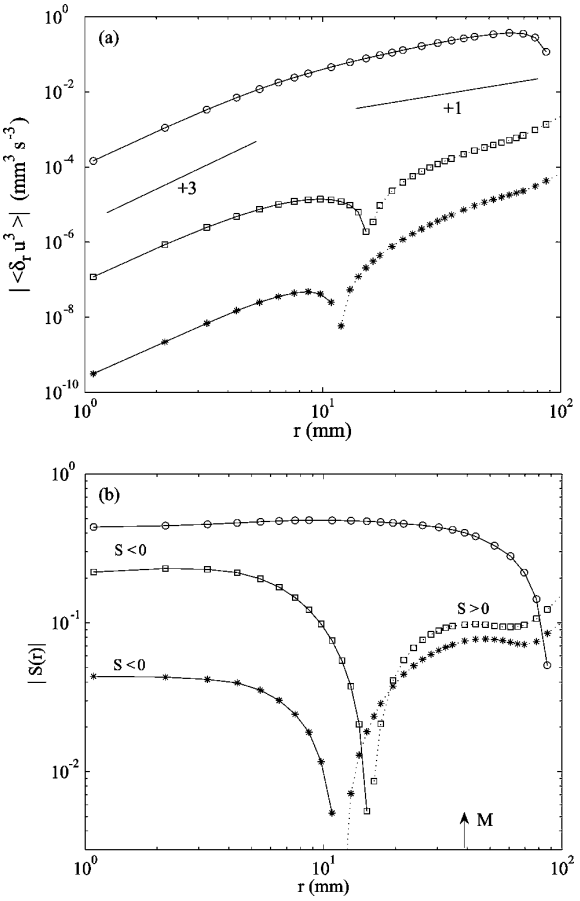


FIG. 7. (a) Third-order moment of the longitudinal velocity increments as a function of the scale $r$, at three different times during the decay. Negative values are plotted with full lines, and positive values with dotted lines. (b) Skewness of the longitudinal velocity increments (5). ○, $\tau=80$; □, $\tau=820$; *, $\tau=2200$.

Since the energy dissipation rate $\epsilon$ decreases in time during the decay, at a rate that may moreover depend on the Rossby number, it is convenient to normalize $\langle \delta_r u^3 \rangle$ by introducing the skewness of the velocity increments

$$S(r) = \frac{\langle \delta_r u^3 \rangle}{\langle \delta_r u^2 \rangle^{3/2}} \tag{5}$$

to characterize the instantaneous relative energy transfers. Assuming normal scaling (i.e., neglecting intermittency effects), one has $\langle \delta_r u^2 \rangle \sim (\epsilon r)^{2/3}$, so that the skewness factor $S(r)$ should be independent of $r$ for inertial scales. The direction of the energy cascade may be then solely described by the sign of the skewness: $S(r)<0$ for the direct cascade, $S(r)>0$ for the inverse cascade, and $S(r)=0$ in the absence of energy transfers.

The skewness of the velocity increments, $S(r)$, is plotted in Fig. 7(b) for the same data set as in Fig. 7(a). It must be noted that computing $S(r)$ from PIV measurements is a delicate issue, as very large statistics are needed to ensure a correct convergence of odd moments. Assuming a symmetrically distributed PIV noise, a bias is introduced towards small values of $|S(r)|$, which may be significant at small scales. A smoothing procedure using a Gaussian filter is applied to the velocity fields in order to minimize this effect. The size of the smoothing windows is carefully chosen as the smallest size leading to a nondecreasing $|S(r)|$ as $r \to 0$. No bias is expected from this procedure, since in 3D turbulence $|S(r)|$ should monotonically increase as $r \to 0$. Filter sizes between 1 and 1.5 collocation points have been used for the three curves in Figs. 7(a) and 7(b). This procedure is expected to give reliable results for moderate Reynolds numbers, for which the Kolmogorov scale $\eta$ is slightly smaller or of the same order of the spatial resolution, but may significantly underestimate the actual skewness for larger Reynolds numbers. The relative error can be estimated to about 20% for small $r$ when averaging over 50 statistically independent velocity fields, but may be even larger for separations $r$ comparable to the image size, for which poor statistics is available.

At early time $S(r)$ is approximately constant for scales $r<6$ cm, taking values around $-0.45 \pm 0.03$. Values in the range 0.4–0.5 are typical for nonrotating experiments and simulations.[41] As time proceeds, the magnitude of $|S(r)|$ decreases at small scales, a clear indication of the inhibition of the energy transfers by the background rotation. For the second and third curves, the Reynolds number $\mathrm{Re}_M$ is 750 and 320, respectively, values for which $S(r) \simeq -0.4$ in the nonrotating case, confirming that the decrease of $|S(r)|$ is not a weak Reynolds number effect but a true effect of the rotation. The positive skewness at larger scales, in the inverse energy cascade, is weak, $S(r) \simeq 0.06-0.10$, a value in qualitative agreement with numerical simulations of strictly 2D forced turbulence.[45]

### B. Velocity derivative skewness

In order to further characterize the influence of the Reynolds and Rossby numbers on the energy transfers, we finally focus on the longitudinal velocity derivative skewness,

$$S = \frac{\langle (\partial u/\partial r)^3 \rangle}{\langle (\partial u/\partial r)^2 \rangle^{3/2}}, \tag{6}$$

which is approximated by taking $r \to 0$ in Eq. (5). This quantity is of first interest, since it is directly related to the enstrophy production.[2,3] Direct cascade of energy in 3D turbulence is associated to a positive enstrophy production, and hence to a negative velocity derivative skewness. On the other hand, no enstrophy production is present in 2D turbulence, and $S$ is zero (this result follows from a purely kinematical constraint, since incompressibility requires that the two normal strain rates are opposite and of equal magnitude for a 2D flow). In rotating 3D turbulence, the scrambling effect of inertial waves leads to a damping of the velocity derivative skewness,[16] so that $|S| \to 0$ just reflects the inhibition of the energy transfers but is not a sufficient condition for a 2D state.

The skewness of the velocity derivative is plotted as a function of the instantaneous micro-Rossby number in Fig. 8, for the five different data sets in Table I. All the measured skewness are found negative. As previously mentioned, the

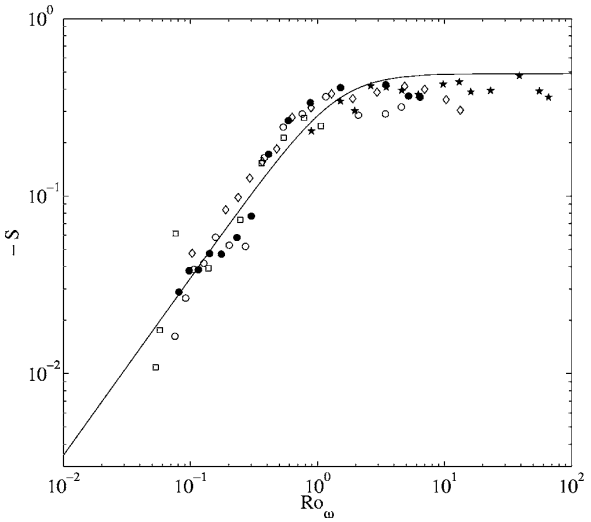


FIG. 8. Skewness of the longitudinal velocity derivative (6) as a function of the instantaneous micro-Rossby number $\mathrm{Ro}_\omega$, for the five data sets (see symbols in Table I). Time proceeds from large to small $\mathrm{Ro}_\omega$. The line is the model equation (7) from Cambon *et al.* (Ref. 16).

error bar is of about 20%, a value which is consistent with the scatter of the different data sets. For large $\mathrm{Ro}_\omega$, $S$ is approximately constant, $S \simeq -0.40 \pm 0.05$, while for smaller $\mathrm{Ro}_\omega$ it decreases approximately as $|S| \propto \mathrm{Ro}_\omega$. The crossover between these two regimes, $\mathrm{Ro}_\omega \simeq 1-2$, remarkably coincide with the crossover found for the spectral slope $n$ (Fig. 6). As previously mentioned, at this crossover, $\mathrm{Re}_M$ is in the range 200–2000, ruling out a possible Reynolds number effect on the transition. These observations indicate that the energy spectrum starts departing from the Kolmogorov form $k^{-5/3}$ at the point where the background rotation starts inhibiting the energy transfers. This is a nontrivial result, since $S$ is a small-scale quantity, while the spectral exponent $n$ describes the full inertial range.

The experimental data are found to compare well with the model equation

$$S = \frac{-0.49}{(1 + 2\mathrm{Ro}_\omega^{-2})^{1/2}}, \tag{7}$$

proposed by Cambon *et al.*[16] to fit earlier DNS results, which is also shown in Fig. 8. In their analysis, the denominator was suggested from the isotropic EDQNM closure,[46] where the effect of the rotation was taken into account by simply replacing in the eddy-damped coefficient the nonlinear time scale estimated from the enstrophy, $\langle \omega^2 \rangle^{-1/2}$, by the one from the absolute enstrophy, $[\langle \omega^2 \rangle + (2\Omega)^2]^{-1/2}$. The value $-0.49$ for $\mathrm{Ro}_\omega \gg 1$ was borrowed from the infinite Reynolds isotropic EDQNM model without rotation.[46] A slightly lower magnitude for $|S|$ at large $\mathrm{Ro}_\omega$ is measured experimentally, $|S| \simeq 0.40 \pm 0.05$ instead of 0.49, probably due to the insufficiently resolved small scales from the PIV computations, which are more pronounced at large Reynolds number. A model similar to (7) was also derived by Park and Chung,[47] on the basis of the $k^{-2}$ spectrum proposed by Zhou.[21] Although anisotropy effects are ignored in both approaches, these crude models remarkably capture the behavior of the experimental data. This agreement with isotropic models indicates that the damping of the velocity derivative skewness at small $\mathrm{Ro}_\omega$ is not directly related to the two-dimensionalization process, but just reflects the inhibition of the energy transfers originating from the scrambling effect of the inertial waves.

## VI. DISCUSSION AND CONCLUSION

A series of grid-generated turbulence experiments in a rotating frame has been carried out, with the aim of investigating the influence of the background rotation on the turbulence decay starting from approximately homogeneous and isotropic initial conditions (large initial Reynolds and Rossby numbers). Three quantities have been systematically characterized in the course of the decay: the vorticity skewness, which traces the asymmetry between the cyclonic and anticyclonic vorticity, the spectral slope of the energy spectrum, and the skewness of the velocity derivative, which characterizes the scale-to-scale energy transfers in physical space.

Starting from approximately homogeneous 3D turbulence with symmetric vorticity fluctuations, an asymmetry towards cyclonic vorticity gradually builds up, with a growth of the vorticity skewness as $S_\omega \sim (\Omega t)^{0.6 \pm 0.1}$, up to values $O(1)$. This growth is interrupted for times $t_c \simeq 0.1 h (\nu \Omega)^{-1/2}$ (typically three to ten tank rotations), for which nonlinear Ekman friction on the top and bottom walls preferentially reduces the cyclonic vorticity.[38] As a consequence, the observed maximum of $S_\omega$ probably results from finite size effects, and larger values should be observable in larger experiments, for which the Ekman friction effects should be delayed.

Although the background rotation is shown to have a deep influence on the vorticity asymmetry from the early time, it has been shown to have no significant effect on the spectrum and the energy transfers as long as the instantaneous micro-Rossby number remains sufficiently large. The slope of the energy spectrum and the velocity derivative skewness are found to remain close to their classical values for $\mathrm{Ro}_\omega > 2 \pm 0.5$ ($n \simeq 5/3$ and $S \simeq -0.4$), as for nonrotating turbulence. On the other hand, as $\mathrm{Ro}_\omega$ decreases below 2, the energy spectrum becomes steeper, and the magnitude of the velocity derivative skewness starts decreasing as $|S| \propto \mathrm{Ro}_\omega$, which is a clear signature of the inhibition of the energy transfers by the background rotation. This transition takes place at a time long before the Ekman friction time, $t < t_c$, suggesting that the observed behaviors of $E(k)$ and $S$ are generic features of homogeneous decaying rotating turbulence.

Finally, it was noted that, in the range of Reynolds and Rossby numbers spanned by the present experiment, no saturation of the spectral exponent $n$ could be observed as $\mathrm{Ro}_\omega \to 0$. Although the observed trend is not inconsistent with the limit $n \to 3$ that may be expected for turbulence dominated by rotation, this limit is very far from what can be achieved in our system. Crude extrapolation of the trend for $n$ in Fig. 6 would lead to a $k^{-3}$ spectrum for $\mathrm{Ro}_\omega < 10^{-2}$. Reaching such a small value while keeping an acceptable Reynolds

number would require rotation rates of about $\Omega \simeq 150$ rad s$^{-1}$, or equivalently dimensions larger by a factor of 5, which is obviously well beyond our experimental setup. One may conclude that using 3D isotropic turbulence as an initial condition in a decaying rotating experiment may hardly allow to observe a $k^{-3}$ spectrum in a laboratory-sized experiment. Of course, this conclusion does not hold for inhomogeneous turbulence or nonisotropic forcing, which may lead to a $k^{-3}$ spectrum at more reasonable Rossby numbers.

## ACKNOWLEDGMENTS

We acknowledge C. Cambon and S. Galtier for fruitful discussions, and A. Aubertin, H. Auradou, G. Chauvin, and R. Pidoux for experimental help. We are indebted to A. Stegner for providing the rotating turntable apparatus.

[1] H. Greenspan, *The Theory of Rotating Fluids* (Cambridge University Press, Cambridge, 1968); J. Pedlosky, *Geophysical Fluid Dynamics* (Springer, New York, 1987).
[2] M. Lesieur, *Turbulence in Fluids* (Kluwer Academic, Dordrecht, 1997).
[3] P. A. Davidson, *Turbulence* (Oxford University Press, New York, 2004).
[4] A. Ibbetson and D. Tritton, "Experiments on turbulence in a rotating fluid," J. Fluid Mech. **68**, 639 (1975).
[5] A. D. McEwan, "Angular momentum diffusion and the initiation of cyclones," Nature **260**, 126 (1976).
[6] E. J. Hopfinger, F. K. Browand, and Y. Gagne, "Turbulence and waves in a rotating tank," J. Fluid Mech. **125**, 505 (1982).
[7] S. C. Dickinson and R. R. Long, "Oscillating-grid turbulence including effects of rotation," J. Fluid Mech. **126**, 313 (1984).
[8] L. Jacquin, O. Leuchter, C. Cambon, and J. Mathieu, "Homogeneous turbulence in the presence of rotation," J. Fluid Mech. **220**, 1 (1990).
[9] F. S. Godeferd and L. Lollini, "Direct numerical simulations of turbulence with confinement and rotation," J. Fluid Mech. **393**, 257 (1999).
[10] J. A. Johnson "The stability of shearing motion in a rotating fluid," J. Fluid Mech. **17**, 337 (1963).
[11] M. Lesieur, S. Yanase, and O. Métais, "Stabilizing and destabilizing effects of a solid-body rotation on quasi-two-dimensional shear layers," Phys. Fluids A **3**, 403 (1991).
[12] D. Tritton, "Stabilization and destabilization of turbulent shear flow in a rotating fluid," J. Fluid Mech. **241**, 503 (1992).
[13] P. Bartello, O. Métais, and M. Lesieur, "Coherent structures in rotating three-dimensional turbulence," J. Fluid Mech. **273**, 1 (1994).
[14] C. Cambon and L. Jacquin, "Spectral approach to nonisotropic turbulence subjected to rotation," J. Fluid Mech. **202**, 295 (1989).
[15] F. Waleffe, "Inertial transfers in the helical decomposition," Phys. Fluids A **5**, 677 (1993).
[16] C. Cambon, N. N. Mansour, and F. S. Godeferd, "Energy transfer in rotating turbulence," J. Fluid Mech. **337**, 303 (1997).
[17] Y. Morinishi, K. Nakabayashi, and S. Q. Ren, "Dynamics of anisotropy on decaying homogeneous turbulence subjected to system rotation," Phys. Fluids **13**, 2912 (2001).
[18] L. M. Smith and F. Waleffe, "Transfer of energy to two-dimensional large scales in forced, rotating three-dimensional turbulence," Phys. Fluids **11**, 1608 (1999).
[19] J. G. Charney, "Geostrophic turbulence," J. Atmos. Sci. **28**, 1087 (1971).
[20] P. Tabeling, "Two-dimensional turbulence: A physicist approach," Phys. Rep. **362**, 1 (2002).
[21] Y. Zhou, "A phenomenological treatment of rotating turbulence," Phys. Fluids **7**, 2092 (1995).
[22] V. M. Canuto and M. S. Dubovikov, "Physical regimes and dimensional structure of rotating turbulence," Phys. Rev. Lett. **78**, 666 (1997); "A dynamical model for turbulence. V. The effect of rotation," Phys. Fluids **9**, 2132 (1997).
[23] P. K. Yeung and Y. Zhou, "Numerical study of rotating turbulence with external forcing," Phys. Fluids **10**, 2895 (1998).
[24] Y. Hattori, R. Rubinstein, and A. Ishizawa, "Shell model for rotating turbulence," Phys. Rev. E **70**, 046311 (2004).
[25] C. N. Baroud, B. B. Plapp, Z.-S. She, and H. L. Swinney, "Anomalous self-similarity in a turbulent rapidly rotating fluid," Phys. Rev. Lett. **88**, 114501 (2002); C. N. Baroud, B. B. Plapp, H. L. Swinney, and Z.-S. She, "Scaling in three-dimensional and quasi-two-dimensional rotating turbulent flows," Phys. Fluids **15**, 2091 (2003).
[26] S. Galtier, "Weak inertial-wave turbulence theory," Phys. Rev. E **68** 015301(R) (2003).
[27] C. Cambon, R. Rubinstein, and F. S. Godeferd, "Advances in wave turbulence: rapidly rotating flows," New J. Phys. **6**, 73 (2004).
[28] M. Hossain, "Reduction in the dimensionality of turbulence due to a strong rotation," Phys. Fluids **6**, 1077 (1994).
[29] X. Yang and J. A. Domaradzki, "Large eddy simulations of decaying rotating turbulence," Phys. Fluids **16**, 4088 (2004).
[30] F. Bellet, F. S. Godeferd, J. F. Scott, and C. Cambon, "Wave-turbulence in rapidly rotating flows," in *Advances in Turbulence X*, edited by H. I. Andersson and P. A. Krogstad, 10th European Turbulence Conference (CIMNE, Barcelona, 2004).
[31] J. E. Ruppert-Felsot, O. Praud, E. Sharon, and H. L. Swinney, "Extraction of coherent structures in a rotating turbulent flow experiment," Phys. Rev. E **72**, 016311 (2005).
[32] O. Praud, J. Sommeria, and A. M. Fincham, "Decaying grid turbulence in a rotating stratified fluid," J. Fluid Mech. (to be published).
[33] P. Constantin, "Energy spectrum of quasigeostrophic turbulence," Phys. Rev. Lett. **89**, 184501 (2002).
[34] M. S. Mohamed and J. LaRue, "The decay power law in grid-generated turbulence," J. Fluid Mech. **219**, 195 (1990).
[35] LaVision GmbH, Anna-Vandenhoeck-Ring 19, D-37081 Goettingen, Germany.
[36] C. Kloosterziel and J. F. van Heijst, "An experimental study of unstable barotropic vortices in a rotating fluid," J. Fluid Mech. **223**, 1 (1991).
[37] C. Mutabazi, C. Normand, and J. E. Wesfreid, "Gap size effects on centrifugally and rotationally driven instabilities," Phys. Fluids A **4**, 1199 (1992).
[38] L. Zavala Sansón and G. J. F. van Heijst, "Nonlinear Ekman effects in rotating barotropic flows," J. Fluid Mech. **412**, 75 (2000).
[39] J. N. Gence and C. Frick, "Naissance des corrélations triples de vorticité dans une turbulence statistiquement homogène soumiseà une rotation," C. R. Acad. Sci. Série IIB **329**, 351 (2001).
[40] J. M. Foucault, J. Carlier, and M. Stanislas, "PIV optimization for the study of turbulent flow using spectral analysis," Meas. Sci. Technol. **15**, 1046 (2004).
[41] U. Frisch, *Turbulence* (Cambridge University Press, Cambridge, 1995).
[42] E. Lindborg, "Correction to the four-fifths law due to variations of the dissipation," Phys. Fluids **11**, 510 (1999).
[43] A. Belmonte, W. I. Goldburg, H. Kellay, M. A. Rutgers, B. Martin, and X. L. Wu, "Velocity fluctuations in a turbulent soap film: The third moment in two dimensions," Phys. Fluids **11**, 1196 (1999).
[44] C. Simand, F. Chillà, and J.-F. Pinton, "Inhomogeneous turbulence in the vicinity of a large-scale coherent vortex," Europhys. Lett. **49**, 336 (2000); "Inhomogeneous turbulence in the vicinity of a large-scale coherent vortex: erratum," *ibid.* **49**, 821 (2000).
[45] G. Boffetta, A. Celani, and M. Vergassola, "Inverse energy cascade in two-dimensional turbulence: Deviations from Gaussian behavior," Phys. Rev. E **61**, R29 (2000).
[46] S. A. Orszag, "Analytical theories of turbulence," J. Fluid Mech. **41**, 363 (1970).
[47] J. Y. Park and M. K. Chung, "An analytical model of velocity-derivative skewness of rotating homogeneous turbulence," Fluid Dyn. Res. **26**, 281 (2000).

# On the decrease of intermittency in decaying rotating turbulence

J. Seiwert, C. Morize, and F. Moisy[a)]
*Université Paris-Sud 11, Université Pierre et Marie Curie-Paris 6, CNRS. Lab FAST, Bât 502, Campus Universitaire, Orsay F-91405, France*

(Received 28 February 2008; accepted 20 May 2008; published online 15 July 2008)

The scaling of the longitudinal velocity structure functions, $S_q(r)=\langle|\delta u(r)|^q\rangle\sim r^{\zeta_q}$, is analyzed up to order $q=8$ in a decaying rotating turbulence experiment from a large particle image velocimetry dataset. The exponent of the second order structure function $\zeta_2$ increases throughout the self-similar decay regime, up to the Ekman time scale. The normalized higher-order exponents $\zeta_q/\zeta_2$ are close to those of the intermittent nonrotating case at small times, but show a marked departure at larger times, on a time scale $\Omega^{-1}$ ($\Omega$ is the rotation rate), although a strictly nonintermittent linear law $\zeta_q/\zeta_2=q/2$ is not reached. © *2008 American Institute of Physics*. [DOI: 10.1063/1.2949313]

Whether intermittency of isotropic three-dimensional (3D) turbulence is decreased or even suppressed in the presence of system rotation has recently received a marked interest.[1,2] Here, intermittency refers to the anomalous scaling of the structure functions (SFs) of order $q$, $S_q(r)=\langle|\delta u(r)|^q\rangle\sim r^{\zeta_q}$, where $\delta u(\mathbf{x},r)=[\mathbf{u}(\mathbf{x}+\mathbf{r})-\mathbf{u}(\mathbf{x})]\cdot\mathbf{r}/r$ is the longitudinal velocity increment, $\mathbf{r}$ an inertial separation normal to the rotation vector $\mathbf{\Omega}$, and $\langle\cdot\rangle$ denotes spatial and ensemble average. A linear variation of the exponents $\zeta_q$ with the order $q$ is the signature of self-similar (nonintermittent) velocity fluctuations, a situation which is found in the inverse cascade of two-dimensional turbulence.[3] On the other hand, anomalous exponents, $\zeta_q/\zeta_2\neq q/2$, are the landmark of 3D isotropic turbulence.[4–6] Based on the qualitative ground that rotating turbulence experiences a partial two dimensionalization, one may naively expect a reduction or a suppression of intermittency by comparison with the 3D nonrotating case. More precisely, describing rapidly rotating turbulence in the limit of zero Rossby numbers as a sum of weakly interacting random inertial waves, the vanishing of nonlinear effects should lead to a special case of nonintermittent wave turbulence.[7,8]

Two papers have recently addressed the issue of the scaling of the SF in rotating turbulence with a stationary forcing. The hot-wire measurements of Baroud *et al.*[1] in a turbulent flow generated by radial jets in a rotating tank showed a transition from an intermittent to a nonintermittent behavior, characterized by a $E(k)\sim k^{-2}$ energy spectrum (i.e., $\zeta_2=1$) and linear higher-order exponents $\zeta_q=q/2$. In a direct numerical simulation (DNS) of rotating turbulence with a large scale isotropic forcing, Müller and Thiele[2] have observed reduced intermittency, also characterized with $\zeta_2\simeq 1$, but higher-order exponents $\zeta_q$ intermediate between $q/2$ and the values usually found in classical (intermittent) 3D turbulence. Those observations are in qualitative agreement with the increase of $\zeta_q$ reported by Simand[9] from hot-wire measurements in the vicinity of a strong vortex, although no clear separation between a constant background rotation and an otherwise homogeneous turbulence advected by the rotation can be defined in this geometry. To date, no theoretical description of the scaling of the anisotropic higher order SF in rotating turbulence is available. Note that in all the above references, only separations $\mathbf{r}$ normal to the rotation vector $\mathbf{\Omega}$ are considered, ignoring the complexity originating from the anisotropic character of rotating turbulence.[8]

In this letter we report new measurements of the high order SF, carried out by particle image velocimetry (PIV), in a freely decaying rotating turbulence experiment, aiming to compare to the results obtained in forced turbulence. The experimental setup is the same as in Morize *et al.*,[10] and is only briefly described here. It consists in a water filled glass tank of square section, of side of 35 cm and height $h=44$ cm, rotating at constant angular velocity. After the fluid is set in solid body rotation, turbulence is generated by towing a corotating square grid, of mesh size $M=3.9$ cm, at a constant velocity $V_g=0.65$ m s$^{-1}$ from the bottom to the top of the tank, and is maintained fixed near the top during the decay of turbulence. The horizontal components of the velocity fields in a centered horizontal area of $17\times 14$ cm$^2$ at midheight of the tank are obtained using a corotating PIV system operating at 1 Hz. The velocity fields are defined on a $160\times 128$ grid, with a spatial resolution of 1 mm and a signal-to-noise ratio of about $2\times 10^{-2}$. Although this fails to resolve the dissipative scales (the Kolmogorov scale is approximately 0.2 mm in the first period of the decay), this resolution allows us to resolve the inertial range, typically for $r>10$ mm.

Two angular velocities have been used in the present experiments, $\Omega=1.13$ and 2.26 rad s$^{-1}$. The corresponding nondimensional parameters are summarized in Table I. The grid Reynolds number is $\mathrm{Re}_g=V_gM/\nu=2.5\times 10^4$ ($\nu$ is the kinematic viscosity) and the grid Rossby numbers $\mathrm{Ro}_g=V_g/(2\Omega M)$ are 7.4 and 3.7, so that the initial state can be considered as a fully developed 3D turbulence weakly affected by the system rotation. A previous investigation[11] showed that, for those rotation rates, the energy decay was approximately self-similar between $t_0\simeq 40M/V_g$ and $t_c\simeq 0.10t_E$, where $t_E=h/(\nu\Omega)^{1/2}$ is the Ekman time, followed by an exponential decay at larger times. The present investigation is restricted to this self-similar range $[t_0,t_c]$. The in-

a)Electronic mail: moisy@fast.u-psud.fr.

 

TABLE I. Nondimensional parameters for the two rotation rates. $[t_0, t_c]$ is the range of approximately self-similar energy decay (Ref. 11). $\mathrm{Re}_g$ and $\mathrm{Ro}_g$ are the grid Reynolds and Rossby numbers. $\mathrm{Re}_M(t)=u'(t)M/\nu$, $\mathrm{Ro}_M(t)=u'(t)/(2\Omega M)$ and $\mathrm{Ro}_\omega(t)=\omega'(t)/2\Omega$ are the instantaneous Reynolds, macro- and micro-Rossby numbers, respectively, based on the horizontal velocity rms $u'(t)$ and vertical vorticity rms $\omega'(t)$.

| $\Omega$ (rad s$^{-1}$) | 1.13 | 2.26 |
|---|---|---|
| $\mathrm{Re}_g=V_gM/\nu$ | $2.5\times10^4$ | $2.5\times10^4$ |
| $\mathrm{Ro}_g=V_g/(2\Omega M)$ | 7.4 | 3.7 |
| $\Omega t_0/2\pi\cdots\Omega t_c/2\pi$ | 1.2$\cdots$7.4 | 0.6$\cdots$10.5 |
| $\mathrm{Re}_M(t=t_0\cdots t_c)$ | 1300$\cdots$360 | 1400$\cdots$380 |
| $\mathrm{Ro}_M(t=t_0\cdots t_c)$ | 0.38$\cdots$0.10 | 0.21$\cdots$0.056 |
| $\mathrm{Ro}_\omega(t=t_0\cdots t_c)$ | 2.1$\cdots$0.23 | 1.1$\cdots$0.17 |

stantaneous Reynolds, macro- and micro-Rossby numbers, $\mathrm{Re}_M$, $\mathrm{Ro}_M$, and $\mathrm{Ro}_\omega$, respectively, are also given for the two limiting values $t_0$ and $t_c$ in Table I.

To ensure proper convergence of the statistics, each decay is repeated approximately 600 times, representing 10 h of run for each rotation rate. It is worth pointing that computing SF from PIV data requires special care, especially when higher order are considered, for which even a small number of spurious vectors may have a large effect. Since those bad vectors may be preferentially found in regions of large velocity or large gradient, finding correct criteria for removing them without introducing biases is a delicate issue. In particular, some of the fields were found to suffer from an inhomogeneous lighting because the imaged area was partially shadowed when the corner of the tank passed through the laser sheet. Using a criteria based on the $Q$-factor (ratio of primary and secondary correlation peaks), 20% of the fields were affected by this problem and have been removed. A median filter is then applied to the remaining fields, and it was checked that the SFs computed from the raw and median-filtered data agreed for the inertial range scales within the error bars $\Delta S_q$ defined below.

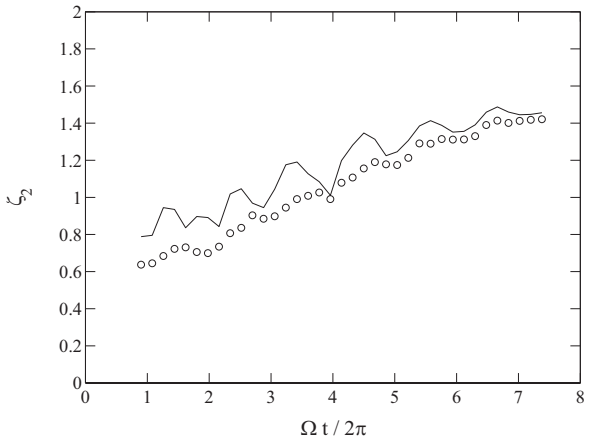


FIG. 1. Time evolution of the second order exponent $\zeta_2$ for $\Omega=1.13$ rad s$^{-1}$. (—) whole velocity field; (○) turbulent field (ensemble average substracted).

We first focus on the time evolution of the exponent $\zeta_2$ of the second order SF, $S_2(r)=\langle|\delta u(r)|^2\rangle$, plotted in Fig. 1 for $\Omega=1.13$ rad s$^{-1}$. This exponent is related to the distribution of energy among scales: Larger values of $\zeta_2$ indicate a favored energy distribution toward larger scales. Significant oscillations of $\zeta_2$ are present, with a period equal to the tank rotation period, indicating the presence of inertial modes. Those inertial modes have been previously detected from oscillations in the decay of the kinetic energy by Morize *et al.*,[11] and their temporal spectrum has been analyzed in details by Bewley *et al.*[12] Since we are interested here in the turbulent fluctuations that superimpose to those slow modes, we have computed the turbulent velocity fields $\tilde{\mathbf{u}}^\alpha(\mathbf{x},t)=\mathbf{u}^\alpha(\mathbf{x},t)-\langle\mathbf{u}^\alpha(\mathbf{x},t)\rangle_\alpha$, where $\alpha$ denotes the realization and $\langle\cdot\rangle_\alpha$ is the ensemble average over the whole data set at a given time $t$ after the grid translation. The time evolution of the corrected exponent $\tilde{\zeta}_2$, measured from the scaling of the turbulent component of the SF, $\tilde{S}_2(r)=\langle|\delta\tilde{u}(r)|^2\rangle$ (also plotted in Fig. 1), is found to follow approximately the lower bound of the oscillations of the raw exponent $\zeta_2$. One may conclude that the inertial mode, by superimposing a large scale modulation to the turbulence, leads to an increased raw exponent $\zeta_2$, of order of 10%. In the following we will discard this slow inertial component of the flow and we will focus on the scaling of the turbulent flow component.

The corrected exponent, hereafter simply noted $\zeta_2$, is found to gradually increase during the decay, starting from values close to 2/3 at $t\simeq t_0$, as expected for an initial state weakly affected by rotation and increasing up to $1.4\pm0.05$ at $t\simeq t_c$, reflecting the growing importance of the large scales compared to the small ones. This behavior compares well with the gradual steepening of the energy spectrum reported by Morize *et al.*,[10] with a spectral exponent $p$ increasing from 1.7 to $2.3\pm0.1$ during the decay [dimensional analysis gives $\zeta_2=p-1$, with $E(k)\sim k^{-p}$ the one-dimensional spectrum computed from the horizontal velocity and $k$ the horizontal wavenumber]. Beyond $t_c$, the energy decreases exponentially as the result of the dissipation by the inertial waves, and no scaling range could be defined from the power spectrum.[10,11] In the following we restrict to times $t<t_c$, where a correct scaling over an appreciable range of scales is observed from both $S_2(r)$ and $E(k)$.

We now turn to the higher order SFs. Figure 2(a), where SFs up to order $q=8$ are plotted at a given time $t$, shows power laws for intermediate scales, here for $12<r<80$ mm. It is worth pointing that the determination of the highest measurable order and its uncertainty for a given sample size is a delicate issue. The highest order for converged SF is determined by visual inspection of the truncated integral,

$$C_q(r;\delta u^*)=\int_{-\delta u^*}^{\delta u^*} p(\delta u)|\delta u(r)|^q d\delta u, \tag{1}$$

which increases up to $S_q(r)$ as the cutoff $\delta u^*$ is increased.[13] Here $p$ is the probability density function (pdf) of the velocity increment $\delta u$. For large separations and/or moderate orders, $C_q$ increases smoothly toward a well defined plateau as

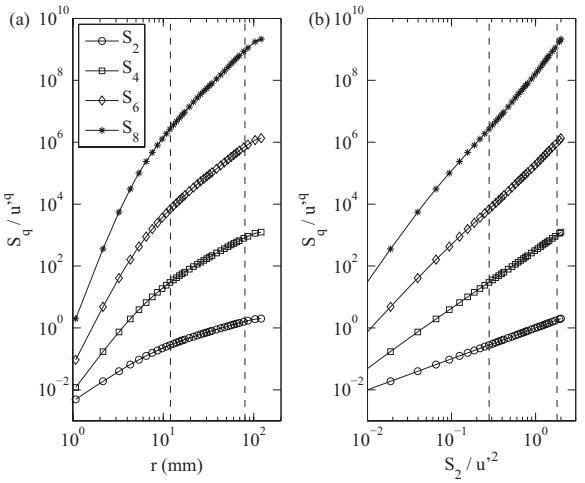


FIG. 2. SFs for increasing orders for $\Omega=1.13$ rad s$^{-1}$ and $\Omega t/2\pi=2.7$, normalized by the velocity rms $u'(t)$ (a) plotted as a function of the separation $r$ and (b) plotted as a function of $S_2$ (ESS method). The curves for $q=4,6,8$ have been vertically shifted by factors of $10^2$, $10^4$, and $10^6$ for visibility. The dashed lines show the range where the exponents are fitted.

$\delta u^* \to \infty$, indicating a correct convergence of the SF. On the other hand, smaller separations, $r<10$ mm, show strong jumps when large velocity increments enter into the integral (1). Those jumps may be due to either spurious vectors or insufficient statistics and are the signature of an unconverged SF. According to this criterion, the range of separations $r$ ensuring a correct convergence of $S_q$ for $q>8$ is found too small for a reliable measurement of the scaling exponents, and measurements are restricted to order $q=8$. For orders $q \leqslant 8$, scales $r>10$ mm were always correctly converged, allowing to safely define scaling exponents in the inertial range. Finally, the uncertainty $\Delta S_q(r)$ is estimated by plotting $S_q(r)$ at a given order and a given separation as a function of the sample size. Defining $\Delta S_q(r)$ as the standard deviation of $S_q(r)$ computed over the last third of the whole sample yields

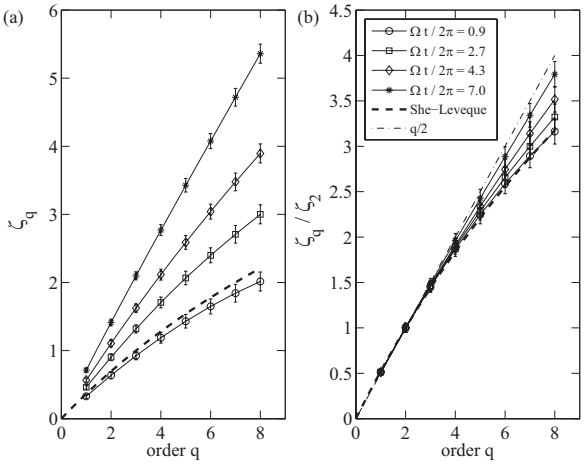


FIG. 3. (a) Raw exponents $\zeta_q$ and (b) normalized exponents $\zeta_q/\zeta_2$ measured using ESS, at various times during the decay, for $\Omega=1.13$ rad s$^{-1}$.

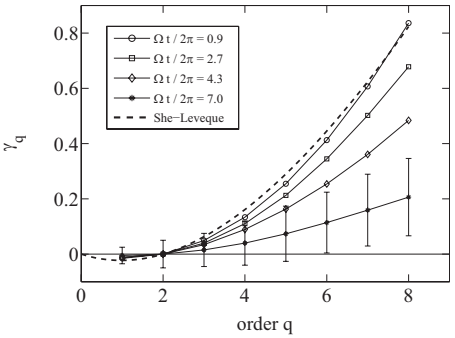


FIG. 4. Intermittency factors $\gamma_q=q/2-\zeta_q/\zeta_2$ (same data as in Fig. 3). Error bars are only shown for the last curve (*) for clarity.

a relative error $\Delta S_q(r)/S_q(r)$ of 4% for $q=4$ and 10% for $q=8$, which is smaller than the symbol size in Fig. 2.

Figure 3 shows both the raw exponents $\zeta_q$ and the normalized exponents $\zeta_q/\zeta_2$ at different times during the decay. Those raw (normalized) exponents are obtained from a linear least-squares fit of $\log S_q$ versus $\log r$ ($\log S_2$), following the extended self-similarity[4] (ESS) procedure [see Fig. 2(b)].[14] The main contribution of the error bars for $\zeta_q$ is due to the uncertainty on the determination of the SF discussed above, $\Delta\zeta_q \simeq 2(\Delta S_q/S_q)/\ln(r_2/r_1)$, where $r_1$ and $r_2$ are the lower and upper cutoffs of the scaling range, yielding $\Delta\zeta_4 \simeq 0.05$ and $\Delta\zeta_8 \simeq 0.14$. At the beginning of the decay, the effect of rotation is small and the exponents are indeed found very close to classical values for 3D nonrotating turbulence.[6] For comparison, the She–Lévèque[5] formula is also plotted, showing good agreement up to order $q=8$, giving confidence on the reliability of our PIV measurements. At larger times, the normalized exponents increase and become closer to the linear law $\zeta_q/\zeta_2=q/2$, confirming the intermittency reduction induced by the background rotation. It is worth noting that the instantaneous Reynolds number at $t \simeq t_c$, $\mathrm{Re}_M \simeq 360$ (see Table I), together with the correct scaling of the SF at that time, ensures that this intermittency reduction is not associated with the trivial scaling $\zeta_q=q$ (and hence $\zeta_q/\zeta_2=q/2$) of a smooth velocity field.

The exponents at the end of the decay are comparable or even slightly larger than those reported by Müller and Thiele,[2] although their macro-Rossby numbers (0.01 and 0.05) are slightly lower and their Reynolds number (2300 and 4000) significantly larger than the present ones (note that the nondimensional numbers here are based on the mesh size $M$, which underestimates the true integral scale). It must also be noted that the present exponents differ from the strictly linear law $q/2$ reported by Baroud *et al.*[1] for similar Rossby numbers. This slight discrepancy may be due to the different forcing mechanisms: In the present experiment, the initial turbulence produced by the grid translation is approximately isotropic, and rotation gradually breaks this initial isotropy in the course of the decay. In the experiment by Baroud *et al.*,[1] turbulence is maintained by radial jets originating from a circular array of holes, generating a strong radial flow deflected by the Coriolis force. This forcing scheme is likely to produce an anisotropic, partially two-dimensional flow, even

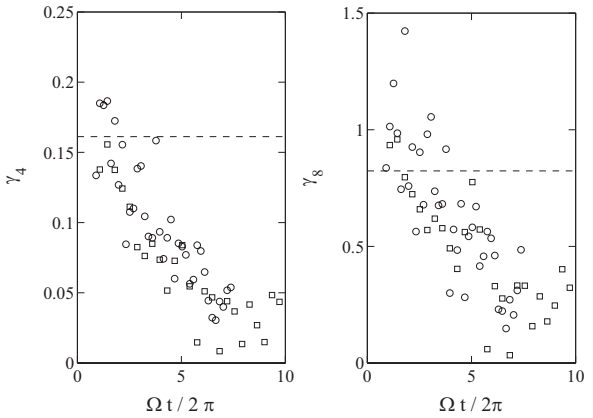


FIG. 5. Time evolution of the fourth and eighth-order intermittency factors for the two experiments. (○) $\Omega=1.13$ rad s$^{-1}$; (□) $\Omega=2.26$ rad s$^{-1}$. The dashed lines show the intermittency factors from the She–Lévèque model, $\gamma_4=0.161$ and $\gamma_8=0.824$. The error bars (not shown) are of the order of the scatter, $\Delta\gamma_4=0.05$ and $\Delta\gamma_8=0.14$.

in the absence of rotation. When rotation is present, this forcing probably reinforces the two-dimensional character of the turbulence, resulting in strictly nonintermittent exponents.

The reduction of intermittency during the decay is best appreciated from the intermittency factors $\gamma_q=q/2-\zeta_q/\zeta_2$ (Figs. 4 and 5), which vanish for nonintermittent fluctuations. Although the scatter is important on these quantities (of the order of $\Delta\zeta_q$), a clear trend toward smaller intermittency is present. It is interesting to note the approximate collapse of the data from the two rotation rates, suggesting that $\Omega^{-1}$ is the relevant time scale for the intermittency reduction.

The fact that the factors $\gamma_q$ start decreasing from the beginning of the decay is probably due to the low instantaneous Rossby numbers when $t\simeq t_0$ (see Table I). A crossover between constant $\gamma_q$ at early time and a decrease at larger times would be actually expected for larger grid Rossby number $\mathrm{Ro}_g$. However, a large grid Reynolds number $\mathrm{Re}_g$ is required for a developed turbulence to remain throughout the self-similar decay regime, up to the Ekman cutoff $t\simeq t_c$, limiting the maximum initial $\mathrm{Ro}_g$ at fixed rotation rate and grid size. We finally note that extrapolating the trend toward $\gamma_q\to 0$ in Fig. 5 suggests that the upper bound $t_c$ of the self-similar decay regime, in our experimental conditions, prevents from a clear observation of a vanishing intermittency, which may occur after 10–15 tank rotations.

To summarize, our measurements of high order SF in decaying rotating turbulence show a strong increase of the exponents $\zeta_q$ during the decay, which essentially follows the increase of the second order exponent $\zeta_2$. It is worth noting that values for $\zeta_2$ larger than 1 are found, in contradiction with the $S_2(r)\sim r$ [i.e., $E(k)\sim k^{-2}$] phenomenological law for rotating turbulence, derived under the assumption of nonlinear interactions governed by the timescale $\Omega^{-1}$.[2,15] Once normalized by $\zeta_2$, a marked increase of $\zeta_q/\zeta_2$ is observed, a clear signature of a reduction of intermittency induced by the background rotation. This intermittency reduction is comparable to the one reported in the forced DNS of Müller and Thiele,[2] but it is less pronounced than in the forced experiment by Baroud *et al.*[1] This difference may originate from the anisotropic forcing mechanism of Ref. 1 or from our limited temporal range of self-similar decay due to the Ekman dissipation regime, which is specific to the decaying case.

We acknowledge L. Chevillard, S. Galtier, W. C. Müller, M. Rabaud, and J. Rupper-Felsot for fruitful discussions. This work was supported by the ANR Grant No. 06-BLAN-0363-01 "HiSpeedPIV."

[1] C. N. Baroud, B. B. Plapp, H. L. Swinney, and Z.-S. She, "Scaling in three-dimensional and quasi-two-dimensional rotating turbulent flows," Phys. Fluids **15**, 2091 (2003).
[2] W. C. Müller and M. Thiele, "Scaling and energy transfer in rotating turbulence," EPL **77**, 15001 (2007).
[3] G. Boffetta, A. Celani, and M. Vergassola, "Inverse energy cascade in two-dimensional turbulence: Deviations from Gaussian behavior," Phys. Rev. E **61**, R29 (2000).
[4] R. Benzi, S. Ciliberto, R. Tripiccione, C. Baudet, F. Massaioli, and S. Succi, "Extended self-similarity in turbulent flows," Phys. Rev. E **48**, R29 (1993).
[5] Z. S. She and E. Lévèque, "Universal scaling laws in fully developed turbulence," Phys. Rev. Lett. **72**, 336 (1993).
[6] U. Frisch, *Turbulence* (Cambridge University Press, Cambridge, 1995).
[7] A. C. Newell, S. Nazarenko, and L. Biven, "Wave turbulence and intermittency," Physica D **152–153**, 520 (2001).
[8] F. Bellet, F. S. Godeferd, J. F. Scott, and C. Cambon, "Wave turbulence in rapidly rotating flows," J. Fluid Mech. **562**, 83 (2006).
[9] C. Simand, "Etude de la turbulence inhomogène au voisinage d'un vortex intense," Ph.D thesis, Ecole Normale Supérieure de Lyon, 2002.
[10] C. Morize, F. Moisy, and M. Rabaud, "Decaying grid-generated turbulence in a rotating tank," Phys. Fluids **17**, 095105 (2005).
[11] C. Morize and F. Moisy, "Energy decay of rotating turbulence with confinement effects," Phys. Fluids **18**, 065107 (2006).
[12] G. P. Bewley, D. P. Lathrop, L. R. M. Maas, and K. R. Sreenivasan, "Inertial waves in rotating grid turbulence," Phys. Fluids **19**, 071701 (2007).
[13] Instead of the convergence test based on Eq. (1), a similar test based on the integrand itself, $p(\delta u)|\delta u(r)|^q$ as $\delta u\to\infty$, has also been used in the literature. However, the visual quality of convergence from this quantity strongly depends on the choice of the bin width used to compute the pdf, especially for the far tails where empty bins are present, so criterion based on the truncated integral (1) were found more reliable.
[14] For nonrotating turbulence, the ESS procedure is based on $S_3$ instead of $S_2$ because of the prediction $\zeta_3=1$ from the Kolmogorov's 4/5 law. No such result applies for rotating turbulence, and $S_2$ were found more reliable because sign changes are present in $S_3(r)$ (computed without absolute values), associated with energy flux reversals (Ref. 10).
[15] Y. Zhou, "A phenomenological treatment of rotating turbulence," Phys. Fluids **7**, 2092 (1995).

*J. Fluid Mech.*, page 1 of 31  
doi:10.1017/S0022112010003733

# Decay laws, anisotropy and cyclone–anticyclone asymmetry in decaying rotating turbulence

F. MOISY[1]†, C. MORIZE[1], M. RABAUD[1] AND J. SOMMERIA[2]

[1]Laboratoire FAST, Université Paris-Sud 11, Université Pierre et Marie Curie, CNRS, Bâtiment 502, F-91405 Orsay Cedex, France

[2]Coriolis/LEGI, 21 avenue des Martyrs, F-38000 Grenoble, France

(Received 4 September 2009; revised 9 July 2010; accepted 10 July 2010)

The effect of a background rotation on the decay of grid-generated turbulence is investigated from experiments in the large-scale 'Coriolis' rotating platform. A first transition occurs at 0.4 tank rotation (instantaneous Rossby number $Ro \simeq 0.25$), characterized by a $t^{-6/5} \to t^{-3/5}$ transition of the energy-decay law. After this transition, anisotropy develops in the form of vertical layers, where the initial vertical velocity fluctuations remain trapped. The vertical vorticity field develops a cyclone–anticyclone asymmetry, reproducing the growth law of the vorticity skewness, $S_\omega(t) \simeq (\Omega t)^{0.7}$, reported by Morize, Moisy & Rabaud (*Phys. Fluids*, vol. 17 (9), 2005, 095105). A second transition is observed at larger time, characterized by a return to vorticity symmetry. In this regime, the layers of nearly constant vertical velocity become thinner as they are advected and stretched by the large-scale horizontal flow, and eventually become unstable. The present results indicate that the shear instability of the vertical layers contribute significantly to the re-symmetrization of the vertical vorticity at large time, by re-injecting vorticity fluctuations of random sign at small scales. These results emphasize the importance of the nature of the initial conditions in the decay of rotating turbulence.

**Key words:** rotating flows, rotating turbulence, wave–turbulence interactions

## 1. Introduction

Turbulence subjected to solid-body rotation is a problem of first importance for engineering, geophysical and astrophysical flows. Its dynamics is dictated by a competition between linear and nonlinear effects. Linear effects, driven by the Coriolis force, include anisotropic propagation of energy by inertial waves (IWs), preferentially along the rotation axis (hereafter referred to as 'vertical' axis by convention), on the time scale of the system rotation, $\Omega^{-1}$, (Greenspan 1968). Nonlinear interactions, on the other hand, are responsible for energy transfers towards 'horizontal' modes (Cambon & Jacquin 1989; Waleffe 1993). For infinite rotation rate, i.e. for vanishing Rossby number, these IWs reduce to Taylor–Proudman columns, corresponding to a two-dimensional flow (2D) invariant along the rotation axis. Importantly, this 2D flow is not two-component (2C) in general, because the third (vertical) velocity component, insensitive to the Coriolis force, behaves as a passive scalar field

† Email address for correspondence: moisy@fast.u-psud.fr

transported by the horizontal flow. This 'passive' vertical velocity, originating from the initial conditions in the case of decaying turbulence, may, however, become 'active' through shear instabilities at small scale. This mechanism may have considerable importance in the nature of the decay and the partial two-dimensionalization of an initially three-dimensional (3D) turbulence subjected to background rotation.

This paper reports an experimental study of the influence of the background rotation on the decay of an initially isotropic turbulence. Turbulence is generated by translating a grid in a channel mounted on the large-scale 'Coriolis' rotating platform. The aim of this paper is first to characterize, in detail, the decay law of the energy, in a situation of weak lateral confinement. This situation contrasts with the previous experiments by Morize, Moisy & Rabaud (2005) and Morize & Moisy (2006), performed in a rotating tank with an aspect ratio of order one, showing significant confinement effects. Second, the anisotropy growth is investigated, with the aim to characterize the influence at large time of the initial vertical fluctuations on the vertical vorticity statistics.

For turbulence, which is subjected to moderate rotation (Rossby number $Ro \simeq O(1)$), the linear and nonlinear time scales are of the same order, resulting in a complex interplay between linear-energy propagation by IWs and anisotropic energy transfers by nonlinear interactions. This complexity is unavoidable in decaying rotating turbulence starting from large initial Rossby number, in which the instantaneous Rossby number decays and crosses $O(1)$ at some transition time. At this time, in the so-called 'intermediate-Rossby-number range' (Bourouiba & Bartello 2007), the effects of the rotation, namely the anisotropy growth and the cyclone–anticyclone symmetry breaking, become significant, and accumulate as time proceeds. Accordingly, the statistical properties of the rotating turbulence at large time are the result of the turbulence history integrated from the initial state and may therefore depend on the details of the initial state. Generic properties should, however, be expected if the initial state is 3D isotropic turbulence with $Ro \gg 1$, which is the situation examined in this paper.

Because of the fast growth of the vertical correlation due to IW propagation (Jacquin *et al.* 1990; Squires *et al.* 1994), confinement along the vertical axis plays a significant role in the dynamics of rotating turbulence, therefore, comparisons with homogeneous turbulence in idealized unbounded systems should be made carefully. One consequence of the vertical confinement is a preferential alignment of the axis of the vortices normal to the walls, therefore, reinforcing the 2D nature of the large scales, as observed by Hopfinger, Browand & Gagne (1982) and Godeferd & Lollini (1999). Second, confinement selects a set of discrete resonant inertial modes (Dalziel 1992; Maas 2003; Bewley *et al.* 2007), which may couple to the small-scale turbulence. Third, an extra mechanism of dissipation of the IWs takes place in the boundary layers, acting on the Ekman time scale $h(\nu\Omega)^{-1/2}$, where $h$ is the confinement scale along the rotation axis, which may dominate the energy decay at large time (Phillips 1963; Ibbetson & Tritton 1975; Morize & Moisy 2006).

The most remarkable feature of rotating turbulence is the spontaneous emergence of long-lived columnar vortices aligned with the rotation axis (Hopfinger *et al.* 1982; Smith & Waleffe 1999; Longhetto *et al.* 2002). Nonlinear mechanisms (Cambon & Scott 1999; Cambon 2001) and linear mechanisms (Davidson, Staplehurst & Dalziel 2006; Staplehurst, Davidson & Dalziel 2008) have been proposed to explain the formation of these columnar structures, and the interplay between the two is still a matter of debate. The recent numerical simulations of Yoshimatsu, Midorikawa &

Kaneda (2010) suggest that both effects should be actually considered to account for the formation of these vertical structures.

A striking property of these vortices for intermediate Rossby numbers is the symmetry breaking between cyclones and anticyclones, observed both in forced (Hopfinger *et al.* 1982; Smith & Lee 2005) and decaying (Bartello, Métais & Lesieur 1994; Smith & Waleffe 1999) turbulence. This symmetry breaking has received considerable interest in recent years. It has been quantified in terms of the vorticity skewness, $S_\omega = \langle \omega_z^3 \rangle / \langle \omega_z^2 \rangle^{3/2}$ (where $\omega_z$ is the vorticity component along the rotation axis), which is found to be positive for $Ro \simeq 1$ (Bartello *et al.* 1994; Morize *et al.* 2005; Bourouiba & Bartello 2007; van Bokhoven *et al.* 2008; Staplehurst *et al.* 2008; Yoshimatsu *et al.* 2010). In decaying rotating turbulence, starting from initial conditions such that $Ro \gg 1$, a power-law growth has been observed in the form $S_\omega \simeq (\Omega t)^{0.6 \pm 0.1}$ by Morize *et al.* (2005), suggesting a build-up of vorticity skewness acting on the linear time scale $\Omega^{-1}$.

Several explanations have been proposed for the cyclone–anticyclone asymmetry growth, although none provides a complete description of the experimental data. First, in a rotating frame, for a given vertical strain, $\partial u_z / \partial z$, the vortex stretching of the axial vorticity, $(2\Omega + \omega_z)\partial u_z / \partial z$, is larger for cyclonic than for anticyclonic vorticity. Gence & Frick (2001) have shown that, for isotropic turbulence suddenly subjected to a background rotation, $S_\omega$ grows linearly at short time, i.e. for $t \ll \Omega^{-1}$. At larger time, the growth is expected to be slower, because the strain $\partial u_z / \partial z$ is reduced by the rotation. Second, anticyclonic vortices are more prone to centrifugal instabilities. This effect can be readily shown for idealized axisymmetric vortices, for which the generalized Rayleigh criterion in a rotating frame (Kloosterziel & van Heijst 1991) is more likely to become negative for anticyclonic vorticity. Sreenivasan & Davidson (2008) have actually shown, using a model of axisymmetric vortex patches, that cyclonic vortices first develop columnar structures, while anticyclonic vortices become centrifugally unstable.

Interestingly, a return to vorticity symmetry has been reported at large times (smaller $Ro$ values) by Morize *et al.* (2005, 2006). This decrease may originate both from internal (2D) diffusion or Ekman-pumping-induced diffusion of the vortices. On the contrary, vortex merging would lead to an increase in $S_\omega$, similarly to what is observed for the vorticity flatness in 2D turbulence (McWillams 1984; Carnevale *et al.* 1991). The decrease in $S_\omega$ was first attributed to confinement effects, more specifically the nonlinear Ekman pumping on the rigid walls. However, this was questioned by the results of van Bokhoven *et al.* (2008), in which a decrease of $S_\omega$ is also observed at large times, but in a numerical simulation with periodic boundary conditions, and hence, without Ekman pumping. According to these authors, the decrease in $S_\omega$ is an effect of the phase mixing of IWs, which damps all triple correlations of turbulent fields in the limit of low Rossby numbers.

The non-monotonic time evolution of the vorticity skewness is confirmed by the present experiments, although the boundary conditions significantly differ from those of Morize *et al.* (2005). The present results suggest an additional contribution for this decrease at large times: as time proceeds, the vertical velocity, initiated by the 3D initial conditions, forms vertically coherent layers transported by the large-scale quasi-2D flow. The horizontal straining of these layers by the large-scale structures produces smaller scales, in a process similar to the enstrophy cascade in 2D turbulence. This mechanism reinforces the horizontal gradient of the vertical velocity, making these layers prone to inertial instabilities, producing small-scale horizontal vorticity. This horizontal vorticity produces in turn random vertical vorticity, resulting in a

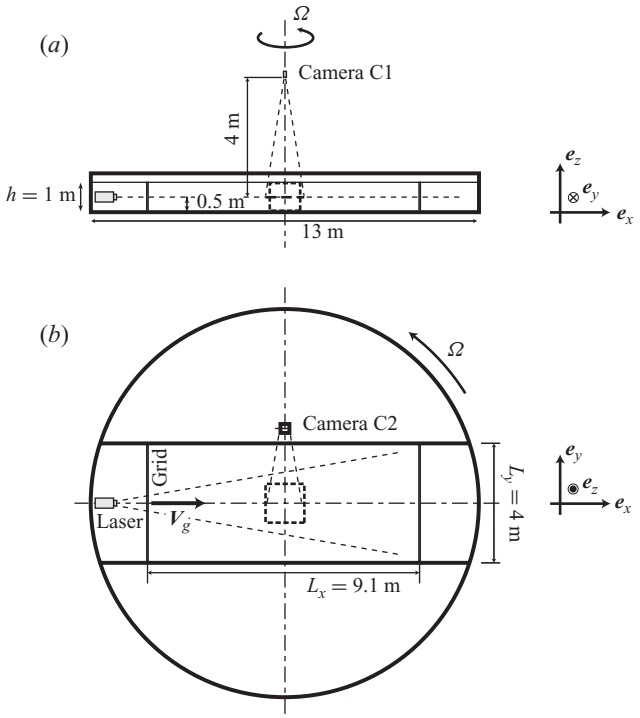


FIGURE 1. Side view (*a*) and top view (*b*) of the experimental set-up. The grid is translated from left to right along $\boldsymbol{e}_x$. The angular velocity is $\Omega = \Omega \boldsymbol{e}_z$, with $\Omega > 0$ (anticlockwise rotation). The PIV camera is located either at C1 or C2, for measurements in the horizontal and vertical planes, respectively. The dashed squares show the corresponding imaged areas.

reduction of $S_\omega$ at large times. This re-injection of symmetric vorticity fluctuations at small scale is thought to be a generic mechanism in decaying rotating turbulence, provided the initial state contains a significant amount of vertical velocity, which is the case for an initial 3D isotropic turbulence.

This paper is organized as follows. Section 2 describes the experimental set-up, the particle-image-velocimetry (PIV) measurements and discusses the separation between the mean flow and the turbulence. The influence of the background rotation on the energy decay and the time evolution of the non-dimensional numbers are presented in § 3. The anisotropy growth and the formation of the vertical layers are characterized in § 4. The structure and dynamics of the vertical vorticity field is described in § 5, with emphasis given on the cyclone–anticyclone asymmetry growth and the influence of the shear instability of the vertical layers. Finally, § 6 summarizes the different regimes observed during the decay.

## 2. Experimental set-up and procedure

### 2.1. *Experimental apparatus*

The experimental set-up, shown in figure 1, consists of a $13\,\mathrm{m} \times 4\,\mathrm{m}$ water channel, filled to a depth of $h = 1\,\mathrm{m}$, mounted on the Coriolis rotating platform. Details about the rotating platform may be found in Praud, Fincham & Sommeria 2005 and Praud, Sommeria & Fincham 2006, and only the features specific to the present

| | | | | |
|---|---|---|---|---|
| Rotation period $T$ (s) | $\infty$ | 120 | 60 | 30 |
| Symbol | ★ | ○ | □ | △ |
| Angular velocity $\Omega$ (rad s$^{-1}$) | 0 | 0.052 | 0.105 | 0.209 |
| Grid Rossby number $Ro_g$ | $\infty$ | 20.4 | 10.2 | 5.1 |
| Ekman layer thickness $\delta_E$ (mm) | $\infty$ | 4.4 | 3.1 | 2.2 |
| Ekman time scale $t_E$ (s) | $\infty$ | 4370 | 3090 | 2185 |

TABLE 1. Flow parameters. The symbols are described in figures.

experiments are described here. One set of experiments without rotation, and three sets with rotation periods of $T = 30$, 60 and 120 s, have been carried out (see table 1). The angular velocity $\Omega = 2\pi/T$ is constant within a precision of $\Delta\Omega/\Omega < 10^{-4}$. The parabolic elevation of the surface height induced by the rotation along the channel length is 0.3 cm (respectively, 4.5 cm) for the lowest (respectively, highest) rotation rate.

Turbulence is generated by horizontally translating a vertical grid, of width equal to the channel width, at a constant velocity $V_g = 30$ cm s$^{-1}$ over a distance of $L_x = 9.1$ m along the channel (see supplementary movie 1 'available at journals.cambridge.org/flm'). The streamwise, spanwise and vertical axis are noted $x$, $y$ and $z$, respectively, with $\boldsymbol{e}_x$, $\boldsymbol{e}_y$ and $\boldsymbol{e}_z$ being the corresponding unit vectors. The grid is made of square bars of width $b = 30$ mm, with a mesh size of $M = 140$ mm and a solidity (ratio of closed to mesh area) $\sigma = 1 - (1 - b/M)^2 = 0.38$. The mesh is significantly smaller than the grid cross-section, ensuring weak vertical confinement effects at small time ($h/M = 7$), and negligible lateral confinement effects even at large time ($L_y/M = 28$). The grid is hung from a carriage moving above the free surface. The velocity of the grid increases linearly from 0 to $V_g$, remains constant in the central part, and decreases linearly back to zero at the end of the channel. The time at which the grid crosses the centre of the channel, where the measurements are performed, defines the origin $t = 0$. Because of the evaporation, a temperature difference may be present between the ambient air and the water, resulting in residual convection cells of maximum velocity of order 1 mm s$^{-1}$ in the absence of forcing and rotation. However, the mixing induced by the grid translation homogenizes the flow temperature and breaks these residual convective motions, therefore, thermal effects could be safely neglected during most of the decay.

The initial conditions of an experiment are characterized by the grid Reynolds and Rossby numbers based on the grid velocity and grid mesh,

$$Re_g = \frac{V_g M}{\nu}, \quad Ro_g = \frac{V_g}{2\Omega M}, \tag{2.1}$$

where $\nu$ is the water kinematic viscosity. The grid Reynolds number is constant for all the experiments, $Re_g = 4.20 \times 10^4$, while the grid Rossby number lies in the range 5.1–20.4 (table 1). The Rossby number based on the bar width ranges between 24 and 96, so the turbulent energy production in the near wake of the grid is expected to be weakly affected by the rotation (Khaledi, Barri & Andersson 2009).

### 2.2. *Particle image velocimetry*

A high-resolution PIV system, based on a 14 bits $2048 \times 2048$ pixels camera (PCO.2000), was used in these experiments. Water was seeded by Chemigum P83 particles, 250 μm in diameter, carefully selected to match the water density better than $10^{-3}$. The corresponding settling velocity, of 0.03 mm s$^{-1}$, is much smaller than the

typical fluid velocity. The flow was illuminated by a laser sheet of thickness 1 cm, generated by a 6 W Argon laser beam and an oscillating mirror. Two fields of views have been used as follows.

(*a*) A centred square area of $1.3\,\mathrm{m} \times 1.3\,\mathrm{m}$ in the horizontal plane $(\boldsymbol{e}_x, \boldsymbol{e}_y)$ at mid-height ($z = 0.5\,\mathrm{m}$). The camera is located 4 m above the horizontal laser sheet (C1 in figure 1), and the area is imaged through the free surface.

(*b*) A $1.1\,\mathrm{m} \times 1\,\mathrm{m}$ area in the vertical plane $(\boldsymbol{e}_x, \boldsymbol{e}_z)$ in the middle of the channel. The plane is imaged through a window in the lateral wall (C2 in figure 1), so that the measurements are not affected by free surface disturbances.

Spatial calibration was achieved by imaging a reference plate at the location of the laser sheet. For the horizontal measurements, the surface elevation of the parabolic surface is less than 2 mm on the imaged area, so the optical distortion could be safely neglected.

Up to six decay experiments of 1 h (7700 grid time scales $M/V_g$) have been carried out for each rotation rate and, for each decay, 400 image pairs are recorded. Since the characteristic velocity decreases in time, the delay between the two successive images of a pair is made to gradually increase during the acquisition sequence, from 125 ms to 2 s, so that the typical particles displacement remains approximately constant throughout the decay. The time delay between image pairs is also gradually increased during the decay, from 2 to 20 s. The results are ensemble averaged over the $N_r = 6$ realizations in the horizontal plane and $N_r = 4$ in the vertical plane. Although this is enough to achieve statistical convergence at small times, when the correlation length is significantly smaller than the imaged area, the convergence becomes questionable at large times, when the imaged area contains in average one large-scale structure or less.

The PIV computations have been performed using the software Davis (LaVision), and the statistical analysis of the velocity fields using the PIVMat toolbox under Matlab. Interrogation windows of size $32 \times 32$ pixels, with an overlap of 16 pixels, were used. For this window size, the corresponding particle displacement resolution is better than 0.1 pixel (Raffel *et al.* 2007), yielding a velocity signal-to-noise ratio of 50. The final velocity fields are defined on a $128 \times 128$ grid, with a spatial resolution is $\Delta x = 10\,\mathrm{mm}$.

Due to this moderate spatial resolution, the velocity field inside the Ekman boundary layer, of thickness $\delta_E = (\nu/\Omega)^{1/2} \simeq 2.2$–$4.4\,\mathrm{mm}$ (see table 1), cannot be resolved. Assuming isotropy in the bulk of the flow, which is valid only in the non-rotating case or at small time, the smallest turbulent scale can be estimated by the Kolmogorov scale $\eta = (\nu^3/\epsilon)^{1/4}$, where the dissipation rate $\epsilon$ can be computed from the energy decay, $\epsilon \simeq -(3/2)\partial(u_x')^2/\partial t$ (energy decays are detailed in § 3). The scale $\eta$ is of order of 0.4 mm $\simeq \Delta x/25$ at $t \simeq 20M/V_g$, for all rotation rates, so that the smallest scales are not resolved at the beginning of the decay. Accordingly, the measured velocity gradients at scale $\Delta x$ underestimate the actual ones (Lavoie *et al.* 2007). Velocity gradients can be considered as well resolved when $\Delta x < 3\eta$ (see e.g. Jimenez 1994), which is satisfied for $t > 350M/V_g$ only. At the end of the decay, $\eta$ is of the order of 8 mm for $\Omega = 0$, in which case the gradients can be accurately computed from the PIV measurements.

Finally, we note that when the flow is imaged from above, an additional source of noise is the refraction through the disturbed free surface, originating either from the wake of the grid or from residual vibrations of the rotating platform. These perturbations generate an additional apparent particle displacement, $\delta\boldsymbol{x}_{FS} = (1 - 1/n_w)\,(h/2)\,\nabla h$, with $n_w$ is the water refraction index, $\nabla h$ is the surface gradient

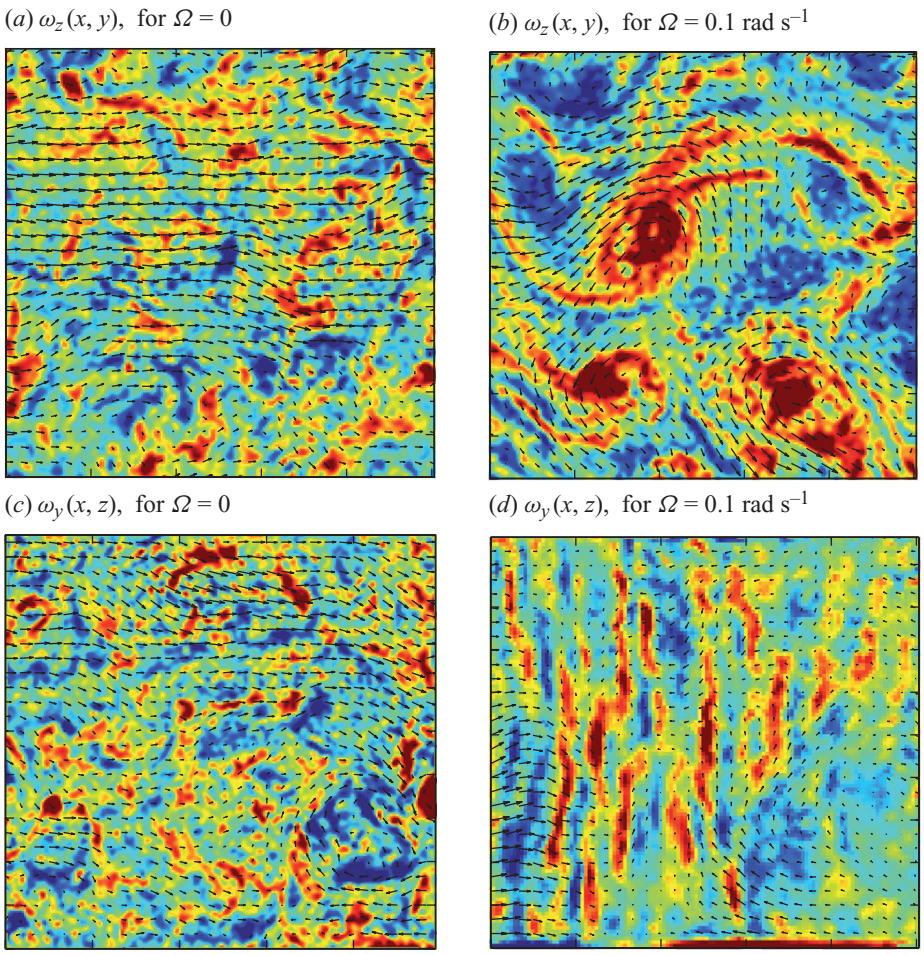


COL-
www+print

FIGURE 2. Horizontal and vertical snapshots of the velocity fields taken at $t = 360\,\mathrm{s} \simeq 770M/V_g$ after the grid translation, without rotation (*a*,*c*) and with rotation at $\Omega = 0.10\,\mathrm{rad\,s^{-1}}$. For the rotating cases, this time corresponds to six tank rotations. The imaged area is $1\,\mathrm{m} \times 1\,\mathrm{m}$. The colour shows the vorticity normal to the plane, $\omega_z(x, y)$ and $\omega_y(x, z)$, ranging from $-0.1$ to $0.1\,\mathrm{rad\,s^{-1}}$. Note that the mean flow in the direction of the grid motion (along $\boldsymbol{e}_x$), with a marked mean shear $\partial\langle U_x\rangle/\partial z$, which is of constant sign for $\Omega = 0$ (*c*), but oscillating for $\Omega \neq 0$ (*d*).

and $h/2$ is the path length of the refracted light rays (see, e.g. Moisy, Rabaud & Salsac 2009), and hence a velocity contamination of order $|\delta \boldsymbol{x}_{FS}|/\delta t$, with $\delta t$ the inter-frame time. This velocity contamination has been estimated by imaging a set of fixed particles sticked on a rigid plate and imaged under the same experimental conditions. It was found that the measurements were significantly altered by this contamination during the first 10 s ($\simeq 20M/V_g$) after the grid translation, but were reliable at larger time.

### 2.3. *Flow visualizations*

First insight into the influence of the background rotation on the turbulence decay may be obtained by comparing the horizontal and vertical vorticity fields shown in figure 2, in the non-rotating case (*a*,*c*) and in an experiment rotating at $\Omega = 0.10\,\mathrm{rad\,s^{-1}}$

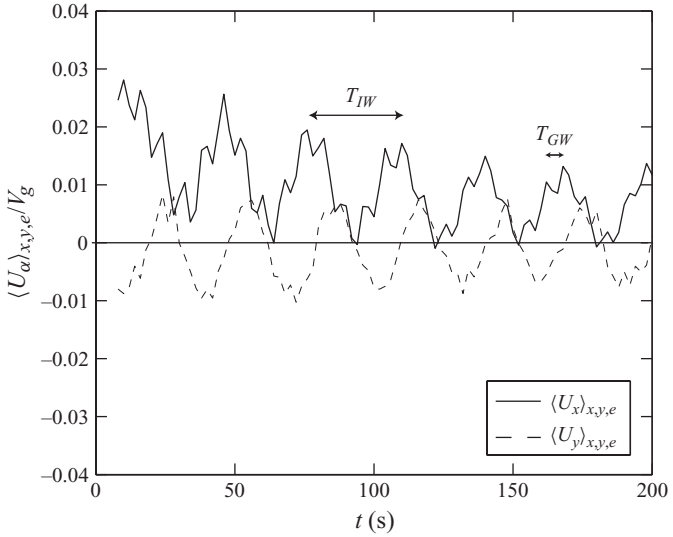


FIGURE 3. Time evolution of the ensemble and spatially averaged streamwise (—) and spanwise (- -) velocity components, for $\Omega = 0.1$ rad s$^{-1}$ (rotation period $T = 60$ s). The fast oscillation, of period $T_{GW} \simeq 7.3$ s, is a longitudinal GW and the slow oscillation, of period $T_{IW} = T/2 = 30$ s, is an anticyclonic IW.

(*b*,*d*). These snapshots are obtained 360 s after the grid translation ($770M/V_g$). At this time, the turbulent Reynolds number is 400 and 700 for the non-rotating and rotating cases, respectively, and the macro-Rossby number for the rotating case is 0.06 (these numbers are defined in § 3.4).

While the vorticity fields $\omega_z$ and $\omega_y$ for the non-rotating cases are similar in the two measurement planes, as expected for approximately isotropic turbulence, they strongly differ in the rotating case. Supplementary movies 2 and 3 of $\omega_z$ and $\omega_y$ clearly show the two essential features of the turbulence decay in the rotating frame, namely the anisotropy growth in the vertical plane and the cyclone–anticyclone asymmetry in the horizontal plane.

The vertical vorticity, $\omega_z$, shows strong large-scale vortices, mostly cyclonic (in red), surrounded by shear layers. In the vertical plane, the spanwise vorticity, $\omega_y$, shows vertically elongated structures of alternating sign, originating from layers of ascending and descending fluid. The dominant contribution of $\omega_y$ comes from the vertical shear, $\partial u_z/\partial x$, except near the top and bottom boundary layers where the horizontal shear $\partial u_x/\partial z$ is dominant.

### 2.4. *Large-scale flows and Reynolds decomposition*

Translating a grid in a closed volume is ideally designed to produce homogeneous turbulence with zero mean flow. However, reproducible flow features are found over successive realizations (Dalziel 1992), therefore, a careful separation between the ensemble average and the turbulent component is necessary. From the time series of the spatially averaged velocity components shown in figure 3, three large-scale flows can be identified:

(*i*) *Large-scale circulation* (LSC): The grid translation generates a slight mean flow along $x > 0$ in the centre of the channel, of initial amplitude $\simeq 2 \times 10^{-2} V_g$, which recirculates along the lateral walls (out of the measurement area). Moreover, because of the boundary condition asymmetry between the solid boundary at $z = 0$ and the

free surface at $z = h$, this streamwise flow has a significant residual shear $\partial\langle U_x\rangle/\partial z > 0$, of initial amplitude $\simeq 0.03 V_g/h \simeq 10^{-2}\,\mathrm{s}^{-1}$.

(*ii*) *Gravity wave* (GW): As the grid is translated along the channel, it pushes a significant amount of water near the endwall, which initiates a fast longitudinal GW (sloshing mode). Its wavelength, $\lambda$, is twice the channel length, and its period, $T_{GW}$, is 7.3 s.

(*iii*) *Inertial wave* (IW): When rotation is present, the mean horizontal shear induced by the grid excites an IW, with a period which is half of the rotation period of the tank, $T_{IW} = T/2$. This IW essentially consists of the oscillating shearing motion of two horizontal layers of thickness $h/2$, compatible with a mode of vertical wavevector (Dalziel 1992; Maas 2003). In the horizontal plane, the signature of this IW is a uniform anticyclonic oscillation, visible by the phase shift of $\pi/2$ between the mean velocity components $\langle U_x\rangle$ and $\langle U_y\rangle$. Its amplitude is of the order of $U_{IW} \simeq 10^{-2} V_g$ (respectively, $5 \times 10^{-4} V_g$) at the beginning (respectively, end) of the decay.

In the non-rotating case, the mean residual shear persists over large times. Although very weak, it becomes unstable and eventually acts as a source of turbulence. On the other hand, when rotation is present, the oscillation of this large-scale shear is found to have a stabilizing effect. This stabilization is probably due to the fact that the growth time for the shear instability, of the order of $(\partial\langle U_x\rangle/\partial z)^{-1}$, is typically 100 times larger than the oscillation period, $\pi/\Omega$. As a consequence, at each half period of oscillation, the growth of the shear instability is inhibited (Poulin, Flierl & Pedlosky 2003), resulting in a reduction of the turbulence production.

The measured velocity field $\boldsymbol{U}$ can be written as the sum of the three large-scale flows $U_{LSC}$, $U_{GW}$ and $U_{IW}$ described above and the turbulent field of interest $\boldsymbol{u}$. Keeping only the dominant spatial dependences of these contributions, one has

$$\boldsymbol{U}^{(n)}(x, y, z, t) \simeq U_{LSC}(z, t)\boldsymbol{e}_x + U_{GW}(t)\cos\left(\frac{2\pi t}{T_{GW}}\right)\boldsymbol{e}_x + U_{IW}(z, t)\left[\cos\left(\frac{2\pi t}{T_{IW}}\right)\boldsymbol{e}_x + \sin\left(\frac{2\pi t}{T_{IW}}\right)\boldsymbol{e}_y\right] + \boldsymbol{u}^{(n)}(x, y, z, t), \quad (2.2)$$

where $n$ is the realization number (the phase origin of the GW and IW flows are not written for simplicity). Since the three large-scale flows are essentially uniform translations, they can be readily subtracted from the measured velocity fields, providing that the turbulent scale is significantly smaller than the field of view. For the measurements in the horizontal plane, one has

$$u_\alpha^{(n)}(x, y, t) = U_\alpha^{(n)}(x, y, t) - \langle U_\alpha^{(n)}(x, y, t)\rangle_{x,y,e}, \quad (2.3)$$

with $\alpha = x, y$. The subscripts indicate the type of average: $\langle\cdot\rangle_{x,y}$ for the spatial average over the $x$- and $y$-directions and $\langle\cdot\rangle_e$ for the ensemble average over the independent realizations. Similarly, for the measurements in the vertical plane, the average $\langle\cdot\rangle_{x,z,e}$ is computed. In order to reduce the statistical noise owing to the limited number of realizations, a temporal smoothing is also performed. The window size of the temporal smoothing is chosen equal to 5 % of the elapsed time, $t$, corresponding to a number of consecutive velocity fields of $N_t = 1$ at the beginning (i.e. no average) up to $N_t = 20$ at the end of the decay.

The statistics in the following combine the spatial average over the $128^2$ PIV grid points, the ensemble average over the $N_r = 4$ or 6 realizations (for the vertical and horizontal measurements, respectively) and the temporal smoothing over $N_t = 1$ to

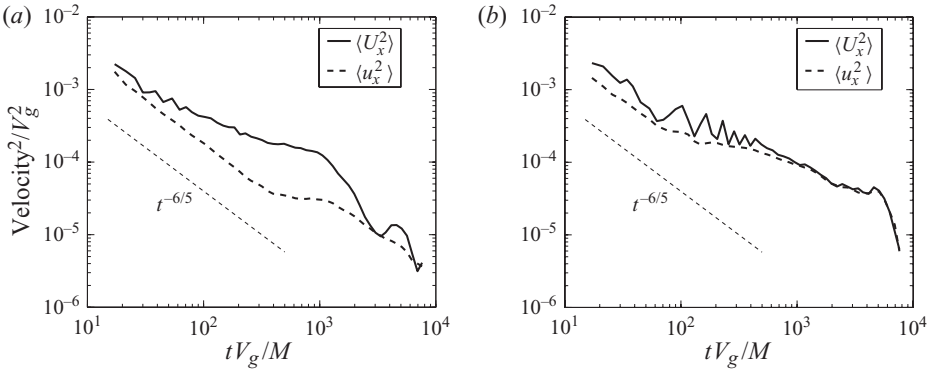


FIGURE 4. Total and turbulent kinetic energy (streamwise variance). (*a*) $\Omega = 0$, (*b*) $\Omega = 0.10\,\mathrm{rad\,s^{-1}}$ ($T = 60\,\mathrm{s}$). The oscillations in the rotating case correspond to IW flow, of period $T_{IW} = T/2 = 30\,\mathrm{s}$.

20 consecutive fields. The resulting number of samples ranges between $8 \times 10^4$ and $1.6 \times 10^6$. When there is no ambiguity, single brackets $\langle \cdot \rangle$ denote both the three types of averages and the root mean square (r.m.s.) is noted as $A' = \langle A^2 \rangle^{1/2}$. The convergence of the averages is determined by computing the standard deviation between the realizations. The standard deviation for the velocity statistics grows from 5 to 30 % during the decay (a wrong separation between the mean flow and turbulence increases the uncertainty when the scale of motion becomes larger than the field of view). The standard deviation for the velocity-gradient statistics is approximately 15 % throughout the decay, indicating that small-scale quantities are less affected by the mean-fluctuation decomposition of the flow.

## 3. Energy and integral scales

### 3.1. *Energy decay*

The time evolution of the streamwise velocity variance for the total flow, $\langle U_x^2 \rangle$, and the turbulent flow, $\langle u_x^2 \rangle = \langle (U_x - \langle U_x \rangle)^2 \rangle$, are shown in figure 4. In the absence of rotation (figure 4*a*), the energy of the mean flow clearly dominates the total energy, by a factor up to 10 for $t \simeq 1000 M/V_g$. On the other hand, when rotation is present (figure 4*b*), the turbulence energy is very close to the total energy, confirming that the mean flow is significantly reduced in the presence of rotation.

In the non-rotating case, once the mean flow is subtracted, the turbulent energy decays as $t^{-n}$ up to $t \simeq 400 M/V_g$, with $n \simeq 1.22 \pm 0.05$. This decay exponent turns out to be very close to the Saffman (1967) prediction $n = 6/5$ for unbounded turbulence (in the early stage of decay, the vertical confinement may indeed be neglected, as shown in § 3.3). The streamwise variance, $\langle u_x^2 \rangle$, is approximately 1.4 times larger than the two spanwise variances $\langle u_y^2 \rangle$ and $\langle u_z^2 \rangle$, reflecting the usual residual anisotropy of grid turbulence (Comte-Bellot & Corrsin 1966). For $t > 400 M/V_g$, the shallower decay probably originates from the turbulence production by the mean residual shear. This transition time, noted $t_{shear}$ in figure 5(*a*), is indeed of the order of the shear time scale, $(\partial U_x/\partial z)^{-1} \simeq 250\,\mathrm{s}$. The ordering of the three velocity variances for $t \gg t_{shear}$, $\langle u_x^2 \rangle > \langle u_y^2 \rangle > \langle u_z^2 \rangle$, actually confirms the shear-dominated nature of the turbulence in the non-rotating case at large times (Tavoularis & Karnik 1989).

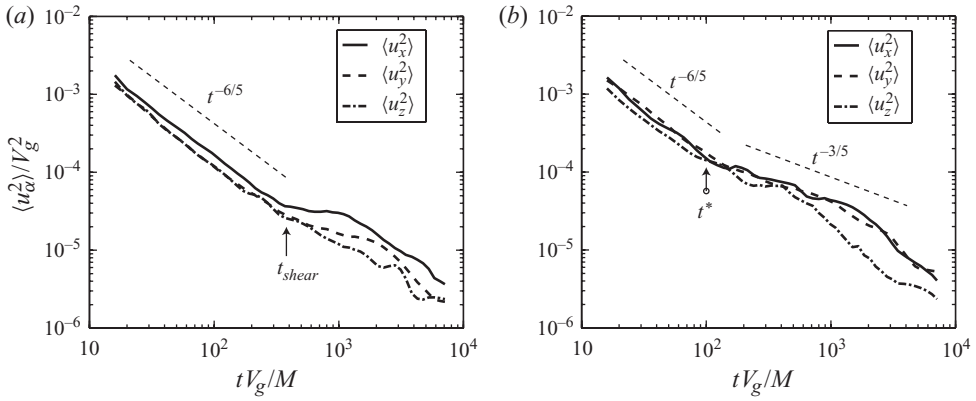


FIGURE 5. Time evolution of the variance of the three velocity components. The variances $\langle u_x^2\rangle$ and $\langle u_y^2\rangle$ are computed from the horizontal PIV fields (camera C1) and $\langle u_z^2\rangle$ from the vertical PIV fields (camera C2), for non-simultaneous experiments. (*a*) $\Omega = 0$. The arrow at $t_{shear}$ indicates the time after which the turbulent energy production by the residual mean shear becomes significant. (*b*) $\Omega = 0.05\,\mathrm{rad\,s^{-1}}$. The arrow at $t^*$ indicates the transition between the $t^{-6/5}$ isotropic decay and the $t^{-3/5}$ decay affected by the rotation.

In non-dimensional form, the decay law of the streamwise variance for isotropic turbulence writes (neglecting possible time origin shift)

$$\frac{\langle u_x^2\rangle}{V_g^2} \simeq A\left(\frac{tV_g}{M}\right)^{-6/5}. \tag{3.1}$$

A best fit for $t < t_{shear}$ yields a decay coefficient $A \simeq 0.045 \pm 0.005$, a value in good agreement with the literature for grid turbulence (Mohamed & LaRue 1990). This indicates that, in spite of the residual mean shear generated by the forcing, the decay of the turbulent kinetic energy is close to that of classical grid turbulence for $t < t_{shear}$, suggesting a negligible coupling between the mean flow and the small-scale turbulence at small time.

The time evolution of the three velocity variances in the rotating case are shown in figure 5(*b*) for $\Omega = 0.05\,\mathrm{rad\,s^{-1}}$. At early time, the three curves are very close to the reference case $\Omega = 0$ (figure 5*a*), confirming that the rotation has no measurable effect at large Rossby numbers. After a crossover time $t^* \simeq 100M/V_g$, the decay of the two horizontal variances $\langle u_x^2\rangle$ and $\langle u_y^2\rangle$ become shallower, showing a clear reduction of the energy decay by the rotation. On the other hand, the vertical variance $\langle u_z^2\rangle$ first follows the horizontal variance short after the crossover time $t^*$, but sharply decreases soon after, reflecting a growth of anisotropy. Since here the turbulence production by the mean shear is essentially suppressed by the background rotation, this departure from the $t^{-6/5}$ decay and the resulting anisotropy growth can now be interpreted as a pure effect of the rotation.

### 3.2. *Crossover between the two decay regimes*

In order to characterize the influence of the rotation on the transition time $t^*$, the decays of the streamwise velocity variance $\langle u_x^2\rangle$ are compared in figure 6 for the four sets of experiments. The crossover time $t^*$ decreases from 100 to approximately $30M/V_g$ as $\Omega$ is increased, which turns out to be approximately 0.4 tank rotation. The small value of $t^*$ found for the highest rotation rate indicates that the turbulent energy production in the wake of the grid may be indeed already affected by the

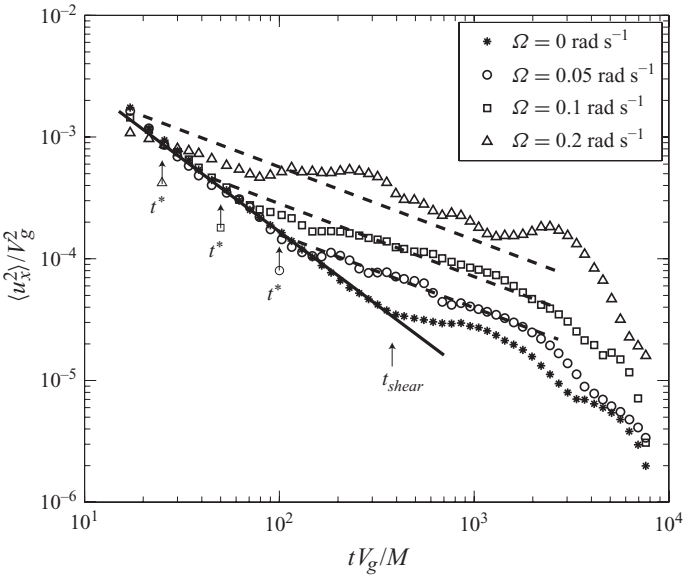


FIGURE 6. Time evolution of the streamwise velocity variance $\langle u_x^2 \rangle$, for the non-rotating and the three rotating experiments. The solid line shows $A(tV_g/M)^{-6/5}$ and the dashed lines show $A_\Omega Ro_g^{-3/5}(tV_g/M)^{-3/5}$. The transition between the non-rotating ($t^{-6/5}$) and rotating ($t^{-3/5}$) decay laws occurs at $t^*$, indicated by the three vertical ticks for each rotation rate. For $t > t_{shear}$ the turbulent energy production by the residual mean shear becomes significant in the non-rotating case.

background rotation in this specific case. The decay curve in this case is indeed particular, showing unexpected large fluctuations.

In the limit of large rotation rate, the energy decay can be modelled by assuming that the energy transfer rate scales as the linear time scale $\Omega^{-1}$. Based on this argument, Squires *et al.* (1994) proposed, using dimensional analysis, the following asymptotic decay law,

$$\frac{\langle u_x^2 \rangle}{V_g^2} \simeq A_\Omega Ro_g^{-3/5} \left( \frac{tV_g}{M} \right)^{-3/5}, \tag{3.2}$$

with $A_\Omega$ being a non-dimensional constant. Although the elapsed time is moderate here, the decay curves in figure 6 are actually compatible with this shallower decay (3.2). Fitting the data for $\Omega = 0.05$ and $0.10\,\mathrm{rad\,s^{-1}}$ yields $A_\Omega \simeq 0.020 \pm 0.005$ (the data at $\Omega = 0.20\,\mathrm{rad\,s^{-1}}$ being excluded for the reason given before). Accordingly, the crossover time $t^*$ between the non-rotating and the rotating decay laws is obtained by equating (3.1) and (3.2),

$$\frac{t^* V_g}{M} \simeq \left( \frac{A}{A_\Omega} \right)^{5/3} Ro_g \simeq (5 \pm 1) Ro_g, \tag{3.3}$$

yielding the values 100, 50 and 25 for the three rotation rates, which reproduce correctly the observed $t^*$ (see the arrows in figure 6). Expressing this crossover time (3.3) in terms of the rotation rate is consistent with a transition occurring at fixed fraction of tank rotation,

$$\frac{\Omega t^*}{2\pi} \simeq (5 \pm 1)/4\pi \simeq 0.4 \pm 0.1. \tag{3.4}$$

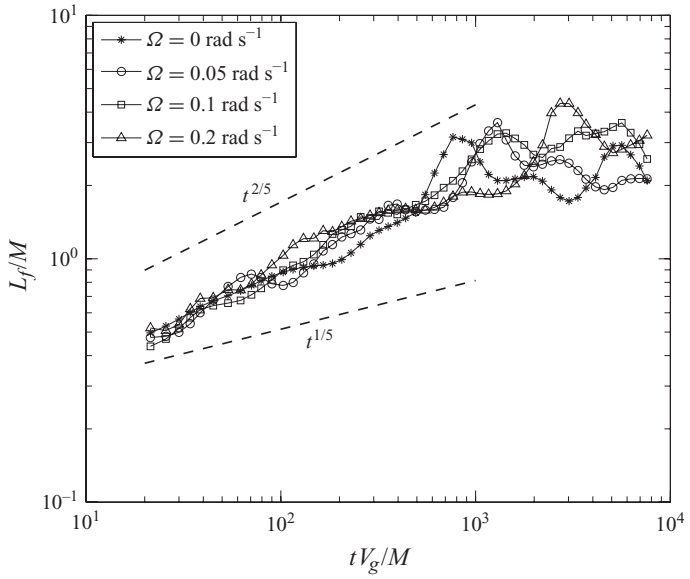


FIGURE 7. Time evolution of the longitudinal integral scale in the horizontal plane, $L_f = (L_{11,1} + L_{22,2})/2$, for the four series of experiments.

It is remarkable that the transition between the two regimes $t^{-6/5}$ and $t^{-3/5}$ is sufficiently sharp, so that the analysis of Squires *et al.* (1994) can be recovered to a correct degree of accuracy. A similar transition in the form $t^{-10/7} \to t^{-5/7}$, with again a factor 2 between the non-rotating and the rotating decay exponents, has been observed in the recent simulation of van Bokhaven *et al.* (2008), the discrepancy with the present exponents being probably associated to different energy content at small wavenumber.

### 3.3. *Integral scales*

We now turn to the time evolution of the integral scales in the horizontal plane, defined as

$$L_{\alpha\alpha,\beta}(t) = \int_0^{r^*} C_{\alpha\alpha,\beta}(r, t)\,\mathrm{d}r, \tag{3.5}$$

from the two-point correlation function of the $\alpha$ velocity component along the $\beta$-direction

$$C_{\alpha\alpha,\beta}(r, t) = \frac{\langle u_\alpha(\boldsymbol{x}, t) u_\alpha(\boldsymbol{x} + r\boldsymbol{e}_\beta, t)\rangle}{\langle u_\alpha^2\rangle}. \tag{3.6}$$

The truncation scale $r^*$ in (3.5) is defined such that $C_{\alpha\alpha,\beta}(r^*) = 0.2$. This truncation is introduced because of the poor convergence of the correlation for separations $r$ approaching the image size. Although this definition systematically under-estimates the true integral scales (defined as $r^* \to \infty$), the trends observed from the truncated integral scales are expected to represent the evolution of the true ones. We first focus here on the horizontal scales, which is useful for the definition of the instantaneous Reynolds and Rossby numbers, and we describe the vertical scales in § 4.3.

The time evolution of the longitudinal integral scale, averaged over the two horizontal directions $x$ and $y$ (noted here 1 and 2 by convention), $L_f = (L_{11,1} + L_{22,2})/2$, is plotted in figure 7. This integral scale shows little influence of the

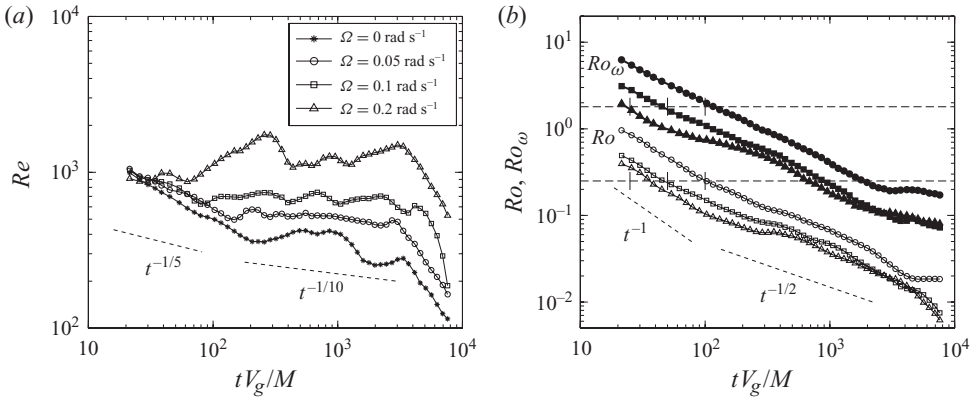


FIGURE 8. (*a*), Reynolds number $Re(t) = u'_x L_f / \nu$. (*b*), Micro- and Macro-Rossby numbers, for the three experiments with background rotation. Upper curves (black symbols): $Ro_\omega = \omega'_z / 2\Omega$. Lower curves (open symbols): $Ro = u'_x / 2\Omega L_f$. The horizontal dotted lines show the thresholds, $Ro_\omega = 1.8$ and $Ro = 0.25$, with the corresponding transition times $t^*$ indicated by the vertical ticks (see (3.3)).

background rotation, in agreement with the observations of Jacquin *et al.* (1990), with $L_f(t) \simeq t^{0.35 \pm 0.05}$ for $t < 1000 M / V_g$, for all rotation rates. The scatter at larger time is probably a consequence of the inadequate subtraction of the mean flow, which may occur when the size of the largest vortices becomes comparable to the imaged area.

Dimensional analysis actually predicts different growth laws for $L_f$ in the non-rotating and rotating cases (Squires *et al.* 1994),

$$\left.\begin{aligned} \frac{L_f}{M} &\simeq B \left(\frac{t V_g}{M}\right)^{2/5} && (t \ll t^*), \\ \frac{L_f}{M} &\simeq B_\Omega Ro_g^{1/5} \left(\frac{t V_g}{M}\right)^{1/5} && (t \gg t^*), \end{aligned}\right\} \tag{3.7}$$

with $B$ and $B_\Omega$ non-dimensional constants. Surprisingly, although the $t^{-6/5} \to t^{-3/5}$ transition at $t = t^*$ is evident in the energy decay curves (figure 6), there is no evidence for the equivalent $t^{2/5} \to t^{1/5}$ transition for $L_f$ in figure 7. Within the experimental uncertainty, a single power law $t^{2/5}$ actually provides a reasonable description for the growth of $L_f$ both in the non-rotating and in the rotating cases.

### 3.4. *Instantaneous Reynolds and Rossby numbers*

The instantaneous Reynolds number, and the macro- and micro-Rossby numbers (Jacquin *et al.* 1990), are finally defined as

$$Re(t) = \frac{u'_x L_f}{\nu}, \quad Ro(t) = \frac{u'_x}{2\Omega L_f}, \quad Ro_\omega(t) = \frac{\omega'_z}{2\Omega}. \tag{3.8}$$

The time evolution of these numbers are plotted in figure 8(*a*,*b*). After a short period of sharp decay similar to the non-rotating case, the Reynolds number in the rotating cases show a very weak decay in the range $t^* < t < 3000 M / V_g$, ranging from 500 to 1300 as the rotation rate is increased. Also shown in this figure are the decay laws

438 expected from (3.1), (3.2) and (3.7),

$$\left.\begin{aligned} Re(t) &\propto Re_g \left(\frac{tV_g}{M}\right)^{-1/5} && (t \ll t^*), \\ Re(t) &\propto Re_g Ro_g^{-1/10} \left(\frac{tV_g}{M}\right)^{-1/10} && (t \gg t^*). \end{aligned}\right\} \tag{3.9}$$

439 The micro-Rossby number, $Ro_\omega$, shown in figure 8($b$), takes values about 10 times
440 larger than $Ro$ throughout the decay (note that $Ro_\omega$ may be underestimated at small
441 times because of the limited PIV resolution). This moderate ratio indicates that the
442 range between the large scales dominated by the rotation and the small scales is
443 indeed limited for the Reynolds number of the present experiments.
444 The joint decay and growth laws for the velocity and integral scale actually lead to
445 a remarkably simple decay law for the macro Rossby number $Ro(t)$. Combining again
446 (3.1), (3.2) and (3.7) shows that, for $t < t^*$, the nonlinear time scale $\tau_{nl} = L_f(t)/u'_x(t)$
447 is simply proportional to the elapsed time, $t$, without dependence on the initial grid
448 time scale $M/V_g$. As a consequence, the Rossby number $Ro = (2\Omega\tau_{nl})^{-1}$ is simply a
449 function of the number of tank rotations,

$$\left.\begin{aligned} Ro(t) &\propto Ro_g \left(\frac{tV_g}{M}\right)^{-1} \propto (2\Omega t)^{-1} && (t \ll t^*), \\ Ro(t) &\propto Ro_g^{1/2} \left(\frac{tV_g}{M}\right)^{-1/2} \propto (2\Omega t)^{-1/2} && (t \gg t^*). \end{aligned}\right\} \tag{3.10}$$

450 At the transition $t = t^*$, which is reached after a fixed number of rotations, the Rossby
451 number is indeed found approximately constant, $Ro(t^*) \simeq 0.25$ (see the vertical ticks
452 at $t^*$ in figure 8$b$). This value is in correct agreement with the transitional Rossby
453 numbers reported by Hopfinger *et al.* (1982) and Staplehurst *et al.* (2008).
454 It is also of interest to characterize this transition in terms of the micro-Rossby
455 number, $Ro_\omega(t)$, which is often used in the literature. For $t \ll t^*$, assuming again
456 isotropic turbulence, the decay law of $Ro_\omega$ can be inferred from the relation between
457 the vorticity r.m.s., the velocity r.m.s. and the dissipation rate,

$$\epsilon = -\frac{1}{2}\frac{\partial \boldsymbol{u}'^2}{\partial t} = -\frac{3}{2}\frac{\partial u_x'^2}{\partial t} = \nu\boldsymbol{\omega}'^2 = 3\nu\omega_z'^2. \tag{3.11}$$

458 Combining the isotropic decay law (3.1) with (3.11) gives

$$Ro_\omega(t) = \sqrt{\frac{3}{5}} A^{1/2} Re_g^{1/2} Ro_g \left(\frac{tV_g}{M}\right)^{-11/10} \qquad (t \ll t^*), \tag{3.12}$$

459 yielding a scaling exponent very close to that of $Ro(t)$. Evaluating $Ro_\omega$ at the transition
460 $t \simeq t^*$, using (3.3), finally yields

$$Ro_\omega(t^*) \simeq \sqrt{\frac{3}{5}} (5 \pm 1)^{-11/10} A^{1/2} Re_g^{1/2} Ro_g^{-1/10}. \tag{3.13}$$

461 Accordingly, no strictly constant micro-Rossby number is expected at the transition,
462 although the dependence with the rotation rate, as $\Omega^{1/10}$, is very weak ($\Omega$ is varied
463 by a factor of 4 only in the present experiment). As shown by the vertical ticks in
464 figure 8($b$), $Ro_\omega$ takes values which actually turn out to be approximately constant at
465 the transition, $Ro_\omega(t^*) \simeq 1.8$. Interestingly, this value is close to the empirical threshold
466 reported by Morize *et al.* (2005), below which the energy spectrum and the velocity

derivative skewness were found to depart from the classical Kolmogorov predictions. Although the macro-Rossby number is probably a more relevant parameter to describe this transition, the similar Reynolds number of the two experiments explains the similar values of $Ro_\omega$ found at the transition.

## 4. Dynamics of the anisotropy

### 4.1. *Visualization of the vertical layers*

We now focus on the growth of anisotropy in the vertical plane $(x, z)$. Figure 9 shows a sequence of six snapshots of the velocity field and spanwise vorticity, $\omega_y$, after the transition $t > t^*$, for $\Omega = 0.20$ rad s$^{-1}$ (see also supplementary movie 3). The anisotropy can be visually detected from the first snapshot, and the presence of vertical layers of ascending or descending fluid becomes evident after eight tank rotations (figure 9*c*). Lower rotation rates show similar layers (see also figure 2*d*), although thicker and less intense than for $\Omega = 0.20$ rad s$^{-1}$. These layers are difficult to infer from the velocity field itself, because of the superimposed strong horizontal flow, but they clearly appear through the surrounding layers of nearly constant $\omega_y$ of alternate sign. These layers of vertical velocity are consistent with a trend towards a three-component two-dimensional (3C2D) flow, with vanishing vertical variations of the velocity field, but non-zero vertical velocity $u_z$. Although compatible with the Taylor–Proudman theorem in an unbounded domain, this 3C2D flow organization is surprising here, because of the the boundary layer conditions which should select a two-component two-dimensional flow (with $u_z = 0$). The persistence of these layers with non-zero $u_z$ is discussed in § 4.4.

As time proceeds, the vertical layers become thinner and more vertically coherent (note that since only the intersection of the layers with the measurement plane can be visualized, the apparent thickness may overestimate the actual one). At large time (figure 9*e*,*f*), although these layers are nearly coherent from the bottom wall up to the free surface, they are not strictly vertical, but rather show wavy disturbances. These disturbances have amplitude and characteristic vertical size of the order of the layer thickness, suggesting the occurrence of a shear instability (discussed in § 4.5). We will examine in § 5 the consequence of this instability on the dynamics and statistics of the vertical vorticity field.

### 4.2. *Decay of the vertical velocity and anisotropy growth*

The time evolution of the vertical velocity variance, $u_z'^2 = \langle u_z^2 \rangle_{x,z,e}$, and the isotropy ratio, $u_z'/u_x'$, plotted in figure 10(*a*,*b*), show a complex behaviour. Here, the spatial average is computed only in the core of the flow, excluding layers of thickness $0.1h$ near the bottom wall and the free surface. Similarly to the horizontal variance (see figure 6), the vertical variance for the rotating cases first departs from the reference curve $t^{-6/5}$ of the non-rotating case, and follows a shallower decay which is compatible again with a $t^{-3/5}$ law, at least during an intermediate range. Although the $t^{-6/5} \to t^{-3/5}$ transition is not as sharp as for the horizontal variance, perhaps because of the limited statistics achieved for the measurements in the vertical plane, the transition time is compatible with the one determined for $\langle u_x^2 \rangle$, corresponding to $\Omega t^*/2\pi \simeq 0.4$ tank rotation. After $\Omega t/2\pi \simeq 2$, the vertical variance follows a significantly faster decay, whereas the horizontal variance still decays as $t^{-3/5}$, yielding a growing anisotropy in the vertical plane. Although the formation of vertical structures is evident in the spanwise vorticity field $\omega_y$ (figure 9), the anisotropy remains moderate when expressed in terms of the ratio of velocity variances. This ratio reaches a weak minimum between

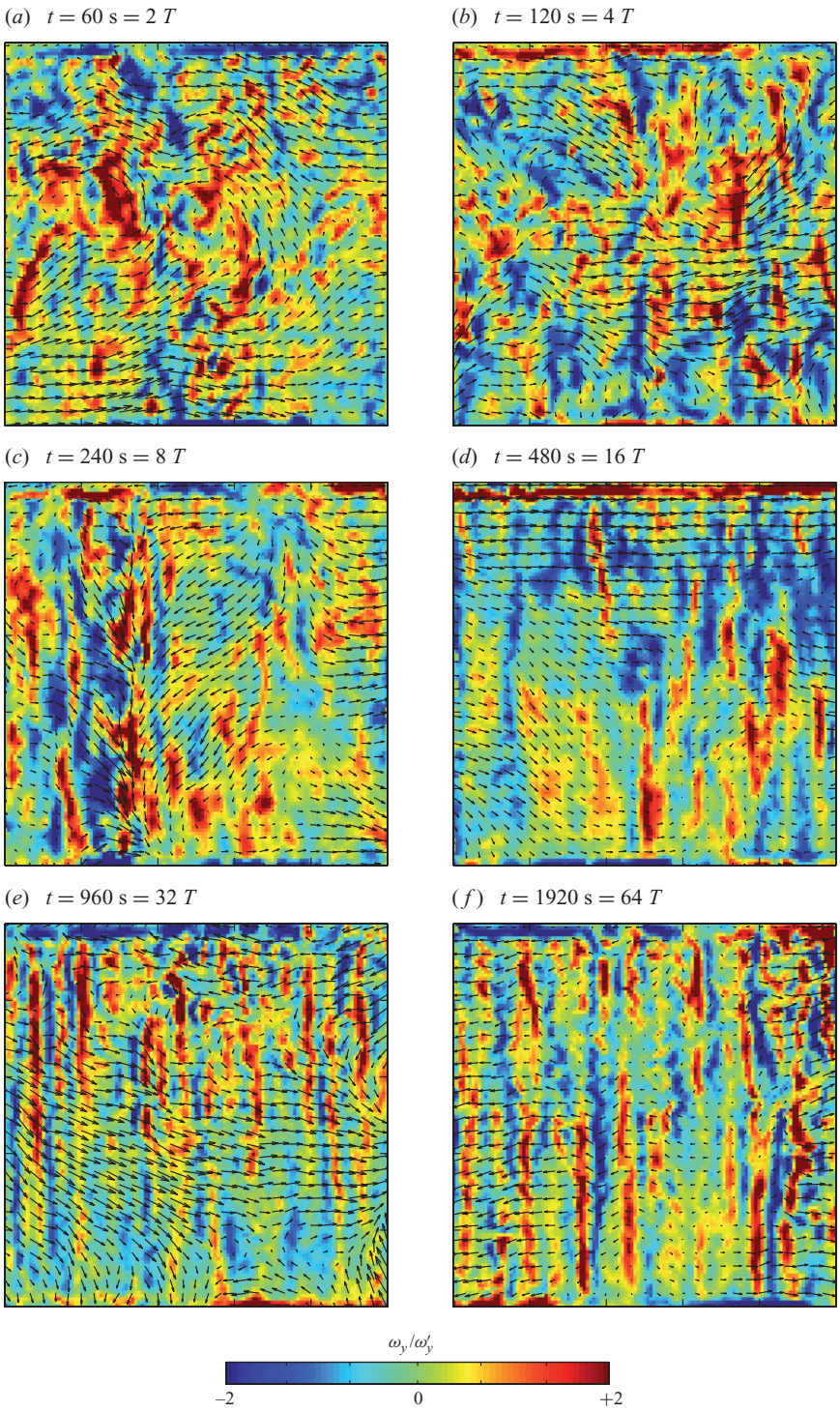


COL-
www+print

FIGURE 9. Sequence of six snapshots of the velocity and spanwise vorticity, $\omega_y$, in the vertical plane $(x, z)$ for $\Omega = 0.20$ rad s$^{-1}$. The imaged area is 1 m $\times$ 1 m. The grid is translated from left to right, and the time origin $t = 0$ is defined as the grid goes through the centre of the imaged area. The colour range is normalized by the r.m.s. $\omega'_y$ computed for each time.

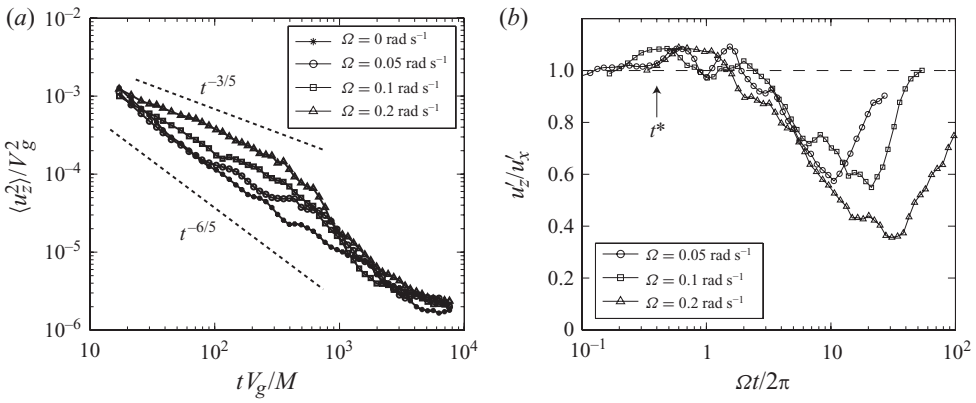


FIGURE 10. (*a*) Time evolution of the vertical velocity variance $\langle u_z^2 \rangle$, for the non-rotating and the three rotating experiments. (*b*) Isotropy factor $u'_z/u'_x$ for the three rotating experiments, as a function of number of tank rotation. The vertical line indicates the transition between the $t^{-6/5}$ and the $t^{-3/5}$ decay regimes at $\Omega t^*/2\pi \simeq 0.4$.

$0.6 \pm 0.2$ and $0.4 \pm 0.15$ only, after 10–30 tank rotations, depending on the rotation rate. This confirms that the velocity field remains significantly three-component, although the dynamics of the large scales becomes nearly two-dimensional (i.e. $z$-invariant). Interestingly, the ratio $u'_z/u'_x$ for the different rotation rates collapse in the anisotropy growth regime when plotted as a function of the number of tank rotations $\Omega t/2\pi$.

An intriguing feature of figure 10(*b*) is the reverse trend $u'_z/u'_x \to 1$ observed at large time. This apparent return to isotropy is associated to the flattening of the decay of $\langle u_z^2 \rangle$ at large time, visible in figure 10(*a*). A similar behaviour is obtained for the Reynolds stress anisotropy in the numerical simulations of Morinishi, Nakabayashi & Ren (2001). It is in apparent contradiction with the clear anisotropy visible in figure 9(*e*,*f*), confirming that the ratio of velocity variances is not an appropriate indicator of anisotropy.

### 4.3. *Integral scales in the vertical plane*

In order to relate the evolution of the vertical velocity variance to the formation, thinning and instability of the vertical layers, we now focus on the statistical geometry of these layers. For this, we have computed the three integral scales $L_{11,3}$, $L_{33,1}$ and $L_{33,3}$, using definitions (3.5) and (3.6) with $\alpha, \beta = 1, 3$. $L_{11,3}$ characterizes the trends towards two-dimensionality, $L_{33,3}$ the vertical coherence of the layers and $L_{33,1}$ the thickness of the layers. No reliable measurement of $L_{11,1}$ could be obtained from the vertical fields, because of the ambiguity of the subtraction of the horizontal LSC flow at large time: large-scale vortices having their axis out of the measurement plane produce strong horizontal velocity which, if subtracted, yield an unphysical decrease of $L_{11,1}$. Here again, in (3.6), the depth-average excludes lower and upper layers over a thickness of $h/10$, in order to avoid boundary effects. In the extreme case of an unbounded $z$-invariant 2D flow, the vertical correlations would be $C_{\alpha\alpha,3}(r) = 1$, yielding $L_{\alpha\alpha,3} = \infty$.

The time evolution of the three integral scales is shown in figure 11, in the case $\Omega = 0.10\,\mathrm{rad\,s^{-1}}$. At short time, the longitudinal integral scale $L_{33,3}$ is, as expected, larger than the two transverse ones (one has $L_{33,3} = 2L_{11,3} = 2L_{33,1}$ for isotropic turbulence). The most spectacular effect is the rapid growth of $L_{11,3}$, characterizing

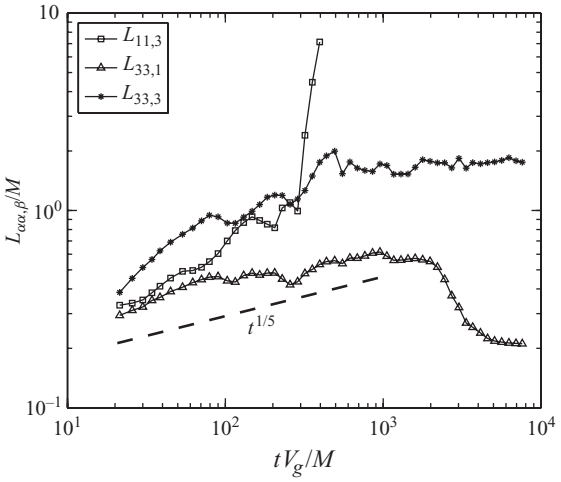


FIGURE 11. Time evolution of the normalized integral scales $L_{\alpha\alpha,\beta}/M$ computed in the vertical plane, for $\Omega = 0.10\,\mathrm{rad\,s^{-1}}$. For $tV_g/M > 400$, $L_{11,3}$ is no longer defined, because the correlation $C_{11,3}$ does not decrease sufficiently for large vertical separations.

the vertical correlation of the horizontal velocity, which is a clear signature of the two-dimensionalization of the large scales of the flow. However, this integral scale could not be computed for $tV_g/M > 400$ because the correlation $C_{11,3}(r)$ does not decrease below the chosen threshold 0.2. Although the limited range of rotation rate prevents from a clear check of the scaling of this divergence time, we can note that it occurs roughly at a constant number of tank rotations. Assuming that energy is contained at scale $L_{11,1} \simeq M$ at early time, and that eddies grow vertically by wave propagation, $L_{11,3}$ is expected to increase by an amount of $L_{11,1}$ at each tank rotation. Accordingly, the divergence of $L_{11,3}$ is expected after a number of tank rotations of order of $h/M \simeq 7$, where $h$ is the channel depth, in qualitative agreement with the present observations. After the divergence of $L_{11,3}$, the vertical correlation of the vertical velocity remains constant until the end of the experiment, with $L_{33,3} \simeq 2M$, indicating a significant, although finite, vertical coherence of the ascending and descending layers. Note that, however, even strictly coherent thin layers of constant velocity would lead to finite integral scale $L_{33,3}$, because the tilting of the layers by the oscillating shear of the IW flow strongly reduces the vertical correlation as the layers become thinner.

A remarkable feature of figure 11 is the sharp decrease of the horizontal correlation of the vertical velocity, described by $L_{33,1}$, for $tV_g/M > 2000$ (corresponding to $\Omega t/2\pi \simeq 16$–$24$ tank rotations), and its subsequent saturation to the very low value $L_{33,1} \simeq 0.2M \simeq 30\,\mathrm{mm}$ at large time. In the final stage of the decay, the strong anisotropy is characterized by the following non-trivial ordering (see figures 7 and 11):

$$L_{33,1} \ll L_{33,3} \simeq L_{11,1} \ll L_{11,3}. \tag{4.1}$$

The low asymptotic value of $L_{33,1}$ suggests that, in the final regime, the vertical-velocity fluctuations have a well-defined characteristic scale in the horizontal direction, i.e. there is no global vertical motion at scales larger than the thickness of the layers. This final value of $L_{33,1}$, which provides an estimate for the average thickness of the layers, is found to slightly decrease, from $0.23M$ to $0.17M$, as $\Omega$ is increased,

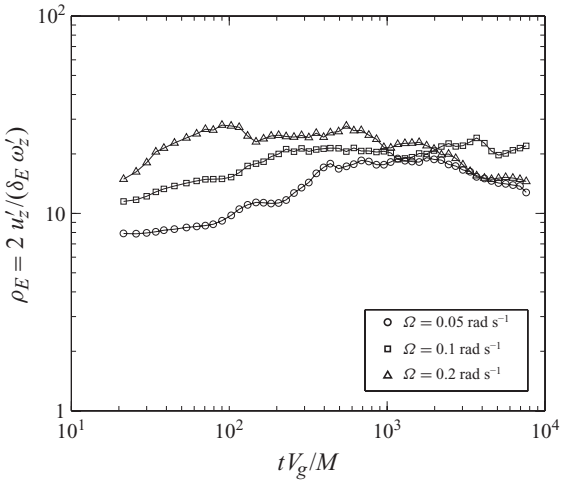


FIGURE 12. Time evolution of the Ekman ratio, $\rho_E$, (4.2), showing that the vertical velocity variance is significantly larger than the expected Ekman-pumping velocity.

suggesting that the thinning of the layers induced by the horizontal straining motion due to the large-scale vortices is stronger at higher rotation rate.

### 4.4. *Origin of the vertical layers*

Figure 10 raises the issue of the origin of the non-negligible vertical-velocity fluctuations found at large time. Although the Taylor–Proudman theorem predicts a 3C2D flow in the limit of low Rossby numbers, boundary conditions at $z = 0$ and $h$ should actually select a 2D2C flow with zero vertical velocity at large time, apart from weak Ekman-pumping effects.

We can first note that the measured vertical velocity variance, even at large time, remains comfortably larger than the one expected for the Ekman pumping induced by the horizontal flow. According to the linear-Ekman-pumping theory, a quasi-2D field of vertical vorticity r.m.s., $\omega_z'$, should lead to a characteristic vertical-velocity r.m.s. of $u_z'^E = \delta_E \omega_z'/2$ for $z \simeq \delta_E$ (Greenspan 1968), where $\delta_E$ is the Ekman-layer thickness (see § 2.2). The discrepancy between the actual $u_z'$ and the Ekman-pumping estimate, $u_z'^E$, may be therefore measured by the ratio

$$\rho_E = \frac{2u_z'}{\delta_E \omega_z'}. \tag{4.2}$$

In figure 12, this ratio starts from about 10 at small time, and slightly increases up to about 20 at larger time, confirming that the Ekman pumping can be neglected in the present experiments.

Another possibility for this vertical velocity is the onset of a residual thermal convection motion at large time. Although the mixing induced by the grid translation homogenizes the flow temperature, a slight cooling of an upper layer of water may be induced by the evaporation, triggering convection cells in the depth of the channel. Although this effect cannot be ruled out in the present experiments, we note that such convection cells are not visually detected at the end of the decay for $\Omega = 0$, so we believe that, if present, thermal convection should not play a significant role for $\Omega \neq 0$.

A remaining possibility for the vertical velocity found at large time is the initial vertical fluctuations induced by the grid. The 2D2C selection by the boundary conditions should be at work only after a sufficient time for the boundary conditions to influence the interior of the flow, and this time is apparently not reached in our experiments. Three relevant time scales may be considered for this problem: the vertical advection time, $\tau_h = h/u_z'$, the viscous time across the layer thickness, $\tau_v = L_{33,1}^2/\nu$, and the recirculation time in the Ekman boundary layers (Ekman time), $\tau_E = h/(\nu\Omega)^{1/2}$. In our experiment, at large times ($tV_g/M > 2000$), all the three time scales are found of the same order: $\tau_h \simeq 2000$ s (from figure 10*a*), $\tau_v \simeq 1000$ s (from figure 12) and $\tau_E \simeq 2000$–$4000$ s (see table 1). Since the three time scales are of the order of the experiment duration itself (3600 s), it is conceivable that only the boundary conditions are marginally felt by the vertical velocity in the shear layers. Accordingly, these layers may be seen as a vestige of early vertical fluctuations induced by the grid and advected by the horizontal large-scale flow, suggesting that even longer experiments would be necessary to observe the selection of a pure 2D2C flow.

### 4.5. *Stability of the vertical layers*

Although the strong anisotropy of the flow in the final stage is well characterized by the ordering of the the integral scales (4.1), the ratio of the velocity variances remains close to 1 (figure 10*b*). More surprisingly, the quasi-isotropy of the velocity also holds at small scales, as shown by the following two velocity gradient isotropy factors,

$$\frac{\omega_y'}{\omega_z'} \quad \text{and} \quad \sqrt{5}\frac{\gamma_z'}{\omega_z'}, \tag{4.3}$$

where $\gamma_z' = \langle(\partial u_z/\partial z)^2\rangle^{1/2}$ is the r.m.s. of the vertical strain rate. The vertical strain rate plays an important role, as it is responsible for the stretching of the absolute vertical vorticity. In the isotropic turbulence, both quantities are equal to 1 (the second equality follows from the classical isotropic relation $\epsilon = 15\nu\gamma_z'^2 = \nu\boldsymbol{\omega}'^2 = 3\nu\omega_z'^2$, where $\epsilon$ is the dissipation rate). For a 2D flow with arbitrary vertical velocity, one has $\gamma_z = 0$, whereas $\omega_y = 0$ is true only for a two-dimensional two-component flow. As a consequence, the two isotropy factors may be considered as signatures of the *dimensionality* and *componentality* of the small scales, respectively (Cambon, Mansour & Godeferd 1997).

Figure 13 shows that the two velocity gradient isotropy factors first slowly decrease according to the linear time scale $\Omega^{-1}$, reaching a moderate minimum of about 0.5 at the largest rotation rate. The time of maximum anisotropy for these quantities is close to that for $u_z'/u_x'$, and here again the collapse of the curves with respect to the linear time scale no longer applies during the increase at large time. This plot shows that, in the final stage, the small scales are both 3D and 3C, although not necessarily isotropic.

Assuming that the vertical velocity, $u_z$, behaves as a scalar field passively advected by the large-scale horizontal flow, provides a qualitative explanation for the increase of $\omega_y'/\omega_z'$ at large time. As shown in figure 14(*a*), a layer of ascending fluid $u_z > 0$ in a horizontal strain field, for instance in the vicinity of a large vortex, is elongated along one direction and compressed along the other one, so it becomes thinner. In this process, $u_z$ is approximately conserved, but its horizontal gradient $\nabla_h u_z$ increases, producing horizontal vorticity $\omega_x$ and $\omega_y$ which may reach, and even exceed, the vertical vorticity, $\omega_z$.

The increase in $\gamma_z'$, on the other hand, may be a consequence of the instability of these vertical layers. If the inertial time scale of the jets, $(\nabla_h u_z)^{-1} \simeq L_{33,1}/u_z'$, remains smaller than the dissipation time scale, $L_{33,1}^2/\nu$, the jets may undergo shear

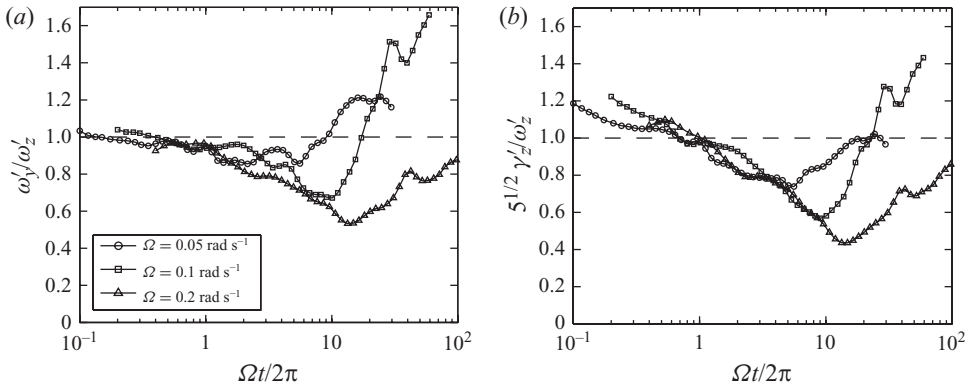


FIGURE 13. Time evolution of the velocity gradient isotropy factors: (*a*) $\omega_y'/\omega_z'$ and (*b*) $\sqrt{5}\gamma_z'/\omega_z'$. In each figure, the horizontal dashed line indicates the isotropic values, $\omega_y'/\omega_z' = \sqrt{5}\gamma_z'/\omega_z' = 1$.

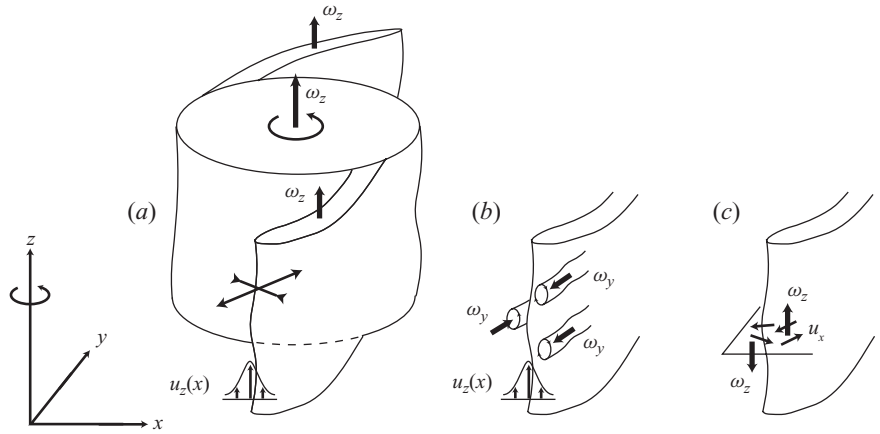


FIGURE 14. Sketch showing the thinning and instability of the vertical layers of vertical velocity advected by the horizontal flow. (*a*) Nearly vertical layer of ascending fluid, $u_z > 0$, strained in the vicinity of a large cyclone $\omega_z > 0$. (*b*) The layer becomes unstable, producing horizontal vortices. (*c*) These horizontal vortices produce random horizontal motion, and hence vertical vorticity of arbitrary sign.

instabilities, producing horizontal vortices (sketched in figure 14*b*), as suggested by the visualizations in figure 9(*e*,*f*). This condition is actually satisfied: the Reynolds number, $Re_l$, based on these layers, defined as the ratio of the two time scales, writes

$$Re_l = \frac{L_{33,1}u_z'}{\nu} = \frac{L_{33,1}}{L_f}\frac{u_z'}{u_x'}Re, \tag{4.4}$$

where $Re$ is the instantaneous Reynolds number defined in (3.8). With $L_{33,1}/L_f \simeq 0.1$, $u_z'/u_x' \simeq 0.5$, and $Re$ ranging between 300 and 1300 in the final period of the decay (see figure 8), one has $Re_l \simeq 10$–$10^2$, which is actually sufficient for a shear instability to develop. Little influence of the background rotation is expected on this shear instability, since the vertical velocity is unaffected by the Coriolis force (the resulting

instability pattern, involving horizontal velocity, may, however, be affected by the rotation). The resulting wavy layers break the vertical invariance of $u_z$, thus producing vertical strain $\gamma_z'$ of the order of the vorticity $\omega_y'$, in agreement with figure 13.

All these results suggest that the flow structure at large time is fully three-dimensional and three-component, with isotropy factors (4.3) close to that of 3D isotropic turbulence, although the large scales are highly anisotropic, as described by the ordering of the integral scales (4.1).

## 5. Cyclone–anticyclone asymmetry

### 5.1. *Dynamics of the cyclones and anticyclones*

We finally turn to the structure of the vertical vorticity field in the rotating case, focusing on the issue of the cyclone–anticyclone asymmetry. The dynamics of the horizontal flow is illustrated by six snapshots in figure 15 for $t > t^*$ (see also the supplementary movie 2). At the beginning of the decay, the vorticity field consists of small-scale disordered fluctuations (figure 15*a*,*b*), which gradually evolve into a complex set of tangled vortex sheets and vortices (figure 15*c*). A set of well defined, nearly circular, cyclones gradually emerges and separates from the turbulent background (figure 15*d*). Anticyclones are also encountered, but they are weaker and less compact than the cyclones. Once formed, visual inspections of the movies indicate that the anticyclones are not specifically unstable compared to the cyclones. This observation suggests that the cyclone–anticyclone asymmetry originates essentially from an enhanced vortex stretching of the cyclonic vorticity operating at early time, and not from a preferential instability of the anticyclones at large time.

At large time, the size of the cyclone grows, and merging of cyclones are frequently encountered, as illustrated in figure 15(*e*). No event of anticyclone merging is observed, probably because of their too small density. At the same time, a background of small-scale-vorticity fluctuations of random sign appears (figure 15*e*,*f*) and, at the end of decay, the flow essentially consists of these small-scale symmetric fluctuations advected by the large scale, mostly cyclonic, vortices.

### 5.2. *Growth of vorticity skewness*

The gradual structuration of the vorticity field is described by the vorticity skewness and flatness factors,

$$S_\omega = \frac{\langle \omega_z^3 \rangle}{\langle \omega_z^2 \rangle^{3/2}}, \quad F_\omega = \frac{\langle \omega_z^4 \rangle}{\langle \omega_z^2 \rangle^2}, \tag{5.1}$$

(where the brackets denote horizontal and ensemble average), which are plotted in figure 16. Both $S_\omega$ and $F_\omega$ show a non-monotonic behaviour, with a collapse in the growth regime when plotted as a function of the number of tank rotations $\Omega t/2\pi$. Note that the residual oscillations visible at small times are associated to the large-scale IW flow (see § 2.4), of period $\Omega t/2\pi = 1/2$. As for the isotropy factors, the re-scaling with $\Omega^{-1}$ no longer holds during the decrease of $S_\omega$ and $F_\omega$ at large time.

For $t < t^*$, the vorticity skewness, $S_\omega$, is essentially zero, within an uncertainty of $\pm 10^{-1}$. For $t > t^*$, it grows according to the power law

$$S_\omega \simeq 0.45 \left( \frac{\Omega t}{2\pi} \right)^{0.7}, \tag{5.2}$$

which is in remarkable agreement with the one reported by Morize *et al.* (2005), both concerning the exponent and the numerical pre-factor. Although in both experiments

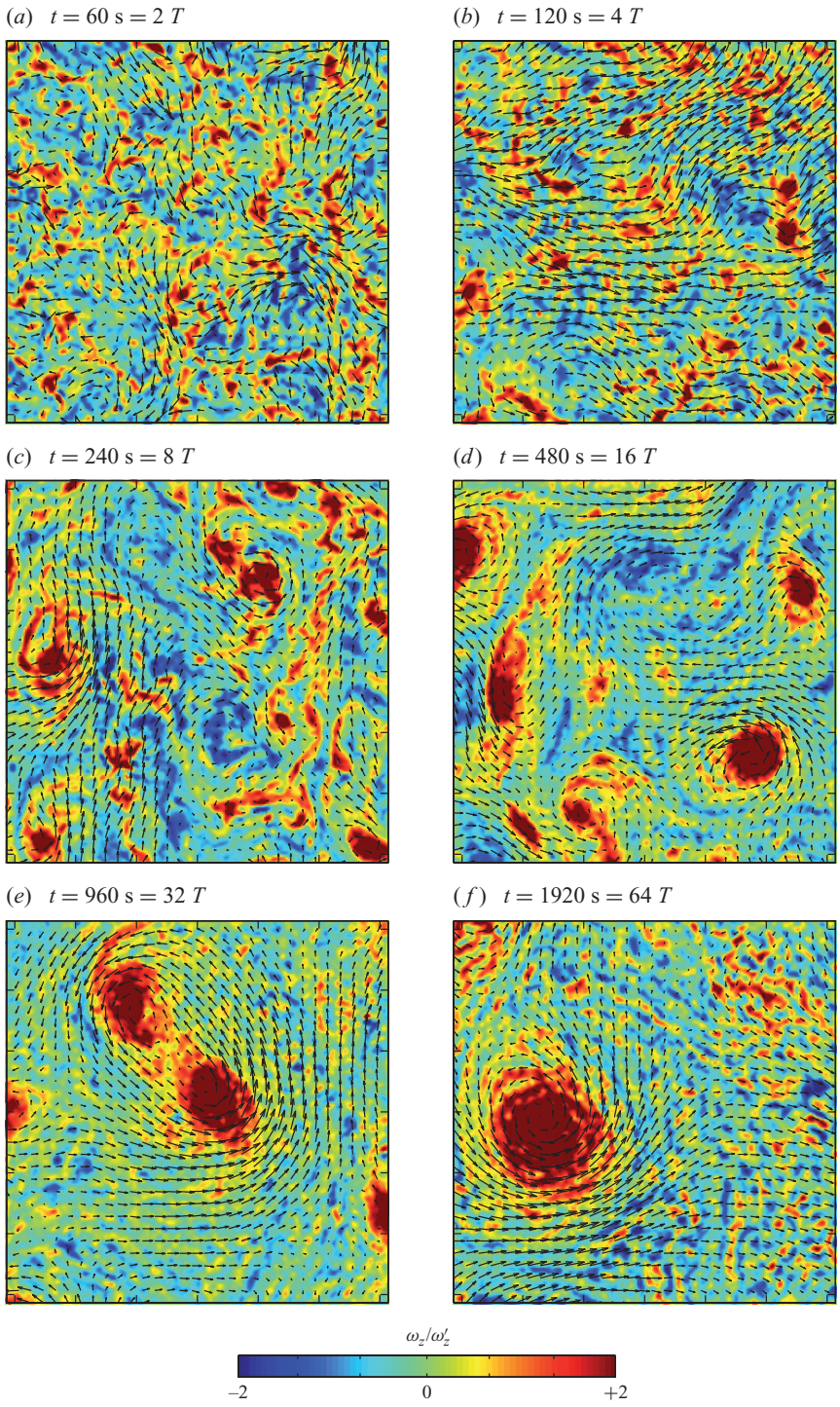


FIGURE 15. Sequence of six snapshots of the velocity and vertical vorticity fields, $\omega_z$, measured in a horizontal plane $(x, y)$ at mid-height for $\Omega = 0.20$ rad s$^{-1}$. The imaged area is 1.3 m $\times$ 1.3 m, representing 4.6 % of the tank section. The tank rotation is anticlockwise. Positive and negative vorticity indicate cyclones (in red) and anticyclones (in blue), respectively. The colour range is normalized by the r.m.s. $\omega_z'$ computed for each time.

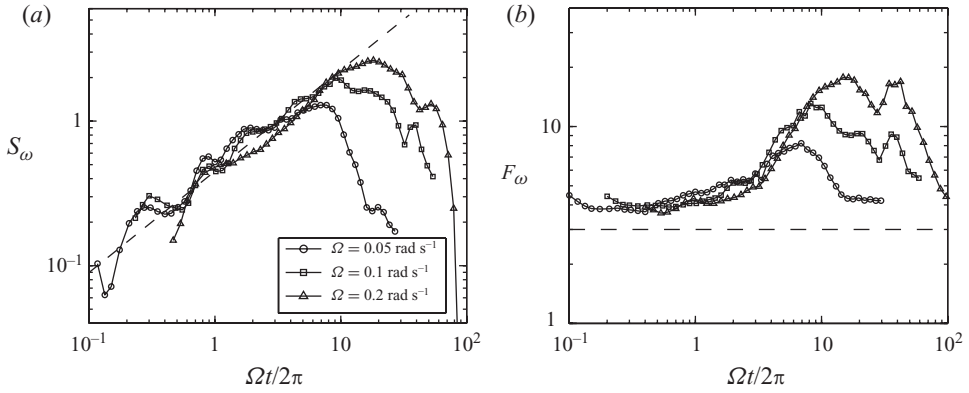


FIGURE 16. Vorticity skewness, $S_\omega$, and ($b$) Vorticity flatness, $F_\omega$, as a function of the number of tank rotation $\Omega t/2\pi$. In ($a$), the dashed line shows the fit $0.45(\Omega t/2\pi)^{0.7}$. In ($b$), the dashed line indicates the value $F_\omega = 3$ corresponding to a Gaussian field.

turbulence is generated by the translation of a grid, the details of the geometry differ in a number of respects: here the grid velocity is normal to the rotation axis and the aspect ratio is significantly lower ($h/L_y = 0.25$ instead of 1.3). The collapse of $S_\omega$ for the two experiments is a clear indication of a generic behaviour of this quantity in decaying rotating turbulence (Morize *et al.* 2006*b*).

The peak values of $S_\omega$, between 1.5 and 3 for increasing $\Omega$, are significantly larger than those obtained in the experiments of Morize *et al.* (2005) and Staplehurst *et al.* (2008), and in the direct numerical simulation of van Bokhoven *et al.* (2008). The corresponding peaks of $F_\omega$, between 8 and 18, are much larger than usually measured in non-rotating turbulence at similar Reynolds number (see, e.g. Sreenivasan & Antonia 1997), an indication of the strong concentration of vorticity in the core of the cyclones.

### 5.3. *The decay of vorticity skewness at large time*

For larger times, when the flow consists mostly of isolated large-scale cyclones, $S_\omega$ starts decreasing back to zero, while $F_\omega$ recovers values around four, similar to the beginning of the decay. The important scatter in the decay is due to the limited sampling: at large times, the number of strong vortices per unit of imaged area is of order of 1, so the statistics become very sensitive to events of vortices entering or leaving the field of view.

There is no general agreement concerning the decrease of $S_\omega$ at large time. It was attributed to confinement effects by Morize *et al.* (2005), namely the diffusion induced by the Ekman pumping on the cyclonic vortices. This suggestion was motivated by the fact that the time $t_{max}$ of maximum $S_\omega$ was approximately following the Ekman time scale, $t_{max} \simeq 0.1h(\nu\Omega)^{-1/2}$. Fitting the times of maximum skewness for the present data would actually give similar values, although the spread of the maximum of $S_\omega$ and here the limited range of $\Omega$ prevent from a clear check of the $\Omega^{-1/2}$ scaling. However, the fact that the Ekman pumping is shown to have no significant effect in the present experiment (see § 4.4) makes this interpretation questionable. The role of the confinement in the decay of $S_\omega$ is also questioned by the numerical data of van Bokhoven *et al.* (2008), who have reported a decrease of $S_\omega$ at large times in a homogeneous turbulence with periodic boundary conditions, and hence without Ekman pumping. Note that no decrease in $S_\omega$ was reported in numerical simulation

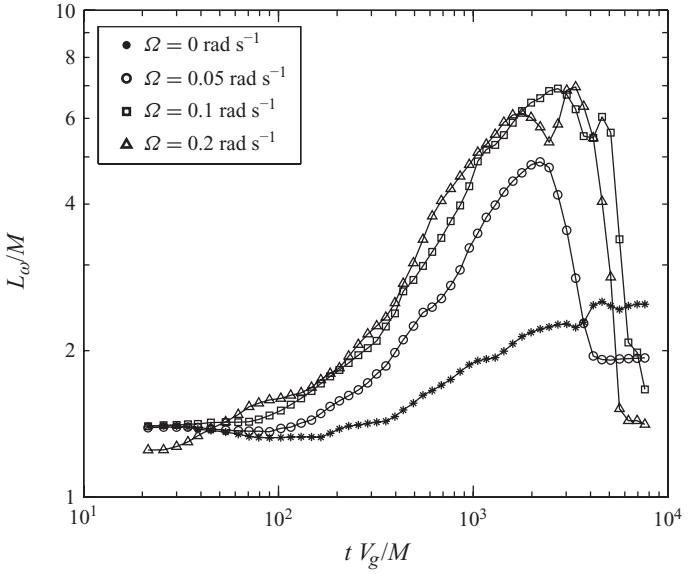


FIGURE 17. Time evolution of the horizontal integral scale of vertical vorticity, $L_\omega$.

of Bourouiba & Bartello (2007) and in the experiment of Staplehurst *et al.* (2008), perhaps because of their limited temporal range. The measurements of the latter were restricted to three tank rotations, whereas the decrease of $S_\omega$ starts typically after 10 rotations here and in Morize *et al.* (2005).

Apart from diffusion effects, another possible contribution for the decrease in $S_\omega$ is based on the fact that vorticity is a small-scale quantity, whereas the cyclone–anticyclone asymmetry is defined by structures of increasing size as time proceeds. In particular, it is observed that the flow outside the cyclones is not smooth, but is made of small scale, approximately symmetric, vorticity fluctuations. These vorticity fluctuations could originate from the instabilities of the vertical shear layers strained by the horizontal large-scale flow, as described in § 4.5. The horizontal vortices resulting from this instability induce a horizontal straining flow (figure 14*b*), which may itself be unstable and produce vertical vorticity of random sign at small scale (figure 14*c*). Accordingly, there is a possibility for the vorticity skewness to return to zero at large time, although the large-scale field remains dominated by a set of large cyclones.

The characteristic size of the vortical structures may be estimated from the horizontal integral scale of the vertical vorticity, $L_\omega = (L^\omega_{33,1} + L^\omega_{33,2})/2$. Here the integral scales for the vorticity are defined similarly as those for the velocity, by modifying (3.5) as

$$L^\omega_{33,\beta} = \int_0^{r^*} \frac{\langle \omega_z(\boldsymbol{x}, t)\omega_z(\boldsymbol{x} + r\boldsymbol{e}_\beta, t)\rangle}{\langle \omega_z^2 \rangle}\,\mathrm{d}r \tag{5.3}$$

(note that the truncation scale $r^*$ is not essential here, because the vorticity correlation decreases sufficiently rapidly). Figure 17 shows the characteristic increase and decrease of $L_\omega$ when rotation is present, whereas it monotonically increases in the absence of rotation. The decrease occurs at $tV_g/M \simeq 2000$ for all rotation rates, which coincides with the sharp decrease in $L_{33,1}$ (figure 11) and the isotropy factors (figure 13), and $L_\omega$ reaches values of order $0.2M \simeq 30$ mm, similar to those found

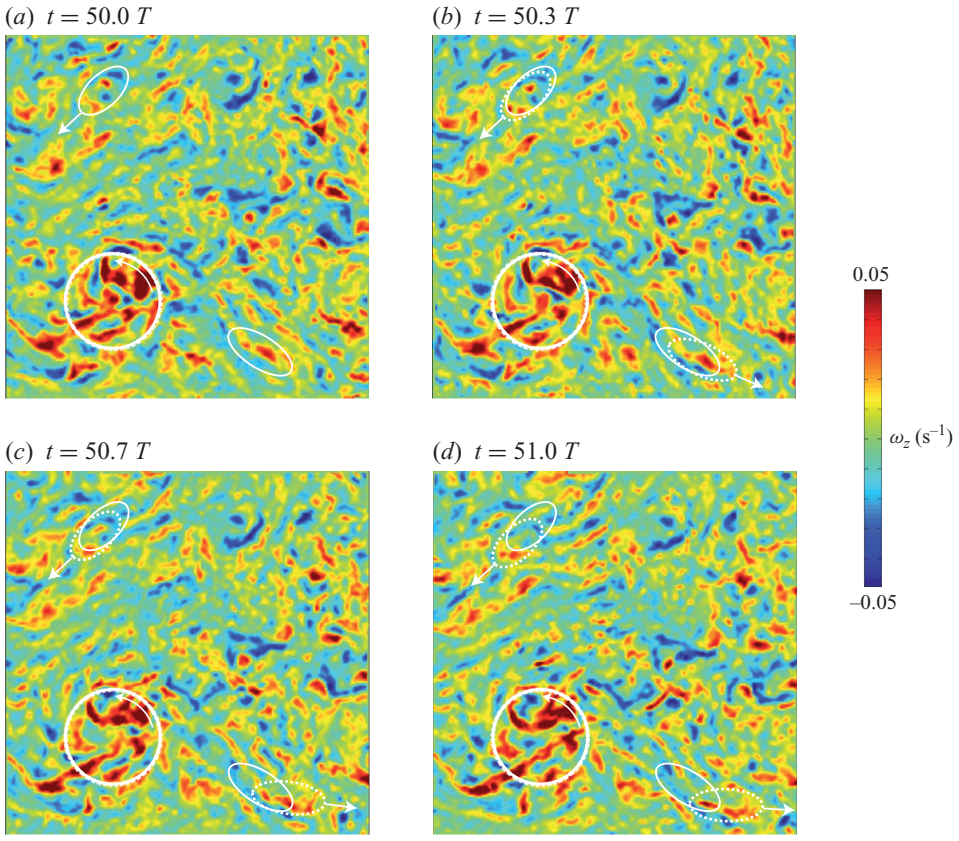


COL-
www+print

FIGURE 18. Sequence of four $\omega_z$-snapshots in the horizontal plane $(x, y)$ at large time, showing the advection of the small-scale symmetric vorticity by the large-scale horizontal motion ($\Omega = 0.10\,\mathrm{rad\,s^{-1}}$, $t \simeq 64M/V_g$). Each image is separated by 20 s $= T/3$, and the field of view is 1.3 m × 1.3 m. The two ellipses track some arbitrary vorticity pattern in time. The angular velocity of the cyclonic structure in the (*c*) (white circle) is $\Omega_c \simeq 0.009\,\mathrm{rad\,s^{-1}}$, corresponding to a local Rossby number of $\Omega_c/\Omega = 0.09$.

for $L_{33,1}$. This suggests that the vertical vorticity field is dominated, at large time, by the small-scale fluctuations induced by the instabilities of the vertical shear layers.

The role of the symmetric small-scale vorticity fluctuation in the decrease in $S_\omega$ must be addressed carefully, because the vorticity field computed from the PIV is affected by measurement noise. If we assume that the PIV noise can be simply described as an additive symmetric noise, it should imply a trivial reduction of $S_\omega$. This is a delicate issue, because the scale $L_\omega$ of these vorticity fluctuation is only slightly larger than the PIV resolution (§ 2.2). However, the temporal coherence of these small-scale fluctuations advected by the large scales is evident at the end of the supplementary movie 2, whereas PIV noise would generate vorticity patterns essentially uncorrelated in time. The temporal coherence of the fluctuations may also be inferred from the four snapshots shown in figure 18, where sets of arbitrary chosen vorticity patterns (marked in dashed ellipses) can be easily tracked in time, confirming that they are essentially advected by the large-scale motions.

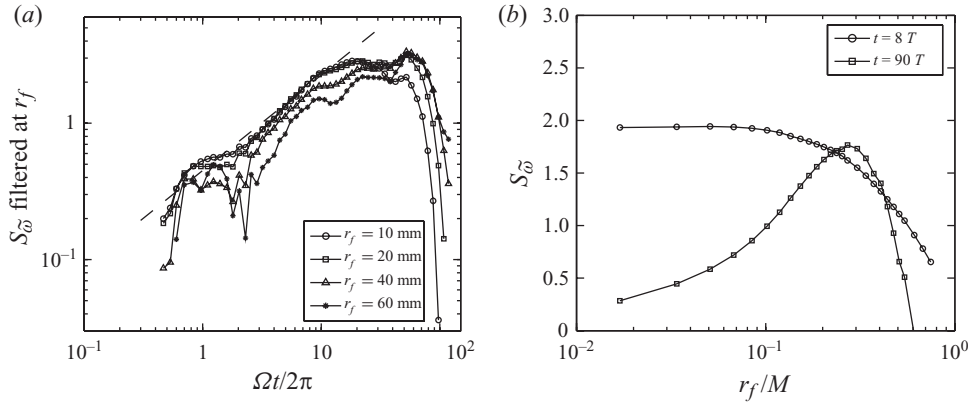


FIGURE 19. (*a*) Time evolution of the skewness of the filtered vorticity field, $S_{\tilde{\omega}}$, for different filter size, $r_f$, for $\Omega = 0.20\,\mathrm{rad\,s^{-1}}$. (*b*) Vorticity skewness as a function of the filter size, at times $t = 8T$ (before the peak of $S_\omega$) and $t = 90T$ (after the peak).

### 5.4. *Skewness of the filtered vorticity field*

In order to characterize more precisely the influence of the measurement noise on the vorticity statistics, we have computed $S_\omega$ from the filtered velocity $\tilde{\boldsymbol{u}}$ obtained by convolution of $\boldsymbol{u}$ with a Gaussian kernel of size $r_f$,

$$\tilde{\boldsymbol{u}}(x, y, t; r_f) = \iint \boldsymbol{u}(x', y', t) \frac{1}{2\pi r_f^2} \mathrm{e}^{-((x-x')^2+(y-y')^2)/2r_f^2}\, \mathrm{d}x'\, \mathrm{d}y'. \tag{5.4}$$

In practice, the integral is restricted to a square of size $6r_f$.

The time evolution of the skewness of the filtered vorticity, $S_{\tilde{\omega}}$, is shown in figure 19(*a*) for various filter sizes $r_f$, in the case $\Omega = 0.20\,\mathrm{rad\,s^{-1}}$. In the growth regime, increasing the filter size leads to a decrease in $S_\omega$, showing that the vorticity asymmetry is essentially contained at the smallest scales. In this situation, although the measured $S_\omega$ may underestimate the actual one because of the finite resolution of the PIV measurement, the vorticity skewness truly reflects the cyclone–anticyclone asymmetry at the smallest scales. On the other hand, after the peak of $S_\omega$, the ordering of the curves is reversed, so that filtering the vorticity field now increases the skewness, showing that now the asymmetry is carried by vortices at larger scales. This is consistent with figure 18, where a large cyclone containing small-scale vorticity fluctuations is shown (white circle). However, it must be noted that although the peak of $S_\omega$ is shifted to larger times, a decrease in $S_\omega$ is still observed. The effect of the filtering is further illustrated in figure 19(*b*), where $S_{\tilde{\omega}}$ monotonically decreases as $r_f$ is increased at $t = 8T$, whereas it shows a non-monotonic behaviour at $t = 90T$. Interestingly, in this latter case, the filter size for which $S_{\tilde{\omega}}$ is maximum at a given time provides a rough estimate of the size of the vortices responsible for the cyclone–anticyclone asymmetry.

One may conclude that, although $S_\omega$ provides a suitable description of the vorticity asymmetry during the growth regime, when the characteristic size of the vortices corresponds to the diffusive scale (the 'Kolmogorov scale' modified by the rotation), it is no longer appropriate as the vortex size grows at larger time, and in that case $S_\omega$ is strongly reduced by the small-scale symmetric vorticity fluctuations. This does not imply, however, that filtering at even larger scales would totally inhibit the decrease

of $S_\omega$, since dissipation (either bulk viscous dissipation or through Ekman pumping) may be also responsible for the reduction in $S_\omega$.

A more suitable statistical quantity, based for instance on the transverse velocity increments, should provide a better description of the cyclone–anticyclone asymmetry at large time. A vortex census approach, such as introduced in 2D turbulence (McWilliams 1990) would also help to decide which contribution dominates the decrease in $S_\omega$. This approach is, however, difficult with the present data, because at large time the average number of vortices per field of view is of the order or less than one.

## 6. Conclusion

The present experiment aims to focus on the transition at Rossby number $Ro \simeq O(1)$ which occurs in the course of the decay of grid turbulence, initially approximately homogeneous and isotropic, in a rotating frame. Emphasis is given on the energy decay, anisotropy growth and asymmetry between cyclonic and anticyclonic vorticity. The different steps of the decay can be summarized as follows.

(*a*) During the first 0.4 tank rotation (between 25 and 100 $M/V_g$), the instantaneous Rossby number, $Ro$, is larger than 0.25 and turbulence is essentially unaffected by the background rotation. Once the large-scale mean flow and inertial oscillations are subtracted, the turbulent energy decays similarly to the classical $t^{-6/5}$ law of isotropic unbounded turbulence.

(*b*) After 0.4 tank rotation, $Ro < 0.25$, and the first effects of the rotation are triggered. Provided the grid Rossby number is large enough, the energy decay in this regime is found to be compatible with the $\Omega^{3/5}t^{-3/5}$ law proposed by Squires *et al.* (1994). Both the large-scale isotropy factor $u'_z/u'_x$ and the small-scale ones $\omega'_y/\omega'_z$ and $\gamma'_z/\omega'_z$ depart from their isotropic value, although reaching only moderate value of about 0.5. On the other hand, the integral scales become strongly anisotropic, with a marked vertical correlation of the horizontal velocity. A cyclone–anticyclone asymmetry develops by preferential vortex stretching of the cyclonic vorticity, and is well described by a power-law growth of the vorticity skewness as $S_\omega \propto (\Omega t)^{0.7}$, consistent with the previous findings of Morize *et al.* (2005).

(*c*) Finally, a last regime is observed for $t > 2000M/V_g$ (corresponding to 10–30 tank rotations), in which the spanwise vorticity field is dominated by thin layers, which are prone to shear instabilities. These instabilities produce small-scale spanwise vorticity, resulting in an apparent return to isotropy for the ratio of the velocity or vorticity components. However, the flow structure remains strongly anisotropic, as revealed by the characteristic ordering of the integral scales. A remarkable consequence of the instability of these vertical shear layers is that it re-injects horizontal velocity disturbances, and hence vertical vorticity with random sign, at small scales.

The mechanism of re-injection of symmetric vorticity fluctuations in the last regime is found to contribute significantly to the reduction of the vorticity skewness, $S_\omega$, although the large-scale vortices still remain preferentially cyclonic. These results suggest that the 2D versus 3D nature of the initial conditions have a critical importance in the asymptotic state of decaying rotating turbulence. For initial isotropic turbulence, as is approximately produced in the wake of a grid, the initial vertical fluctuations, which represents 1/3 of the initial turbulent kinetic energy, is temporarily stored by the horizontal quasi-2D motions and plays no role in its dynamics, except at large time when it is released (and dissipated) directly at small scale via the shear instabilities of the vertical layers, resulting in a shortcut of the energy cascade. A rather different situation is expected for decaying rotating turbulence starting from

strictly 2D initial conditions, as in the experiments of Longhetto *et al.* (2002) and Praud *et al.* (2006), in which no vertical velocity is produced by the translation of a rake instead of a grid. In this situation, the vorticity skewness should reach even larger values, emphasizing the importance of the initial conditions in the nature of the decaying rotating turbulence.

We gratefully acknowledge H. Didelle, S. Viboud and A. Aubertin for experimental help, and C. Cambon, A. Davaille, F. Doumenc, S. Galtier for fruitful discussions. This work was supported by the ANR grant no. 06-BLAN-0363-01 'HiSpeedPIV'.

## REFERENCES

Bartello, P., Métais, O. & Lesieur, M. 1994 Coherent structures in rotating three-dimensional turbulence. *J. Fluid Mech.* **273**, 1–29.

Bewley, G. P, Lathrop, D. P., Maas, L. R. M & Sreenivasan, K. R. 2007 Inertial waves in rotating grid turbulence. *Phys. Fluids* **17**, 071701.

van Bokhoven, L. J. A., Cambon, C., Liechtenstein, L., Godeferd, F. S. & Clercx, H. J. H. 2008 Refined vorticity statistics of decaying rotating three-dimensional turbulence. *J. Turbul.* **9** (6), 1–24.

van Bokhoven, L. J. A., Clercx, H. J. H., van Heijst, G. J. F. & Trieling, R. R. 2009 Experiments on rapidly rotating turbulent flows. *Phys. Fluids* **22**, 096601. Q6

Bourouiba, L. & Bartello, P. 2007 The intermediate Rossby number range and two-dimensional–three-dimensional transfers in rotating decaying homogeneous turbulence. *J. Fluid Mech.* **587**, 139–161.

Cambon, C. 2001 Turbulence and vortex structures in rotating and stratified flows. *Eur. J. Mech. B*/Fluids **20**, 489–510.

Cambon, C. & Jacquin L. 1989 Spectral approach to non-isotropic turbulence subjected to rotation. *J. Fluid Mech.* **202**, 295–317.

Cambon, C., Mansour, N. N. & Godeferd, F. S. 1997 Energy transfer in rotating turbulence. *J. Fluid Mech.* **337**, 303–332.

Cambon, C. & Scott, J. F. 1999 Linear and nonlinear models of anisotropic turbulence. *Annu. Rev. Fluid Mech.* **31**, 1–53.

Carnevale, G. F., McWilliams, J. C., Pomeau, Y., Weiss, J. B. & Young, W. R. 1991 Evolution of vortex statistics in two-dimensional turbulence. *Phys. Rev. Lett.* **66** (21), 2735–2738.

Comte-Bellot, G. & Corrsin, S. 1966 The use of a contraction to improve the isotropy of grid-generated turbulence. *J. Fluid Mech.* **65**, 657–682.

Dalziel, S. B. 1992 Decay of rotating turbulence: some particle tracking experiments. *Appl. Sci. Res.* **49**, 217–244.

Davidson, P. A., Staplehurst, P. J. & Dalziel, S. B. 2006 On the evolution of eddies in a rapidly rotating system. *J. Fluid Mech.* **557**, 135–144.

Gence, J. N. & Frick, C. 2001 Naissance des corrélations triples de vorticité dans une turbulence statistiquement homogène soumise à une rotation. *C. R. Acad. Sci. Paris (Série IIb)* **329**, 351–356.

Godeferd, F. S. & Lollini, L. 1999 Direct numerical simulation of turbulence with confinement and rotation. *J. Fluid Mech.* **393**, 257–308.

Greenspan, H. 1968 *The Theory of Rotating Fluids.* Cambridge University Press.

Hopfinger, E. J., Browand, F. K. & Gagne, Y. 1982 Turbulence and waves in a rotating tank. *J. Fluid Mech.* **125**, 505–534.

Ibbetson, A. & Tritton, D. 1975 Experiments on turbulence in a rotating fluid. *J. Fluid Mech.* **68**, 639–672.

Jacquin, L., Leuchter, O., Cambon, C. & Mathieu, J. 1990 Homogeneous turbulence in the presence of rotation. *J. Fluid Mech.* **220**, 1–52.

Jimenez, J. 1994 Resolution requirements for velocity gradients in turbulence. *Annu. Res. Briefs Center Turbul. Res.* 357–364. Q7

Khaledi, H. A., Barri, M. & Andersson, H. I. 2009 On the stabilizing effect of the Coriolis force on the turbulent wake of a normal flat plate. *Phys. Fluids* **21**, 095104.

Kloosterziel, C. & van Heijst, J. F. 1991 An experimental study of unstable barotropic vortices in a rotating fluid. *J. Fluid Mech.* **223**, 1–24.

Lavoie, P., Avallone, G., De Gregorio, F., Romano, G. P. & Antonia, R. A. 2007 Spatial resolution of PIV for the measurement of turbulence. *Exp. Fluids* **43**, 39–51.

Longhetto, A., Montabone, L. Provenzale, A. & Didelle, H. & Giraud, C. 2002 Coherent vortices in rotating flows: a laboratory view. *Il Nuovo Cimento* **25**, 233–249.

Maas, L. R. M. 2003 On the amphidromic structure of inertial waves in a rectangular parallelepiped. *Fluid Dyn. Res.* **33**, 373–401.

McWilliams, J. C. 1984 The emergence of isolated coherent vortices in turbulent flow. *J. Fluid Mech.* **146**, 21–43.

McWilliams, J. C. 1990 The vortices of two-dimensional turbulence. *J. Fluid Mech.* **219**, 361–385.

Mohamed, M. S. & LaRue, J. 1990 The decay power law in grid-generated turbulence. *J. Fluid Mech.* **219**, 195–214.

Moisy, F., Rabaud, M. & Salsac, K. 2009 A Synthetic Schlieren method for the measurement of the topography of a liquid interface. *Exp. Fluids* **46** (6), 1021–1036.

Morinishi, Y., Nakabayashi, K. & Ren, S. Q. 2001 Dynamics of anisotropy on decaying homogeneous turbulence subjected to system rotation. *Phys. Fluids* **13** (10), 2912–2922.

Morize, C. & Moisy, F. 2006 On the energy decay of rotating turbulence in confined geometry. *Phys. Fluids* **18**, 065107.

Morize, C., Moisy, F. & Rabaud, M. 2005 Decaying grid-generated turbulence in a rotating tank. *Phys. Fluids* **17** (9), 095105.

Morize, C., Moisy, F., Rabaud M. & Sommeria, J. 2006 On the cyclone–anticyclone asymmetry in decaying rotating turbulence. In *Conference on Turbulence and Interactions TI2006, May 29–June 2, 2006*, Porquerolles, France.

Phillips, O. M. 1963 Energy transfer in rotating fluids by reflection of inertial waves. *Phys. Fluids* **6** (4), 513–520.

Poulin, F. J., Flierl, G. R. & Pedlosky, J. 2003 Parametric instability in oscillatory shear flows. *J. Fluid Mech.* **481**, 329–353.

Praud, O., Fincham, A. & Sommeria, J. 2005 Decaying grid turbulence in a strongly stratified fluid. *J. Fluid Mech.* **522**, 1–33.

Praud, O., Sommeria, J. & Fincham, A. 2006 Decaying grid turbulence in a rotating stratified fluid. *J. Fluid Mech.* **547**, 389–412.

Raffel, M., Willert, C., Wereley, S., & Kompenhans, J. 2007 *Particle Image Velocimetry*. Springer.

Saffman, P. G. 1967 Note on decay of homogeneous turbulence. *Phys. Fluids* **10**, 1349.

Smith, L. M. & Lee, Y. 2005 On near resonances and symmetry breaking in forced rotating flows at moderate Rossby number. *J. Fluid Mech.* **535**, 111–142.

Smith, L. M. & Waleffe, F. 1999 Transfer of energy to two-dimensional large scales in forced, rotating three-dimensional turbulence. *Phys. Fluids* **11** (6), 1608–1622.

Squires, K. D., Chasnov, J. R., Mansour, N. N. & Cambon, C. 1994 The asymptotic state of rotating homogeneous turbulence at high Reynolds number. In *74th Fluid Dynamics Symposium on Application of Direct and Large Eddy Simulation to Transition and Turbulence*, Chania, Greece.

Sreenivasan, K. R. & Antonia, R. A. 1997 The phenomenology of small-scale turbulence. *Annu. Rev. Fluid Mech.* **29**, 435–472.

Sreenivasan, B. & Davidson, P. A. 2008 On the formation of cyclones and anticyclones in a rotating fluid. *Phys. Fluids* **20**, 085104.

Staplehurst, P. J., Davidson, P. A. & Dalziel, S. B. 2008 Structure formation in homogeneous freely decaying rotating turbulence. *J. Fluid Mech.* **598**, 81–105.

Tavoularis, S. & Karnik, U. 1989 Further experiments on the evolution of turbulent stresses and scales in uniformly sheared turbulence. *J. Fluid Mech.* **204**, 457–478.

Waleffe, F. 1993 Inertial transfers in the helical decomposition. *Phys. Fluids* A **5** (3), 677–685.

Yoshimatsu, Y., Midorikawa, M. & Kaneda, Y. 2010 Columnar eddy formation in freely-decaying homogeneous rotating turbulence. *J. Fluid Mech.* (submitted). **Q8**

# Chapitre 4

# Ondes de surface

## 4.1 Introduction

Le dernier chapitre de ce mémoire, relatif aux ondes de surface, est en fait constitué de 2 contributions originales : la première, de nature instrumentale, présente une nouvelle technique optique de mesure d'interface extrêmement sensible, nommée "Free-Surface Synthetic Schlieren" (FS-SS), et développée avec Marc Rabaud depuis 2007. La seconde concerne l'étude d'une instabilité sous-harmonique apparaissant dans un système d'ondes capillaires excitées localement, menée avec Marc Rabaud et Guy-Jean Michon depuis 2008.

Parmi les méthodes destinées à la mesure des ondes de surface, les méthodes optiques sont de loin les plus intéressantes : non intrusives, elles sont potentiellement de résolution spatiale et temporelle largement supérieures aux échelles caractéristiques considérées. Le point de départ de cet axe de recherche se trouve en fait dans le chapitre précédent, au sujet des mesures par PIV effectuées à travers la surface libre dans les expériences menées sur la plateforme Coriolis. En effet, dans cette expérience, la présence d'ondes de surface induites par le passage de la grille se trouve contribuer significativement au bruit de mesure : au déplacement "réel" des particules advectées à la vitesse $\mathbf{U}$ du fluide, $\delta\mathbf{x} = \mathbf{U}\delta t$, s'ajoute un déplacement "apparent" lié à la réfraction des rayons lumineux allant de la particule à la caméra à travers la surface libre, de l'ordre de $\delta\mathbf{x}' = (1 - 1/n)(h/2)\nabla h$, où $n$ est l'indice optique de l'eau, $h/2$ la distance entre le plan des particules éclairées par la nappe laser et la surface, et $\nabla h$ la pente locale de l'interface au point d'incidence. En remplaçant les particules de PIV par un motif fixe de "particules synthétiques" imprimées, il est ainsi possible de mesurer $\delta\mathbf{x}'$ seul, et l'on peut remonter à la pente $\nabla h$ puis, par intégration, à la hauteur locale $h(x, y)$.

Dans la suite de ce chapitre, nous présenterons le principe de la méthode FS-SS, en s'attachant à décrire son domaine d'application comparé à quelques autres techniques "concurrentes". Les détails de la méthode sont donnés dans l'article Moisy *et al.* (2009) [99], reproduit à la suite de ce chapitre. Dans une deuxième partie, nous introduirons une expérience originale de génération d'ondes capillaires paramétriques de type Faraday, excitées par un forçage local. Enfin, nous proposerons un certain nombre de perspectives concernant les améliorations possibles de la méthode de mesure, pouvant ouvrir vers d'autres applications, comme l'étude de la turbulence d'ondes gravito-capillaires.

## 4.2 Technique de Free-Surface Synthetic Schlieren

### 4.2.1 Quelques précurseurs

L'idée d'utiliser la réflexion ou la refraction pour mesurer la pente locale d'une interface fluide remonte aux travaux de Cox (1958) [38], dans le contexte de l'utilisation des scintillements dûs à la reflection du soleil à la surface de la mer, afin de détecter le passage de navires depuis le ciel. Dans cet exemple, la source de lumière peut être considérée comme collimatée (soleil à l'infini), ce qui conduit à un résultat particulièrement simple : les points scintillants sont les points I à la surface de l'eau tels que la pente locale satisfait la condition de réflexion soleil $\rightarrow$ I $\rightarrow$ oeil, sans influence de la hauteur locale.

L'utilisation de la réfraction en lumière diffuse, et non collimatée, simplifie considérablement la mise en œuvre pratique de la configuration optique, au détriment de la formulation géométrique du problème. La réfraction de lumière diffuse correspond à la situation usuelle dans laquelle on observe un objet à travers un milieu présentant des variations d'indice optique. Cette situation s'apparente alors à la technique de la strioscopie, ou "Schlieren" (de l'allemand "déformer"), très utilisée en aérodynamique pour les écoulements supersoniques.

La version numérique du Schlieren, avec utilisation d'un algorithme d'intercorrélation pour la mesure du déplacement des points, a été proposée en 1999 par Sutherland *et al.* [125], sous le nom de "Synthetic Schlieren" (SS), puis en 2002 par Meier [85], sous le nom de "Background-Oriented Schlieren" (BOS). Dix ans plus tard, ces deux noms sont largement employés, le premier l'étant plutôt dans la communauté des fluides stratifiés (les variations de densité, et donc d'indice, étant liées aux variations de concentration, le plus souvent la salinité), et le second dans la communauté des fluides compressibles (les variations de densité étant alors liées aux effets de compressibilité).

Qu'il s'agisse d'effets de stratification ou de compressibilité, les méthodes SS ou BOS conduisent à une mesure essentiellement qualitative : les déplacements apparents induits par les gradients d'indice sont le résultat des déplacements élémentaires accumulés le long du chemin optique traversant le milieu considéré. Ainsi, sauf dans le cas de géométries très simplifiées, il n'est pas possible de remonter au champ 3D d'indice optique, et donc de densité, ayant donné lieu au déplacement 2D observé.

Dans le cas où le milieu traversé présente un saut d'indice optique séparant deux régions d'indice constant, il est possible, moyennant certaines approximations, de pousser la méthode un pas au-delà, et de relier le déplacement apparent à la hauteur locale de l'interface, offrant ainsi une méthode quantitative de mesure. C'est Kurata (1990) [72] qui, le premier, propose cette approche, sans disposer alors de méthode d'intercorrélation pouvant automatiser la mesure du déplacement. Dalziel *et al.* (2000) [39] note que la méthode de Synthetic Schlieren peut être utilisée pour une mesure quantitative de la surface, et une première mise en œuvre expérimentale est présentée dans la thèse de Elwell (2004) [53]. Notre contribution à cette méthode a été de proposer une formulation bi-dimensionnelle complète du problème, et de démontrer sous quelles conditions la linéarité entre déplacement apparent et gradient de hauteur pouvait être obtenue.

### 4.2.2 Principe de la méthode

Le principe général de la méthode consiste à reconstruire la hauteur de l'interface $h(x, y)$ étant donné un couple d'images $(I_0, I_1)$, où $I_0(x, y)$ est l'image d'un objet de référence obtenue lorsque l'interface est plane ($h = cste$), et $I_1(x, y)$ l'image de ce même objet vu à travers

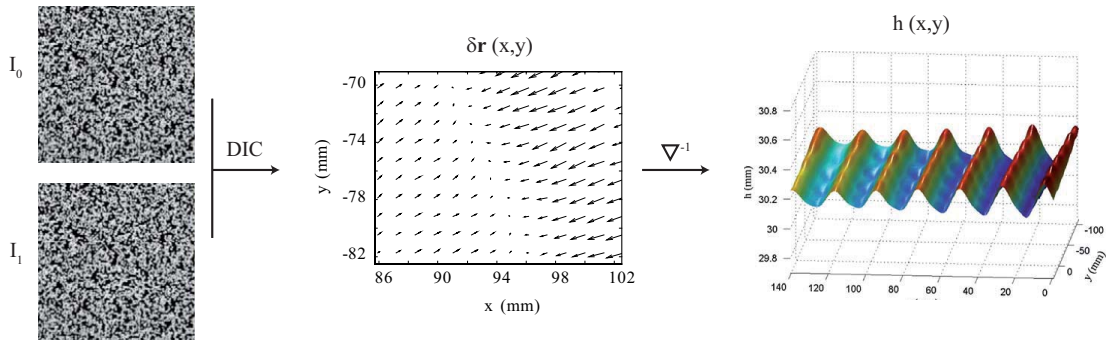


FIG. 4.1 – Principe de la méthode Free-Surface Synthetic Schlieren : L'image de référence $I_0$ est obtenue à travers l'interface plane, et l'image $I_1$ à travers l'interface déformée à un instant donné. Le champ de déplacement apparent $\delta\mathbf{r}(x, y)$ est obtenu par un algorithme de DIC (Digital Image Correlation) à partir du couple $(I_0, I_1)$. Enfin, le champ de déformation $h(x, y)$ est obtenu par intégration numérique du champ de déplacement.

l'interface déformée $h(x, y)$ :

$$(I_0, I_1) \rightarrow h(x, y).$$

En pratique l'objet de référence est un motif plan situé sur le plan focal objet lorsque l'interface est plane. Une telle reconstruction n'est possible que si l'application $F_h : I_0 \rightarrow I_1$ est bijective, donc inversible, ce qui revient à supposer qu'il n'existe pas de croisement de rayons lumineux, i.e. de "caustiques".

Même en l'absence de caustiques, ce problème reste particulièrement délicat dans le cas général. Une première simplification est obtenue en supposant qu'il existe un champ de déplacement $\delta\mathbf{r}(x, y)$ permettant de passer de $I_0$ à $I_1$. La méthode FS-SS telle que nous l'avons développée se décompose ainsi en deux étapes distinctes, résumées en figure 4.1 : la détermination du déplacement $\delta\mathbf{r}$ à partir du couple d'images $(I_0, I_1)$, puis la reconstruction de la hauteur $h(x, y)$ à partir de $\delta\mathbf{r}$ :

$$(I_0, I_1) \rightarrow \delta\mathbf{r}(x, y) \rightarrow h(x, y).$$

Une solution générale de la première étape du calcul, $(I_0, I_1) \rightarrow \delta\mathbf{r}$, peut s'obtenir en supposant que le déplacement $\delta\mathbf{r}$ est infinitésimal, et est donc solution de l'équation de continuité exprimée pour le champ d'intensité lumineuse,

$$\delta I + \nabla(\delta\mathbf{r}\, I) = 0,$$

avec $\delta I = I_1 - I_0$. Cette hypothèse est à la base de l'approche dite de *flot optique* [4].

La seconde étape, $\delta\mathbf{r} \rightarrow h(x, y)$, nécessite une modélisation géométrique du tracé des rayons lumineux entre les différents points de l'objet, l'interface et le capteur de la caméra. Là encore, des hypothèses simplificatrices sont nécessaires, et notre contribution se limite au cas le plus simple, lorsque 3 approximations sont simultanément satisfaites. Ces 3 approximations permettent une linéarisation du problème vis-à-vis de 3 petits paramètres :

1. Angle de paralaxe $\beta$ négligeable, obtenu lorsque la caméra est située à l'infini ;
2. Faible pente de l'interface $(\delta h/\lambda \ll 1)$ ;
3. Amplitude de déformation petite comparée à la distance surface - objet $(\delta h/h_p \ll 1)$.

A noter que l'hypothèse d'inversibilité (absence de caustiques), utilisée dans la première étape $(I_0, I_1) \rightarrow \delta\mathbf{r}$, implique en fait que $\delta h/h_p \ll (\delta h/\lambda)^2$, ce qui fait que la 3ème approximation est nécessairement satisfaite dès lors que la 2ème l'est.

Lorsque ces 3 approximations sont satisfaites, nous avons montré qu'il existait une relation linéaire entre le gradient local $\nabla h$ et le déplacement apparent $\delta\mathbf{r}$,

$$\nabla h = -\left(\frac{1}{\alpha h_p} - \frac{1}{H}\right)\delta\mathbf{r}, \tag{4.1}$$

où $H$ est la distance surface-caméra, et $\alpha = 1 - 1/n$. La reconstruction du champ de hauteur $h(x, y)$ s'obtient alors par inversion de l'équation (4.1), soit formellement

$$h = -\left(\frac{1}{\alpha h_p} - \frac{1}{H}\right)\nabla^{-1}\delta\mathbf{r}. \tag{4.2}$$

### 4.2.3 Mise en œuvre pratique et résolution

D'un point de vue pratique, le champ de déplacement $\delta\mathbf{r}$ est obtenu par un algorithme de DIC, *Digital Image Correlation*, appliqué aux images $I_0$ et $I_1$. Dans cette approche, un vecteur déplacement est obtenu pour chaque fenêtre d'interrogation, de taille typique $16\times16$ pixels. Un tel algorithme est utilisé classiquement en PIV, où le champ de vitesse recherché est simplement donné par $\mathbf{v} = \delta\mathbf{r}/\delta t$, avec $\delta t$ est le temps entre les 2 images. La construction optimale de l'objet, en pratique un motif de points aléatoires imprimés, est rendue possible grâce aux tests reportés dans l'abondante littérature sur les algorithmes de PIV [1, 114]. Empiriquement, le motif de point et le calcul DIC doivent satisfaire les 3 "règles d'or" :

1. Taille caractéristique des petites structures du motif ("particules") $\simeq 2-3$ pixels,
2. Au moins 5 "particules" par fenêtre d'interrogation,
3. Déplacement apparent typique de l'ordre du tiers de la fenêtre d'interrogation.

La mise en œuvre de la seconde étape, $\delta\mathbf{r} \rightarrow h(x, y)$, repose sur l'inversion numérique du gradient discrétisé sur la grille de mesure. En notant $M\times N$ la dimension de cette grille, l'équation (4.2) fournit $2MN$ équations (les valeurs des 2 composantes du champ de déplacement mesuré) pour $MN$ inconnues (la hauteur en chaque point) : le système est dit *sur-déterminé*. L'inversion de ce système peut donc être réalisée au sens des moindres carrés, en recherchant le champ $h(x, y)$ minimisant le résidu $|\nabla h - \xi|^2$, où $\xi = -(1/h_p - 1/H)\delta\mathbf{r}$. Une telle approche présente l'avantage d'être très efficace numériquement, et très robuste à la présence de vecteurs erronés.

Au final, une reconstruction du champ de hauteur avec une précision de l'ordre de 1 % de l'amplitude des déformations est obtenue par cette méthode. En pratique, pour des champs de l'ordre de quelques cm à quelques dizaines de cm, une résolution verticale de l'ordre de 1 à 10 $\mu$m, pour des amplitudes typiques de l'ordre de 0.1 à 1 mm, est obtenue. Bien qu'une étude systématique n'ait pas été réalisée concernant le degré de sensibilité vis-à-vis des 3 petits paramètres du problème, en pratique nous avons constaté que cette résolution de l'ordre de 1 % restait valide lorsque les 3 paramètres étaient de l'ordre de 10 %.

### 4.2.4 Quelques applications

La méthode FS-SS n'est pas adaptée à toutes les situations : elle nécessite un accès optique par réfraction, et est limitée à la mesure de déformations de pente et d'amplitude assez

faibles. Cependant, lorsqu'elle est applicable, cette méthode est probablement celle présentant la meilleure résolution spatiale comparée aux méthodes concurrentes. De plus, il n'existe aucune limitation intrinsèque de la résolution temporelle : la dynamique des ondes capillaires à haute fréquence peut ainsi être résolue, avec la démocratisation des caméras rapides (des caméras CMOS à 5 kHz, de résolution $1024^2$ pixels, sont maintenant disponibles en laboratoire).

En revanche, lorsque les pentes ou amplitudes relatives deviennent plus prononcées, typiquement au-delà de 20%, des méthodes alternatives sont préférables, comme la méthode de profilométrie par transformée de Fourier, récemment décrite par Cobelli *et al.* (2009) [32], qui fonctionne par réflexion et non par réfraction.

Nous avons exploré quelques applications potentielles de cette méthode. Nous en décrirons brièvement deux ci-après : le problème de l'étalement d'une goutte d'huile sur un substrat, et le sillage de Kelvin d'un obstacle translaté à la surface de l'eau. L'application au problème de l'impact d'une goutte d'eau dans un bain d'eau est présentée dans l'article Moisy *et al.* (2009) [99]. La section suivante décrit plus en détail la mise en oeuvre de cette technique pour l'étude des ondes de Faraday, au travers de deux expériences originales : la dynamique d'une goutte "marchant" à la surface d'un bain liquide oscillé verticalement [51], et une expérience d'ondes capillaires excitées par un forçage paramétrique local, qui fait actuellement l'objet d'une étude plus approfondie [94].

Une routine disponible sous Matlab a été mise au point pour la reconstruction de la surface libre, et intégrée à la toolbox "PIVMat" [1] (librement distribuée sous licence BSD). En dehors des applications décrites ci-après, nous sommes en contact avec un certain nombre d'équipes utilisant aujourd'hui la méthode FS-SS :

- Structuration induite par séchage de films de polymère (groupe de J. Krenn, Université de Karlsruhe) [71],
- Déformation de microcanaux (groupe de C. Baroud, LadHyx, Ecole Polytechnique) [41],
- Ressaut hydraulique et interaction ondes-écoulement (groupe de G. Rousseaux, Laboratoire J.A. Dieudoné, Université de Nice Sophia Antipolis).

### Etalement d'une goutte d'huile

Le problème de l'étalement d'une goutte sur un substrat est un problème classique de mécanique des fluides, aux nombreuses applications pratiques [12]. La dynamique de l'étalement résulte d'une compétition entre l'effet de la gravité, qui tend à accélérer l'étalement, et l'effet joint de la viscosité et de la tension de surface, qui tendent à le freiner.

Nous avons réalisé quelques expériences préliminaires d'étalement d'une goutte basée sur la méthode FS-SS [98]. La figure 4.2 montre une image reconstruite de la surface de la goutte lors de l'étalement. Cette géométrie est *a priori* délicate, car l'hypothède de faible variation de l'amplitude ne peut être satisfaite au niveau de la ligne de contact, pour laquelle l'amplitude passe d'une valeur nulle à une valeur finie. L'astuce expérimentale consiste ici à intercaller, entre la goutte et le motif de points, une plaque de plexiglass épaisse, d'indice optique proche de celui de la goutte, de sorte que les variations d'amplitude totale restent faibles (figure 4.2a). En revanche, l'hypothèse de faible pente rend impossible la reconstruction de la goutte à temps court. Les mesures de l'évolution du rayon de la goutte à temps long (figure 4.2c) sont en excellent accord avec les prédictions théoriques [12].

[1] Téléchargeable à l'adresse `http://www.fast.u-psud.fr/pivmat`. Un tutorial pour la mise en œuvre d'un système de FS-SS est disponible à l'adresse `http://www.fast.u-psud.fr/~moisy/sgbos/tutorial.php`.

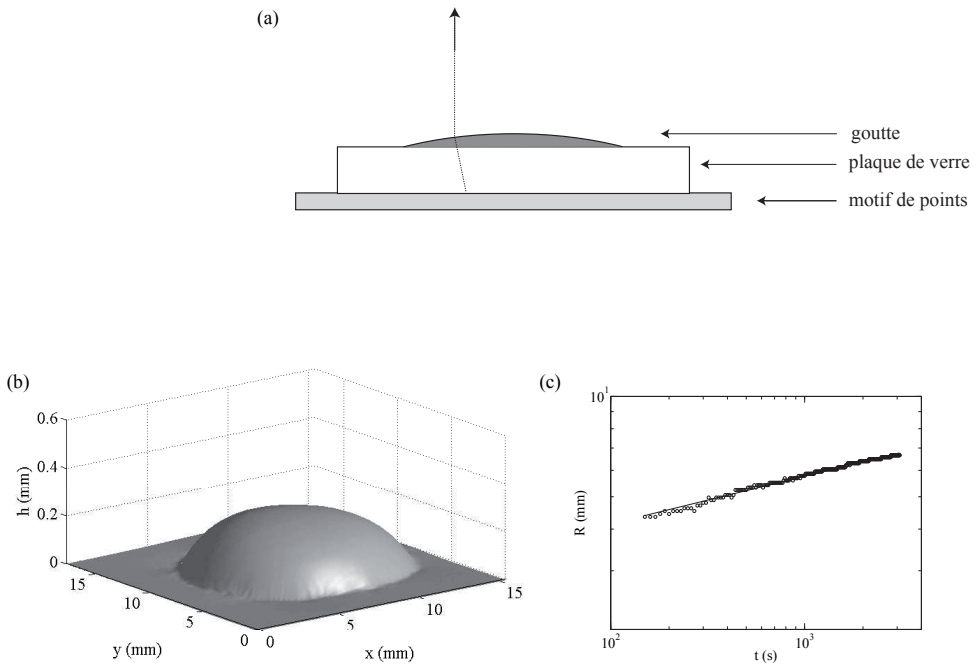


FIG. 4.2 – (a) Montage optique pour la mesure de la topographie d'une goutte en étalement. La plaque de verre est destinée à satisfaire la condition de faible variation de hauteur motif de point – surface. Le rayon lumineux représenté suppose l'égalité des indices optiques verre - goutte, et une caméra à l'infini. (b) Exemple de mesure de surface de goutte par FS-SS, obtenu 800 s après le dépôt de la goutte (échelle verticale dilatée). (c) Evolution temporelle du rayon de la goutte, et ajustement avec $t^{0.14}$.

### Sillage de Kelvin

Au-delà d'une certaine vitesse, la translation d'un obstacle à la surface d'un liquide génère un sillage en aval de celui-ci : il s'agit du sillage de Kelvin [75]. L'existence d'une vitesse seuil, de l'ordre de 23 cm/s dans le cas de l'interface eau-air, est une conséquence de la variation non monotone de la vitesse de phase des ondes gravito-capillaires, qui présente un minimum lorsque la longueur d'onde est égale à la longueur capillaire $\ell_c = (\gamma/\rho g)^{1/2}$. Si la vitesse de translation est suffisamment grande, un angle de sillage constant est sélectionné, dont la valeur dépend du rapport entre vitesse de phase et vitesse de groupe, et valant classiquement 39° dans le cas des ondes de gravité.

L'apparition de ce sillage s'accompagne d'une force de traînée venant s'ajouter à la traînée visqueuse ou inertielle classique, et dont le travail correspond à l'énergie rayonnée dans le sillage. Un certain nombre de problèmes ouverts concernent cette traînée de vague à la transition : discontinuité ou non de la force de traînée, existence d'une "pré-transition", rôle de la viscosité, etc. [15, 17]. Une mesure non intrusive de cette force de traînée, s'affranchissant des autres contributions, permettrait d'aborder expérimentalement ces questions sous un angle nouveau. Une telle mesure pourrait être réalisée indirectement, grâce à un bilan de quantité de mouvement et d'énergie réalisé à partir du champ d'amplitude mesuré.

Des résultats préliminaires prometteurs ont été obtenus dans cette direction, grâce à la mise en place d'un montage expérimental original permettant d'accéder au sillage au voisinage de l'obstacle (fig. 4.3a). Dans cette expérience, un obstacle de petite taille est translaté à vitesse

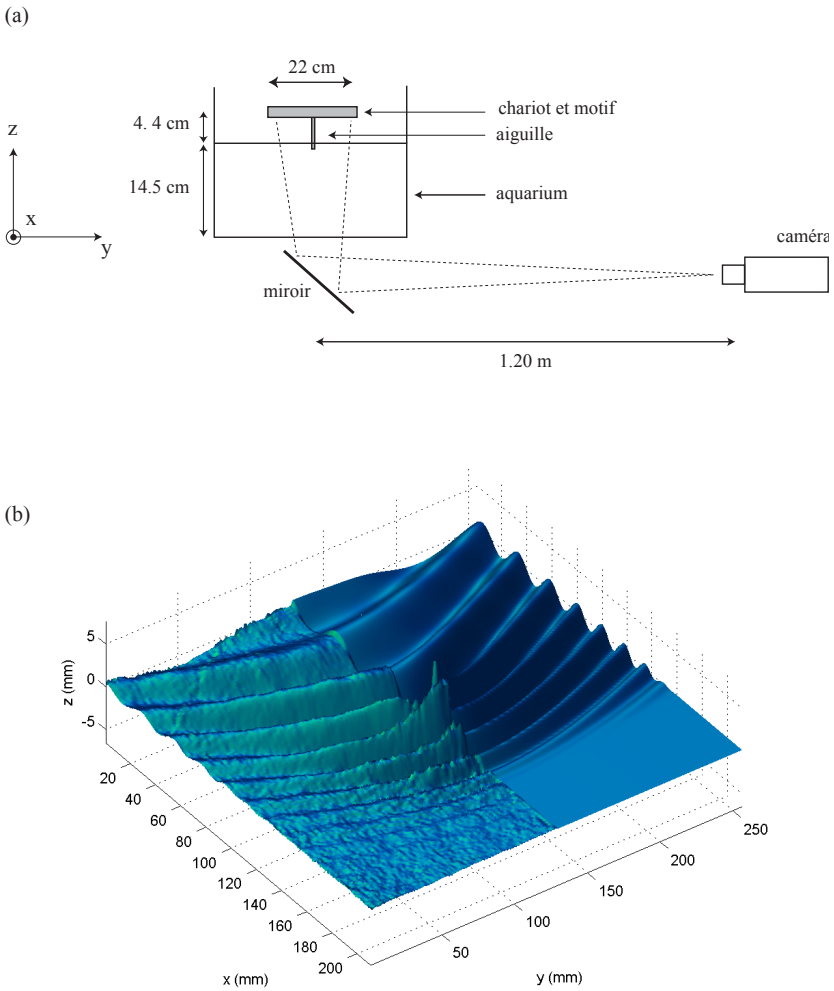


FIG. 4.3 – (a) Vue en coupe du dispositif expérimental destiné à mesurer le sillage en aval d'un obstacle. Une aiguille de diamètre 1 mm, solidaire d'un support du motif de points, est translaté à vitesse constante selon $x$ le long dun canal. L'image dans le plan $(x, y)$ est prise par une caméra située sous le canal. (b) Comparaison entre simulation numérique (à droite) et mesure par FS-SS (à gauche) du sillage (vitesse 24 cm $s^{-1}$).

constante, proche de la valeur critique de 23 cm/s, le long d'un canal de 2 m de long. Le passage de l'obstacle dans le champ de vision de la caméra située sous le canal (dont le fond est transparent) déclenche l'acquisition de l'image. Le sillage reconstruit est en très bon accord avec la forme de sillage prédite par une simulation numérique, dans laquelle la perturbation est modélisée par une déformation gaussienne de l'interface (fig. 4.3b). Des expériences similaires, basées sur le sillage d'un objet translaté complètement immergé, sont actuellement à l'étude dans le groupe de C. Clanet (LadHyx, Ecole Polytechnique).

## 4.3 Expériences de Faraday

### 4.3.1 Instabilité paramétrique

Lorsqu'une surface libre est excitée périodiquement, sa réponse peut être sous-harmonique : l'énergie injectée par l'excitation vient amplifier une oscillation à une fréquence moitié moindre [87]. Un tel mécanisme est qualifié de *paramétrique*, par analogie avec le pendule paramétrique pour lequel un des paramètres, par exemple la longueur $l$ ou la gravité $g$, et donc la fréquence propre $\sqrt{g/l}$, varie avec le temps. Ainsi, si l'on considère une surface libre comme un ensemble d'oscillateurs, présentant un continuum de pulsations propres potentiellement excitables, alors une pulsation propre donnée, $\omega$, sera sélectionnée et entrera en résonnance si elle est excitée par un forçage de pulsation $2\omega$ [9]. L'équation d'évolution de l'amplitude associée à cet oscillateur de pulsation $\omega$ est une équation de Mathieu, qui décrit classiquement la dynamique d'un pendule excité périodiquement. En pratique, la dissipation visqueuse viendra s'opposer à un tel mécanisme d'amplification paramétrique, et l'instabilité ne pourra se développer qu'au-delà d'un certain seuil d'excitation [26].

Une telle instabilité sous-harmonique d'une surface libre est classiquement observée dans l'expérience dite "de Faraday" (1831) [56] : un bain liquide est oscillé verticalement, et est donc soumis à une gravité apparente périodique dans le référentiel de l'oscillation. Dans cette situation, l'homogénéité spatiale du forçage fait que, si un vecteur d'ondes $\mathbf{k}$ donné est excité par un tel mécanisme paramétrique, alors le vecteur d'onde opposé $-\mathbf{k}$ le sera également : il en résulte donc de façon générique un motif d'ondes sous-harmoniques nécessairement stationnaires. Il n'en ira pas de même au § 4.3.3, dans lequel le forçage sera inhomogène, conduisant de façon plus générale à l'existence d'ondes sous-harmoniques propagatives cette fois-ci.

L'instabilité de Faraday homogène a été étudiée de façon approfondie ces dernières années [30, 48, 46, 52]. Une des motivations de ces études était la transition vers le chaos spatio-temporel dans ce système loin du seuil de l'instabilité, et l'apparitions de phénomènes non-linéaires remarquables, comme la propagation de solitons. Dans la suite, nous décrirons deux systèmes physiques voisins : l'expérience du "marcheur", étudiée dans le cadre d'une collaboration avec l'équipe d'Y. Couder (MSC, Université Paris-Diderot), et l'expérience d'ondes transverses excitées localement, étudiée avec M. Rabaud (FAST).

### 4.3.2 L'expérience du "marcheur"

Considérons une expérience "de Faraday" classique, consistant en un bain liquide soumis à une oscillation verticale, d'accélération légèrement inférieure à l'accélération critique de Faraday (fig. 4.4a). Alors, sous certaines conditions, une goutte du même liquide déposée sur le bain va se mettre à rebondir sans coalescer, grâce au film d'air sans cesse renouvelé situé entre la goutte et le bain. Si la période du rebond est double de celle du forçage, comme

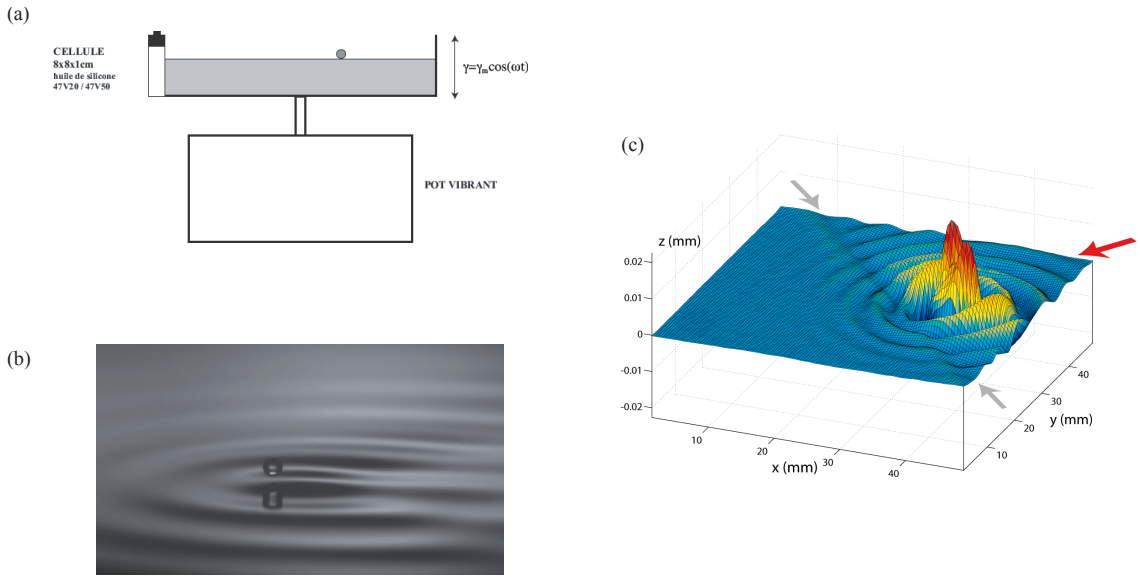


FIG. 4.4 – Expérience du "marcheur" (Couder *et al.* (2005) [37]). (a) Dispositif expérimental : sur un bain d'huile oscillé verticalement, une goutte d'huile de taille millimétrique est déposée. (b) Vue en perspective d'un marcheur. (c) Exemple de champ d'onde reconstruit par la méthode FS-SS, illustrant l'atténuation de l'onde du "marcheur" lorsque celui-ci passe d'une zone profonde (à droite) vers une zone de moindre profondeur à gauche. D'après Eddi *et al.* (2009) [51].

dans l'expérience classique de cascade par dédoublements de période d'une bille sur un plateau oscillant [112], alors la goutte va exciter localement des ondes de Faraday évanescentes (fig. 4.4b). L'interaction entre la goutte et les ondes ainsi émises peut alors conduire à une brisure de symétrie, et à l'apparition d'une impulsion dans une direction arbitraire : la goutte se met spontanément à "marcher" à vitesse constante à la surface du bain liquide.

Un tel "marcheur" constitue ainsi un objet physique original, introduit par Couder *et al.* (2005) [37], résultat de l'association d'une goutte rebondissant sur un bain liquide oscillé verticalement et du champ d'onde généré par celle-ci. Le double aspect "onde" et "particule" de cet objet composite lui confère un certain nombre de propriétés remarquables, reproduisant à l'échelle macroscopique certains comportements des systèmes quantiques : motifs d'interférences lors du passage par des fentes d'Young, ou encore franchissement stochastique d'une barrière de potentiel par effet tunnel.

Dans l'expérience d'effet tunnel, qui a fait l'objet de l'article Eddi *et al.* (2009) [51], un "marcheur" est confiné dans une région de l'espace délimité par une "barrière de potentiel", modélisée ici par une variation locale de la profondeur du bain liquide. La figure 4.4(c) montre l'onde evanescente générée par un tel marcheur située en bordure de la barrière. Dans ces expérience, les mesures par FS-SS ont permis de reconstruire le champ d'onde entourant la goutte en disposant le motif de points aléatoires au fond de la cuve oscillée, et en déclanchant l'acquisition sur la phase de l'oscillation du bain liquide. Les pentes trop élevées n'ont pas permis de réaliser de mesure du champ de déplacement apparent au voisinage immédiat de la goutte. Cependant, la zone non mesurée est ici de taille suffisament faible pour que la reconstruction soit fiable jusqu'à une distance à la goutte de l'ordre d'une fraction de longueur d'onde de Faraday, ce qui s'est avéré suffisant pour analyser le champ d'onde lointain.

Ces mesures ont permis de mettre en évidence que, bien que le marcheur ne puisse exister

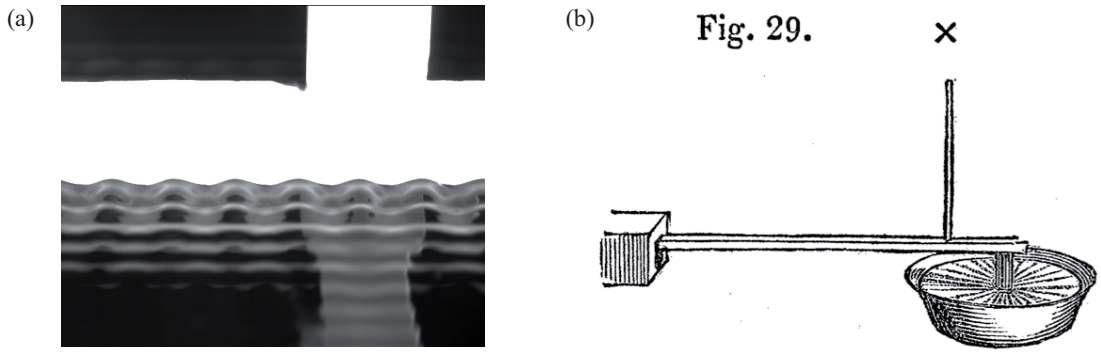


FIG. 4.5 – (a) Ondes capillaires générées par l'oscillation verticale d'une plaque partiellement immergée. On distingue une onde longitudinale, dont les crêtes sont parallèles à la plaque et se propageant à fréquence $f$, et une onde transverse, dont l'intersection avec la plaque est stationnaire, et oscillant à fréquence $f/2$. (b) Reproduction de la figure de l'article de Faraday (1831) [56], montrant la génération d'ondes transverses par oscillation verticale d'un obstacle cylindrique à la surface de l'eau.

en régime stationnaire sur l'épaisseur de la barrière elle-même, le caractère non-local de l'onde lui permet toutefois de franchir cette barrière, avec une probabilité qui dépend de l'épaisseur de celle-ci. Ces observations suggèrent donc que ce système fournit une modélisation "classique" de l'effet tunnel.

### 4.3.3 Ondes Transverses

Nous avons vu au § 4.3 que, dans le cas d'une excitation périodique homogène en espace, l'absence de direction privilégiée sélectionnait les vecteurs d'ondes par paire, $\pm\mathbf{k}$, conduisant à un motif d'ondes sous-harmoniques stationnaires. Nous nous intéressons ici à une situation nouvelle plus riche, résultant d'un forçage cette fois-ci localisé dans l'espace : les ondes sous-harmoniques qui en résultent ne sont plus nécessairement stationnaires. Lorsque l'excitation est confinée dans une région de l'espace, situation obtenue typiquement par l'oscillation d'un obstacle circulaire ou allongé, on obtient ainsi un motif d'ondes transverses, ou *cross-waves* [7, 128].

Le terme "transverse" vient du fait que la crête de ces ondes sous-harmoniques est en général perpendiculaire à la crête des ondes propagatives harmoniques usuelles. Une illustration d'une telle onde transverse excitée localement est donnée en figure 4.5(a). Dans cette expérience, une plaque verticale partiellement immergée dans l'eau est mise en oscillation verticale, et il apparaît le long de cette plaque une modulation stationnaire oscillant à une fréquence moitié moindre de celle de la plaque. En d'autres termes, après un aller-retour de la plaque, les maxima et les minima du profil sont échangés, tandis que les nœuds de l'onde sont restés immobiles.

Il est remarquable de noter que la première observation de telles ondes transverses est due à Faraday lui-même, dans son article fondateur de 1831 [56]. L'usage a consacré aujourd'hui le terme "instabilité de Faraday" au cas particulier d'un forçage homogène (vu comme une gravité modulée dans le référentiel de l'oscillation), tandis que le terme "ondes transverses" prévaut dans le cas d'un forçage localisé. Nous reproduisons en figure 4.5(b) le dessin original de l'article de Faraday (1831) [56] : dans cette expérience ingénieuse, l'obstacle cylindrique est partiellement immergé, et est oscillé verticalement grâce à une tige reliée à un verre dont le pourtour humidifé est simplement frotté au doigt (à la manière d'un *harmonica de verre*). Les

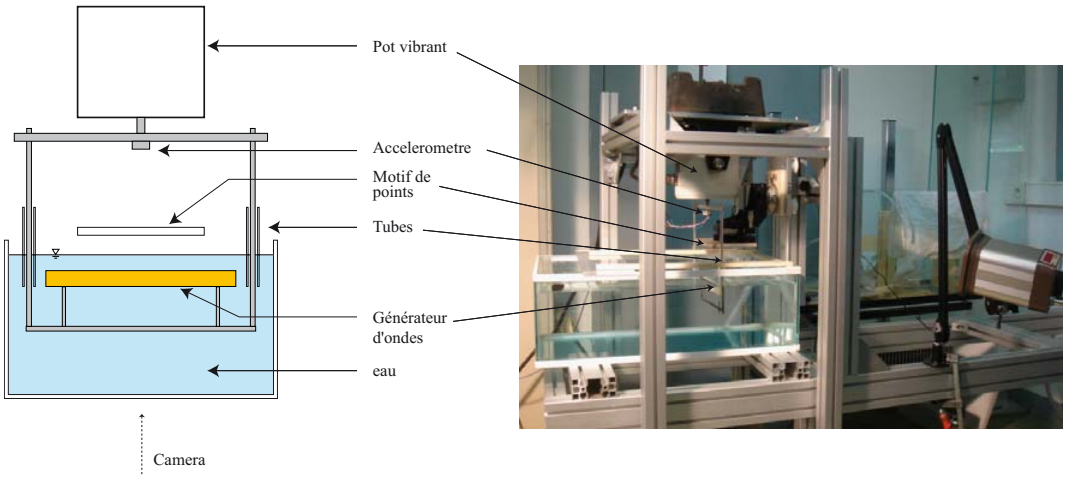


FIG. 4.6 – Schéma et photo du dispositif expérimental. Le générateur d'onde est une plaque plane verticale, complètement immergée, et tenue sur un cadre rigide oscillé verticalement à l'aide d'un pot vibrant. Afin de minimiser les perturbations de la surface libre, les deux tiges latérales de ce cadre traversent la surface libre à l'intérieur de tubes fixes.

ondes transverses ainsi obtenues ont leurs crêtes orientées radialement autour du cyclindre, suggérant un vecteur d'onde local purement azimuthal (voir aussi Taneda (1995) [128] pour d'autres visualisations).

### Dispositif expérimental

Dans la figure 4.5, on voit que l'amplitude de l'onde transverse est maximale le long de la plaque partiellement immergée, suggérant un rôle important joué par le ménisque. La dynamique d'un ménisque oscillant, même stable, est un problème complexe [46] et rend l'analyse des ondes transverses assez délicate dans cette situation. De plus, d'un point de vue pratique, la ligne de mouillage vient s'accrocher sur de petits défauts de surface et devient difficile à contrôler.

Afin d'éviter la complexité liée à la dynamique du ménisque oscillant, nous avons introduit le montage original représenté en figure 4.6, dans lequel une plaque totalement immergée est mise en oscillation verticale à quelques millimètres sous la surface de l'eau. L'oscillation de la plaque, générée au moyen d'un pot vibrant, est dans la gamme de fréquence 20-60 Hz, et donc dans le régime des ondes capillaires. Pour la reconstruction de la surface libre par la méthode FS-SS, le motif de points est positionné au-dessus de l'interface, tandis que la visualisation est effectuée par dessous.

Nous remarquons que l'instabilité d'ondes transverses est toujours présente dans cette configuration, mais dans une situation épurée, sans la présence de ménisque (figure 4.7a). En outre, l'amplitude des ondes transverses ainsi générées est très supérieure à celle des ondes propagatives longitudinales résiduelles (figure 4.7b), suggérant fortement que ces ondes transverses ne sont pas une instabilité du train d'onde longitudinal primaire.

### Structure spatio-temporelle des ondes transverses

Une propriété remarquable des ondes transverses générées localement est qu'elles sont effectivement stationnaires le long du générateur (selon $y$), comme dans la situation classique

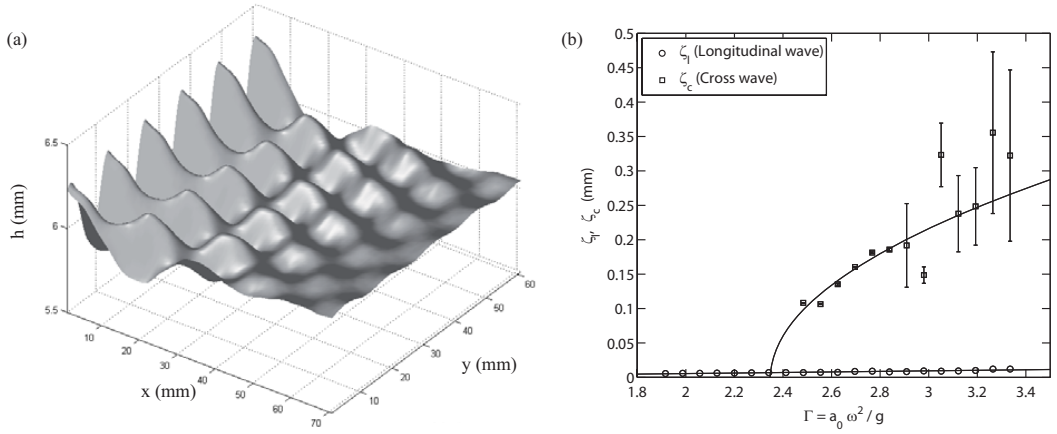


FIG. 4.7 – (a) Interface reconstruite par FS-SS, montrant l'onde transverse. Le générateur d'onde est selon l'axe $y$, en oscillation verticale à la fréquence de 40 Hz. (b) Amplitudes des ondes transvers $\zeta_c$ et des ondes primaires $\zeta_l$ en fonction de l'accélération imposée. Au-delà d'une accélération de l'ordre de 2.8, une instabilité secondaire apparaît sous forme de modulations temporelles lentes du motif d'ondes transverses (représentées par les barres d'erreur) [94].

de Faraday, mais qu'elles présentent aussi une composante propagative selon $x > 0$. La pulsation de cette composante propagative est deux fois inférieure à celle de l'excitation, indiquant qu'il s'agit bien d'une réponse sous-harmonique de type Faraday et non d'une composante longitudinale résiduelle.

Ce motif d'ondes transverses peut s'interpréter comme l'interférence de 2 trains d'ondes propagatifs sous-harmoniques, de vecteurs d'ondes $\mathbf{k}_+$ et $\mathbf{k}_-$ presque alignés avec le générateur (figure 4.8b) : on obtient ainsi une projection anti-parallèle des vecteurs d'onde selon $y$, conduisant donc à un motif stationnaire le long du générateur, et une projection parallèle selon $x > 0$, conduisant à une propagation. L'angle $\theta$ entre $\mathbf{k}_\pm$ et $y$ est de l'ordre de 20°, et correspond à l'angle du motif en quinconce de la figure 4.8(a). Cette configuration fournit ainsi une situation intéressante où il est possible d'observer une réponse sous-harmonique de type Faraday, mais sous forme propagative.

L'angle d'environ 20° du motif d'ondes transverses semble une propriété assez robuste de ce système, ne dépendant pas en particulier de la fréquence d'excitation ni de l'écart au seuil d'instabilité. Cette observation semble exclure la possibilité d'un angle sélectionné par un mécanisme de résonance à 3 ou 4 ondes, pour lequel une dépendance en fréquence peut être prédite. Une explication basée sur un effet de taille finie du générateur peut également être proposée : on pourrait s'attendre en particulier à ce que, dans la limite d'un générateur de longueur infinie, cet angle tende vers 0 par symétrie (invariance selon $y$). On peut cependant remarquer que l'existence d'une angle $\theta$ non nul est nécessaire pour avoir une composante selon $x > 0$ de la vitesse de groupe, et assurer ainsi la possibilité de rayonner à l'infini l'énergie injectée par un tel générateur de longueur infini. Toutefois, des observations préliminaires pour différentes longueurs de générateur (entre 6 et 44 cm) ne semblent pas montrer d'évolution significative de $\theta$.

L'origine de cet angle $\theta$ fait actuellement l'objet d'expériences complémentaires. Une comparaison avec une analyse numérique a été initiée dans le cadre d'une collaboration avec E.

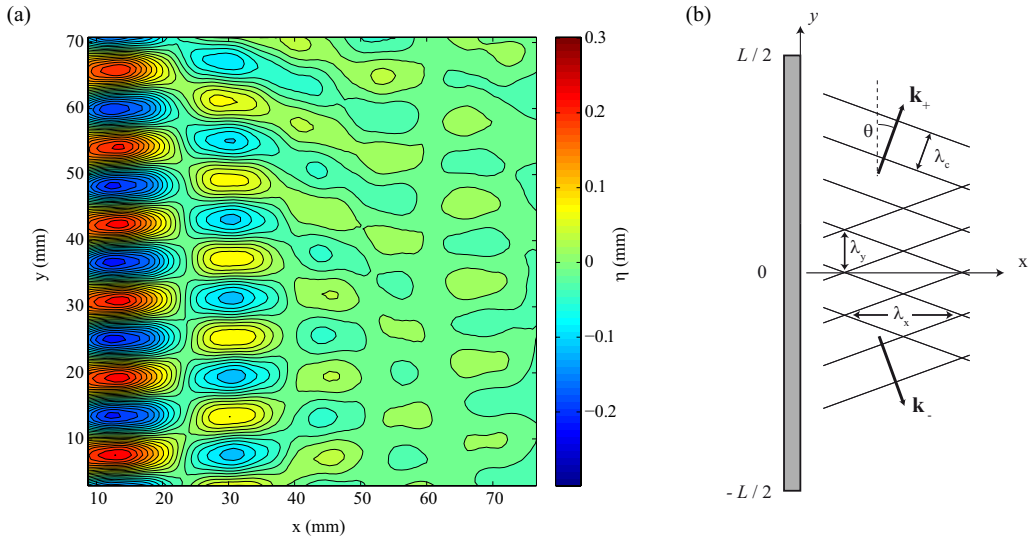


FIG. 4.8 – (a) Motif d'ondes transverses, stationnaire selon $y$ et propagatif selon $x > 0$ (le générateur d'onde est selon l'axe $y$, en $x = 0$). (b) Décomposition du motif d'ondes transverses comme l'interférence de 2 ondes paramétriques de vecteurs d'ondes $\mathbf{k}_+$ et $\mathbf{k}_-$ formant un angle $\theta$ avec le générateur d'ondes.

Sultan (FAST), et devrait permettre d'identifier le mécanisme de sélection de cet angle.

## 4.4 Perspectives

Nous conclurons ce dernier chapitre sur les ondes de surface par deux pistes de recherche dans la continuité des travaux présentés ici. La première piste est de nature instrumentale, et vise à repousser le domaine de validité de la méthode FS-SS. La seconde piste discute de l'application de cette méthode de mesure à l'étude de la turbulence d'ondes gravito-capillaires.

### 4.4.1 Améliorations de la méthode FS-SS

La linéarisation vis-à-vis des 3 petits paramètres (parallaxe, pente et amplitude relative) évoquée au § 4.2.2, nécessaire à l'obtention de la relation linéaire (4.1) entre gradient de hauteur et déplacement apparent, restreint significativement les domaines d'application de la méthode FS-SS. Si la limite d'apparition de caustiques (croisement de rayons lumineux) est intrinsèquement infranchissable, de par la nature non inversible de la relation pente - déplacement apparent, on peut toutefois envisager de relâcher au moins partiellement la triple contrainte des 3 petits paramètres. Une telle extension serait très fructueuse pour les applications où les champs sont de grande taille (problèmes de sillages en champ lointain), ou dans des situations de fortes pentes (problèmes de ressaut, de solitons, de turbulence d'ondes...)

Une première approche consiste à étendre le résultat (4.1) par un développement à l'ordre suivant vis-à-vis d'un ou plusieurs des 3 paramètres du problème. La seule généralisation accessible semble être dans le cas de pentes faibles et d'amplitudes arbitraires, mais seulement à 1 dimension, et ne présente donc pas d'intérêt *a priori*. La difficulté est que, même si un résultat non-linéaire généralisant (4.1) peut être obtenu, son inversibilité afin de déterminer $h(x, y)$ à partir de la mesure de $\delta\mathbf{r}(x, y)$ n'est pas assurée.

Une généralisation plus ambitieuse consisterait à s'affranchir de la décomposition en 2

étapes, $(I_0, I_1) \rightarrow \delta\mathbf{r}(x,y) \rightarrow h(x,y)$ (§ 4.2.2), et à formuler directement le problème de la reconstruction de la hauteur $h(x,y)$ à partir du couple d'images $(I_0, I_1)$. Une telle formulation revient à un problème de flot optique sous contrainte, reposant sur une méthode d'optimisation non-linéaire (par exemple la minimisation d'un résidu de la forme $|h - \mathcal{F}(I_0, I_1)|^2$). Bien entendu, même avec une telle formulation, la présence de caustiques, rendant le problème intrinsèquement non inversible, continuera à poser problème. En revanche, on peut supposer qu'une reconstruction de la hauteur reste possible dans des situations de très fortes déformations du champ d'intensité lumineuse.

### 4.4.2 Turbulence d'ondes gravito-capillaires

La turbulence d'ondes (ou turbulence faible), déjà abordée au § 3.3.4 au sujet des ondes d'inertie, vise à décrire la statistique hors d'équilibre d'un système d'ondes dispersives en faible interaction non-linéaire. Jusqu'à peu, les études de turbulence d'ondes dans le cas des ondes gravito-capillaires étaient restreintes à des mesures en un point, au moyen de sondes capacitives immergées, ou de mesures optiques selon une ligne par projection d'une nappe laser [81] (on pourra se reporter à Falcon (2010) [54] pour une une revue expérimentale récente sur ce sujet).

Un des grands enjeux de ce problème est d'établir dans quelle limite le formalisme de la turbulence d'onde constitue une description valide pour une réalisation expérimentale donnée d'ondes de surface. Ce formalisme suppose que les ondes sont d'amplitude suffisament faible pour que la relation de dispersion linéaire s'applique, mais suffisamment élevée toutefois pour que les interactions non-linéaires donnent lieu à un régime turbulent, avec transferts d'énergie entre modes. Si ce régime de turbulence d'ondes est vérifié, alors les spectres temporels mesurés en un point, $E(\omega)$, et les spectres spatiaux en un temps, $E(k)$, sont simplement reliés par la vitesse de groupe issue de la relation de dispersion des ondes. La plupart des expériences supposent ce régime effectivement atteint, et se concentrent sur la mesure de $E(\omega)$ en un point pour en déduire le spectre spatial $E(k)$. Toutefois, l'existence d'objets non-linéaires localisés (de type soliton) met en défaut une telle relation.

Ainsi, une méthode optique résolue en temps, capable de mesurer simultanément $E(\omega)$ et $E(k)$, permettrait de vérifier sans hypothèse la validité de ce formalisme. Une telle approche a été menée récemment avec profit dans le cas d'une turbulence de plaque vibrée [31]. Dans le contexte de la turbulence d'ondes gravito-capillaires, l'utilisation de la méthode FS-SS constitue une voie attractive. En particulier, l'étape 1 de la méthode (mesure du déplacement apparent, avant intégration) fournit directement le champ de gradient de hauteur, dont le spectre $E_{\nabla h} = k^2 E_h(k)$ est moins pentu que celui de hauteur $E_h(k)$, et donc plus facilement accessible expérimentalement (pour une gamme de $k$ mesurable donnée, l'exigence de rapport signal/bruit est moindre si le spectre est moins pentu).

Néanmoins, les pentes et les courbures d'interface élevées présentes en turbulence d'ondes n'ont pas permis à ce jour d'utiliser la méthode FS-SS de façon robuste. Les tests, réalisés avec un motif de points très proches de la surface libre (comme dans l'exemple de la figure 4.6) n'ont pas permis d'éviter le problème de déformations trop prononcées, voire d'apparition de caustiques. Les pistes évoquées dans le § 4.4.1 devraient permettre de repousser cette limitation, et ainsi de bénéficier de la très bonne résolution de la méthode FS-SS pour ce problème de turbulence d'ondes gravito-capillaires.

Exp Fluids (2009) 46:1021–1036
DOI 10.1007/s00348-008-0608-z

RESEARCH ARTICLE

# A synthetic Schlieren method for the measurement of the topography of a liquid interface

**Frédéric Moisy · Marc Rabaud · Kévin Salsac**

Received: 10 June 2008 / Accepted: 19 December 2008 / Published online: 13 January 2009


**Abstract** An optical method for the measurement of the instantaneous topography of the interface between two transparent fluids, named free-surface synthetic Schlieren (FS-SS), is characterised. This method is based on the analysis of the refracted image of a random dot pattern visualized through the interface. The apparent displacement field between the refracted image and a reference image obtained when the surface is flat is determined using a digital image correlation (DIC) algorithm. A numerical integration of this displacement field, based on a least square inversion of the gradient operator, is used for the reconstruction of the instantaneous surface height, allowing for an excellent spatial resolution with a low computational cost. The main limitation of the method, namely the ray crossing (caustics) due to strong curvature and/or large surface-pattern distance, is discussed. Validation experiments using a transparent solid model with a wavy surface or plane waves at a water–air interface are presented, and some additional time-resolved measurements of circular waves generated by a water drop impact are discussed.

F. Moisy (✉) · M. Rabaud · K. Salsac
Fluides, Automatique et Systèmes Thermiques (FAST),
University of Paris-Sud, Bâtiment 502, Campus Universitaire,
91405 Orsay, France
e-mail: moisy@fast.u-psud.fr

F. Moisy · M. Rabaud · K. Salsac
Fluides, Automatique et Systèmes Thermiques (FAST),
University Pierre et Marie Curie, Bâtiment 502,
Campus Universitaire, 91405 Orsay, France

F. Moisy · M. Rabaud · K. Salsac
Fluides, Automatique et Systèmes Thermiques (FAST), CNRS,
Bâtiment 502, Campus Universitaire, 91405 Orsay, France

## 1 Introduction

### 1.1 Review of optical methods measuring surface slopes

The measurement of the deformation of a liquid surface is of fundamental and practical interest in numerous research fields, from small scales (e.g. painting or coating industry) to large scales (e.g. wind waves, ship wakes). Optical methods, being non-intrusive and able to provide an instantaneous two-dimensional measurement, are of much practical interest. Among those methods, the measurement of the surface slope based on light reflection or refraction are the most promising. Those methods have been widely used for one-point measurements of one or two components of the surface slope using laser beam refraction (Tober et al. 1973; Lange et al. 1982; Liu et al. 1993), with possible extension to line measurement using a fast scanning technique (Savalsberg et al. 2006).

Extensions of this approach for two-dimensional fields, pioneered by Cox (1958) for only one slope component, are based on the use of collimated light beam encoded with a linearly increasing intensity, so that a one-to-one mapping between light intensity and slope can be obtained. The main advantage of using collimated light is that the measured gradient is insensitive to the surface height. Zhang et al. have extended the method to the measurements of the two components of the surface gradient, using a system of color-encoded collimated beams, generated by a suitably colored screen and a large lens, operating either in refraction or reflection on the free surface (Zhang and Cox 1994; Zhang et al. 1996). A calibration of the color-slope mapping is required, and can be performed using a glass sphere. From those measurements, the surface elevation could be obtained by integrating the gradient components

in the Fourier domain (Zhang 1996). This method has been succesfully used for the investigation of surface deformations induced by vortices in a shear layer flow (Dabiri and Gharib 2001).

Roesgen et al. (1998) introduced a new approach, also based on collimated light, using an array of microlenses of 200 μm in diameter placed above the free surface. The surface deformation leads to a displacement of the light spots in the focal plane of the microlens array that could be measured using a digital image correlation (DIC) algorithm. The surface height reconstruction was obtained by these authors by a least-square inversion of the linear system built from a finite-difference scheme expressed on the hexagonal lattice of the microlens array. Here again, the size of the microlens array, usually 2–3 cm, limits the size of the imaged area, restricting this approach to small fields.

Using scattered light instead of collimated light allows for simplification of the optical setup, since no collimating lens or mirror is needed, but the resulting measurement is a combination of the surface slope and height. Keller and Gotwols (1983), and later Jähne and Riemer (1990), used a light source of varying intensity along one direction, imaged through the free surface. This approach has been recently combined with a direct measurement of the surface height based on light absorbtion (Jähne et al. 2005).

Another image-encoding approach, first discussed by Kurata et al. (1990), relies on the use of scattered light emitted from a structered pattern, such as a grating or a set of random dots, imaged through the interface. Here the displacement field is obtained by comparing the refracted images of the pattern obtained with flat and deformed surfaces. A similar approach has been used for the measurement of the contact angle of a drop on a solid substrate (Andrieu et al. 1995).

Although originally introduced for surface slope measurements, the approach of Kurata et al. (1990) has been extensively applied to measurements in fluids with density variations, in the so-called "synthetic Schlieren" (SS) (Sutherland et al. 1999; Dalziel et al. 2000) and "Background-Oriented Schlieren" (BOS) methods (Meier 2002). The name "synthetic Schlieren" has been more widely used for stratification-induced density variations in the geophysical fluid dynamics community, whereas the name "Background-Oriented Schlieren" has been mainly used for compressible fluids in the aerodynamics community. In all cases, the displacement field between a reference image and a refracted image originates from the continuous variation of the optical index induced by the density variations, and is measured using a DIC algorithm. However, the displacement at one point being the result of the index variation integrated along a light ray, the refraction index field cannot be inferred in general from those measurements. On the other hand, in the case of a free surface, the step-like variation of the refraction index makes possible a complete reconstruction of the surface height, as noted by Dalziel et al. (2000). Elwell (2004) successfully used this idea to obtain quantitative measurements of the surface deformation induced by vortices in a shallow water flow, using a cumulative sum scheme of the measured gradient components for the surface height reconstruction.

### 1.2 Outline and scope of the paper

This paper presents a detailed characterisation of the method originally introduced by Kurata et al. (1990) and quantitatively developed by Elwell (2004). We propose the name free-surface synthetic Schlieren (FS-SS) for this method, as it relies on the same physical principle as the now standard synthetic Schlieren method for density-varying fluids. This methods allows for an accurate and low-cost measurement of the instantaneous topography of the interface between two transparent fluids. We show that a precision of 1 μm for a 10-cm field can be readily achieved, making this method attractive for investigation of small-scale waves dynamics or coating phenomena.

The FS-SS method consists in two steps:

1. measurement of the surface gradient from the displacement field of the refracted image of a random pattern using a DIC algorithm;
2. reconstruction of the surface height using a least-square integration of the surface gradient.

Compared to the methods based on collimated light, which require an elaborate optical setup and a delicate calibration scheme, the present method, like the standard synthetic Schlieren method, is simply based on a black-and-white imaging system with simple optics. As a consequence it may be easily reproduced for a large range of applications using standard laboratory equipment. The drawback of this simplified setup is that, since no collimating optics is used, oblique light rays have to be considered, yielding to a more delicate analysis of the ray geometry in the general case. It is shown however that, to first order in paraxial angles, in surface slopes, and in relative deformations, the surface gradient is simply proportionnal to the displacement field.

The computation of the displacement field from the refracted images of the flat and deformed interface is based on a standard DIC algorithm. Due to its wide use in solid and fluid mechanics, DIC (or other pattern matching technics, such as optical flow, Barron et al. 1994) have received considerable interest in recent years, and several commercial and open-source packages are now available. DIC is mainly used in solid mechanics for the measurement

of the strain field at the surface of a solid (Périe et al. 2002; Hild and Roux 2006). In fluid mechanics, apart from synthetic Schlieren applications, DIC algorithms are mostly used in particle image velocimetry (PIV) applications, where the velocity field is given by the displacement field of tracer particles per unit of sampling time (Adrian 1991; Raffel et al. 1998).

The second step of the method, the integration of the gradient field, is based on a least-square inversion of the gradient operator. This procedure, first used by Roesgen et al. (1998) for an hexagonal lattice, is formulated here for a Cartesian lattice. It relies therefore on a simpler numerical scheme, here again available from standard linear algebra packages.

The paper is organized as follows. The relation between the surface gradient and the displacement field is derived in Sect. 2. The experimental set-up and the numerical methods for the measurement of the displacement field and for the reconstruction of the surface height are presented in Sect. 3. Two validation experiments are described in Sect. 4: one using the deflection of a laser beam to validate the displacement field measurement, and one using a transparent solid model to validate the surface height reconstruction. Section 5 discusses the maximum acceptable distorsion for a reliable reconstruction of the surface height. Additional time-resolved experiments of circular waves generated by the impact of a water drop in water are presented in Sect. 6. Finally, Sect. 7 discusses some possible applications of the method.

## 2 Relation between the surface gradient and the displacement field

### 2.1 Optical configurations and approximations

We want to determine the optical displacement field $\delta\mathbf{r}(x, y)$ induced by the refraction of the light scattered from a pattern located at $z = 0$ through the interface $z = h(x, y)$. At each object point $M$ of the pattern, we need to determine the virtual objects $M'$ and $M''$ corresponding to the flat and deformed interface, respectively, and to relate the displacement $\mathbf{M'M''} = \delta\mathbf{r}$ with the surface gradient $\nabla h$ at the same point.

The surface is assumed to be smooth enough, so that the light rays reaching the camera cross the surface only once. The pattern may be located either above or below the surface. The refraction indices of the fluids on the camera side and on the pattern side are noted $n$ and $n'$, respectively. This generic formulation encompasses the two following configurations:

**Configuration 1** Camera above and pattern below the surface (the most common situation). A limitation of this configuration is that the surface-pattern distance has to be equal or larger than the liquid depth, which may cause ray crossings and caustics for large surface curvature or large depth (discussed in Sect. 2.5).

**Configuration 2** Camera below and pattern above the surface (assuming the container has a transparent bottom). In this case, the surface-pattern distance is arbitrary, and may be increased for better resolution, or set as close as possible to the surface to avoid ray crossings when strong curvature of the surface are present.

Configuration 1 is illustrated in Fig. 1 when the interface is flat, and is used as a reference for the derivation of the relation between $h(x, y)$ and $\delta\mathbf{r}(x, y)$. In this configuration,

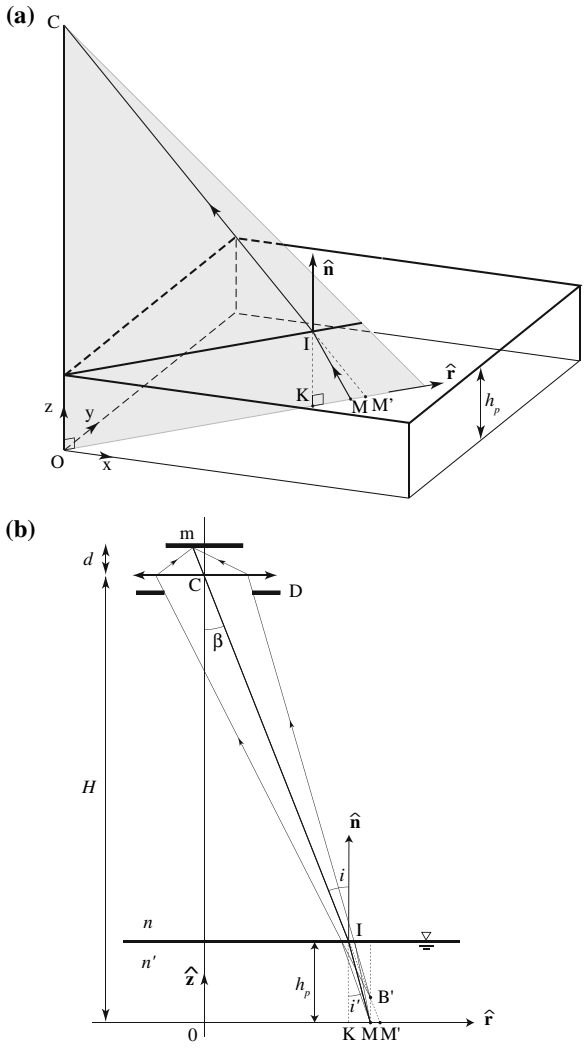


**Fig. 1** **a** Three-dimensional ray geometry for a horizontal interface (reference case). **b** Two-dimensional view of the vertical incidence plane COM. A ray coming from a point $M$ located on the pattern appears to come from the virtual object $B'$. In the pattern plane, it appears to come from the point $M'$

$n' > n$, so that wave crests and troughs will act as magnifying (convex) and reducing (concave) lenses, respectively. We will use a cartesian frame with the vertical optical axis $z$ crossing the origin $O$ and the camera $C$, the plane $z = 0$ corresponding to the pattern plane. We note $D$ the diaphragm diameter of the camera, and $\beta$ the paraxial angle. For the sake of simplicity, the pattern-surface distance $h_p$ is chosen equal to the liquid depth $h_0$, but optical corrections for additional intermediate layers between the pattern and the surface can be easily included.

In the following, three approximations are considered, based on the three small parameters: the paraxial angle $\beta$, the surface slope $\gamma$ and the relative surface deformation.

1. *Paraxial approximation* The pattern-camera distance $H$ is much larger than the field size $L$, yielding a maximum paraxial angle $\beta_{max} \simeq L/(\sqrt{2}H) \ll 1$ .
2. *Weak slope approximation* The angle $\gamma$ between the unit vector normal to the interface $\hat{\mathbf{n}}$ and the vertical vector $\hat{\mathbf{z}}$ is small. As a consequence, the surface slope $\theta$ measured in the incidence plane is also small.
3. *Weak amplitude approximation* Denoting $h(x, y) = h_p + \eta(x, y)$ the surface height, the amplitude $|\eta|$ is small compared to the mean height $h_p$.

In the derivation of the relation between $\nabla h$ and $\delta\mathbf{r}$, linearisation with respect to those three parameters is performed.

### 2.2 Refracted image through a horizontal interface

We first consider the refracted image of the pattern at $z = 0$ through a flat interface at $z = h_p$ (Fig. 1). For each point $M$, located in $(x_M, y_M, 0)$, a vertical incidence plane COM can be defined, crossing the pattern plane along the radial unit vector $\hat{\mathbf{r}} = \mathbf{OM}/|\mathbf{OM}|$. The image of $M$ is $m$ in the image plane (camera sensor), and the corresponding virtual object $B'$ is located above the pattern, in $(x_M, y_M, \alpha h_p)$ with

$$\alpha = 1 - n/n'. \tag{1}$$

In practice, the focus is made on this vertically shifted focal plane at $z = \alpha h_p$. For convenience, since rays reaching the image plane in $m$ appear to come from a point $M'$ in the pattern plane, in the following, the apparent displacements are simply given in the plane $z = 0$.

The displacement from $M$ to $M'$ is outward, in the radial direction, and is given by

$$\mathbf{MM'} = h_p(\tan i - \tan i')\hat{\mathbf{r}}, \tag{2}$$

where the incidence and refracted angles are related by the Snell-Descarte law, $n \sin i = n' \sin i'$. For the flat interface, the incidence angle $i$ is simply equal to the paraxial angle $\beta$. Within the paraxial approximation and using Eq. 1, Eq. 2 simplifies to:

$$\mathbf{MM'} = \alpha h_p i\hat{\mathbf{r}}. \tag{3}$$

From the image of the pattern seen through the flat interface, we can determine the location of any point $M$ from the position of its image $M'$ given $h_p$, $H$ and the location of the optical center $O$.

### 2.3 Refracted image through a deformed interface

We consider now the refracted image of the pattern through an arbitrary deformed interface, and we want to determine the new virtual object $M''$ associated to the given object point $M$ (Fig. 2). This problem is more delicate, since now the incidence plane is not vertical (except for axisymmetric deformations), and does not contain the optical axis $z$. For a given point $M$, the incidence plane is defined as the plane containing $M$, the camera $C$, and the unit vector $\hat{\mathbf{n}}$ measured at the point $I$ where the light ray MIC intercepts the interface, with

$$\hat{\mathbf{n}} = \frac{\hat{\mathbf{z}} - \nabla h}{\sqrt{1 + |\nabla h|^2}}. \tag{4}$$

Assuming weak slopes, $|\nabla h|^2 \ll 1$, Eq. 4 simply gives:

$$\nabla h = \hat{\mathbf{z}} - \hat{\mathbf{n}}. \tag{5}$$

The displacement $\mathbf{MM''}$ takes place along the direction $\mathbf{s}$ (see the top view in Fig. 3), defined as the intersection of the incidence plane and the horizontal plane $z = 0$, yielding

$$\mathbf{s} = \mathbf{OM}/H - \nabla h.$$

The incident plane CAM, where $A$ is the projection of the origin $O$ on the line $MM''$, is shown in Fig. 2b. For a camera far above the surface $(H \gg L)$, the plane CAM tends to be vertical and $\mathbf{s}$ becomes aligned with the surface gradient (except for very weak slopes $|\nabla h| \ll |\mathbf{OM}|/H$, for which $\mathbf{s}$ remains essentially radial).

Since $\hat{\mathbf{n}}$, $\mathbf{CM''}$ and $\hat{\mathbf{s}} = \mathbf{MM''}/|\mathbf{MM''}|$ are contained in the incident plane CAM, $\hat{\mathbf{n}}$ can be written as

$$\hat{\mathbf{n}} = a\hat{\mathbf{s}} + b\frac{\mathbf{CM''}}{|\mathbf{CM''}|}.$$

The coefficients $a$ and $b$ are determined from the following geometrical relations (Fig. 2b),

$$\hat{\mathbf{n}} \cdot \hat{\mathbf{s}} = -\sin\theta$$

$$\hat{\mathbf{n}} \cdot \frac{\mathbf{CM''}}{|\mathbf{CM''}|} = -\cos i$$

$$\hat{\mathbf{s}} \cdot \frac{\mathbf{CM''}}{|\mathbf{CM''}|} = \sin(i + \theta),$$

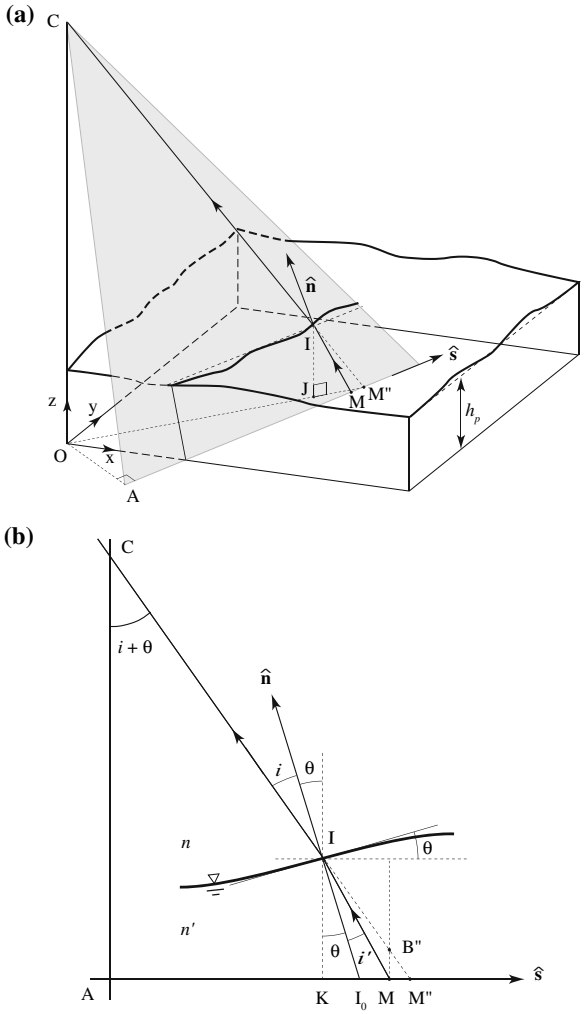


**Fig. 2** **a** Three-dimensional ray geometry for an arbitrary deformed interface. The incidence plane CAM is now defined by the object point $M$, the camera $C$, and the unit normal vector $\hat{\mathbf{n}}$ at point $I$ where the light ray MIC intercepts the interface. This plane is not vertical in general, and does not contain the optical axis $OC$. **b** Two-dimensional view of the incidence plane CAM (only the principal ray is shown for clarity). A ray coming from $M$ appears to come from the virtual object $B''$. In the pattern plane, it appears to come from the point $M''$

where $\theta$ is the angle *measured in the incident plane* between the surface and the horizontal (i.e. the angle of the intersection of the surface with the oblique incidence plane CAM), yielding

$$\hat{\mathbf{n}} = \frac{\sin(i+\theta)\cos i - \sin\theta}{\cos^2(i+\theta)}\hat{\mathbf{s}} + \frac{\sin(i+\theta)\sin\theta - \cos i}{\cos^2(i+\theta)}\frac{\mathbf{CM}''}{|\mathbf{CM}''|}. \quad (6)$$

Within the weak slope and the paraxial approximations, to first order in $i$ and $\theta$, Eq. 6 reduces to

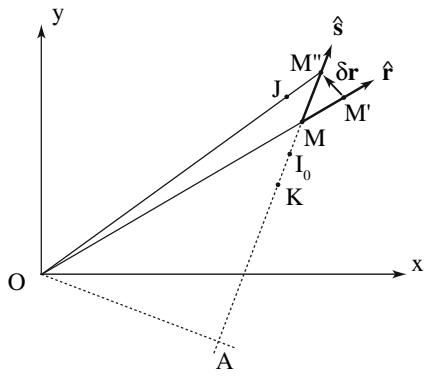


**Fig. 3** Top view of the pattern plane, showing the object point $M$ and its two virtual objects $M'$ and $M''$ for the flat and deformed interface, respectively. The line $AMM''$ is the intersection of the incident plane CAM with the pattern plane $Oxy$. $J$ is the vertical projection of the point $I$ where the light ray MIC intercepts the interface. $\mathbf{M'M''} = \delta\mathbf{r}$ is the displacement measured by digital image correlation

$$\hat{\mathbf{n}} = i\hat{\mathbf{s}} - \frac{\mathbf{CM}''}{|\mathbf{CM}''|}. \quad (7)$$

Writing $\mathbf{CM}'' = \mathbf{CO} + \mathbf{OM}''$ and taking $|\mathbf{CM}''| \simeq H$, Eqs. 5 and 7 give

$$\nabla h = \frac{\mathbf{OM}''}{H} - i\frac{\mathbf{MM}''}{|\mathbf{MM}''|}. \quad (8)$$

Figure 2b shows that, in the oblique incidence plane CAM, the apparent displacement is given by:

$$\mathbf{MM}'' = \mathbf{KM}'' - \mathbf{KM} = IK[\tan(\theta+i) - \tan(\theta+i')]\hat{\mathbf{s}}, \quad (9)$$

where $K$ is the projection of $I$ on the line $MM''$. One has $IK = II_0\cos\theta$, with $II_0$ along the normal vector $\hat{\mathbf{n}}$, and $II_0 = h(I)/\cos\gamma$, with $\gamma$ the angle between $\hat{\mathbf{n}}$ and the vertical unit vector $\hat{\mathbf{z}}$ and $IJ = h(I)$ the local height of the interface at the vertical of point $I$, yielding

$$\mathbf{MM}'' = h(I)\frac{\cos\theta}{\cos\gamma}[\tan(\theta+i) - \tan(\theta+i')]\hat{\mathbf{s}}. \quad (10)$$

Considering again small angles, and assuming weak deformations $h(I) \approx h_p$, Eq. 10 becomes:

$$\mathbf{MM}'' = \alpha h_p i\hat{\mathbf{s}}, \quad (11)$$

which is similar to Eq. 3, except that now the displacement is along $\hat{\mathbf{s}}$ instead of $\hat{\mathbf{r}}$ (see Fig. 3). Note that the focal surface where lies the virtual object $B''$ associated to $M''$ is now deformed according to the shape of the interface (see Fig. 2), so that $B''$ cannot be exactly focused. However, for weak deformations, this focal surface remains close to the horizontal focal plane at $z = \alpha h_p$ determined for a flat interface (point B' in Fig. 1). In practice, since the characteristic size of the

dots on the pattern is larger than one pixel, this small out of focus effect can be neglected.

From Eq. 11, one has $i\hat{\mathbf{s}} = \mathbf{MM}''/\alpha h_p$, so that the surface gradient (Eq. 8) becomes:

$$\nabla h = \frac{\mathbf{OM}''}{H} - \frac{\mathbf{MM}''}{\alpha h_p}. \tag{12}$$

Introducing $\mathbf{OM}'' = \mathbf{OM}' + \delta\mathbf{r}$ and $\mathbf{MM}'' = \mathbf{MM}' + \delta\mathbf{r}$ (with $\delta\mathbf{r} = \mathbf{M}'\mathbf{M}''$) into Eq. 12 yield

$$\nabla h = -\delta\mathbf{r}\left(\frac{1}{\alpha h_p} - \frac{1}{H}\right) + \frac{\mathbf{OM}'}{H} - \frac{\mathbf{MM}'}{\alpha h_p}.$$

Finally, recalling Eq. 3, the last two terms cancel (see Fig. 1b), and a simple linear relation between $\nabla h$ and $\delta\mathbf{r}$ is obtained,

$$\nabla h = -\frac{\delta\mathbf{r}}{h^*}, \quad \text{with} \quad \frac{1}{h^*} = \frac{1}{\alpha h_p} - \frac{1}{H} > 0. \tag{13}$$

This demonstrates that, to first order in paraxial angle, surface slope and relative surface deformation, the displacement $\delta\mathbf{r}$ is simply proportional to the surface gradient $\nabla h$. In practice, with a camera far above the imaged surface, $H \gg \alpha h_p$ (with $\alpha \simeq 0.24$ for an air–water interface), we can simply consider $h^* \simeq \alpha h_p$.

We recall here that the surface-pattern distance was considered equal to the liquid depth, $h_0 = h_p$. In practical situations, one or more intermediate materials of various indices are also present between the lower fluid and the pattern, and the distance $h_p$ should be replaced by an effective distance. Consider, for instance, the common situation depicted in Fig. 4, where a glass plate of thickness $h_g$ and an air gap $h_a$ are inserted between the fluid and the pattern. Assuming that the camera is far above the surface, only vertical light rays can be considered, so that the total

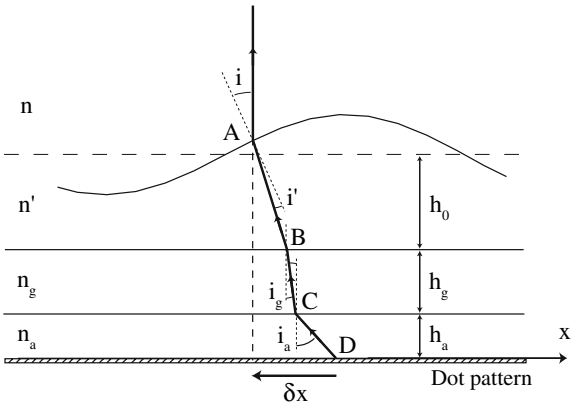


**Fig. 4** Apparent displacement $\delta x$ when several intermediate materials are inserted between the interface and the pattern, assuming that the camera is located far above the surface ($H \gg \alpha h_p$).In this example, two intermediate layers, denoted g and a (for glass and air) are present, with $n_a < n' < n_g$

displacement $\delta x$ along the direction $\hat{\mathbf{x}}$ is the sum of the elementary displacements, yielding

$$\delta x = \left(-h_0 + \frac{n}{n'}h_0 + \frac{n}{n_g}h_g + \frac{n}{n_a}h_a\right)\frac{\partial h}{\partial x}.$$

Finally, summing up the displacement components along each direction $\hat{\mathbf{x}}$ and $\hat{\mathbf{y}}$, the result can be written in the form (13), where the effective surface-pattern distance $h_p$ is the sum of the thickness of the layers weighted by the refraction index ratio,

$$h_p = h_0 + \frac{n'}{n_g}h_g + \frac{n'}{n_a}h_a. \tag{14}$$

Note finally that, considering the finite aperture $D$ (see Fig. 1), the light beam selected by the diaphragm will intercept the interface in a small ellipse of typical size $\delta \approx Dh_p/H$ around the point $I$. It is implicitly assumed here that the surface slope is nearly constant within this ellipse, i.e. $\partial^2 h/\partial s^2 \ll \delta^{-1}$. However, this assumption is not critical, since the the curvature $\partial^2 h/\partial s^2$ is also constrained by the much restrictive invertibility condition (see Sect. 2.5) in order to avoid ray crossings.

### 2.4 Parallax distorsion

If the camera is far above the surface, the points $M$, $M'$ and $M''$ are very close, and the displacement $\delta\mathbf{r}$ measured at a point $M$ can be considered as originating from the gradient $\nabla h$ at the vertical of $M$ for simplicity. However, the finite camera distance $H$ introduces a parallax distorsion, since the surface gradient is actually measured at the point $I$ (intersection of the light ray MIC with the interface) which is not at the vertical of $M$.

The location of point $J$, defined as the vertical projection of $I$ in the horizontal plane (see Figs. 2a and 3), can be expressed by remarking that the two triangles $COM''$ and $IJM''$ are similar, so that $JM''/OM'' = IJ/H$. Accordingly, assuming weak deformations (i.e. $IJ = h(I) \simeq h_p$), one has

$$\mathbf{OJ} = \left(1 - h_p/H\right)\mathbf{OM}''. \tag{15}$$

If a resolution better than $h_p/H$ is needed for the surface height reconstruction, a remapping of the measured gradient field onto the original reference frame of the pattern, based on a suitable interpolation scheme, has to be performed before the integration. An illustration of this remapping procedure is given in Sect. 4.2.

### 2.5 Invertibility condition (IC)

In the previous sections, it was implicitly assumed that the displacement field $\delta\mathbf{r}$ could be determined from the refracted image of the pattern. However, this is not true if crossings of light rays occur between the pattern and the

interface, which would result in the formation of caustics, as explained in Fig. 5.

A necessary condition to determine the displacement field $\delta\mathbf{r}$ from the refracted image is that a given image $m$ on the camera should originate from a single object $M$ of the pattern. In the case of a pattern below the interface ($n' > n$), ray crossings may appear below the wave crests, which act as magnifying lenses (Fig. 5). This invertibility condition (IC) requires that the focal length associated to the surface curvature is larger than the surface-pattern distance everywhere in the imaged field. For example, in the case of a sinusoidal plane wave of amplitude $\eta_0$ and wavelength $\lambda$, $h(x, y) = h_p + \eta_0 \cos(2\pi x/\lambda)$, and approximating the curvature as $\partial^2 h/\partial x^2$, ray crossings are avoided by chosing a surface-pattern distance smaller than the critical distance $h_{p,c}$,

$$h_p < h_{p,c} = \frac{\lambda^2}{4\pi^2 \alpha \eta_0}. \tag{16}$$

Consider, for instance, a wave amplitude of $\eta_0 = 0.5$ mm and wavelength $\lambda = 3$ cm, with $h_p = 3$ cm. The characteristic displacement is given by $|\delta\mathbf{r}| \simeq \alpha 2\pi h_p \eta_0/\lambda \simeq 0.8$ mm (see Eq. 13, assuming $H \gg \alpha h_p$ ). In this situation, caustics would form well below the surface, at a distance of $h_{p,c} = 18$ cm, so that accurate measurements of the displacement field can be readily achived when taking $h_p = 3$ cm.

The invertibility condition 16 may be more conveniently formulated directly from the displacement field. Consider $\ell'$ and $\ell''$ the abscissa of the virtual objects $M'$ and $M''$ (for the flat and deformed interfaces respectively) taken along any arbitrary direction $\hat{\boldsymbol{\ell}}$. To avoid ray crossing, $\ell''$ has to be a strictly increasing function of $\ell'$, i.e., $\partial\ell''/\partial\ell' > 0$. Denoting $\delta\ell = \delta\mathbf{r} \cdot \hat{\boldsymbol{\ell}} = \ell'' - \ell'$ the displacement along $\hat{\boldsymbol{\ell}}$, and introducing the strain $\sigma = \partial\delta\ell/\partial\ell'$ along $\hat{\boldsymbol{\ell}}$ (one has $\sigma > 0$ and $< 0$ for magnified and reduced images respectively), the condition for no ray crossing is $\sigma < 1$. In terms of the magnification factor $m = \partial\ell'/\partial\ell'' = 1/(1-\sigma)$ along $\hat{\boldsymbol{\ell}}$, this condition simply writes $m > 0$.

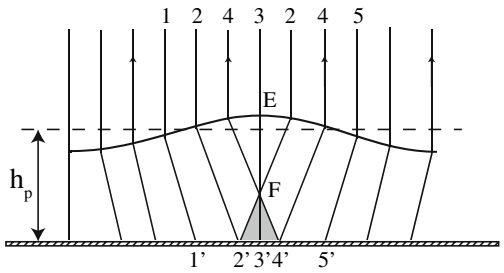


**Fig. 5** Large curvature of the interface or large pattern-surface distance induce ray crossings when the invertibility condition (IC) is not satisfied, Eq. 16. Here the pattern-surface distance $h_p$ (taken equal to the liquid depth $h_0$) is larger than the focal length $EF$ of the point of maximum convex curvature, under the wave crest. The sequence of points $2'3'4'$ on the pattern will be seen as 432, with $2'$ and $4'$ having multiple images

Satisfying the condition for no ray crossing for arbitrary direction requires that the largest (extensional) strain remains everywhere bounded by 1 (note that there is no limitation in principle for the compressive strain when $n' > n$). Formally, denoting $\sigma_1 < \sigma_2$ the two ordered principal strains (these are the eigenvalues of the strain tensor $\partial\delta r_i/\partial x_j$), the invertibility condition (IC) is

$$\sigma_2 < 1 \tag{17}$$

at each point of the field. For instance, a plane wave produces an oscillating (compressive and extensional) strain along the direction of propagation and zero strain along the perpendicular direction, so that $\sigma_2$ shows oscillations clipped at 0.

Criterion 17 is clearly an a posteriori test, since the computation of the principal strains requires the displacement field to be determined, which is possible only if Eq. 17 is satisfied. However, the measurement of the principal strains provides an interesting test of *how far* the light rays are from crossing. An empirical criterion based upon the largest absolute principal strain is discussed in Sect. 5.

## 3 Set-up and numerical methods

### 3.1 Experimental set-up

Experiments were carried out in a 60 cm × 40 cm glass tank, filled with tap water up to an height $h_0$ of the order of a few centimeters (Fig. 6). The water depth is measured by a depth gauge with a 0.1 mm resolution.

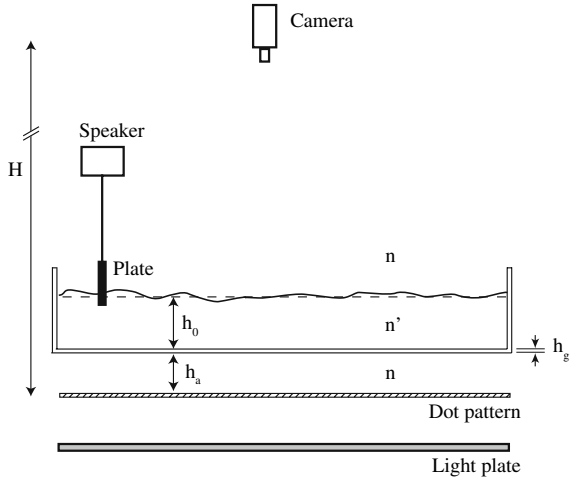


**Fig. 6** Sketch of the experimental set-up (camera above, configuration 1). Not at scale, $h_0/H \sim 1{,}000$

Two series of experiments were carried out: Validation experiments, performed with a 2,048 × 2,048 camera at 8 frames per second (Sect. 4), and some time-resolved experiments of drop impacts, with a 1,280 × 1,024 camera at 100 frames per second (Sect. 6). For most experiments, the camera is located above the water tank (configuration 1), at a distance $H = 2.0$ m from the pattern, and the imaged area is a square of side $L = 14$ cm. The maximum paraxial angle is $\beta_{max} = L/(\sqrt{2}H) \simeq 2.8°$. In this case, the pattern is placed below the transparent bottom of the tank, of thickness $h_g = 5$ mm, and an additional air gap of adjustable thickness $h_a$ may also be present between the glass plate and the pattern. For experiments where the camera is located below the water tank (configuration 2), a 45° standard glass-silvered mirror is placed below the tank, and the total camera-pattern distance is $H = 2.9$ m.

The imaged pattern has been carefully designed to allow for unambiguous reconstruction of the displacement field by the DIC algorithm with a good spatial resolution. The camera resolution and the expected displacement magnitude have to be taken into account to optimize the characteristic size of the fine structure of the pattern. In order to maximize the quantity of information and to reduce fortuitous coincidences, a set of randomly distributed dots, partially overlaping, is used. In the example shown in Fig. 7, dots of diameter 0.4 mm, made of concentric circles of increasing grayscale, with an overall black-on-white density ratio of approximately 1:2, have been numerically generated. The pattern is printed on an overhead transparency using a standard 1,200-dpi Laserjet printer, and is lighted using a uniform lighting plate. It must be noted that, due to the halftoning rendering of the printer, the actual resolution of the pattern is significantly lower than the nominal 1,200 dpi, especially when overhead transparencies are used. The resulting dot diameter in Fig. 7, as imaged by the $2{,}048^2$ camera, is approximately 6 pixels.

### 3.2 Displacement field computation

A reference image of the pattern is taken when the air/water interface is flat, and a second image or a movie is taken during the experiment. The displacement field $\boldsymbol{\delta r}$ between each image and the reference image is obtained by the DIC algorithm available in the commercial software DaVis.

Interrogation windows of size 16 × 16 pixels, with an overlap of 8 pixels, are used for the computations of the correlation functions. Although the dot diameter of 6 pixels is larger than the optimal size of 2–3 pixels usually recommended for PIV applications (Raffel et al. 1998), the high "seeding" density used here allows to satisfy the criterion of approximately 5 dots per interrogation window (see Fig. 7). The final displacement field is defined on a 256 × 256 grid, with a spatial resolution of order 0.5 mm (the numbers given here correspond to the 2,048 × 2,048 camera). Classical postprocessing schemes are applied, such as median filter to remove bad vectors. An example of displacement field obtained for plane waves is shown in Fig. 8.

The uncertainty of the cross-correlation method is already well documented, e.g., in the literature for PIV (Raffel et al. 1998). Since the random dot pattern is generated to meet the requirements for an optimal cross-correlation resolution, one may expect to reach the theoretical resolution of this method. Using interrogation windows of decreasing size, with final size of 16 × 16 pixels, a resolution of 0.1 pixel (about 7 μm) can be achieved using a classical subpixel interpolation scheme for the maximum of the correlation function. For typical

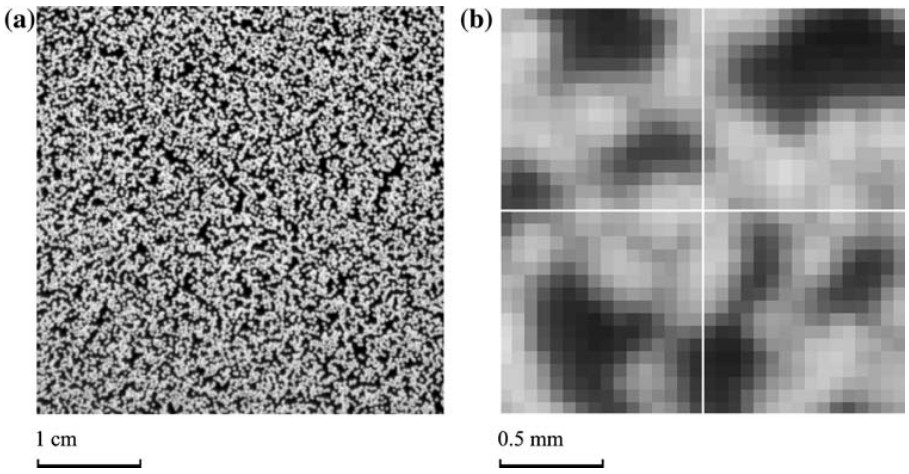


**Fig. 7** Magnifications at scales 1:1 (**a**) and 20:1 (**b**) of the random dot pattern used in the present experiments, as imaged by the $2{,}048^2$ pixels camera on a 14 × 14 cm field. Dots of diameter $d = 0.4$ mm were numerically generated, with a density of 50%, resulting in dots of approximately 6 pixels in the camera sensor. The magnification (**b**) represents 32 × 32 pixels, and four interrogation windows of size 16 × 16 pixels, used for the digital image correlation, are shown for reference

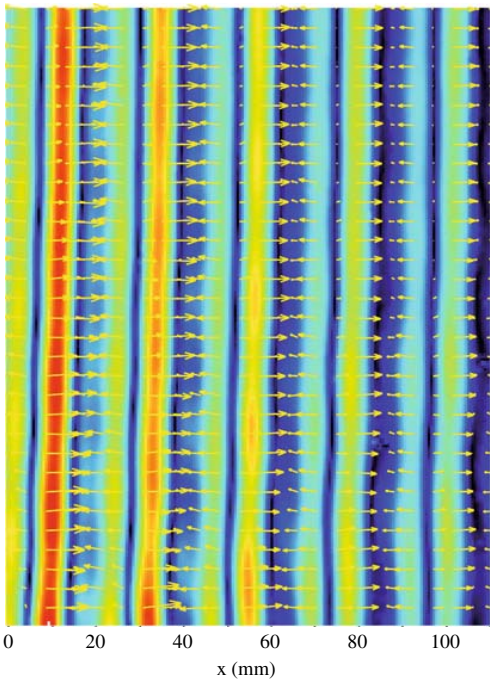


**Fig. 8** Displacement field for an approximately plane wave, generated from a vibrated plate on the left. Color codes the displacement norm

displacement of order 5 pixels, and assuming moderate strain so that the dots remain essentially circular, this relative uncertainty is about $\epsilon = 2 \times 10^{-2}$. Larger values may however be expected when the refracted pattern is significantly strained. Note also that decreasing the window size would result in a better spatial resolution, but worse displacement resolution.

### 3.3 Surface height reconstruction

The numerical integration of the surface height field $h(x, y)$ from the displacement field $\boldsymbol{\delta}\mathbf{r}(x, y)$ requires the computation of the inverse gradient operator, $\nabla^{-1}$. Denoting $\boldsymbol{\xi} = -\delta\mathbf{r}/h^*$ the measured surface gradient, see Eq. 13, we have to compute

$$h(x, y) = h_{\mathrm{p}} + \nabla^{-1}\boldsymbol{\xi}. \tag{18}$$

This integration is performed by a numerical inversion of the linear system built from the second-order centered difference gradient operator. Since the gradient field $\boldsymbol{\xi} = \xi_x\hat{\mathbf{x}} + \xi_y\hat{\mathbf{y}}$ is defined on a $M \times N$ grid, this linear system has 2 $MN$ equations and $MN$ unknown. A solution may however be defined for this over-determined linear system: the resulting surface height $h(x, y)$ is the "best" solution in the least-square sense, i.e., the solution minimizing the residual $||\nabla h - \boldsymbol{\xi}||^2$. An example is shown in Fig. 9 for an approximately plan wave. The details of

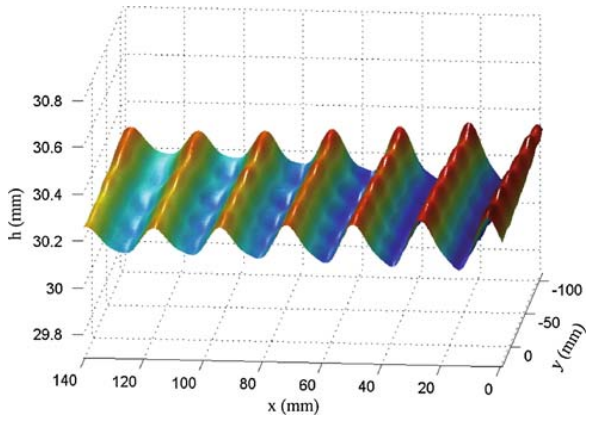


**Fig. 9** Perspective view of the reconstructed surface height of an approximately plane wave, propagating from right to left, showing a slight transverse modulation

the numerical integration method are discussed in the Appendix 1.

An alternative method for the inversion of the gradient operator using Fourier transform has been proposed by Zhang et al., but suffered from border effects and was limited to rectangular domains (Zhang and Cox 1994; Zhang et al. 1996; Zhang 1996). The least-square inversion method proposed here is similar to the one introduced in Roesgen et al. (1998), which was based on the hexagonal lattice implied by the specific geometry of their microlens array. Here the inversion is expressed in a simpler Cartesian lattice, which is easier to implement and suitable for the processing of the surface gradient data obtained from typical DIC algorithms.

Note that the displacement field $\delta\mathbf{r}$ being irrotational in principle, this property may be used as a constrain to improve the measurement of the maximum of the correlation function. However, if a residual rotational component is present in the displacement field $\delta\mathbf{r}$, it will not contribute to the integrated surface height, and a classical unconstrained DIC algorithm has been used here.

Being non-local, the least-square solution $h(x, y)$ is robust to localized bad vectors. This method is suitable for square or rectangular areas, but may be delicate to implement for more complex geometries (see Appendix 1). A strong limitation of this method is its inability to detect changes of the mean surface height, originating for example from waves of characteristic length of the order or larger than the imaged area. Another example is provided by a wavepacket entering into the imaged area, producing an artificial change of the mean height of the unperturbed surface.

It is worth noting that some vibrations in the optical setup may have a strong influence on the reconstructed surface height. In our experiments, vibrations in the camera position due to the internal cooling fan were found to

produce an apparent circular translation of the image of about 5 μm (about 0.1 pixel) when imaging at a distance of 2 m. Although very weak, the resulting uniform displacement field, once integrated, produces a noticeable mean slope which superimposes to the measured height field. This uniform displacement can be readily substacted before integration, but prevents from the measurement of slopes of characteristic length of the order or larger than the imaged area.

### 3.4 Resolution

The integration method for solving Eq. 18 being linear, the relative uncertainty of the surface height reconstruction is expected to depend linearly upon the uncertainty $\epsilon$ of the input displacement field. Based on numerical tests (described in the Appendix 2), assuming a displacement field perturbed with an additive, spatially uncorrelated, Gaussian noise of relative magnitude $\epsilon$, the resolution of the surface reconstruction is found to be

$$\frac{\Delta\eta}{\eta_{\mathrm{rms}}} \simeq 5\frac{L}{\lambda}\frac{\epsilon}{N}, \tag{19}$$

Taking $L = 14$ cm, $\lambda = 3$ cm, $N = 256$ and $\epsilon = 0.02$ gives $\Delta\eta \simeq 10^{-3}\eta_{\mathrm{rms}}$ : a wave of amplitude 1 mm should be measurable with a precision of 1 μm.

However, the estimate given by Eq. 19 should be considered as a lower bound for the true uncertainty. First, the displacement field noise $\epsilon$ may be larger than 2% when large strains are present. Moreover, a noise with significant spatial correlation is likely to be produced by the DIC algorithm: patterns with fortuitous coincidence, or optical defects (impureties, reflections) result in clustered bad vectors, and strongly strained refracted patterns will produce bad vectors correlated with regions where displacements or displacement variations are large.

## 4 Validation experiments

### 4.1 Validation of the slope measurement

A first validation experiment has been carried out to assess the accuracy of the displacement field measurement, using the deflection of a reflected laser beam. Plane waves were generated by oscillating a PVC plate attached to a speaker. The plate length is equal to the tank width, and generates nearly plane waves. A laser beam, making an angle of $\phi = 17°$ with the horizontal, is reflected at a given point of the surface, and the reflected beam is visualized on a vertical screen located 1 m from the reflection point (Fig. 10). An angle of $\theta$ of the liquid surface results in an angle of $\phi + 2\theta$ of the reflected

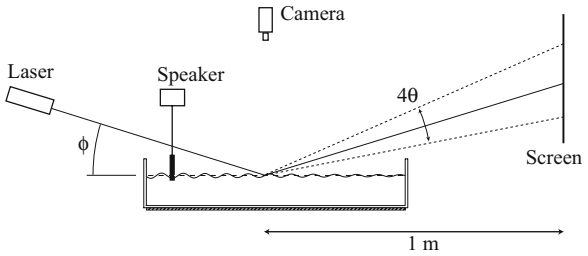


**Fig. 10** Setup for the validation of the slope measurement. The laser beam deflection angle is twice the surface local slope

beam. Plane waves have been generated with various amplitudes, at a fixed frequency of 10 Hz. For each amplitude, the peak-to-peak deviation of the reflected beam is measured on the screen, and the displacement field measured by synthetic Schlieren in a small area around the reflecting point is determined independently.

The maximum slopes $\xi = \tan\theta$ measured from the two methods are compared in Fig. 11. The error bars result from the non-strictly sinusoidal wave produced by the wavemaker, producing higher frequency oscillations of the reflected beam around the main oscillation. Although the uncertainty of each data point is significant, a nearly perfect correlation between the two methods is obtained. The measurements have been restricted to $\xi < 0.1$, for which non-harmonic effects can be neglected. Larger slopes are obviously measurable for the correlation algorithm, but they could not be compared to the ones measured from the beam deflection method because of the uncertainties due to the higher order modes.

### 4.2 Validation of the surface height reconstruction

In order to test the full measurement procedure (slope measurement, surface reconstruction and parallax distorsion),

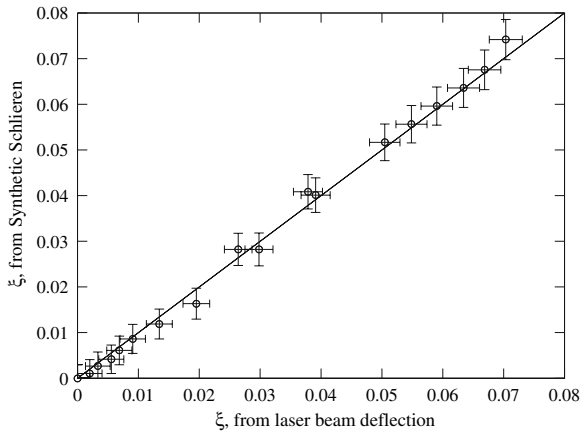


**Fig. 11** Comparison of the maximum slopes measured independently by the laser beam method and by synthetic Schlieren

a solid model of a wavy surface with a well controlled geometry has been used. A sinusoidal plane wave of wavelength 20 mm and amplitude 0.5 mm was carved on the upper surface of a 23 mm thick parallelepiped plexyglass plate of size 10 × 14 cm by a computer controlled milling machine with a 1 mm diameter hemispherical tool. A similar plexyglass plate with a flat upper surface was used for the reference image.

Figure 12 shows the reconstructed profile of the plexiglass model as a function of $x$ along the line $y = 0$. In order to quantify the influence of the parallax, the plexiglass model was placed at a location $x = 20$–$120$ mm off the optical center, and the camera was located at a moderate distance of $H = 1.55$ m from the dot pattern. The wavelength measured from the raw profile (without the remapping correction) is $20.30 \pm 0.05$ mm, which over-estimates the expected value of about 1.5%. After application of the remapping correction Eq. 15, the measured wavelength and amplitude are $20.01 \pm 0.05$ mm and $1.03 \pm 0.02$ mm, in remarkable agreement with the expected values.

## 5 Influence of the pattern-surface distance

An important feature of the FS-SS method is the maximum acceptable strain for a reliable reconstruction of the surface height. For a given free surface topography, the strain of the refracted image is essentially controlled by the surface-pattern distance $h_p$. This parameter should be set as large as possible to increase the resolution, but smaller than the critical distance (Eq. 16) where ray crossings appear.

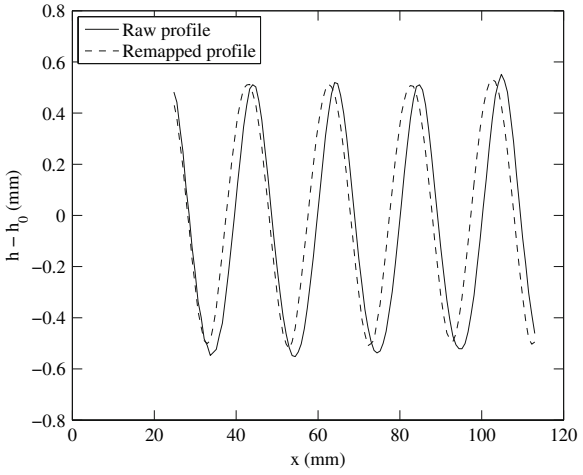


**Fig. 12** Surface profile measured on a plexiglass model machined with a sinusoidal plane wave of wavelength 20 mm and amplitude 0.5 mm. The opical axis is located at $x = 0$ mm, and the model is placed off-axis *continuous line* represents raw profile, *dotted line* represents remapped profile using Eq. 15, correcting for the parallax distorsion.

However, even for $h_p < h_{p,c}$, although no ray crossing is present, regions of large strain (either compression or extension) may prevent from an accurate measurement of the displacement field, and a looser criterion than Eq. 17 is desirable to assess the measurement accuracy.

A systematic series of experiments has been carried out, varying the air gap between the bottom glass plate and the pattern, $h_a$, in the range 0–300 mm, so that the pattern-surface distance $h_p$ (corrected by the intermediate air and glass layers, see Eq. 14) is varied between 30 and 430 mm. Plane waves, of amplitude 0.15 mm and wavelength 22 mm, are generated in a 22-mm depth water layer. For each value of $h_a$ a reference image with flat interface and a series of images with the waves are taken.

Five examples are shown in Fig. 13. Only a 2 × 2 cm square is shown, whose location is chosen to show similar wave pattern for each $h_p$. As $h_p$ is increased, the refracted image of the pattern above the wave crests show increasingly elongated patches. In this situation, the cross-correlation algorithm is likely to produce wrong results, since the location of an initial circular patch of the reference image may be matched all along the ellipse of the refracted image.

Since in most situations curvatures of both sign are equally present, a convenient indicator which gets rid of the ordering of the principal strains is provided by the largest absolute principal strain field,

$$\sigma^*(x,y) = \max(|\sigma_1(x,y)|, |\sigma_2(x,y)|)$$

Large values of $\sigma^*$ indicate both regions of strong compression (under troughs) or strong extension (under crests). Since the integration method is non-local, one has to check that the largest value of $\sigma^*$ over the whole field remains moderate. However, some bad vectors from the cross-correlation may produce non-physical large $\sigma^*$, preventing from using a simple criterion based on $\max_{x,y} \sigma^*$. It was found that, in a roughly homogeneous region, a quite robust criterion may be built from the root-mean-square of this quantity,

$$\sigma^*_{\rm rms} = \sqrt{\frac{1}{N_x N_y} \sum_{x,y} \sigma^{*2}(x,y)}.$$

Reliable results were obtained when the rms principal strain satisfies

$$\sigma^*_{\rm rms} < 0.15. \qquad (20)$$

This criterion corresponds here to an air gap of $h_a = 50$ mm (see picture 4 in Fig. 13), which shows a maximum strain of 0.71 (magnification factor $m = 1/(1 - \sigma) \simeq 3.5$ under the wave crests). Figure 14, where cuts of the surface height along the $x$ direction are shown for the different values of $h_a$, confirms that no change are detectable for $h_a$ up to 50 mm. This criterion gives the maximal screen-pattern distance for a reliable measurement of a given

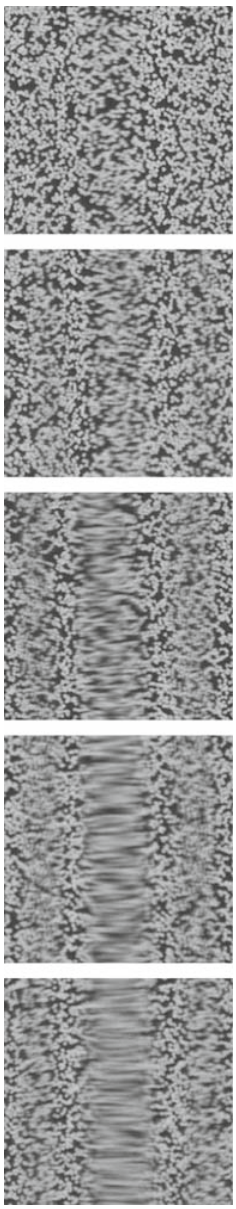


**Fig. 13** Snapshots of the refracted image for five values of the air gap $h_a$ between the glass plate and the pattern. Only a 2 × 2 cm square is shown (the whole field is 14 cm). Blurry elongated horizontal segments appear under the wave crests at large $h_a$

surface curvature or, equivalently, the largest curvature measurable for a given distance. In practice, a safe choice would be $\sigma^*_{\rm rms} \simeq 0.05{-}0.10$.

## 6 Circular wave generated by a water drop impact

Time-resolved visualizations of the circular wave pattern generated by the impact of a water drop have been finally carried out, aiming to demonstrate the ability of the FS-SS method to investigate complex wave phenomena. A water drop of 1 mm diameter is dropped one centimeter above a 4 cm water layer at time $t = 0$, and the surface height is reconstructed on a 20 × 20 cm$^2$ field at 100 Hz. The invertibility condition was satisfied only 0.4 s after the impact.

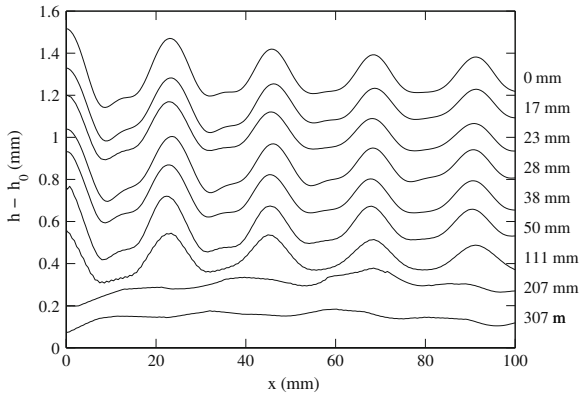


**Fig. 14** Surface height of the same waves, measured with different air gap $h_a$ between the pattern and the glass bottom of the tank. The profiles are shifted vertically

The two perspective views of the surface elevation in Fig. 15 clearly shows the growing circular wavepacket. The largest waves have amplitude of 100 μm and wavelength of order of 30 mm, but much smaller waves, of amplitude of 1 μm and wavelength around 10 mm, can also be distinguished at the front of the wavepacket. Shortly after the impact, the surface near the impact is almost perfectly flat, showing only residual plane waves of amplitude less than 1 μm originating from slight background vibrations from the lateral tank walls.

Phase and group velocities may be estimated from the spatio-temporal diagrams shown in Fig. 16. In these diagrams the surface elevation along a radial line is represented in color scale as a function of time. The phase velocities (measured here as the slope following a given wave crest) are 26 cm/s near the rear, for the largest wavelengths, and 23 cm/s near the front, for the smallest ones. The front velocity is found to be close to the expected minimum phase velocity for capillary-gravity waves in deep water, $c_{\rm min} = (4\gamma g/\rho)^{1/4} \simeq 23.1$ cm/s for $\lambda_c = 2\pi(\gamma/\rho g)^{1/2} \simeq 17$ mm (here $\gamma \simeq 0.070$ N/m is the air–water surface tension, $\rho$ the water density and $g$ the gravity). The measured rear velocity of the wavepacket is 18 cm/s, a value which compares well to the expected minimum group velocity, $c_{g,\rm min} \simeq 17.7$ cm/s. Since the phase velocity is larger than the front velocity at the rear edge, new wave crests appear at the rear and travel along the wavepacket. On the other hand, the front edge

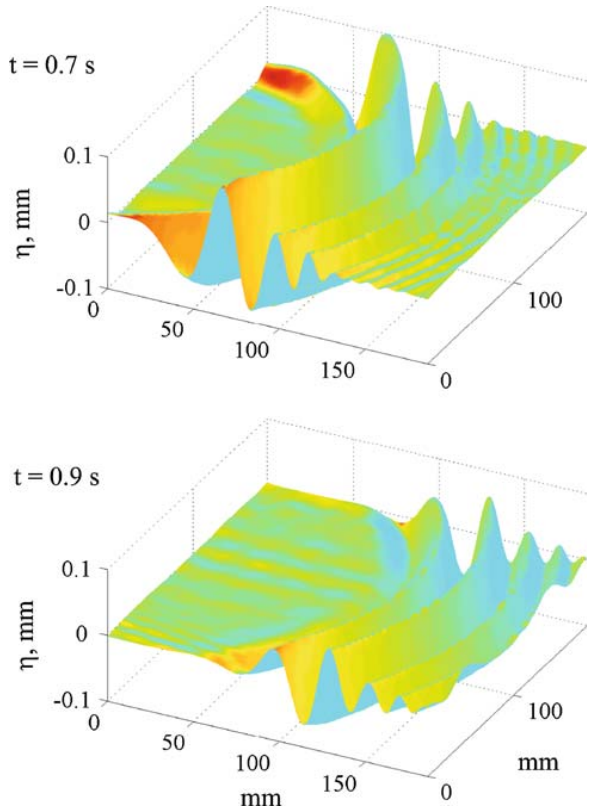


**Fig. 15** Perspective view of the circular waves created by the impact of a drop, at times $t = 0.7$ and $t = 0.9$ s after the impact

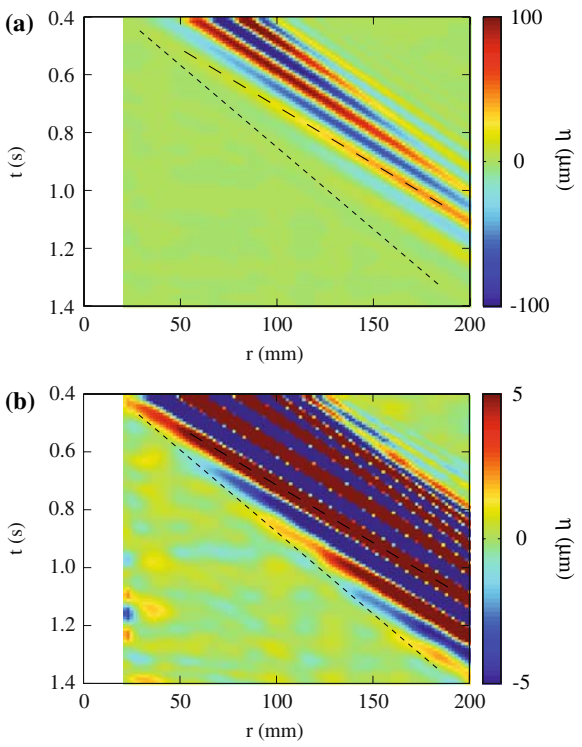


**Fig. 16** Spatio-temporal diagram of the surface height profile taken along a radius of the circular wave shown in Fig. 15. Only the color scale is changed between (**a**) and (**b**). The *long dashed line* shows the phase velocity of a wave crest, and the *short dashed line* shows the rear front velocity of the wavepacket (approximate group velocity)

velocity can be hardly determined from those diagrams, because of capillary waves of very weak amplitude which have their wavecrest line almost parallel to the wavepacket border itself.

## 7 Conclusion

The FS-SS method presented in this paper relies on the same ground as the synthetic Schlieren (or equivalently Background-oriented Schlieren) method, namely the quantitative analysis of the refracted image of a random dot pattern when viewed through a deformed interface, following the works of Kurata et al. (1990) and Elwell (2004).

To first order in paraxial angle, surface slope and the relative surface deformation, we have shown that the displacement field is simply proportional to the surface gradient (Eq. 13). Compared to the classical synthetic Schlieren method, which is applied in situations where the refraction index varies continuously, here the step-like variation of the index at the interface allows for a complete reconstruction of the topography of the interface from the measured surface gradient. This low-cost and versatile optical method gives quantitative measurement with a vertical resolution of order of 2% of the maximum deformation amplitude. The numerical reconstruction of the surface height, being based on a least square inversion of the gradient operator, is very robust and has a low computational cost. When used with a high speed imaging system, this method allows for time-resolved investigation of complex wave phenomena.

The main limitations of the FS-SS method are:

1. Being based on the measurement of the surface gradient, it is not able to detect uniform changes of the surface height.
2. It is extremely sensitive to slight vibrations (including vibrations generated by the internal fan of a cooled camera).
3. It is unable to determine the displacement field for strong curvature and/or large surface-pattern distance.
4. It applies only for weak deformations, weak slopes and weak paraxial angle.

Limitation no. 2 can be circumvented by substracting the mean displacement field before numerical integration.

However, this substraction prevents from measuring mean surface slopes of characteristic scale of the order or larger than the imaged area. Applications where the measurement of a constant slope is needed would require an extremely stable optical setup.

For the limitation no. 3, an empirical criterion has been proposed, based on the rms strain, namely $\sigma^*_{\mathrm{rms}} < 0.15$, Eq. 20, where $\sigma^*$ is the largest absolute principal strain. Note however that this constrain is partly due to the use of a DIC algorithm for the measurement of the displacement field, which produces wrong results for strongly strained images. Other approaches, such as the Optical Flow (Barron et al. 1994), may behave better than DIC in this situation, and may allow to work closer to the theoretical invertibility condition (IC) given by $\sigma_2 = 1$, where $\sigma_2$ is the largest principal strain.

Finally, the limitation no. 4 is probably the most restrictive for this method. Best accuracy can be actually achieved by maximizing the distance $H$ between the camera and the pattern, so that nearly vertical refracted rays enter the camera. However, even for vanishing paraxial angles, a fully consistent formulation of the problem beyond a first-order approximation with respect to the surface slope and relative amplitude is a very delicate task, which is left for future investigation.

A possible application of FS-SS is the measurement of the contact angle and the dynamics of the wetting of a drop on a substrate (Moisy et al. 2008). Although a slope discontinuity is present at the contact line, the surface curvature along a radius (second derivative) is large but positive, so no ray crossing occurs and the method should apply. However, in order to minimize the relative surface-pattern height changes, a gap between the (transparent) substrate and the pattern should be used.

Finally, wave turbulence is another application where FS-SS may be useful. Here the major limitation is certainly the formation of caustics under the largest curvature at small scales, even if the configuration 2 (camera below and pattern above the surface) is chosen. If applicable, this method should be able to provide the true spatial spectrum of the wave fields, instead of the temporal spectrum usually obtained from classical one-point measurements.

**Acknowledgments** The authors whish to thank Harold Auradou, Raphael Pidoux, Edouard Pinsolle, Joran Rolland and Jacopo Seiwert for their help during the experiments, Maurice Rossi for enlightening comments on the optical part, and the Reviewers for pointing key references. Guy Demoment and John D'Errico are also acknowledged for fruitful discussions about the algorithm of inversion of the gradient operator, and Francois Lusseyran and Luc Pastur for interesting discussions about the use of Optical Flow algorithms. This work was supported by the ANR grant no. 06-BLAN-0363-01 "HiSpeedPIV".

## Appendix 1: Numerical integration of the inverse gradient operator

We seek the solution $h(x, y)$ given the two local slope components $\xi_x$ and $\xi_y$ measured at each point. We first note that a naive integration along one single arbitrary path joining a reference point (0, 0) and a given point $(x, y)$, e.g.

$$\eta(x,y) = \eta(0,0) + \int_0^x \xi_x(x',0)\mathrm{d}x' + \int_0^y \xi_y(x,y')\mathrm{d}y',$$

would suffer from an important noise accumulation effect: a wrong measurement of the slope $\xi_x$ or $\xi_y$ at a given point would propagate along the whole path. Consider, for instance, a one-dimensional signal $\eta(x)$, from which a perturbed local slope $\tilde{\xi} = \partial\eta/\partial x + \epsilon\xi_{\mathrm{rms}}a$ is measured on a discrete set of points, with $a$ is a Gaussian noise of zero mean and unit variance. Computing the perturbed signal $\tilde{\eta}(x)$ from a cumulative sum introduces a drift, as $(\tilde{\eta} - \eta)_{\mathrm{rms}} = \epsilon\xi_{\mathrm{rms}}\sqrt{n}$, where $n$ is the number of grid steps.

For the 2D problem, this drift problem may be partially overcome by averaging over all possible paths joining the reference point (0, 0) to any desired point $(x, y)$. Summing $\xi_x$ from 0 to $x$ averaged over each horizontal stripe for each $y$, and vice-versa for $\xi_y$, would lead to a relative uncertainty for $\eta$ equals to that for $\boldsymbol{\xi}$.

A more efficient and accurate approach consists in writing the gradient operator using linear algebra. Noting $\mathsf{H}$ the vector of length $MN$ representing the height field $h(x, y)$ sampled on a $M \times N$ grid, the two vectors of length $MN$ representing each component of the gradient field can be written

$$\begin{aligned} \mathsf{G}_x\mathsf{H} &= \Xi_x, \\ \mathsf{G}_y\mathsf{H} &= \Xi_y \end{aligned} \tag{21}$$

where $\mathsf{G}_x$ and $\mathsf{G}_y$ are two sparse matrices, of size $MN \times MN$, defining the linear combinations of the elements of $\mathsf{H}$ to produce each gradient. $\mathsf{G}_x$ and $\mathsf{G}_y$ may be defined to produce second-order centered differences, with suitable treatment of the border elements. These two systems (21) may be merged into a single linear system,

$$\mathsf{G}\mathsf{H} = \Xi, \tag{22}$$

where now $\mathsf{G} = (\mathsf{G}_x, \mathsf{G}_y)^{\mathrm{T}}$ is a rectangular sparse matrix of size $2MN \times MN$, and $\Xi = (\Xi_x, \Xi_y)^{\mathrm{T}}$ is a vector of length $2MN$. This system thus gives $2MN$ equations with $MN$ unknowns. It is over-determined, so a direct inversion is not possible. However, an estimate of $\mathsf{H}$ may be obtained, by minimizing the residual

$$||\mathsf{G}\mathsf{H} - \Xi||^2 \tag{23}$$

This method produces a solution of the over-determined linear system (22) in a least squares sense. Using Matlab, a convenient and efficient implementation of this algorithm of least-square solution for over-determined linear systems is available with the "\" (backslash) operator. A complete solution based on Matlab for inverting a 2D gradient using second-order centered differences is available using `intgrad2` (D'Errico, http://www.mathworks.com/matlabcentral/).

Although this approach is most easily implemented for rectangular domains, more complex geometries can also be considered. For domains of arbitrary shapes, a rectangular $2Q \times Q$ (where $Q$ is the number of points of the domain) matrix$\mathsf{G}$ , whose elements produce the finite differences over each point of the domain, has to be constructed. From this matrix$\mathsf{G}$, the estimate for $\mathsf{H}$ is obtained by minimizing Eq. 23 as before.

## Appendix 2: Resolution of the numerical integration

From the measurement of local slope $\boldsymbol{\xi}$ at each grid point, with a relative uncertainty given by that of the displacement $\epsilon$, we estimate here the uncertainty $\Delta\eta$ arising from the numerical integration of Eq. 18.

An empirical estimate for $\Delta\eta$ has been obtained from a series of numerical tests. A sinusoidal wave $\eta(x, y)$, of wavelength $\lambda = 2\,\pi/|\mathbf{k}|$ and amplitude $\eta_0$, is considered in a square domain of size $[0, L]^2$ discretized to $N^2$ collocation points. The discrete gradient $\boldsymbol{\xi}$ is computed from a second order finite different scheme, and a Gaussian noise $\mathbf{a}$ is added,

$$\tilde{\boldsymbol{\xi}} = \boldsymbol{\xi} + \epsilon\xi_{\mathrm{rms}}\mathbf{a},$$

where $a_x$ and $a_y$ are of zero mean and unit variance. We further assume that $\mathbf{a}$ and $\boldsymbol{\xi}$ are uncorrelated, and that $\mathbf{a}$ has no spatial correlation. Computing the surface height $\tilde{\eta}$ from the numerical integration of the perturbed gradient $\tilde{\boldsymbol{\xi}}$ yields $\tilde{\eta} = \eta + \epsilon\xi_{\mathrm{rms}}\nabla^{-1}\mathbf{a}$. From this, the rms of the difference height is computed, $\Delta\eta_{\mathrm{rms}} = (\tilde{\eta} - \eta)_{\mathrm{rms}} = \epsilon\xi_{\mathrm{rms}}(\nabla^{-1}\mathbf{a})_{\mathrm{rms}}$.

The following parameters have been systematically varied: the relative noise $\epsilon$ from 1 to 8%, the number of points $N$ from 32 to 256, the wavelength $\lambda$ from 0.1 $L$ to $L$ and the amplitude $\eta_0$ from 0.01 $L$ to 0.1 $L$. For each set of parameters, the results are averaged from 10 realizations with random orientation of the wavevector $\mathbf{k}$. The following empirical law is obtained,

$$\frac{\Delta\eta}{\eta_{\mathrm{rms}}} = (5.0 \pm 0.2)\frac{L}{\lambda}\frac{\epsilon}{N},$$

where $\eta_{\mathrm{rms}} = \eta_0/\sqrt{2}$ is taken for a sinusoidal wave.

## References


Adrian RJ (1991) Particle-image techniques for experimental fluid mechanics. Annu Rev Fluid Mech 23:261–304

Andrieu C, Chatenay D, Sykes C (1995) Measuring dynamic contact angles. C R Acad Sci Paris 320:351–357

Barron JL, Fleet DJ, Beauchemin SS (1994) Performance of optical flow techniques. Int J Comput Vis 12(1):43–77

Cox CS (1958) Measurement of slopes of high frequency wind waves. J Mar Res 16: 199–225

Dabiri D, Gharib M (2001) Simultaneous free-surface deformation and near-surface velocity measurements. Exp Fluids 30:381

Dalziel SB, Hughes GO, Sutherland BR (2000) Whole-field density measurements by "synthetic Schlieren". Exp Fluids 28:322–335

DaVis, by LaVision GmbH, Anna-Vandenhoeck-Ring 19, 37081 Goettingen, Germany, complemented with the PIVMat toolbox for Matlab. http://www.fast.u-psud.fr/pivmat

D'Errico J, "Inverse (integrated) gradient" for Matlab. http://www.mathworks.com/matlabcentral/. File 9734

Elwell FC (2004) Flushing of embayments. PhD thesis, University of Cambridge

Hild F, Roux S (2006) Digital image correlation: from displacement measurement to identification of elastic properties—a review. Strain 42:69–80

Jähne B, Riemer KS (1990) Two-dimensional wave number spectra of small-scale water surface waves. J Geophys Res 95:11531–11546

Jähne B, Schmidt M, Rocholz R (2005) Combined optical slope/height measurements of short wind waves: principle and calibration. Meas Sci Technol 16:1937–1944

Keller WC, Gotwols BL (1983) Two-dimensional optical measurement of wave slope. Appl Opt 22:3476–3478

Kurata J, Grattan KTV, Uchiyama H, Tanaka T (1990) Water surface mesurement in a shallow channel using the transmitted image of a grating. Rev Sci Instrum 61(2):736

Lange PA, Jähne B, Tschiersch J, Ilmberger I (1982) Comparison between an amplitude-measuring wire and a slope-measuring laser water wave gauge. Rev Sci Instrum 53:651

Liu J, Paul JD, Gollub JP (1993) Measurements of the primary instabilities of film flows. J Fluid Mech 250:69–101

Meier GEA (2002) Computerized background-oriented Schlieren. Exp Fluids 33:181

Moisy F, Rabaud M, Pinsolle E (2008) Measurement by digital image correlation of the topography of a liquid interface, ISFV13—13th international symposium on flow visualization, and FLUVISU12—12th French congress on visualization in fluid mechanics, paper 326, 1–4 July 2008, Nice

Périe JN, Calloch S, Cluzel C, Hild F (2002) Analysis of a multiaxial test on a C/C composite by using digital image correlation and a damage model. Exp Mech 42:318–328

Raffel M, Willert CE, Kompenhans J (1998) Particle image velocimetry: a practical guide. Springer, Heidelberg

Roesgen T, Lang A, Gharib M (1998) Fluid surface imaging using microlens arrays. Exp Fluids 25:126

Savalsberg R, Holten A, van de Water W (2006) Measurement of the gradient field of a turbulent free surface. Exp Fluids 41:629–640

Sutherland BR, Dalziel SB, Hughes GO, Linden PF (1999) Visualization and measurement of internal waves by 'synthetic Schlieren'. Part 1. Vertically oscillating cylinder. J Fluid Mech 390: 93–126

Tober G, Anderson RC, Shemdin OH (1973) Laser instrument for detecting water ripple slopes. Appl Opt 12(4):788–794

Zhang X (1996) An algorithm for calculating water surface elevations from surface gradient image data. Exp Fluids 21:43–48

Zhang X, Cox CS (1994) Measuring the two-dimensional structure of a wavy water surface optically: a surface gradient detector. Exp Fluids 17:225–237

Zhang X, Dabiri D, Gharib M (1996) Optical mapping of fluid density interfaces: concepts and implementations. Rev Sci Instrum 67(5):1858–1868

# Bibliographie


[1] R.J. Adrian. Particle-image techniques for experimental fluid mechanics. *Annu. Rev. Fluid Mech.*, 23 :261–364, 1991.

[2] M.H. Alford and M.C. Cregg. Near-inertial mixing : Modulation of shear, strain and microstructure at low latitude. *J. Geophys. Res.*, 106(C8) :947–968, 2001.

[3] C. N. Baroud, B. B. Plapp, Z.S. She, and H. L. Swinney. Anomalous self-similarity in a turbulent rapidly rotating fluid. *Phys. Rev. Lett.*, 88 :114501, 2002.

[4] J.L. Barron, D.J. Fleet, and S.S. Beauchemin. Performance of optical flow techniques. *Int. J. Comput. Vis.*, 12(1) :43–77, 1994.

[5] P. Bartello, O. Métais, and M. Lesieur. Coherent structures in rotating three-dimensional turbulence. *J. Fluid Mech.*, 273 :1–29, 1994.

[6] G. K. Batchelor. Note on a class of solutions of the navier–stokes equations representing steady rotationally–symmetric flow. *Q. J. Mech. Appl. Maths*, 4 :29–41, 1951.

[7] J.M. Becker and J.W. Miles. Standing radial cross-waves. *J. Fluid Mech.*, 222 :471–499, 1991.

[8] F. Bellet, F.S. Godeferd, J.F. Scott, and C. Cambon. Wave turbulence in rapidly rotating flows. *J. Fluid Mech.*, 562 :83–121, 2006.

[9] T.B. Benjamin and F. Ursell. The stability of a plane free surface of a liquid in vertical periodic motion. *Proc. R. Soc. Lond. A*, 225 :505–515, 1954.

[10] R. Benzi, S. Ciliberto, R. Tripiccione, C. Baudet, Massaioli F., and S. Succi. Extended self-similarity in turbulent flows. *Phys. Rev. E*, 48 :R29, 1993.

[11] G.P. Bewley, D.P. Lathrop, L.R.M. Maas, and K.R. Sreenivasan. Scaling in three-dimensional and quasi-two-dimensional rotating turbulent flows. *Phys. Fluids*, 19 :071701, 2007.

[12] D. Bonn, J. Eggers, J. Indekeu, and E. Rolley. Wetting and spreading. *Rev. Mod. Phys.*, 2008.

[13] L. Bourouiba and P. Bartello. The intermediate rossby number range and two-dimensional-three-dimensional transfers in rotating decaying homogeneous turbulence. *J. Fluid Mech.*, 587 :139–161, 2007.

[14] J.F. Brady and L. Durlofsky. On rotating disk flow. *J. Fluid Mech.*, 175 :363–394, 1987.

[15] J. Browaeys, J.-C. Bacri, R. Perzynski, and M. I. Shliomis. Capillary-gravity wave resistance in ordinary and magnetic fluids. *Europhys. Lett.*, 53(2) :209, 2001.

[16] G.L. Brown and A. Roshko. On density effects and large structure in turbulent mixing layers. *J. Fluid Mech*, 64 :775–816, 1974.

[17] T. Burghelea and V. Steinberg. Onset of wave drag due to generation of capillary-gravity waves by a moving object as a critical phenomenon. *Phys. Rev. Lett.*, 86 :2557, 2001.

[18] F. H. Busse and K.E. Heikes. Convection in a rotating layer : A simple case of turbulence. *Science*, 208 :173, 1980.

[19] C. Cambon. Turbulence and vortex structures in rotating and stratified flows. *Eur. J. Mech. B Fluids*, 20(4) :489–510, 2001.

[20] C. Cambon, L. Danaila, F. Godeferd, and J.F. Scott. Detailed anisotropy in the statistical description and dynamical approach to turbulent flows. *J. Fluid Mech. (soumis)*, 2010.

[21] C. Cambon and L. Jacquin. Spectral approach to nonisotropic turbulence subjected to rotation. *J. Fluid Mech.*, 202 :295, 1989.

[22] C. Cambon, N. N. Mansour, and F. S. Godeferd. Energy transfer in rotating turbulence. *J. Fluid Mech.*, 337 :303, 1997.

[23] C. Cambon, R. Rubinstein, and F. S. Godeferd. Advances in wave turbulence : rapidly rotating flows. *New Journal of Physics*, 6 :73, 2004.

[24] V.M. Canuto and M.S. Dubovikov. Physical regimes and dimensional structure of rotating turbulence. *Phys. Rev. Letters*, 78(4) :666, 1997.

[25] G.F. Carnevale, McWilliams, Y. J.C., Pomeau, J.B. Weiss, and Young W.R. Evolution of vortex statistics in two-dimensional turbulence. *Phys. Rev. Lett.*, 66(21) :2735–2738, 1999.

[26] E.A. Cerda and E.L. Tirapegui. Faraday's instability in viscous fluid. *J. Fluid Mech.*, 368 :195–228, 1998.

[27] S. Chakraborty and J.K. Bhattacharjee. Third-order structure function for rotating three-dimensional homogeneous turbulent flow. *Physical Review E*, 76 :036304, 2007.

[28] S. Chandrasekhar. *Hydrodynamic and hydromagnetic stability.* Dover Publications, Inc., 1961.

[29] T.K. Chereskin. Direct evidence for an ekman balance in the california current. *J. Geophys. Res.*, 100(C9) :18261–18269, 1995.

[30] S. Ciliberto and J.P. Gollub. Chaotic mode competition in parametrically forced surface waves. *J. Fluid Mech.*, 158 :381–398, 1985.

[31] P. Cobelli, P. Petitjeans, A. Maurel, V. Pagneux, and Mordant N. Space-time resolved wave turbulence in a vibrating plate. *Phys. Rev. Lett.*, 103 :204301, 2009.

[32] P. J. Cobelli, A. Maurel, V. Pagneux, and P. Petitjeans. Global measurement of water waves by fourier transform profilometry. *Exp. Fluids*, 46(6) :1037–1047, 2009.

[33] G. G. Coriolis. *Théorie Mathématique des effets du jeu de billard ; Sur le principe des forces vives dans les mouvements relatifs des machines ; Sur les équations du mouvement relatif des systèmes de corps (1835).* Réédition Jacques Gabay, 1990.

[34] P.P. Cortet, S. Atis, A. Chiffaudel, F. Daviaud, L. Divaret, and B. Dubrulle. Symmetry-breaking susceptibility and fluctuations crisis of a turbulent closed flow around $re = 10^5$. *to be subm.*, 2010.

[35] P.P. Cortet, P. Diribarne, R. Monchaux, A. Chiffaudel, F. Daviaud, and B. Dubrulle. Normalized kinetic energy as a hydrodynamical global quantity for inhomogeneous anisotropic turbulence. *Phys. of Fluids*, 21 :025104, 2009.

[36] P.P. Cortet, C. Lamriben, and F. Moisy. Viscous spreading of an inertial wave beam in a rotating fluid. *Phys. Fluids*, 22 :086603, 2010.

[37] Y. Couder, S. Protiere, Fort E., and Boudaoud A. Walking and orbiting droplets. *Nature*, 437 :208, 2005.

[38] C.S. Cox. Measurement of slopes of high frequency wind waves. *J. Marine Res*, 16 :199–255, 1958.

[39] S. B. Dalziel, G. O. Hughes, and B. R. Sutherland. Whole-field density measurements by "synthetic schlieren". *Exp. Fluids*, 28 :322–335, 2000.

[40] S.B. Dalziel. Decay of rotating turbulence : some particle tracking experiments. *Applied Scientific Research*, 49 :217–244, 1992.

[41] R. Dangla, F. Gallaire, and C.N. Baroud. Microchannel deformations due to solvent-induced pdms swelling. *Lab Chip, in press*, 2010.

[42] P.A. Davidson. *Turbulence*. Oxford University Press, 2004.

[43] M. Debacq, V. Fanguet, J.P. Hulin, D. Salin, and B. Perrin. Self-similar concentration profiles in buoyant mixing of miscible fluids in a vertical tube. *Phys. Fluids*, 13(11) :3097–3100, 2001.

[44] S.C. Dickinson and R.R. Long. Oscillating-grid turbulence including effects of rotation. *J. Fluid Mech.*, 126 :315–333, 1983.

[45] D. Dijkstra and G.J.F. van Heijst. The flow between finite rotating disks enclosed by a cylinder. *J. Fluid Mech.*, 128 :123–154, 1983.

[46] S. Douady. Experimental study of the faraday instability. *J. Fluid Mech.*, 221 :383–409, 1990.

[47] S. Douady, Y. Couder, and M. E. Brachet. Direct observation of the intermittency of intense vorticity filaments in turbulence. *Phys. Rev. Lett.*, 67 :983–986, 1991.

[48] S. Douady and S. Fauve. Pattern selection in faraday instability. *Europhys. Lett.*, 6 :221–226, 1988.

[49] P.G. Drazin and W.H. Reid. *Geophysical fluid dynamics*. Springer-Verlag, 1987.

[50] Y. Duguet. Oscillatory jets and instabilities in a rotating cylinder. *Phys. Fluids*, 18 :104104, 2006.

[51] A. Eddi, E. Fort, F. Moisy, and Y. Couder. Unpredictable tunneling of a classical wave-particle association. *Phys. Rev. Lett.*, 102 :240401, 2009.

[52] W.S. Edwards and S. Fauve. Patterns and quasipatterns in the faraday experiment. *J. Fluid Mech.*, 278 :123–148, 1994.

[53] F.C. Elwell. Flushing of embayments. *PhD thesis, University of Cambridge*, 2004.

[54] E. Falcon. Laboratory experiments on wave turbulence. *Discrete and continuous dynamical systems - Series B*, 13(4) :819–840, 2010.

[55] A. J. Faller. Instability and transition of the disturbed flow over a rotating disc. *J. Fluid Mech.*, 230 :245–269, 1991.

[56] M. Faraday. On a peculiar class of acoustical figures ; and on certain forms assumed by groups of particles upon vibrating elastic surfaces. *Philosophical transactions of the Royal Society of London*, 121 :299–340, 1831.

[57] U. Frisch. *Turbulence*. Cambridge University Press, 1995.

[58] S. Galtier. Weak inertial-wave turbulence theory. *Physical Review E*, 68 :015301(R), 2003.

[59] S. Galtier. Exact vectorial law for homogeneous rotating turbulence. *Phys. Rev. E*, 80 :046301, 2009.

[60] G. Gauthier, P. Gondret, and M. Rabaud. Axisymmetric propagating vortices in the flow between a stationary and a rotating disk enclosed by a cylinder. *J. Fluid Mech.*, 386 :105–126, 1999.

[61] G. Gauthier, Gondret P., F. Moisy, and M. Rabaud. Instabilities in the flow between co and counter-rotating disks. *J. Fluid Mech.*, 473 :1–21, 2002.

[62] F.S. Godeferd and L. Lollini. Direct numerical simulations of turbulence with confinement and rotation. *J. Fluid Mech.*, 393 :257–308, 1999.

[63] L. Gostiaux, T. Dauxois, H. Didelle, J. Sommeria, and S. Viboud. Quantitative laboratory observations of internal wave reflection on ascending slopes. *Phys. Fluids*, 18 :056602, 2006.

[64] L. Gostiaux, H. Didelle, S. Mercier, and T. Dauxois. A novel internal waves generator. *Exp. Fluids*, 42 :123, 2007.

[65] H. Greenspan. *The theory of rotating fluids*. Cambridge University Press, 1968.

[66] J. Hazewinkel, P. van Breevoort, S.B. Dalziel, and L.R.M. Maas. Observations on the wavenumber spectrum and evolution of an internal wave attractor. *J. Fluid Mech.*, 598 :373–382, 2008.

[67] R. Hide and C.W. Titman. Detached shear layers in a rotating fluid. *J. Fluid Mech.*, 29 :39–60, 1967.

[68] E. J. Hopfinger, F. K. Browand, and Y. Gagne. Turbulence and waves in a rotating tank. *J. Fluid Mech.*, 125 :505–534, 1982.

[69] A. Ibbetson and D. Tritton. Experiments on turbulence in a rotating fluid. *J. Fluid Mech.*, 68 :639–672, 1975.

[70] L. Jacquin, O. Leuchter, C. Cambon, and J. Mathieu. Homogeneous turbulence in the presence of rotation. *J. Fluid Mech.*, 220 :1, 1990.

[71] J. Krenn, P. Scharfer, and W. Schabel. Visualization of surface deformations during thin film drying using a digital image correlation method. subm. to Chemical Engineering and Processing : Process Intensification. Special Issue : Coating and Drying of Thin Films, 2010.

[72] J. Kurata, K. T. V. Grattan, H. Uchiyama, and T. Tanaka. Water surface mesurement in a shallow channel using the transmitted image of a grating. *Rev. Sci. Instrum.*, 61 :736–739, 1990.

[73] A. La Porta, G.A. Voth, F. Moisy, and E. Bodenschatz. Using cavitation to measure statistics of low-pressure events in large-reynolds-number turbulence. *Phys. Fluids*, 12(6) :1485–1496, 2000.

[74] C. Lamriben, P.P. Cortet, F. Moisy, and L.R.M. Maas. Excitation of inertial modes in a closed grid turbulence experiment under rotation. *subm. to Phys. Fluids*, 2010.

[75] J. Lighthill. *Waves in fluids*. Cambridge University Press, 1978.

[76] A. Linn. Oh, what a spin we're in, thanks to the coriolis effect. *Smithsonian*, 13(11) :66–73, 1983.

[77] M.S. Longuet-Higgins. Mass transport in water waves. *Phil. Trans. Roy. Soc. London. Ser. A.*, 245 :535–581, 1953.

[78] M.S. Longuet-Higgins. On the transport of mass by time-varying ocean currents. *Deep Sea Research*, 16 :431–437, 1969.

[79] J. M. Lopez. Characteristics of endwall and sidewall boundary layers in a rotating cylinder with a differentially rotating endwall. *J. Fluid Mech.*, 359 :49–79, 1998.

[80] J.M. Lopez, J.E. Hart, F. Marques, S. Kittelman, and J. Shen. Instability and mode interactions in a differentially-driven rotating cylinder. *J. Fluid Mech.*, 462 :383–409, 2002.

[81] S. Lukaschuk, S. Nazarenko, S. McLelland, and P. Denissenko. Gravity wave turbulence in wave tanks : Space and time statistics. *Phys. Rev. Lett.*, 103(6) :044501, 2009.

[82] L.R.M. Maas. On the amphidromic structure of inertial waves in a rectangular parallelepiped. *Fluid Dyn. Res.*, 33 :373–401, 2001.

[83] L.R.M. Maas. Wave focusing and ensuing mean flow due to symmetry breaking in rotating fluids. *J. Fluid Mech.*, 437 :13–28, 2001.

[84] A.D. McEwan. Inertial oscillations in a rotating fluid cylinder. *J. Fluid Mech.*, 40 :603–639, 1970.

[85] G.E.A. Meier. Computerized background-oriented schlieren. *Exp. Fluids*, 33 :181, 2002.

[86] L. Messio, M. Morize, M. Rabaud, and F. Moisy. Experimental observation using particle image velocimetry of inertial waves in a rotating fluid. *Experiments in Fluids*, 44 :519–528, 2008.

[87] J. Miles and D. Henderson. Parametrically forced surface waves. *Ann. Rev. Fluid Mech.*, 22 :143–165, 1990.

[88] F. Moisy. *Etude expérimentale des fluctuations de vitesse, de température et de pression en turbulence développée.* PhD thesis, Université Pierre et Marie Curie - Paris 6, 2000.

[89] F. Moisy, L. Agostini, and G. Tan. Structure functions and energy transfers in a decaying rotating turbulence experiment. Advances in Turbulence XII, Springer Proceedings in Physics 132, Ed. by B. Eckhardt, 427-430, 2009.

[90] F. Moisy, J.S. Andersen, P. Tabeling, and H. Willaime. Passive scalar intermittency in low temperature helium flows. *Phys. Rev. Lett.*, 86(21) :4827–4830, 1999.

[91] F. Moisy, O. Doaré, T. Pasutto, O. Daube, and M. Rabaud. Experimental and numerical study of the shear layer instability between two counter-rotating disks. *J. Fluid Mech.*, 507 :175–202, 2004.

[92] F. Moisy and J. Jimenez. Geometry and clustering of intense structures in isotropic turbulence. *J. Fluid Mech.*, 513 :111–133, 2004.

[93] F. Moisy and J. Jimenez. Clustering of intense structures in isotropic turbulence : numerical and experimental evidence. IUTAM Symposium on Elementary Vortices and Coherent Structures : Significance in Turbulence Dynamics, Kyoto, Japan, 26-28 October 2004. Ed. S. Kida, Springer-Verlag, 3-12, 2006.

[94] F. Moisy, G. J. Michon, and M. Rabaud. Cross-waves induced by vertical oscillations of a fully immersed vertical plate. *in preparation for Phys. Fluids*, 2010.

[95] F. Moisy, C. Morize, M. Rabaud, and J. Sommeria. Decay laws, anisotropy and cyclone-anticyclone asymmetry in decaying rotating turbulence. *J. Fluid Mech., in press*, 2010.

[96] F. Moisy, Tabeling P., and Willaime H. Kolmogorov equation in a fully developed turbulence experiment. *Phys. Rev. Lett.*, 82(20) :3994–3997, 1999.

[97] F. Moisy, T. Pasutto, and M. Rabaud. Instability patterns in the flow between counter-rotating disks. *Nonlinear processes in Geophysics*, 10(3) :281–288, 2003.

[98] F. Moisy, M. Rabaud, and E. Pinsolle. Measurement by digital image correlation of the topography of a liquid interface. ISFV13 - 13th International Symposium on Flow Visualization, and FLUVISU12 - 12th French Congress on Visualization in Fluid Mechanics, Paper no. 326, July 1-4, 2008, Nice, 2008.

[99] F. Moisy, M. Rabaud, and K. Salsac. A synthetic schlieren method for the measurement of the topography of a liquid interface. *Exp. Fluids*, 46(6) :1021–1036, 2009.

[100] R. Monchaux, M. Berhanu, M. Bourgoin, M. Moulin, Ph. Odier, J.-F. Pinton, R. Volk, S. Fauve, N. Mordant, F. Pétrélis, A. Chiffaudel, F. Daviaud, B. Dubrulle, C. Gasquet, L. Marié, and F. Ravelet. Generation of a magnetic field by dynamo action in a turbulent flow of liquid sodium. *Phys. Rev. Lett.*, 98 :2007, 2004.

[101] C. Morize. *De la turbulence 3D en déclin à la turbulence anisotrope dominée par la rotation.* PhD thesis, Univ. Paris Diderot, 2006.

[102] C. Morize, M. Le Bars, P. Le Gal, and A. Tilgner. Zonal winds driven by tides. *Phys. Rev. Lett.*, 104 :214501, 2010.

[103] C. Morize and F. Moisy. Energy decay of rotating turbulence with confinement effects. *Phys. Fluids*, 18 :065107, 2006.

[104] C. Morize, F. Moisy, and M. Rabaud. Decaying grid-generated turbulence in a rotating tank. *Phys. Fluids*, 17 :095105, 2005.

[105] C. Morize, F. Moisy, M. Rabaud, and J. Sommeria. On the cyclone-anticyclone asymmetry in decaying rotating turbulence. Conference on Turbulence and Interactions TI2006, May 29 - June 2, 2006, Porquerolles, France, 2006.

[106] D.E. Mowbray and B.S.H. Rarity. A theoretical and experimental investigation of the phase configuration of internal waves of small amplitude in a density stratified liquid. *J. Fluid Mech.*, 28 :1–16, 1967.

[107] H. Niino and N. Misawa. An experimental and theoretical study of barotropic instability. *J. Atmos. Sci.*, 41 :1992–2011, 1984.

[108] C. Nore, F. Moisy, and L. Quartier. Experimental observation of near-heteroclinic cycles in the von karman swirling flow. *Phys. Fluids*, 17 :064103, 2005.

[109] C. Nore, M. Tartar, O. Daube, and L.S. Tuckerman. Survey of instability thresholds of flow between exactly counter-rotating disks. *J. Fluid Mech.*, 511 :45–65, 2004.

[110] C. Nore, L.S. Tuckerman, O. Daube, and S. Xin. The 1 :2 mode interaction in exactly counter-rotating von kármán swirling flow. *J. Fluid Mech.*, 477 :51–88, 2003.

[111] K.S. Peat. Internal and inertial waves in a viscous rotating stratified fluid. *Appl. Sci. Res.*, 33 :481–499, 1978.

[112] P. Pieranski. Measurement of slopes of high frequency wind waves. *J. Phys.*, 44 :573, 1983.

[113] F.J. Poulin, G.R. Flierl, and J. Pedlosky. Parametric instability in oscillatory shear flows. *J. Fluid Mech.*, 481 :329–353, 2003.

[114] M. Raffel, C. E. Willert, and J. Kompenhans. *Particle Image Velocimetry : a practical guide*. Springer-Verlag, 1998.

[115] F. Ravelet, L. Marié, A. Chiffaudel, and F. Daviaud. Multistability and memory effect in a highly turbulent flow : Experimental evidence for a global bifurcation. *Phys. Rev. Lett.*, 93 :164501, 2004.

[116] N. Riley. Steady streaming. *Ann. Rev. Fluid Mech.*, 33 :43–65, 2001.

[117] J. E. Ruppert-Felsot, O. Praud, E. Sharon, and H. L. Swinney. Extraction of coherent structures in a rotating turbulent flow experiment. *Phys. Rev. E*, 72 :016311, 2005.

[118] P.G. Saffman. Large scale structure of homogeneous turbulence generated at initial instant by distribution of random impulsive forces. *Phys. Fluids*, 10 :1349, 1967.

[119] P. Sagaut and C. Cambon. *Homogeneous Turbulence Dynamics*. Cambridge University Press, 2008.

[120] J. Seiwert, C. Morize, and F. Moisy. On the decrease of intermittency in decaying rotating turbulence. *Phys. Fluids*, 20 :071702, 2008.

[121] E. Serre. *Instabilités de couche limite dans des écoulements confinés en rotation. Simulation numérique directe par une méthode spectrale de comportements complexes*. PhD thesis, Université de la Méditérannée Aix-Marseille II, Ecole Supérieure de Mécanique de Marseille, 2000.

[122] K.D. Squires, J.R. Chasnov, N.N. Mansour, and C. Cambon. The asymptotic state of rotating homogeneous turbulence at high reynolds numbers. In *74th Fluid Dynamics Symposium on "Application of Direct and Large Eddy Simulation to Transition and Turbulence," Chania, Greece*, pages 1–9, 1994.

[123] P.J. Staplehurst, P.A. Davidson, and S.B. Dalziel. Structure formation in homogeneous freely decaying rotating turbulence. *J. Fluid Mech.*, 598 :81–105, 2008.

[124] A. Stegner, T. Pichon, and M. Beunier. Elliptical-inertial instability of rotating karman vortex streets. *Phys. Fluids*, 17 :066602, 2005.

[125] B. R. Sutherland, S. B. Dalziel, G. O. Hughes, and P. F. Linden. Visualization and measurement of internal waves by 'synthetic schlieren'. part 1. vertically oscillating cylinder. *J. Fluid Mech.*, 390 :93–126, 1999.

[126] B.R. Sutherland. Internal wave instability : Wave-wave versus wave-induced mean flow interactions. *Phys. Fluids*, 18 :074107, 2006.

[127] P. Tabeling. Two-dimensional turbulence : a physicist approach. *Physics Reports*, 362 :1–62, 2002.

[128] S. Taneda. An experiment on cross-waves. *Fluid Dynamics Research*, 16(2-3) :61–70, 1995.

[129] M. Thiele and W.C ; Müller. Structure and decay of rotating homogeneous turbulence. *J. Fluid Mech.*, 637 :425–442, 2009.

[130] N.H. Thomas and T.N. Stevenson. A similarity solution for viscous internal waves. *J. Fluid Mech.*, 54(3) :495–506, 1972.

[131] A. Tilgner. Zonal wind driven by inertial modes. *Phys. Rev. Lett.*, 99 :194501, 2007.

[132] S.S. Traugott. Influence of solid body rotation on screen produced turbulence. Technical report, NACA, 1958.

[133] L. J. A. van Bokhoven, C. Cambon, L. Liechtenstein, F. S. Godeferd, and H. J. H. Clercx. Refined vorticity statistics of decaying rotating three-dimensional turbulence. *Journal of Turbulence*, 9(6) :1–24, 2008.

[134] L. J. A. van Bokhoven, H. J. H. Clercx, G. J. F. van Heijst, and R. R. Trieling. Experiments on rapidly rotating turbulent flows. *Phys. Fluids*, 21 :096601, 2009.

[135] G. Veronis. The analogy between rotating and stratified fluids. *Ann. Rev. Fluid Mech.*, 2 :37–66, 1970.

[136] B. Voisin. Limit states of internal waves. *J. Fluid Mech.*, 496 :243–293, 2003.

[137] F. Waleffe. The nature of triad interactions in homogeneous turbulence. *Phys. Fluids A*, 4(2) :350–364, 1992.

[138] F. Waleffe. Inertial transfers in the helical decomposition. *Phys. Fluids A*, 5(3) :677–685, 1993.

[139] R. Wigeland and H. Nagib. Grid-generated turbulence with and without rotation about the streamwise direction. *Fluids and Heat Transfer*, R78 :1, 1978.

[140] H. Willaime, J. Maurer, , F. Moisy, and P. Tabeling. Turbulence over arrays of obstacles in low temperature helium gas. *Eur. Phys. J.B*, 18(20) :363–369, 2000.

[141] B. Zakharov, V.S. L'vov, and G. Falkovitch. *Kolmogorov spectra of turbulence*. Springer, Berlin, 1992.

[142] P.J. Zandbergen and D. Dijkstra. Von kárman swirling flows. *Ann. Rev. Fluid Mech.*, 19 :465–491, 1987.

[143] O. Zeman. A note on the spectra and decay of rotating homogeneous turbulence. *Phys. Fluids*, 6(10) :3221–3223, 1994.

[144] Y. Zhou. A phenomenological treatment of rotating turbulence. *Phys. Fluids*, 7 :2092, 1995.

[145] J. Znaien. *Etude locale du mélange induit par gravité de deux fluides dans la géométrie confiné d'un tube incliné*. PhD thesis, Université Paris-Sud 11, 2009.

[146] J. Znaien, Y. Hallez, F. Moisy, J. Magnaudet, J.P. Hulin, and E.J. Salin, D. Hinch. Experimental and numerical investigation of flow structure and momentum transport in a turbulent buoyancy-driven flow inside a tilted tube. *Phys. Fluids*, 21 :115102, 2009.

[147] J. Znaien, F. Moisy, and J.P. Hulin. Flow structure and momentum transport for buoyancy driven mixing flows in long tubes at different tilt angles. *subm. to Phys. Fluids*, 2010.

**Résumé**

Ce mémoire présente une synthèse de mes travaux de recherche effectués depuis mon recrutement au laboratoire FAST en septembre 2000. Mes travaux sont essentiellement organisés autour de 4 axes : les instabilités dans les écoulements de von Kármán, les ondes d'inertie, la turbulence en rotation, et les ondes de surface. Ces 4 axes de recherche ont entre eux un certain nombre de connections, comme l'influence de la rotation sur la nature d'un écoulement laminaire ou turbulent, ou encore les systèmes d'ondes dispersives en interaction, qu'il s'agisse des ondes capillaires ou des ondes d'inertie en référentiel tournant. D'un point de vue expérimental, ces axes de recherche ont également en commun l'utilisation de méthodes de mesure optiques, qu'il s'agisse de la Vélocimétrie par Images de Particules (PIV), méthode aujourd'hui standard en mécanique des fluides, ou encore du "Synthetic Schlieren", que nous avons étendu au cas des ondes de surface.

**Abstract**

This manuscript presents a synthesis of my research activities since September 2000, and is organized around four themes : instabilities in the von Kármán swirling flows, inertial waves, rotating turbulence, and surface waves. These four research areas have a number of connections between them, such as the influence of rotation on the nature of laminar or turbulent flows, and the interaction of dispersive waves, either capillary waves or inertial waves in a rotating frame. On the experimental point of view, these research areas also share the use of optical methods, from Particle Image Velocimetry (PIV), now standard in mechanics fluids, to the "Synthetic Schlieren", which we have extended to the measurement of surface waves.